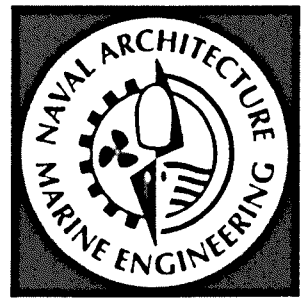

BREAKING WAVE SLAP LOADING ON FPSO BOWS AND SHALLOW WATER CYLINDERS

by

LI XU

A thesis submitted for the degree of Doctor of Philosophy

Department of Naval Architecture and Marine Engineering
Universities of Glasgow and Strathclyde

May 2006

Li Xu

May 2006

Acknowledgements

Firstly, I would like to thank my supervisor Prof. Nigel Barltrop for guidance, support and encouragement through my studies. His support and stimulation in last four years were very important to finalize this work.

Also I would like to acknowledge the important technical contributions from all the people in the Acre Road Hydrodynamics Laboratory of the department, including Barbaros Okan (Research assistant for the Schiehallion experiments); Bill Wright, Bernard Reilley, Jack Sharky and Donald Nicholson for Model making; Grant Dunning, David Sinclair and Donald Nicholson for Testing; finally Frank Sweeney and David Percival for Electronics and Data Acquisition.

Many thanks will also go to the partners in the SAFE-FLOW EU project, particularly Bas Buchner and Arjan Voogt (Marin), Trevor Hodgson (Atkins and now Galbraith Consulting) and Sandy Fyfe (PAFA), since there was a continuous and useful exchange of results and ideas between this work and the SAFE-FLOW project.

Finally I would say big big thank to my family and all my friends without whom I could not be able to finish my study. Thank you for your understanding, support and encouragement.

Abstract

In 1989 the Schiehallion FPSO suffered bow damage from a steep fronted wave slap and the uncertainty in how to design for this type of loading became a concern to the oil industry and the regulators. The aim of this study is to research the insight of breaking wave impact on the bow of ship-type offshore structures experimentally and develop a methodology on how to design this type of loading.

Steep wave impact pressures and the structural dynamic response on FPSO (ship-shaped Floating oil Production Storage and Offloading vessel) bows are studied using 1/80 scale instrumented models and time domain simulation with the funding from HSE and BP, a grant from EPSRC, associated in-kind industrial contributions, a University/Departmental Scholarship and an IMarEST Scholarship.

This work has increased the understanding of the nature of the breaking waves that can cause large slap forces that are important for the design of offshore floating structures (and should also be relevant to ship design).

Methods of generating model scale wave groups that should produce approximately the 1 in 3 hour maximum loads, when large waves break in unidirectional sea states prescribed by Hs and Tz, have been developed.

These methods have been extended to spread seas and also to a 'partial' breaking wave in less steep seas, but no testing has taken place in spread seas or the longer period seas.

In addition an empirical relationship has been determined that represents the steepening of a wave front based on the underlying linear wave.

The forces and pressures from these waves have been measured on 1/80 scale models of the Schiehallion FPSO and Loch Rannoch shuttle tanker.

A time history simulation method of bow loading in random seas has been developed. It uses the wave front steepening relationship derived from the tests and a relatively simple slap force prediction based on velocity times rate of change of added mass. Incident wave pressure effects (with a non-linear correction) and added mass times acceleration forces are also included.

Simple slam coefficient type formula has also been derived for easy application. The formula accounts for the effect of the size of the loaded area on the average pressure and the rise and decay times of the average pressure and, hence, the dynamic amplification of the response at the bow.

The above experimental and theoretical work has considerably advanced the quantitative understanding of bow slap. Quantitatively we have some confidence in the most probable maximum slap force predictions in: long-crested seas with sea state steepnesses around 1/14 - 1/15 and when no air is trapped.

CONTENTS

List of Figures

List of Tables

Nomenclature

Without specific explanation, the symbols used in this thesis are referred to as follows:

α	Front steepness balance
a	Acceleration
β	Deadrise angle
c	Wave celerity
cz	Zero crossing celerity
C_f	Impact force coefficient
C_p	Impact pressure coefficient
d	Width of the wetted area
d_w	Water depth
D	Cylinder diameter
e	Aspect ratio
f	Wave frequency
f_p	Peak frequency of spectrum
F_I	Impact force
γ	Jonswap spectrum enhancement factor
H	Wave height
H_0	Deep water wave height
H_s	Significant wave height
k	Wave number
L	Length
L_z	Zero crossing wave length
m	Structure mass
m_v	Added mass per unit length
M	Total mass including added mass
p	Impact pressure
ρ	Water density

r	Half width of the wetted area
S	Scale, = Model size/Prototype size
S_{ea}	Sea state steepness
S_z	Inverse of sea state steepness
t_d	Decay time
t_r	Rise time
T	The effective thickness for the given mode for a plate vibrating in water
T_z	Zero crossing period
u	Velocity
v	Relative velocity between the structure and the water surface
V	Wedge velocity
V_I	Impact velocity
w	Width of the wetted area with spray
W	Panel width
Z	Panel height

1 Introduction

1.1 The Problem

In rough seas with large relative ship motion, slamming may occur with large water impact loads. Usually. Slamming loads are much larger than other wave loads. Sometimes ships suffer local damage from the impact load or large-scale buckling on the deck. For high-speed ships, even if each impact load is small, frequent impact loads accelerate fatigue failures of hulls. Thus, slamming loads may threaten the safety of ships.

Therefore a rational and practical estimation method of wave impact loads is one of the most important prerequisites for safe design of ships and ocean structures. Wave impact is a strongly nonlinear phenomenon and a random process which is very sensitive to relative motion and contact angle between body and free surface. Since the duration of wave impact loads is very short, hydro-elastic effects are large. In addition, because of air trapping, the wave impact phenomenon is difficult to describe by theory. Wave impact has challenged many researchers for more than half a century since Karman's work in 1929. Nowadays, mechanisms of wave impacts are correctly understood for the 2-D case, and accurate impact loads can be also given in the framework of linear stochastic theories. Our knowledge on wave impact is still far from sufficient. Therefore a need for rational and practical estimation of wave impact loads is keenly felt.

The wave impact caused by slamming has been roughly classified into four types (Figure 1.1) by Sumitoshi Mizoguchi et al (1996). Bottom slamming (1) occurs when emerged bottoms re-enter the water surface. Bow-flare slamming (2) occurs for high relative speed of bow-flare to the water surface. Both slamming types occur in head sea with large pitching and heaving motions. Breaking wave

impacts (3) are generated by the superposition of incident wave and bow wave hitting the bow of a blunt ship even for small ship motion. Wet-deck slamming (4) occurs when the relative heaving amplitude is larger than the height of a catamaran's wet-deck. These water impacts are all 3-D phenomenon but have been treated as 2-D for simplicity. E.g., types (1) and (2) were idealized as 2-D wedge entry to the calm water surface. Type (3) was also studied as 2-D

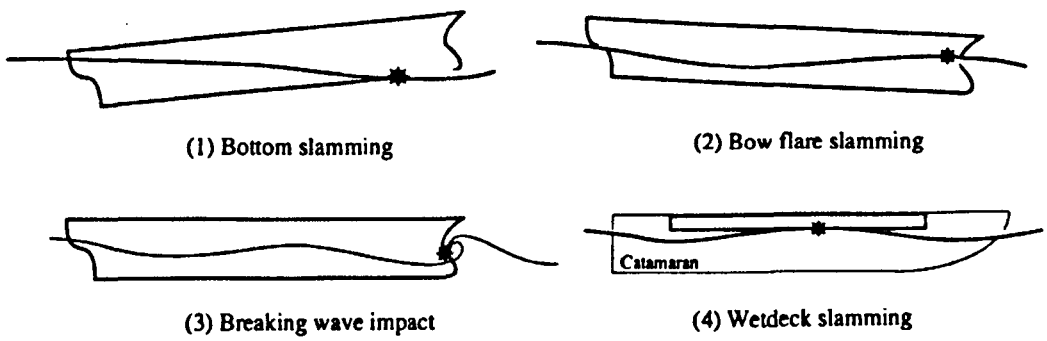

phenomenon similar to wave impact on breakwaters.

Figure 1.1 Types of slamming impact of a ship (Sumitoshi Mizoguchi *et al*, 1996)

1.2 Historical Overview

1.2.1 Studies on Bottom and Bow-flare types of slamming

Von Karman (1929) was the first to theoretically study water impact. He idealized the impact as 2-D wedge entry problem on the calm water surface to estimate the water impact load on a seaplane during landing. Mass, deadrise angle, and initial penetrating velocity of the wedge are denoted as m, β and V_0. Since the impact is so rapid, v.Karman assumed very small water surface elevation during impact and negligible gravity effects. Then the added mass per unit length is approximately $m_v = (1/2)\pi\rho r^2$. ρ is the water density and r the half width of the wet area implicity computed from $dr/dt = V\cot\beta$. The momentum before the impact mV_0

must be equal to the sum of the wedge momentum mV and added mass momentum $m_v V$, yielding the impact load as

$$F_I = \frac{V_0^2 \cot\beta}{(1+\frac{\rho\pi r^2}{2m})^3}\rho\pi r \tag{1.1}$$

Since v.Karman's impact model neglects the water surface elevation, the added mass and impact load are underestimated, particularly for small deadrise angle. Wagner (1932) derived a more realistical water impact theory including the hydrodynamic effect for small deadrise angle β. If β is small and gravity neglected, the flow under wedge can be approximated by the flow around an expanding flat plate in uniform flow with velocity V. Wagner's theory can be applied to arbitrary shaped bodies as long as the dearise angle is small enough not to trap air. Toyama (1993) applied Wagner's theory to various bodies including curved wedges, unsymmetrical wedges, knuckled wedged, wing sections, ect. Wagner's impact theory is simple and useful, but not consistently linearized. Many experimental studies have checked the accuracy of Wagner's theory. Chuang (1967) measured peak impact pressures for 2-D wedges with various deadrise angles from $\beta = 0^0$ to $\beta = 45^0$ in free fall. Peak impact pressures were a little lower than estimated. This suggested that Wagner's theory gives conservative estimates for practical use. Takemoto (1984) pointed out that a correction is needed on the peak pressure measured by pressure gauges with finite gauge area. He analysed the dynamic response of the pressure gauge diaphragm by FEM to correct the measured data. Corrected peak pressures agreed well with estimated by Wagner's theory. Allen and Jones (1987) present the same idea. Today, Wagner's theory is believed to give accurate peak impact pressure for practical use. The singularity of Wagner's theory can be removed taking spray into account. Watanabe (1986a,b) matched the planing plate solution for the splash region to the expanding plate solution of Wagner (asymptotic expansion). But, as far as only the peak impact pressure is concerned, Watanabe and Wagner show no big differences. Cointe (1989) derived a similar theory independently. Howison et al. (1991) applied these theories to various shapes.

For many practical impact problems, the body shape is not simple, the effect of gravity is considerably large, and the elasticity of the body is important for the damage analysis. In such cases, numerical methods can be powerful tools. Belytschko and Mullen (1981) solved the water impact of an elastic cylinder using Marker-and Cell method for fluid analysis and a FEM for the elastic body analysis. The numerical results agree well with experimental results. Arai and Matsunage (1989) used the same code to simulate the water impact of a 2-D flared body including the effect of gravity. Their computations agree qualitatively and quantitatively well with their experiments. Greenhow (1987) simulated free fall experiments of a 2-D wedge on a calm water surface by a boundary element method. He took gravity into account and showed the applicability of his method. Maskew et al (1993) developed a 3-D panel code. For most problems, the code generally has a fixed panel format, however, for intersecting free surface problems the code must re-panel the surface automatically each time step in order to keep the free surface intersection and panel edge aligned. Engle and Lewis (2003) compared selected methods of predicting hydrodynamic impacts with available drop test data of 2-D wedge shaped section shapes with two deadrise angles 10^0 and 20^0 and also compared with Wagner and Chuang theories.

1.2.2 Studies on breaking wave impact

The determination of breaking wave forces on coastal structures has been of considerable interest since the beginning of the century. Tests have been carried out at both full and reduced scales to determine the pressures and forces due to breaking wave impact on sea walls and breakwaters.

Because of the lack of necessary laboratory equipment, early investigators (Gaillard, 1905; Hiroi, 1920) had to measure the wave forces in full-scale experiments using spring-type dynamometers as the pressure measuring devices

which were incapable of responding to impacts of very short duration. However, these early experiments did provide guidance to later investigators on the magnitude of impact pressures to be expected. Kirkgöz (1995) pointed out that the laboratory and field investigations of Larras (1937) and Rouville *et al.* (1938), with the aid of sensitive measuring equipment, brought new insight into the breaking wave impact phenomenon both in terms of pressure magnitudes and durations. Following those studies, numerous investigators in both laboratory and the field have collected data to determine temporal and spatial variations of wave impact pressures and the major parameters affecting them.

Measurements of full-scale wave impact pressures on seawalls have been made over a period of four years, up to and including the winter of 1980/1981, on seawalls in the South and West of England (Blackmore and Hewson, 1984). This investigation is the first of its kind to be carried out in the U.K. using modern measuring and recording techniques and has produced significantly more wave impact pressure data than all previous full-scale investigations. Poor correlation was found between the semi-empirical equations at present used to estimate wave impact pressures and the prototype data obtained during this investigation. A rational expression for the estimation of wave impact pressures on coastal structures has thus been derived based on the local wave parameters at impact and includes a coefficient related to the percentage of air entrained in the incident wave. Later Müller and Whittaker (1996) compared two formulas recommended by the Coastal Engineering Research Center and by the British Standard Institution for calculation of wave impact pressures. Neither formula considers all relevant parameters. Both formulas showed poor agreement with field measurements. Recently Breaking Wave IMpacts on steep fronted COastal STructures (the BWIMCOST project) are being investigated by means of a combination of field, laboratory and analytical/numerical studies by a team from the University of Plymouth (UoP), the Queen's University of Belfast (QUB) and the University of Bristol (UoB). The overall aim is to gain a better understanding of wave loading and its effects on coastal structures leading to the development of

better prediction methods and scaling laws. Greater understanding of the mechanics of the violent wave impacts and of the role of aeration is being developed from mathematical and numerical modelling of wave impacts (Bredmose, *et al.* 2003; Peregrine, *et al.* 2004; Wolters, *et al.* 2004). New measurements of wave impact loads on vertical/steep walls at large scale in the CIEM/LIM flume at Barcelona under the VOWS project (Violent Overtopping of Waves at Seawalls) have been compared with historical prediction methods. Scatter is large over the range of condition tested. A simple and intuitive new prediction formula has been suggested which uses the most informative parameters and seems to give a better estimation of wave impact loads (Cuomo and Allsop, 2004).

Oumeraci *et al.* (1993) measured the impact pressures and forces together with simultaneous video records of the wave motion at and in front of caisson breakwaters in a wave flume. The results obtained suggest that the observed breaker shapes can be identified into four main breaker types by the recorded force histories, as well as by the impact pressure histories and distribution, without any use of the corresponding video pictures: 1) Turbulent Bore; 2) Well-Developed Plunging Breaker with Large Cushion of Air; 3) Plunging Breaker with Small Cushion Air; 4) Upward Deflected Breaker. Similar work on vertical cylinders has been done by Chan et al. (1995). The results can serve as a useful reference for numerical and theoretical modelling of extreme wave loads on surface-piercing vertical cylinders.

Breaking wave impact on vertical and sloping coastal structures has been studied in detail experimentally and theoretically by Kirkgöz (1991, 1995, 2004) and Tanrikulu *et al.* (2002). Laboratory tests were conducted to measure the impact pressures of breaking waves on vertical, 5° forward, and 5, 10, 20, 30 and 45° backward sloping walls. It was found that the impact pressures and resulting forces on sloping walls can be greater than those on a vertical wall and the still-water level can be taken as the acting place for the maximum impact pressure on

the wall. The results from a theoretical approach based on the pressure impulse were found to agree well with the experimental data. Large-scale experiments were carried out by Wienke et al. (2001) to investigate impact forces on cylinders due to breaking waves and the same conclusions have been drawn.

From design point of view, Kortenhaus *et al.* (2001) have summarised a number of formulae available for different types of waves breaking at the structure (see Table 1.1). These formulae generally include magnitudes of maximum pressures, their distributions and forces. All formulae are fully empirical or semi-empirical as the process of wave breaking at the structure is still not fully explained. Burcharth and Hughes (2005) did the similar work (see Table 1.2) and also presented the detailed calculation process of each method.

Table 1.1 Overview of design methods for wave loading (Kortenhaus *et al.*, 2001)

Author	Year	Pressures	Forces	Comments
		Quasi-Static Waves		
Sainflou	1928	yes	Yes, but difficult	Vertical wall, no berm
Miche-Rundgren	1944 1958	yes	yes	Design curves from SPM, 1984
Goda	1958	yes	yes	Most-widely used design method
		Impact Waves		
Hiroe	1919	yes	yes	Vertical wall
Bagnold	1939	-	-	Conceptual model only
Minikin	1963	yes	yes	Sometimes incorrect simensions
Ito	1971	yes	yes	
Blackmore & Hewson	1984	yes	yes	
Partenscky	1988	yes	Not given	Air content of wave needed
Kirkgöz	1995	yes	yes	Vertical wall only
Takahashi *et al.*	1994	yes	yes	Extension of Goda model
Allsop *et al.*	1996	no	yes	
Walkden *et al.*	1996	no	yes	Relation of forces and rise time
Oumeraci & Kortenhaus	1997	yes	yes	Time-dependent approach
McConnell	1998	no	yes	Amendment of O&K, 1997
Hull & Müller	1998	yes	yes	Amendment of O&K, 1997
Vicinanza	1998	yes	yes	Amendment of O&K, 1997
		Broken Waves		
SPM	1984	yes	yes	Vertical wall only
Camfield	1991	yes	yes	Amendment of SPM, 1984
Jensen	1984	yes	yes	Grown walls
Bradbury & Allsop	1988	yes	yes	Grown walls
Pedersen	1997	yes	yes	Grown walls
Martin *et al.*	1997	yes	yes	Grown walls

Table 1.2 Design formulae for wave-generated forces on vertical walls and caissons (Burcharth and Hughes, 2005)

Formulae	Waves	Structure
Sainflou	Standing	Impermeable vertical wall
Goda	2-D oblique	Impermeable vertical wall
Goda formula, modified by Takahashi, Tanimoto, and Shimosako, 1994a	Provoked breaking	Impermeable vertical wall
Goda formula forces and moments	2-D head-on	Impermeable vertical wall
Goda formula modified by Tanimoto and Kimura 1985	2-D head-on	Impermeable vertical wall
Goda formula modified by Takahashi and Hosoyamada 1994	2-D head-on	Impermeable sloping top
Goda formula modified by Takahashi, Tanimoto, and Shimosako, 1990	2-D head-on	Horizontal composite structure
Goda formula modified by Takahashi, Tanimoto, and Shimosako, 1994b	3-D head-on	Vertical slit wall

Breaking wave impacts on vertical cylinders and breakwaters were studied by many researchers. The work on FPSOs is scarce.

1.2.3 Studies on wet-deck slamming

In heavy storms, the waves and ship motions can become so large that water flows onto the deck of a ship. This problem is known as 'shipping of water', 'deck wetness' or 'green water loading'.

Green water (or 'deck wetness') has been the subject of study and debate since early days of research into ship behaviour at the end of the Nineteenth Century. However, the work by Newton (1959) is generally seen as the first large systematic study in this field. His investigations were mainly based on visual

observations of the deck wetness, which he categorised as 'dry', 'wet' or 'very wet'. Other contributions came from Tasaki (1963) who investigated the wet-deck problem by measuring the amount of shipped water with a special water collection mechanism in his model, and Ochi (1964) who applied his statistical methods to the prediction of slamming and shipping of green water.

In later years, a number of experimental studies have been carried out, such as the work of Hoffman and Maclean (1970) and the studies presented by Hong, Lee and Gong (1993) and by Gu, Miao and Gu (1993). A predicting method of green water loading was developed by Fukuda et al (1973) and later by Kawakami and Tanaka (1975, 1977). In a study evaluating existing green water methods with their assumptions, Buchner (1994) performed model tests in regular and irregular waves with a frigate of Royal Netherlands Navy. He derived a new calculation method for the pressure of the water on the deck, based on the evaluation of Newton's momentum relations for a control volume on the deck. Later the method has been validated by work carried out by Ogawa et al (1998) and Wang et al (1998).

1.2.4 Water impact with air trapping

Breaking wave impacts may include air trapping. Bagnold's (1939) impact model is simply constructed from added mass, rigid wall, and nonlinear air cushion between them. The peak impact pressure of this model is proportional to V_I (impact velocity) and $\sqrt{H}$ (H is the representative scale of impact, usually the wave height) for slight impact and weak nonlinearity of air cushion; but for severe impact, the peak impact pressure is proportional to V_I^2 and H. Bagnold's (1939) and Mitsuyasu's (1966) experiments validated these scaling laws.

Bullock et al. (2001) found that the maximum impact pressures and rise times are influenced by both the level of aeration and the violence of the impact and the

aeration levels are higher in seawater breakers than in freshwater breakers, even at a 1:25 model scale. And also the field results indicate that impact pressures up to 396 kPa can occur without air entrainment. However, air still seemed to play a part in the process as the pressure generally began to rise before water made contact with the structure. This is broadly compatible with Bagnold's (1939) idea.

Air bubble entrainment by breaking waves is a significant factor in the surf zone under high wave conditions, in terms of water quality and energy dissipation. Air-water mass transfer across the air bubble interface is significant as the net surface area of thousands of tiny bubbles is much greater than the surface area above the bubble clouds (e.g., Daniil and Gulliver, 1991;Chansom and Cummings, 1994). Later the unsteady air bubble entrainment at a pseudo-plunging breaking wave was physically modelled at near full-scale in the laboratory by Chanson, Aoki and Maruyama (2002). Experimental observations highlighted a number of unsteady air-water flow patterns: splashing at jet impact, underwater bubble plume, boiling region next to jet impact. The results demonstrated that air entrainment in the surf zone is an important process by inducing a temporary water level rise and modifying the transmitted wave climate, and it cannot be ignored.

1.2.5 Studies on 3-D water impact

The study of 3-D water impact started from the simple extension of Wagner's theory to axisymetric bodies. Chuang (1969) studied the water impact of a cone with small deadrise angle using the expanding circular plate approximation and it gave slightly lower peak impact pressure than Wagner's theory. Later Toyama (1993) improved Chuang's theory and gave 14% lower peak impact pressure than Chuang's theory. Chuang (1969) experimentally confirmed that the impact pressure on the cone was lower than that on a 2-D wedge with the same deadrise angle. So the 3-D effect reduces the impact pressure at least for convex bodies. This indicates that Wagner's theory gives conservative estimates for practical

purpose. Since the impact on a ship hull is usually a very local phenomenon, Wagner's equation has been used also for 3-D surfaces using local relative velocity and angle between ship hull and water surface, Stavovy and Chuang (1976). Watanabe (1986) extended his 2-D impact theory to 3-D oblique impact of flat-bottom ships. He derived an expression for the pressure distribution on the inclined bottom of a ship penetrating the water surface by matched asymptotic expansion assuming shallow draft. Watanabe et al. (1988) validate this 3-D model observing 3-D bottom slamming with high-speed video camera and transparent models.

1.2.6 Stochastic theory of impact load

To determine design loads, it is necessary to accurately estimate the maximum impact load during the life span of a ship. This can be done by the following statistical analysis. First, a typical rough weather condition along the sea route of the designed ship is chosen from wave statistics, e.g. Watanabe et al. (1992), and fixed as the design weather. Next, the maximum impact load acting on the ship for continuous navigation for a long term is estimated statistically, where long term means the expected total days of navigation under this weather condition during the life span of the ship. This term is given from the past record of the same kind of ships or determined from wave statistics. This estimation called long term prediction. But for ships a full-scale long time durability test is almost impossible. Therefore the rough weather is usually reproduced in a wave basin during small-scale model tests. The experimental results are extrapolated by statistical theory to full-scale long-term predictions.

In 1951, Denny examined statistically the pressure data and later Weggel (1971) concluded that the maximum impact pressure had a log-nomal distribution. More recently some investigators have analysed the wave impact pressures by means of stochastic methods (Mogridge and Jamieson, 1980). Führböter (1985) has done

model and prototype tests for wave impact and run-up on a uniform 1:4 slope and found that in agreement with theory, the probability distributions of the wave impact pressures as log-normal functions was the same in the model and in the prototype.

1.2.7 Review of FPSOs

During the past decade new developments in flexible riser, swivel, drag chain and subsea technologies, combined with the demand to move into greater water depths, have resulted in an increase in the use of Floating Production Storage and Offloading (FPSO) units.

FPSOs have many attractive features when compared with TLPs, Semi-submersibles and other types of structures. For example, FPSOs have the following merits.

- Relatively low cost and short construction time (CMPT, 1998; ISSC, 2000), which make it a favourite type
- Large working area, loading capacity, and storage capacity, which are important for a platform to support processing facilities and provide storage for processed hydro-carbon products
- Large water surface area, which makes the FPSO relatively insensitive to variations in payload
- Good stability and floatability, which make the transition, installation, and maintenance easier.

Since FPSOs have these advantages, they are the most attractive offshore oil production facilities for marginal and small fields in remote waters and have utilised in almost every part of the would. The rate at which FPSOs are entering the world's oil and gas producing regions has accelerated significantly over the last few years.

The first applications of the FPSO concept in oil production were done by conversion from trading tankers. Sogstad (1995) has considered the differences in the environmental parameters applicable in the design of an FPSO versus a merchant vessel and proposed a simplified method to predict wave induced vertical midship bending moments and shear forces in an early design stage for an FPSO.

Huang et. al. (1993) has presented model test and analytical correlation results of a single point moored FPSO. Zhao et. (2001) has presented a systematic method to predict extreme response and conduct fatigue assessment for FPSO structural analysis, in which the site-specific wave conditions and the service history are considered. The extreme response is predicted using both short-term and long-term approaches, and the fatigue strength is assessed using a closed-form spectral fatigue integration method. This proposed approach may be applied to newly built or converted FPSOs.

In recent years, increased attention has been focused on damages caused through local interaction effects between steep waves and FPSO's. Wave impact loads may have severe consequences if they are not properly designed for. However, present tools are still incomplete, as the physical mechanisms of the actual wave-structure interactions are highly nonlinear and therefore complex to model theoretically in full detail. Various developments have been published, and are in progress, on the accurate numerical modelling of the problem. There exist numerous publications on this topic, the green water study by Greco *et. al.* (2000), the run-up simulations by Ferrant (1999) and Buchmann *et. al.* (1998) and the slamming force modelling by Zhao et. al. (1996). At the present time, experimental data, as presented by Buchner (1995), Buchner & Voogt (2000), Neidzwecki & Duggal (1992), Kriebel (1992) and Stansberg (1999), play a significant role in the development of reliable tools. In order to study the nonlinear wave-structure interactions, Stansberg (2001) has carried out new model

test measurements of wave overtopping (green sea) on FPSO in steep waves. Model tests with a turret-moored FPSO in head seas were carried out in scale 1:55 in MARINTEK's 50m*80m Ocean Basin. The main purpose of the tests was to observe and measure bow slam and green sea (water on deck) phenomena and their load effects in realistic steep storm sea states, by a specially designed measuring set-up. Random wave of 3 hours duration (full scale) were run, and the tests were planned to yield information on events that can be analysed deterministically, as well as on the probability of occurrence.

1.3 Problem Definition And Objective Of This Study

As reviewed in previous section, in recent years, FPSOs have become the most attractive offshore oil production facilities for marginal and small fields in remote waters and have been utilised in many parts of the world due to their many attractive features. Moored permanently at a certain location at sea, these FPSOs should be able to survive the most critical environmental conditions occurring. This requires an adequate mooring system, but also attention to the problem of possible green water on the deck and breaking wave slamming. There has been a lot of experimental work done on green water but no work on the impact loading at the real bow from breaking waves. And again although breaking wave slamming has been investigated by lots of researchers experimentally and theoretically as presented in Section 1.2.2, there is no work on the bow impact of a real ship-type of structure due to breaking waves.

During the night of the 9th November 1998, in a sea state estimated as: H_s = 14m, T_p = 15-16 sec, the Schiehallion FPSO suffered bow damage from a steep fronted breaking wave impact. An area of forecastle plating, 20m above the mean water line and above the main deck level, was ruptured and pushed in by 0.25m. See Figure 1.2. There was some associated minor plating deformation inside the forepeak (in the main hull below the main deck). There was no damage to the

flare tower supports or to any process equipment. Following the bow damage of Schiehallion FPSO the uncertainty in how to design for this type of loading became a concern to the oil industry and the regulators.

Figure 1.2 The bow damage of Schiehallion FPSO

Considering the lack of study on the problem and the failure in reality caused by the problem described above, the main objective of this study is:

To research the nature of breaking wave impact on the bow of ship-type offshore structures experimentally and to develop a methodology on how to design for this type of loading.

To achieve this objective two models, the Schiehallion FPSO model, which had a blunt elliptical bow and a tanker (Loch Rannoch) model with a more conventional bow shape, have been tested in the department's Acre Road tank (76m long, 4.6m wide, 2.6m overall depth) and a considerable amount of desk based investigation has also been done.

1.4 Previous Work For Msc Degree And Present Work For Phd Degree

In 2002 the author was awarded an MSc degree by Dalian University of Technology, P.R.China based on the experimental work of Schiehallion FPSO model. This includes the generation of all the tank waves for Schiehallion model test and the early stage of data analysis. The main findings from the above work are:

- The predicted time history for the wave matches the measured time series quite accurately and the peak values of the pressure and the load coincide with the predicted wave peak, the focus point as expected.
- The front steepness of waves is an important parameter in calculation of wave loads during impact. For the same sea state different front steepness wave will result in much difference wave loads.
- The impact force is influenced by both the sea state steepness and front steepness. However, the global bending moment is dominated by the wave height.
- The impact pressures for the whole bow were predicted by $\frac{1}{2}\rho C_p c v_{imm}$, where c is the celerity, v_{imm} is the immersion velocity which is calculated from the celerity and the front slope of the water surface and C_p is the slamming coefficient, 0.5π here. By using the measured celerity and the measured front slope of the water surface, this formula gave a reasonable good prediction of impact pressures on the whole bow. The coefficient of variation of the ratio between measured and predicted pressures is 0.324.

To accomplish the PhD study, the author did more research continuing with the above work:

- Additional tests were made with Schiehallion and the Loch Rannoch model was tested for the first time

- The New Wave Theory used for generating tank waves has been further developed to generate different velocity based waves, wave groups with varying frequency cut-off; different JONSWAP enhancement factor, target position, front steepness and vertical velocity.
- Since it has been concluded from previous work that the front steepness of waves is an important parameter for wave impact, it is vital to predict the front steepness as accurately as possible. An enhancement factor of front steepness for critical and near critical waves has been deduced from the experiments. It has been used to get the actual wave shape and the particle velocities in the time history simulation of impact developed here.
- Again it has been concluded from previous work that the impact force is influenced much by both sea state steepness and front steepness, so the critical combinations of sea state steepness and front steepness, which are the worst case for impact have been determined. In this way the required front steepness to cause the worst slap impact for a given sea state can be approximately predicted.
- A semi-empirical mathematical model of time history simulation was developed for the bow impact. The enhancement factors of front steepness described earlier have been used to steepen the linear wave fronts and increase the particle kinematics in the near breaking waves in order to get a better estimate of the actual wave profile. By calculating the same wave with tank testing, the results have been compared with experiments. It shows the same phenomena and the overall statistics of the response are reasonably good. Later the critical combination of sea state steepness and front steepness has been incorporated into the simulation program to simulate the worst wave slap for each sea state. The results from large numbers of long time random waves and new wave groups have confirmed that the new wave simulation is a good predictor of the average maximum slap impact for a random sea.
- Finally simplified design rules for curved bows are proposed based on the above experimental and theoretical work. These rules account for the

effect of the size of the loaded area on the average pressure and the rise and decay times of the average pressure and, hence, the dynamic amplification of the response at the bow.

- Additionally, shoaling breaking wave loads on a vertical cylinder were also investigated in the same tank. The estimation of breaking wave celerity in shallow water was made by taking into account the influence from the increase of wavelength and breaking wave height. The impact pressures were then predicted by using the estimated celerities.

1.5 Outline Of The Thesis

To achieve the above objective, the following structure was chosen for this thesis:

First in Chapter 2 the wave theories to generate large steep fronted deep-water waves in the test tank are described in detail and the non-linear effects are also discussed here.

Then the model test methodology is discussed, in Chapter 3, including the design and instrumentation of the models, measurements during the test, calibration of each instrument and experimental procedure.

Following that the experimental results were listed in Chapter 4 and some conclusions from each parameter study are also drawn here.

Some approximate calculations for slamming simulation and reliability calculation are studied in Chapter 5.

Then the derivation of design guidance is presented in Chapter 6. A final form of the design equations is given here and the details of each component are also discussed throughout this Chapter.

In Chapter 7 the additional work on shoaling breaking wave loads on a vertical cylinder are investigated. The results in combination with the previous findings are discussed.

Finally the thesis is completed with conclusions and recommendations for further research in Chapter 8.

2 Waves For FPSO Model Tests

2.1 Introduction

Model tests of ships in still water and in waves have historically played an important role in the design of vessel's propulsion system, the determination of its sea keeping characteristics and its maneouvrability. In recent years, developments in offshore industry have prompted the use of wave tanks for the testing of a variety of floating, fixed and compliant offshore structures. These model tests are generally aimed at simulating the response of these structures to the harsh wave environments they will encounter in service and also to verify hydrodynamic theories used for the design of such structures.

As a result of the bow damage sustained by the Schiehallion FPSO on 9/11/98, the Naval Architecture Department at Glasgow University (Now Naval Architecture & Marine Engineering (NAME) of Glasgow & Strathclyde Universities) had been awarded an EPSRC-Link grant (later additional funds from BP, HSE, University and IMarEST Scholarships) to carry out an experimental investigation of wave impacts on FPSO bows. Among others, the immediate question that had to be dealt with is 'What type of waves should be used?'

Regular waves were ruled out because they do not represent the ocean environment closely enough when the extreme events that are of interest do occur and would probably not produce the steep fronts anticipated to cause the large impact loads.

It was clear that some form of irregular waves had to be used; however, the classical method of random wave generation widely applied in the experimental facilities also had its drawbacks. It is based on the summation of a range of

regular waves representing a given spectrum where the phase angles are determined by random choice. For a statistically meaningful set of results, especially when the loading is highly non-linear and events occur only rarely in a 3 hour period, numerous tests have to be conducted for any one sea state resulting in high testing time and cost. Long time histories lead to reflections building up and this introduces errors, so there is a need to break the long time history up into shorter segments and to let the tank quieten down between each segment or to use the wavemaker to actively absorb the reflected waves.

Even if a large number of time history segments are generated the understanding of the results is not ideal. It would be better to have some control of the wave-forms that could be systematically varied whilst still being able to understand the results in a statistical sense. Fortunately recent research can be combined and extended to do this:

In the last decade a lot of effort has gone into exploiting frequency focused wave groups aimed at generating episodic waves in the model tanks. Frequency focusing, made possible by the dispersive nature of gravity waves, is based on producing constructive interference among a number of wave components at a desired point in the tank. In practice three different methods for creating the constructive interference to generate large waves have been used. One way is to select the phases of the individual wave components in such a way that they mutually reinforce one another at a given point in the tank to create a rogue wave. This method is referred to as the 'phase speed method' and was used by, among others, Baldock, Swan and Taylor (1995) in the laboratory studies of nonlinear surface waves.

The second method, described in detail by Mansard and Funke (1982), is based on the idea that a time history of a surface wave can be reversed and it is referred to as the 'reverse dispersion method'. An impact of a given energy can be created at any point in a tank and the time history of the resulting wave can be recorded at

some other point. Because the dispersion relationship is reversible due to negligible viscous dissipation, it is possible to create a wave with the energy content of the original impact at the point of impact by running the recorded time history backwards in time.

Finally the 'group celerity method' in which the rogue wave is created by manipulating the instantaneous celerity is used by Chaplin et al., (1992) for investigating the breaking waves. The idea is to select the instantaneous group velocity in such a way that the amount of energy required for the focused wave is delivered to the selected point in the tank just before the wave appears at that point. This method was shown to offer an advantage over the other methods when large reflections were experienced and Chaplin (1996) also suggested a method of improving the control over precisely where and when the rogue wave was created.

In general short and high wave groups with highly nonlinear characteristics evolve from long waves with linear characteristics. This principle was exploited by Clauss and Kuehnlein (1997) in order to create tailor made rogue waves for tank experiments. The idea is to use the Fourier transform of the linear long waves as the characteristic information and introduce nonlinearity at the selected focus point by integrating mutually dependant particle motion equations in time domain. During the whole process the total energy content of the wave is preserved provided that wave breaking does not occur. This method has been successfully applied particularly in sea-keeping test (Clauss and Kuehnlein, 1999).

Another development during this period has been the 'new wave theory' proposed by Tromans, Anaturk and Hagemeijer (1991) which defines the statistically average shape of the highest wave for a given sea-state and the associated wave kinematics. Comparison of load predictions with other wave models and with measurements on the Tern structure during a severe storm prove the applicability of the New Wave method (Rozario and Tromans, 1993, Jonathan and Taylor, *et al.*, 1994). Similarly, de Jong ant Vugts, *et al.* (1996) have compared the New

Wave with Stokes V and Dean 7-stream function and found nearly congruent loading for the Europipe platform. The advantage of this method is that it offers the chance of predicting the random process realistically with a deterministic calculation method. Although the theory was developed for only the highest waves, the potential for extending it to other extreme events seemed obvious. This meant that generating 'new waves' could offer an ideal opportunity for cheaper tank testing where 'dynamic memory' was negligible. Where 'dynamic memory' is of essence the use of 'new wave theory' would require some modifications to incorporate a time history around the particular 'new wave group'. If narrow banded transfer function is being used the New wave group becomes a longer wave group which will allow the dynamic response.

In the end 'new wave theory' was chosen for generating most waves for the tank testing due to its simplicity arising from its determinism while retaining all the probabilistic values associated with the particular sea-state. During the tank testing program 'new wave theory' was extended to account for other types of extreme events at the first instance and later 'constrained random waves' were generated which contains a statistically averaged extreme event within a random sea-state. The aim of this Chapter is to present the experiences gained during the experimental program. Firstly, a brief description of the 'new wave theory' and its extension to arbitrary extreme events is given. Secondly, the generalisation of the 'constrained random waves' is discussed. Following these theoretical discussions, the application of these wave groups to tank testing is given. Then a small desk study on spread seas is given and other types of extreme wave groups are discussed. And lastly, some conclusions are drawn.

2.2 Highest Waves

2.2.1 Random waves

In classical random wave theory the ocean surface is described by:

$$\zeta(x,t) = \sum_n \zeta_n \cos\left(\frac{2\pi}{L_n}x - \frac{2\pi}{T_n}t + \varphi_n\right) \tag{2.1}$$

where $\zeta_n = \sqrt{2S_{\zeta\zeta}(f)df}$ is the amplitude of frequency component n,

$S_{\zeta\zeta}$ is the water surface elevation spectrum and

L_n is the wave length of frequency component n

T_n is the wave period of frequency component n

$0 \le \varphi_n < 2\pi$ is the phase angle of frequency component n and selected randomly

2.2.2 New waves

In the 'new-wave theory' (Tromans, Anaturk and Hagemeijer 1991) the random ocean surface can still be described by:

$$\zeta(x,t) = \sum_n \zeta_n \cos\left(\frac{2\pi}{L_n}x - \frac{2\pi}{T_n}t + \varphi_n\right)$$

However, here the individual wave components ζ_n and the phase angles φ_n are determined based on probability theory, to represent the extreme event.

To define the statistics of the time history of a crest of a given elevation at a given plan position (x,y), the crest itself is defined as occurring at $t = 0$ and having

1. an elevation ζ_a
2. a zero vertical velocity $\zeta_a' = 0$

The elevation $\zeta(\tau)$ at some other time τ is to be determined.

Each of the three variables is assumed to follow a Gaussian distribution, the joint probability density of $\zeta(\tau)$, ζ_a and ζ_a' is then given by the Gaussian joint probability:

$$p(\zeta(\tau),\zeta_a,\zeta_a') = \frac{1}{(2\pi)^{3/2}\sqrt{|COV|}} \exp\left\{-\frac{1}{2}(\zeta(\tau),\zeta_a,\zeta_a')[COV]^{-1}\begin{pmatrix}\zeta(\tau)\\ \zeta_a\\ \zeta_a'\end{pmatrix}\right\} \tag{2.2}$$

where COV is the covariance matrix:

$$COV = \begin{bmatrix} \sigma^2 & \rho(\tau)\sigma^2 & -\dot{\rho}(\tau)\sigma^2 \\ \rho(\tau)\sigma^2 & \sigma^2 & 0 \\ -\dot{\rho}(\tau)\sigma^2 & 0 & \Omega^2\sigma^2 \end{bmatrix} \tag{2.3}$$

The covariance matrix accounts for:

- the variance of the water surface elevation (about the mean water level) $\sigma^2 = \int_0^\infty S_{\zeta\zeta}\,df$
- the variance of the water surface velocity $\Omega^2\sigma^2 = \int_0^\infty (2\pi f)^2 S_{\zeta\zeta}\,df$ note $\Omega = 2\pi / T_z$
- the zero correlation between surface elevation ζ_a and the surface velocity ζ_a' at the same time
- the correlation $\rho(\tau)$ between the surface elevations measured time τ apart ($\rho(\tau)$ is the inverse Fourier transform of the water surface elevation spectrum divided by the variance)
- a correlation $-\dot{\rho}(\tau)$ between the surface elevation and the surface velocity at time τ apart is the inverse Fourier transform of the (surface elevation – vertical surface velocity) cross spectrum divided by the variance of the water surface elevation. (zero for small and large values of τ)

The probability density for the surface time history, $p(\zeta(\tau))$, is given by the joint probability of all three variables divided by the probability density of the crest value. Since a crest is defined by an elevation, a velocity and these are

independent, the probability density for the crest is the product of the two Gaussian probabilities and hence:

$$p(\zeta(\tau)) = \frac{p(\zeta(\tau), \zeta_a, \zeta_a')}{p(\zeta_a)p(\zeta_a')} \tag{2.4}$$

where

$$p(\zeta_a) = \frac{1}{\sigma\sqrt{2\pi}} \exp\left\{-\frac{\zeta_a^2}{2\sigma^2}\right\} \qquad p(\zeta_a') = \frac{1}{\Omega\sigma\sqrt{2\pi}} \exp\left\{-\frac{\zeta_a'^2}{2\Omega^2\sigma^2}\right\} \tag{2.5a,b}$$

Substituting equations (2.1), (2.2) and (2.4) into equation (2.3) and taking into account that as τ approaches 0, $\zeta(\tau)$ tends to ζ_a and ζ_a' vanishes then, the probability density of crest time history, conditional on a crest of elevation ζ_a at $\tau = 0$ can be shown to be:

$$p(\zeta(\tau)) = \frac{1}{s(\tau)\sqrt{2\pi}} \exp\left\{-\frac{[\zeta(\tau) - \mu(\tau)]}{2s(\tau)^2}\right\} \tag{2.6}$$

where $\mu(\tau) = \rho(\tau)\zeta_a$ & $s(\tau) = \sigma\sqrt{(1 - \rho(\tau)^2 - \dot{\rho}(\tau)^2/\Omega^2)}$

Equation (2.6) is in the well known Gaussian probability density form: $\mu(\tau)$ is the mean value of the water surface elevation at time τ from the pre-defined crest and $s(\tau)$ is the standard deviation of possible water surface elevations at time τ (about the mean $\mu(\tau)$). Note:

1. $\mu(\tau) = \rho(\tau)\zeta_a$, so the mean water surface elevation at time τ from the crest is the autocorrelation function times the crest elevation. (This would be zero if a crest had not been predefined at $\tau = 0$.)
2. $s(\tau) = \sigma\sqrt{(1 - \rho(\tau)^2 - \dot{\rho}(\tau)^2/\Omega^2)}$ and as $\tau \to 0, \rho \to 1$ and $\dot{\rho} \to 0$ so $s(t) \to 0$ i.e. the standard deviation of the water surface elevation becomes zero at the (predefined) crest.
3. As time τ increases (to several times T_z from the predefined crest) the autocorrelation function will tend to zero and equation (2.6) will become equal to equation (2.5a), so the mean water surface elevation will become

zero (mean water level) and the predefined crest will have no long duration affect on the statistics.

Overall the time history of the water surface elevation near the predefined crest can be split into a mean part and a distribution about the mean.

$$\zeta(\tau) = \zeta_a \rho(\tau) + \psi(\tau) \tag{2.7}$$

In this equation the first component on the right hand side is the mean value of the water surface shape time history which, given a predefined crest height, is deterministic. The second component is the stochastic variation about the mean time history. The statistical average time history of the most probable wave with the predefined crest height is simply the deterministic component.

This is shown in Figure 2.1 for H_s = 20.2m, T_z = 15.3s, γ= 2 and cut-off frequency = 5. The mean curve is $\zeta_a\rho$, the ± standard deviation indicates the effect of ψ. The shape of the wave at a distance ξ from the wave crest can be found from a similar argument if $2\pi / L$ is substituted for $2\pi f$ in the above equations.

Both solutions are linked through the deterministic relationship between wave length and frequency for each frequency component in the sea state. Therefore the time and distance results can be combined in one equation for water surface elevation at some time τ at distance ξ from a crest as:

$$\zeta(\xi,\tau) = \zeta_a \rho(\xi,\tau) + \psi(\xi,\tau) \tag{2.8}$$

The deterministic component only is considered here. The effect of the distribution is considered in Section 2.4.

The average shape can also be written in terms of the water surface elevation spectrum. The autocorrelation function is the inverse Fourier transform of the water surface elevation spectrum ie.

$$\rho(\xi,\tau) = \frac{1}{\sigma^2}\int_0^\infty S_{\zeta\zeta}\cos(k\xi - 2\pi f\tau)d\omega = \frac{1}{\sigma^2}\sum_n S_{\zeta\zeta}(\omega_n)\cos(k_n\xi - 2\pi f_n\tau) \tag{2.9}$$

The individual wave component amplitudes are therefore:

$$\zeta_n = \frac{\zeta_a}{\sigma^2} S_{\zeta\zeta}(f_n) \tag{2.10}$$

The phase angles require all the components to be in phase at the focus point. If an alternative origin for distance and time (x, t) is required with the focus point and time to be (x_o, t_o) then a phase angle must be introduced such that:

$$\cos(k_n x_o - 2\pi_n t_o + \varphi_n) = 1 \qquad \text{or} \qquad \varphi_n = 2\pi f_n t_o - k_n x_o \tag{2.11}$$

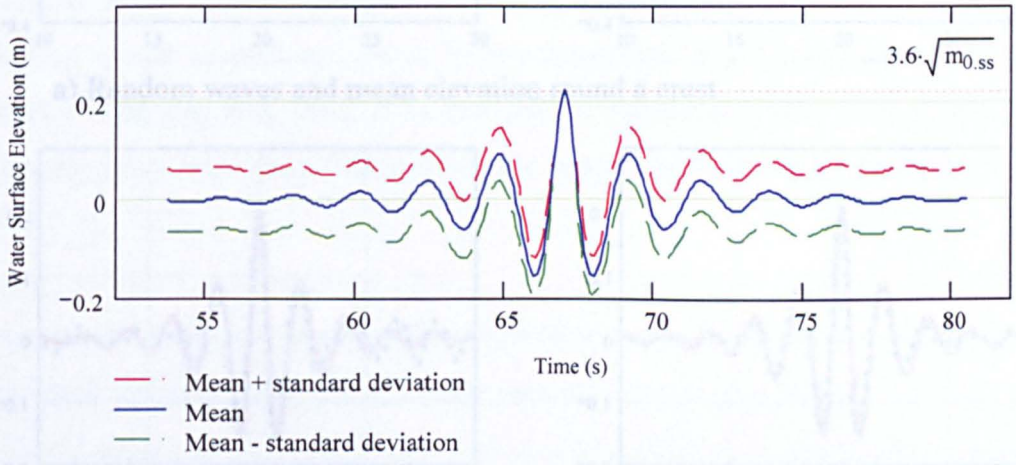

Figure 2.1 Representation of equation (2.7) showing the mean curve $\zeta_a\rho(\tau)$ and the ± 1 standard deviations of the stochastic part $\psi(\tau)$

2.2.3 Comparison of New-wave theory and random waves

Figure 2.2 shows a comparison of the highest new wave with random waves for a sea-state with hundred year return period and steepness of one sixteenth. The solid red curves are the random waves whose average is represented by the dashed blue curve while the highest new wave is represented by the solid red bold curve. On the left hand side plot only ten random waves are used for comparison but on the right hand side the number of random waves is increased to thirty. It is clear, as expected, from the results that the new wave is very close to the averages even for as few as ten waves and the discrepancy is almost vanished when the number of random waves is increased to thirty.

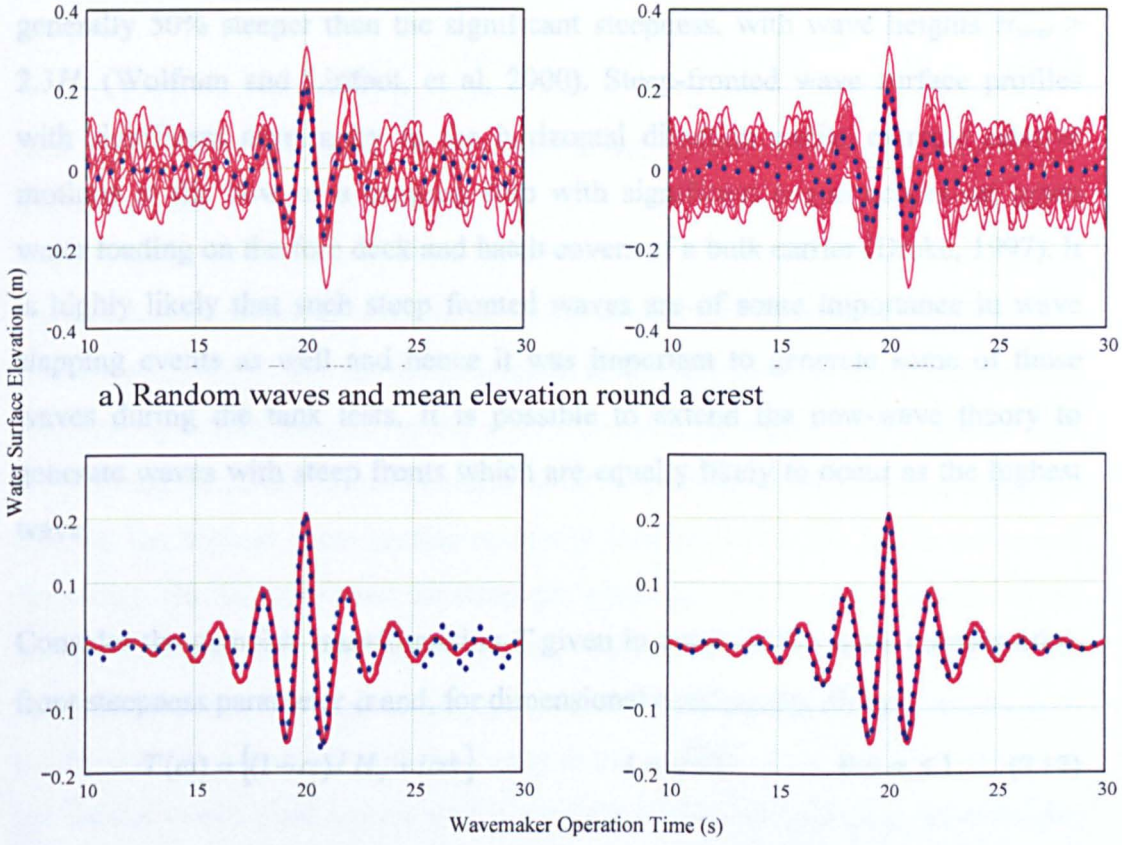

a) Random waves and mean elevation round a crest

b) Mean elevation around crest of random waves compared with new-wave

Figure 2.2 Comparison of the 'highest new-wave' with ten random waves and thirty random waves.

(Dots show the mean of the random wave results)

2.3 Steep Fronted New-Waves

Although the highest waves have been regarded as the most damaging type of waves, in recent years there has been a lot of research that suggest that characteristics other than wave height and sea-state steepness might be of some significance. Most notably there is considerable evidence that wave steepness, characterized by front and rear steepness as well as by horizontal and vertical wave asymmetries seems to be a parameter at least as important as wave height

(Kjeldsen and Myrhaug, 1997). A probability analysis of rogue wave data recorded at North Alwyn from 1994 to 1998 reveals that these waves are generally 50% steeper than the significant steepness, with wave heights $H_{max} > 2.3H_s$ (Wolfram and Linfoot, et al, 2000). Steep-fronted wave surface profiles with significant asymmetry in the horizontal direction excite extreme relative motions at the bow of a cruising ship with significant consequences on green water loading on the fore deck and hatch covers of a bulk carrier (Drake, 1997). It is highly likely that such steep fronted waves are of some importance in wave slapping events as well and hence it was important to generate some of those waves during the tank tests. It is possible to extend the new-wave theory to generate waves with steep fronts which are equally likely to occur as the highest wave.

Consider the complex transformation T given in terms of the wave number $k(\omega)$, front steepness parameter α and, for dimensional consistency, H_s by

$$T(\omega) = \left[(1-\alpha)/H_s + i\alpha k\right] \qquad i = \sqrt{-1} \qquad 0 \le \alpha \le 1 \qquad (2.12)$$

When this transformation is applied to the water surface elevation it produces a combination of the water surface elevation and the surface steepness. In a similar way the transformation can be applied to the wave spectrum to obtain a transformed spectrum $S_{\chi\chi}$, which, when processed using the new-wave theory described above yields the shape of the highest wave for $\alpha = 0$ and the steepest wave for $\alpha = 1$ as follows: (Note α is also referred to as Steepness Balance or *SB*)

$$S_{\chi\chi}(\omega) = |T(\omega)|^2 S_{zz}(\omega) \qquad (2.13)$$

For the transformed quantity the coefficients will be derived similarly from

$$\chi_n = \frac{\chi_a}{\sigma_\chi^2} S_{\chi\chi}(\omega_n) \qquad (2.14)$$

where σ_χ^2 is the variance of the transformed quantity and χ_a is the e.g. 1 in 3 hour most probable maximum value of the transformed quantity, determined using the statistics of the transformed value. To obtain the water surface elevation for each

frequency component n: ζ^{χ}_{n}, corresponding to the maximum of the transformed value, the inverse transformation is applied yielding:

$$\zeta^{\chi}_{n} = \left| \frac{\chi_n}{T(\omega_n)} \right| \tag{2.15}$$

The phase of the amplitude components is determined by the argument of the above function.

At this point it is useful to point out a theoretical difficulty associated with the steepness spectrum used for the generation of the steep fronted wave. The surface elevation spectrum reduces rapidly with increasing frequency (at f^{-5}) and at high frequencies the further contribution to water surface elevation becomes negligible making the highest wave results relatively insensitive to the choice of cut-off frequency. On the other hand the steepness spectrum, involving the product of the energy spectrum and the wave number^2, reduces at f^{-1} and the area under the spectrum does not converge as frequency increases. Consequently the steepness of the front keeps increasing with frequency at the expense of the wave height and in the limit it would yield a wave with a very steep front but vanishing wave height. Although such waves have the same likelihood as the other waves, they have no significance in terms of their impact on the structure. Therefore it is reasonable to include a cut-off in the frequency range used for the steep fronted waves. For most of the work a value of 2.25 times the spectral peak frequency was used, with sensitivities to the cut-off frequency also studied. Statistically this is equivalent to permitting the waves with frequencies bigger than the cut-off frequency to remain random but, because they make negligible contribution to the wave shape, they can be ignored.

A related wave is the different particle velocity wave. This is calculated using the transfer function:

$$T(\omega) = \left[(1-\alpha)\omega \cdot i + \alpha\omega\right] \qquad 0 \le \alpha \le 1 \tag{2.16}$$

When $\alpha = 1.0$ means the wave has maximum horizontal particle velocity, and when $\alpha = 0$ means the wave has maximum vertical particle velocity. A limited

number of waves of this type were generated in the tank but they did not cause as severe impacts as the high – steep waves described previously.

In Figure 2.3 spatial and time domain predictions for a steep fronted new-wave of a hundred year return and sea-state steepness of one sixteenth is compared with the theoretical values of the highest new-wave for the same sea-state. The steep fronted new-wave[1] has a much steeper front. Also, whereas the highest wave is symmetrical about the peak the steepest wave is anti-symmetric about the pointy of highest slope.

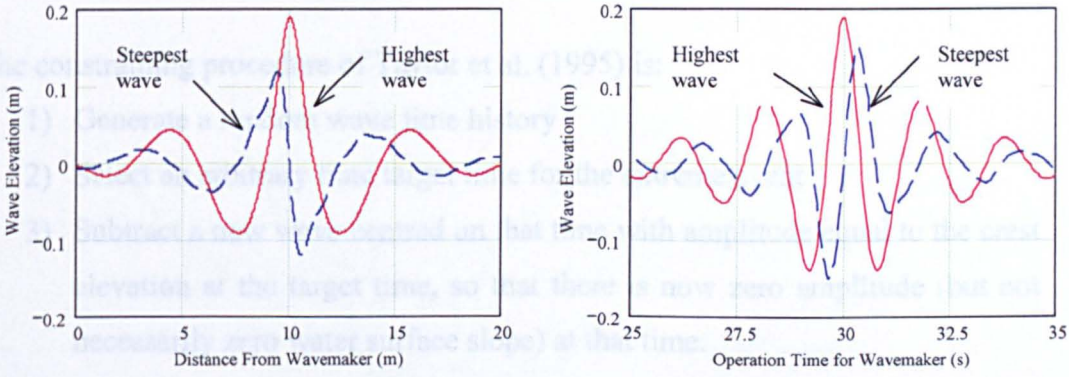

Figure 2.3 Comparison of the steepest fronted new-wave with the highest new-wave

In this section only front steepness is considered as an extreme condition but the same logic can be applied to any extreme condition for which a linear transformation can be defined. For example wave particle horizontal velocity or hull structure midship bending.

[1] Some researchers reserve the name New Wave for the highest wave only.

2.4 Constrained Random Waves

Taylor *et al.* (1995) point out that the extreme response of dynamically responding structures does not always correspond to the extreme input surface elevation as the load history and the structural dynamics may interact with local extreme wave conditions. They propose a constrained random time domain simulation, which integrates a large crest into a random time series for surface elevation (Harland *et al.*, 1996). This technique is used to investigate the variability of global extreme wave forces on offshore structures in directional spread seas (Harland *et al.*, 1997)

The constraining procedure of Taylor et al. (1995) is:

1) Generate a random wave time history
2) Select an arbitrary time target time for the extreme event
3) Subtract a new wave centred on that time with amplitude equal to the crest elevation at the target time, so that there is now zero amplitude (but not necessarily zero water surface slope) at that time.
4) Subtract a steepest new wave (Figure 2.3) from the time history, factored to obtain a zero slope at the target time.
5) Add a new-wave of the required amplitude.

Taylor has shown that this method provides the correct statistics in the vicinity of the crest.

Purely out of interest it has been decided to try and generate extreme events with a predefined probability of amplitude or amplitude and steepness, at a specified time and position in the tank, but without requiring the assumption of new-wave theory.

Two methods were developed. To explain the methods it is necessary to consider a complex plane representation of random waves. Figure 2.4 shows, in simplified

form, an evolving random wave. The instantaneous water surface elevation at any time t, is the real value (the projection onto the x axis) of a sum of phasors. Each phasor represents a spectral frequency component as in equation (2.1) has an amplitude ζ, rotational frequency f and instantaneous phase angle equal to the angle between the phasor and the x axis. If the frequency of the components increase from the middle out as f, $2f$, $3f$ etc the outer, higher frequency components are rotating faster than the inner, low frequency components.

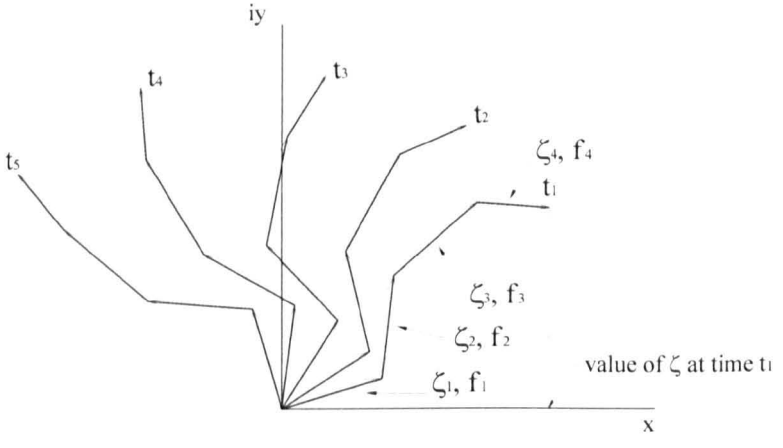

Figure 2.4 Evolution of a random wave

Figure 2.5 shows a new-wave, at the time of the peak, on the complex plane. Each phasor represents the amplitude of a group of frequencies that is on average in phase at the time of an extreme event.

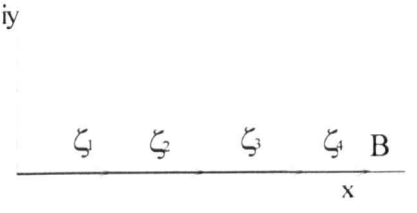

Figure 2.5 New-wave, at time of maximum, on complex plane

To obtain an average extreme event in a random sea the sum of the random components must equal the sum of the new-wave components. The amplitudes must be those for the underlying random sea (not the new-wave which represents an average sum of more components as described above). In Figure 2.6 a random phase angle selection effectively starts from the origin and ends up at a random point A. The constrained random wave must, using constrained, random phase angles start at the origin and finish at B. Two methods were devised for doing this.

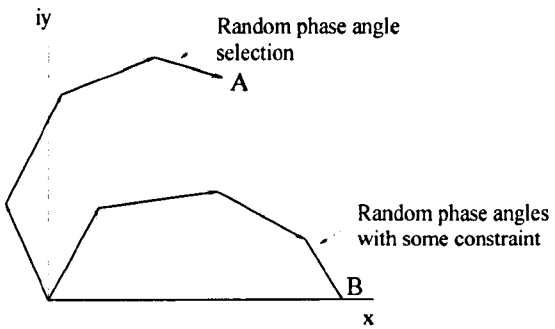

Figure 2.6 Random wave and a constrained random wave, on the complex plane

The first method uses a large number of frequency components selected in random frequency order. Initially phase angles are selected randomly for each component, in the usual way, to be uniformly distributed in the range $-\pi < \phi < \pi$ and the components are added to the complex plane.

However part way through the addition of components the total amplitude of the remaining components limits the phase angles that may be selected if the point B is to be met. The phase angle ϕ is then selected randomly from the range $\alpha-\beta < \phi < \alpha+\beta$, as shown in Figure 2.7, until the last but one component, for which there is a choice of two angles, and the last component for which only one angle is possible.

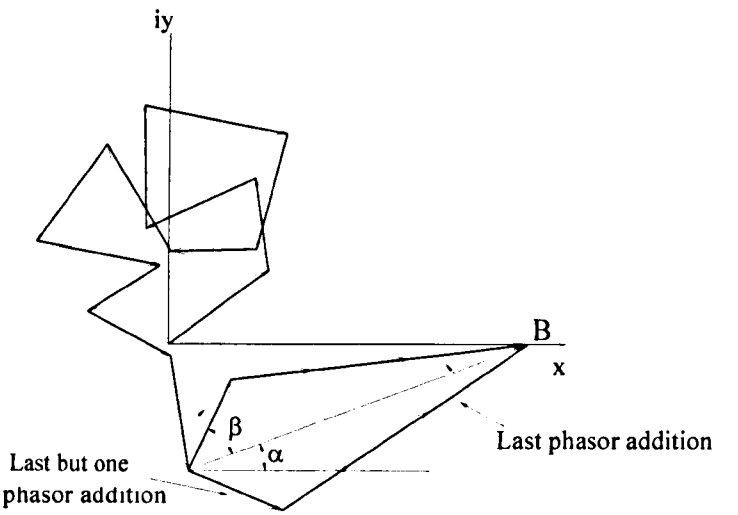

Figure 2.7 Constrained random wave showing the mean angle α and possible range of angle ± β

The second method splits the spectrum into N (two or more) parts, each covering the full range of frequencies but each having $1/N$ of the total variance. The time history of the modulus of each part is calculated $\zeta_n(x_0,t)$ $(n=1...N)$ and the time corresponding to the maximum sum value $\zeta_{\max_n}$ is selected. At this time the N parts can be plotted, as shown for N = 2, in Figure 2.8. By rotating each part through the angles γ and δ respectively, the two parts are then arranged to fit between the origin and point B as shown in Figure 2.9. The required value of N is dependent on the length of time history used in the calculation. Short time

histories require a larger value of N to make sure that the sum of the N parts is large enough to span from the origin to B.

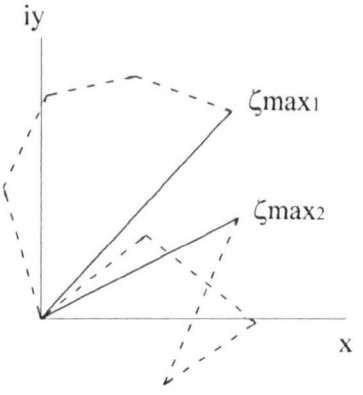

Figure 2.8 Two time histories, plotted on the complex plane at the time of the maximum of the sum of their moduli

(Dashed line shows the resultant of each)

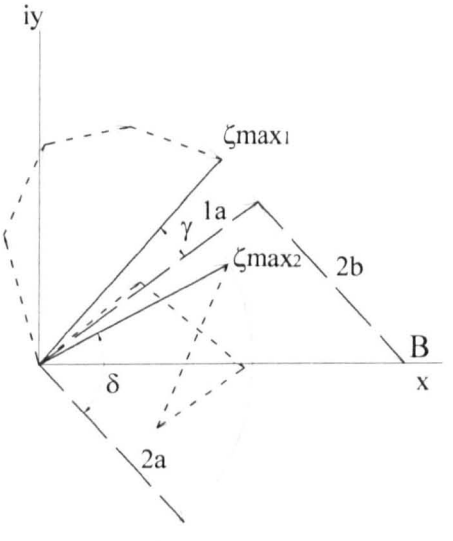

Figure 2.9 The two time histories added together, with modified phases, to ensure that the required maximum is achieved

For both methods, once the phase angles are determined at the extreme event the complete irregular time and spatial history is determined. Both methods can be

applied to a transformed spectrum such as wave front slope. The calculations are performed in terms of the transformed quantity and the amplitudes and phases are transformed back to those of the water surface elevation by dividing by the complex transfer function. (Note for frequency components where the transfer function equals zero the components do not contribute to the required response and may be added in with random phases.)

Figure 2.10 shows 10 random waves with H_s = 18.73m, T_z = 14.0s, γ= 2, each constrained to have the same peak value occurring at time τ = 25s and x = 10m, as described above. It can be seen that in the vicinity of the focus point the wave shapes are nearly the same and away from the focus point the waves retain their randomness both in the time history and spatial variation.

Figure 2.11 shows the comparison of a constrained random wave and the corresponding new-wave again with H_s = 18.73m, T_z = 14.0s, γ= 2. The left hand side graph shows the time series and the right hand side is the wave profile in space. In both graphs solid curves are the constrained random waves and the dotted curves are the new-waves. As for the random waves, the results show that the constrained random wave is closely represented by the new-wave near the focus point and away from the focus point the constrained random wave retains its randomness.

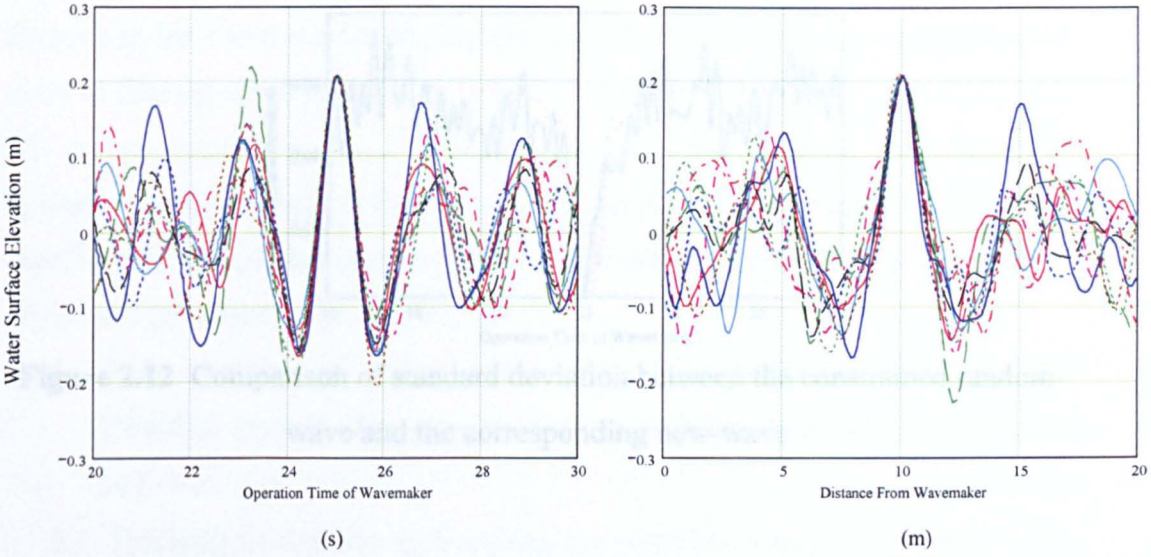

Figure 2.10 Ten random waves with constrained same peak value

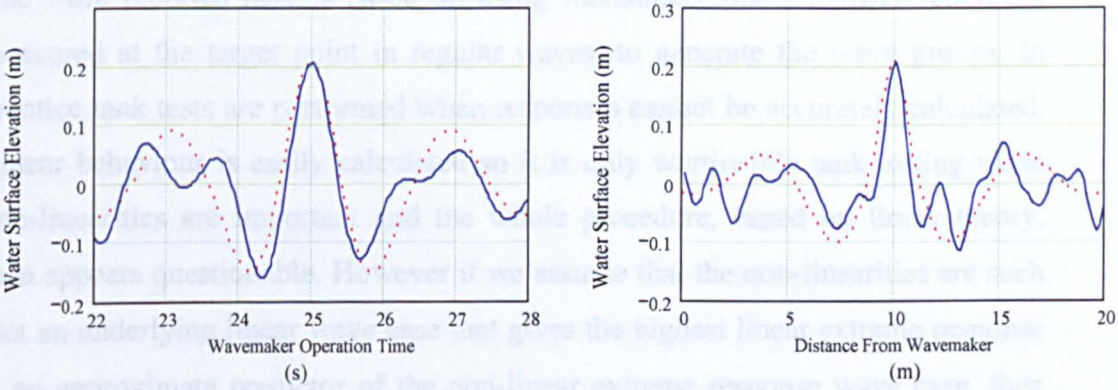

Figure 2.11 Comparison of constrained random waves and the corresponding new-wave

Figure 2.12 shows the standard deviation at each τ for the constrained random wave and the corresponding new-wave. The solid curve is the standard deviation of the constrained random wave and the dotted curve is for the corresponding new-wave. Again the results are close to the new-wave predictions and it is anticipated that the results would become closer if more random new waves were included in the standard deviation calculation.

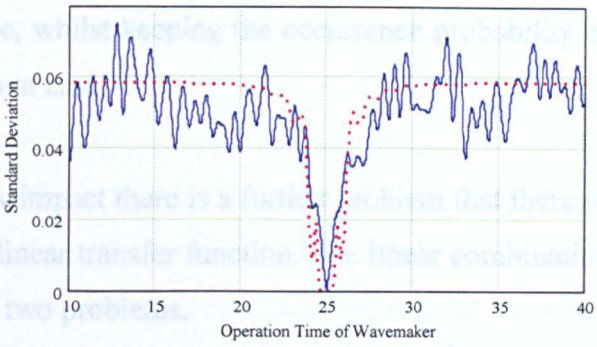

Figure 2.12 Comparison of standard deviation between the constrained random wave and the corresponding new-wave

2.5 New-Wave Groups In The Tank

The work reported here is based on using wavemaker linear transfer functions, measured at the target point in regular waves, to generate the wave groups. In practice tank tests are performed when responses cannot be accurately calculated. Linear behaviour is easily calculated so it is only worthwhile tank testing when non-linearities are important and the whole procedure, based on linear theory, then appears questionable. However if we assume that the non-linearities are such that an underlying linear wave case that gives the highest linear extreme response is an approximate predictor of the non-linear extreme response wave case, then we can use the linear theory as the starting point, let the tank introduce the wave non-linearities as the waves progress down the tank and focus at the extreme event where the model can introduce further non-linearities. There was little point in pre-calculating a non-linear wave to generate in the tank because the required wave characteristics were not known. So the work reported here is based on linear wave theory and let the tank introduce the non-linearities.

The probability of this non-linear wave should be approximately that calculated by linear theory but the response may not be the extreme value because the wave that causes the largest linear response may not be quite the wave that would cause

the largest non-linear response. It is therefore necessary to investigate small changes in the wave, whilst keeping the occurrence probability constant, in order to try to find the worst case.

For steep wave-bow impact there is a further problem that there is not an obvious, even approximate, linear transfer function. The linear combination of amplitude + slope used here has two problems.

1. The spectrum of water surface slope $(ik)^2$ times the water surface elevation spectrum has a long tail, the area under which does not converge as $f \rightarrow \infty$.
2. This transfer function says nothing about the behaviour of the ship.

The convergence problem has been discussed in previous section. It can be handled by using a transfer function that drops to zero at an arbitrary high frequency and checking the effect on the response of the assumed cut off value. During the experiment different frequency cut-off has been chosen. Each cut off frequency produces a wave with the required return period, it is simply a question of finding the worst response value.

The lack of information about the behaviour of the ship is more difficult to deal with. However there are several effects which may be important.

- Firstly the precise position of the ship relative to the target point for the steep fronted wave. This could be varied by moving the target point of the wave group relative to the ship.
- Secondly the vertical position of the bow at the wave encounter. This is partly affected by the period of the sea state but may also be affected by the previous waves, so it was decided to run various nearly random seas containing the extreme event. This required the development of a method for obtaining the required event at a given time and place in the tank. This method has been described previously.

To generate the wave in the tank the complex transfer function of the wavemaker need to be measured – by running a series of waves of different frequencies and low steepness down the tank, measuring their amplitude and phase at the target point, some distance from the wavemaker, and using linear theory to predict the wave at the wavemaker. The complex wave at the wavemaker divided by the complex signal to the wavemaker is the required transfer function.

To perform the tests, the required linear wave group at the target point were calculated first, the amplitude and phase angle of each frequency component was decided based on the new wave theory, then they divided by the transfer function of the wavemaker in order to get the signal for the wavemaker. Finally, the signal was sent to the wavemaker to get the desired wave at the target point with the non-linearity introduced by the tank.

The alternative formulation of JONSWAP spectrum developed by Barltrop and Adams (1991) has been chosen here for the spectrum calculation:

$$S_{\zeta\zeta}(f) = \frac{k_b^4 H_s^2 k_\gamma}{4\pi (k_p T_z)^4 f^5} \exp\left(-\frac{1}{\pi}\left(f \frac{k_p}{k_b} T_z\right)^{-4}\right) \gamma^a \qquad (2.17)$$

where:

k_b	1.4085	(T_p/T_z for $\gamma = 1$)
k_p	$0.327e^{-0.315\gamma}$	(T_p/T_z for selected γ)
k_γ	$1-0.285\ln(\gamma)$	
a	$f(T_z, k_p) = \exp[-(k_p T_z f-1)^2 / 2\sigma^2]$	
σ	0.07 for $f < (k_p T_z)^{-1}$	
	or	
σ	0.09 for $f > (k_p T_z)^{-1}$	

During the experiment, the steepness balance, frequency cut-off, target position and JONSWAP peak enhancement factor γ have been varied in order to get the worst case.

In Figure 2.13 the time series for a designed highest new-wave is compared with the experimental data recorded while generating the same wave in the tank. The predicted and measured are very similar except

- At the wave peak where the experimental crest is higher, steeper and arrives a little earlier than in the theoretical calculation. The error in the peak value is around 15% and is consistent with expected nonlinear effects.
- After the wave peak, where there is more high frequency energy evident in the time history.

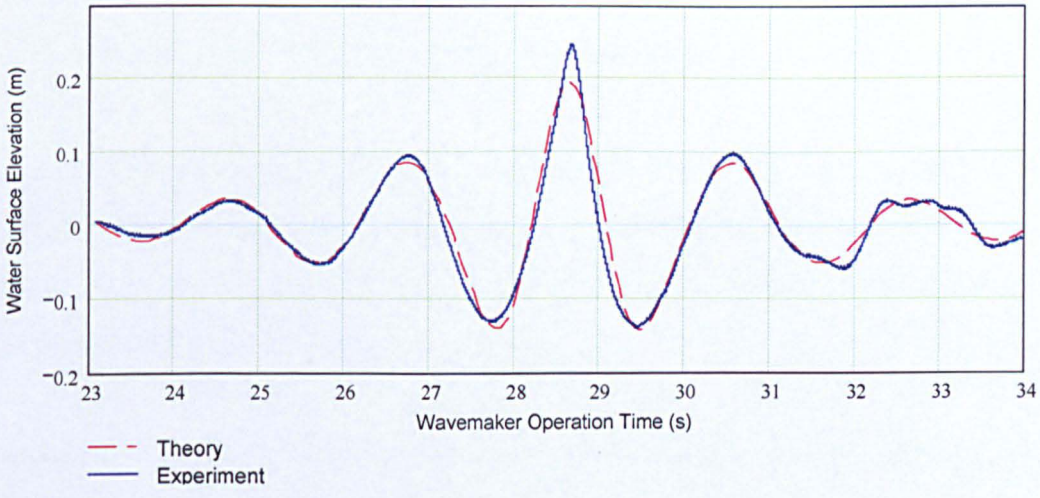

Figure 2.13 Comparison of a theoretical highest new-wave with the recorded data (model scale)

The shape of the highest new-wave in the vicinity of the focus point as generated in the tank is presented in Figure 2.14. To construct the new-wave, the smaller and slower high frequency waves are sent down the tank earlier and the large peak is achieved at the focus point when the larger and faster long waves catch up with the earlier waves. This means that there are long periods of very small waves in

the tank followed by a rapid build up of the main peak. With a significant steepness $2\pi H_s / gT_z^2$ of one seventeenth, this wave did not break.

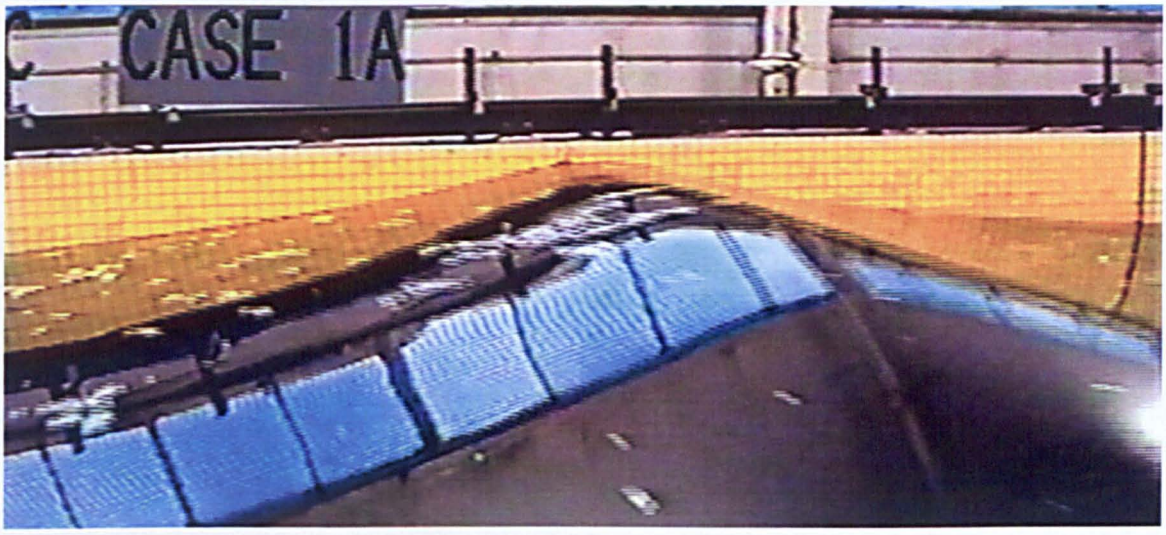

Figure 2.14 Highest new-wave as generated in the model tank

As previously shown that the steep fronted new-wave $\alpha = 1$ has a steeper front slope but a smaller wave height than the highest wave $\alpha = 0$. In tests with a model the steeper fronted waves (typically with $\alpha \approx 0.5$) cause largest impact loads and are most effective at capsizing ships.

Comparison of the theoretical time series with the measured wave elevations in the tank is presented in Figure 2.15.

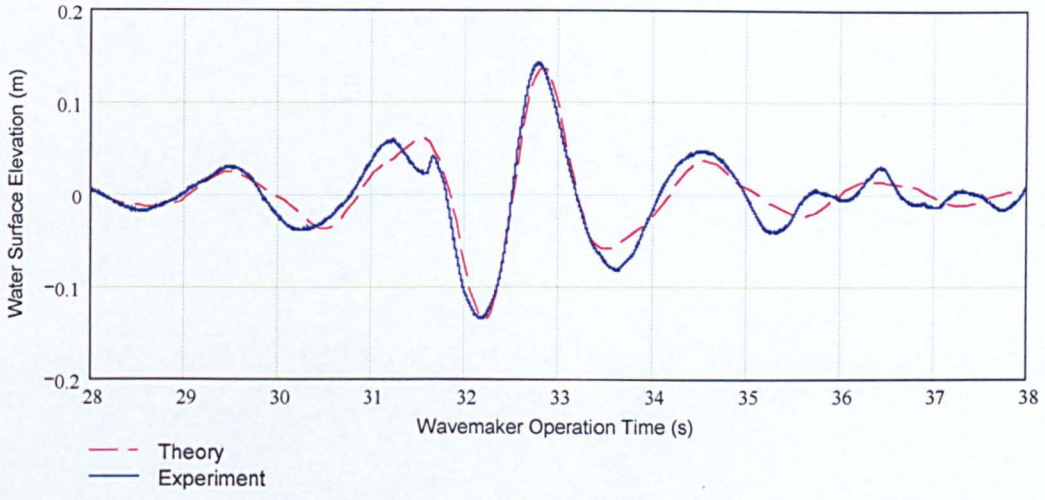

Figure 2.15 Comparison of the theoretical prediction and experimental results for a steep fronted new-wave (model scale)

The agreement between theoretical and measured time series is good with some nonlinear discrepancy still evident. In particular the wave (at about 14.5 sec) prior to the targeted steep front has become very steep and the target steep front at 15.5 sec has also steepened more. In fact the steeper waves are breaking: In Figure 2.16, on the left hand side the highest new-wave and on the right hand side the steep fronted wave for the same sea state is shown at the focus point in the tank. It can be seen that breaking occurs in the steep fronted wave while the highest new-wave does not experience breaking.

It is important to point out that although the sea-state steepness for both the highest new-wave and the steep fronted new-wave is the same, breaking occurs for the steep fronted wave while the highest wave does not break. The breaking is induced in the steep fronted waves as a result of the particular phase relationships between the different wave frequency components which bring the steeper parts of the underlying sine waves into phase (ie a sum of $\eta\cos(\omega t)$ for high waves but a sum of $\eta\sin(\omega t)$ for steep fronted waves). Also, when the return period is kept constant, as a result of the high frequency components being steeper than the low

frequency components of the same height the higher frequencies will be more dominant in the 1 in 3 hour steep fronted waves than in the 1 in 3 hour high wave.

These results support the observations of Myrhaug and Kjeldsen (1987) that wave height and wave period alone are not sufficient to describe the damaging waves in a random sea.

Figure 2.16 Highest and steep fronted new-wave as generated in the model tank

For ship bow impact the steepness of the front of the wave is an important parameter. Front steepness is particularly affected by non-linearities. The front steepness, as measured using a grid on the wall of the tank (Schiehallion Model Test) and by using closely spaced water surface elevation gauges (Loch Rannoch Model Test), was found to be larger than predicted using linear theory. The proportional increase over a range of α values was found to be related to the acceleration in the wave crest predicted by linear wave theory, as shown in Figure 2.17 (which shows fits two different data sets). Note that a/g = velocity/celerity in a regular wave.

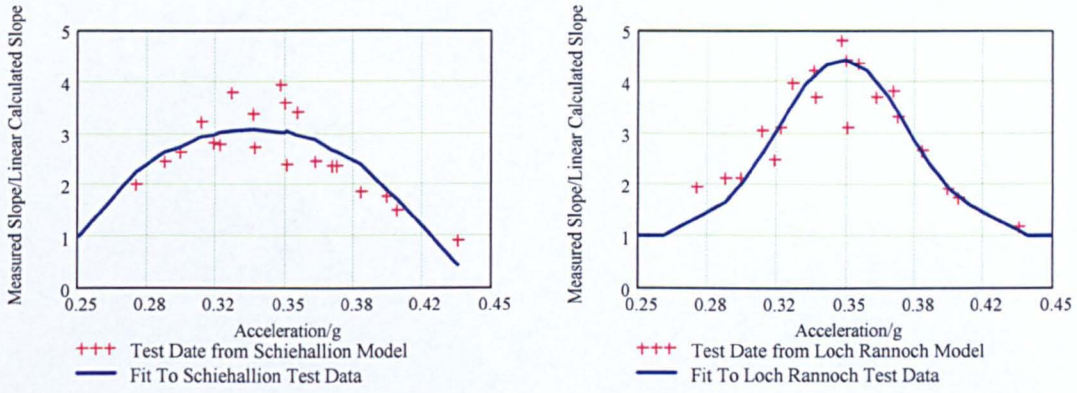

Figure 2.17 Relationship between increase in front slope and mean water level particle acceleration from linear wave theory (two data sets)

The steepness at the target point increases up to 4.5 times linear prediction around a/g = 0.35, an example is shown in Figure 18 and 19 as the 'Breaking Wave'. After this the ratio between measured and linear prediction decreases. Examination of the videos shows that the when a/g is greater than 0.35 the waves break before the target point. An example of this kind of wave is shown in Figure 18 and 19 as the 'Pre-Breaking Wave'.

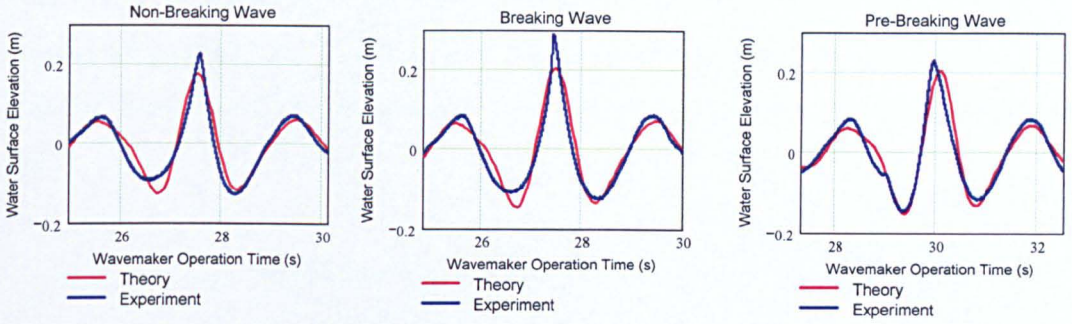

Figure 2.18 Examples of the comparison of the theoretical prediction and experimental results for different types of wave

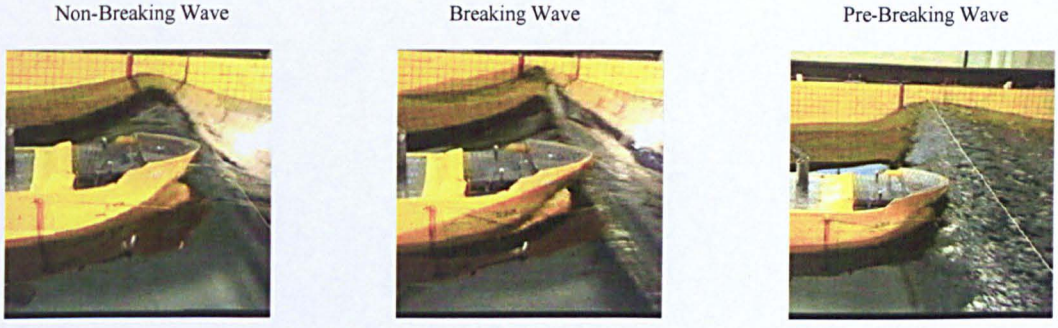

Figure 2.19 Photographs for different types of wave

As discussed above the non-linearities in the structural response will make the actual structural response in the wave groups approximate: As well as checking the sensitivity to the shape of the wave group the sensitivity to the previous random conditions (which are perfectly accounted for if the response is linear) has been determined by modelling a series of sea conditions with the same extreme event but a different superimposed randomness, which has been described in Section 2.4. An example of the comparison of the theoretical prediction and experimental results for a constrained random new wave is given in Figure 2.20. The agreement is good with some nonlinear discrepancy also evident. The poor agreement at the early stage (before 19s) was caused by the high frequency components. Theoretically it will require 19s for all frequency components to get to the target position from the wavemaker. It has shown in Section 2.4 that

theoretically the constrained random wave is closely represented by the new-wave near the focus point and away from the focus point the constrained random wave retains its randomness. The experimental results show that even with some non-linearity introduced by the tank, the same phenomena can also be seen (see Figure 2.21).

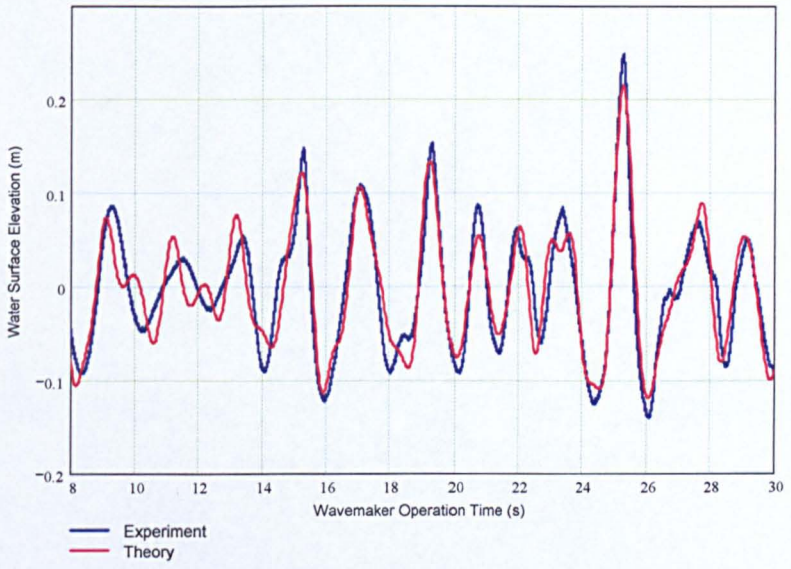

Figure 2.20 Comparison of the theoretical prediction and experimental results for a constrained random new wave

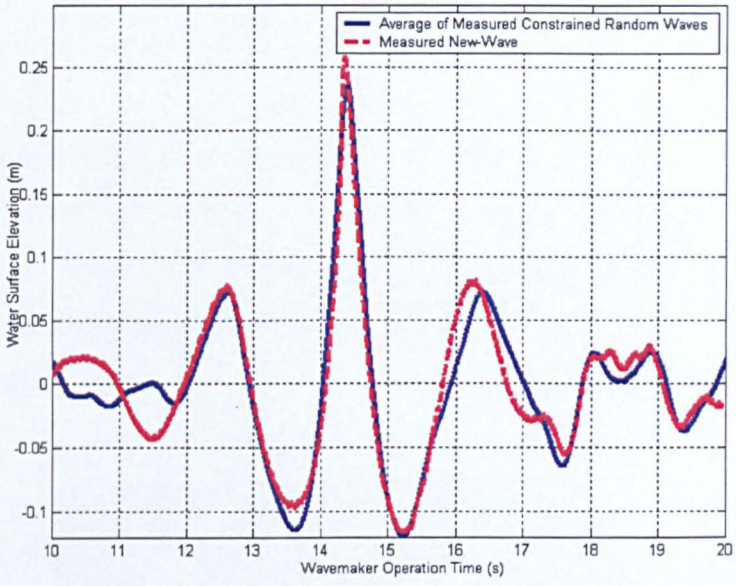

Figure 2.21 Comparison of experimental constrained random waves and the corresponding new-wave

2.6 Spread Seas

All the tank testing and most of the theoretical work were performed in uni-directional waves. A small desk study was undertaken to attempt to predict the nature of extreme wave slap events in spread seas as defined by a Mitsuyasu-Goda (1976) spreading function. The results, though not yet confirmed by model tests, suggested a very considerable reduction in maximum slap loading because a steeper and therefore lower sea state is required to produce the same type of breaking wave. It should be noted that the main direction of the calculated spread sea is the same with the tank wave, which means that for head sea case the main direction of the calculated spread sea is head sea, but for the yawed sea cases the main direction of the calculated spread sea is the yawed sea.

Figures 2.22 and 2.23 show contours of average water surface elevation in the vicinity of extreme high and steep event. Figure 2.24 shows a simulated view of the steep fronted wave from a ship's bridge. Figure 2.25 shows the predicted change in shape of the high wave group, which along with the predicted changes in the horizontal particle velocities in Figure 2.26, in comparison with non-spread seas. It has been found that the spreading significantly reduces the extreme slapping forces in sea states of significant steepness less than 1/13. The maximum reduction occurs in sea state steepness around 1/15 and is about 35%. The detail will be discussed later.

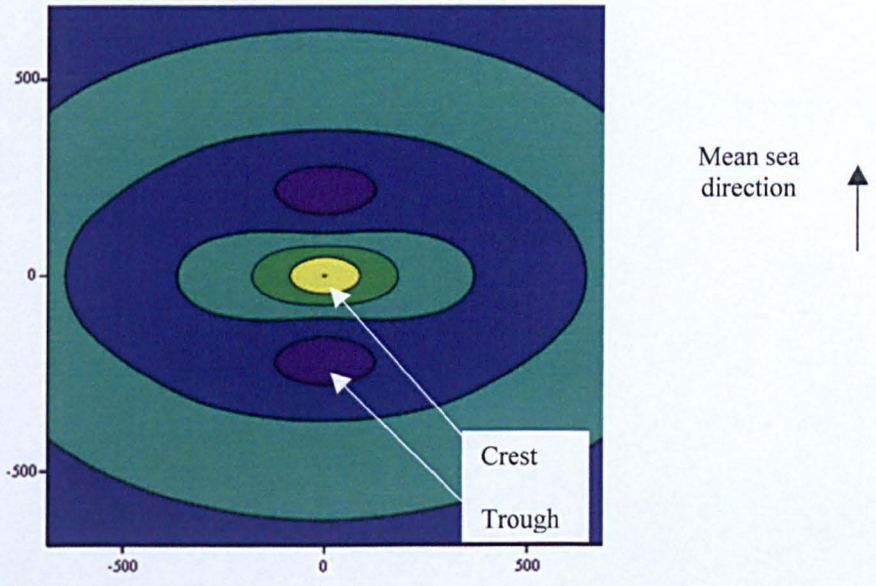

Figure 2.22 Contours of average water surface elevation of an extreme height wave group in a spread sea (Mitsuyasu Goda spreading function)

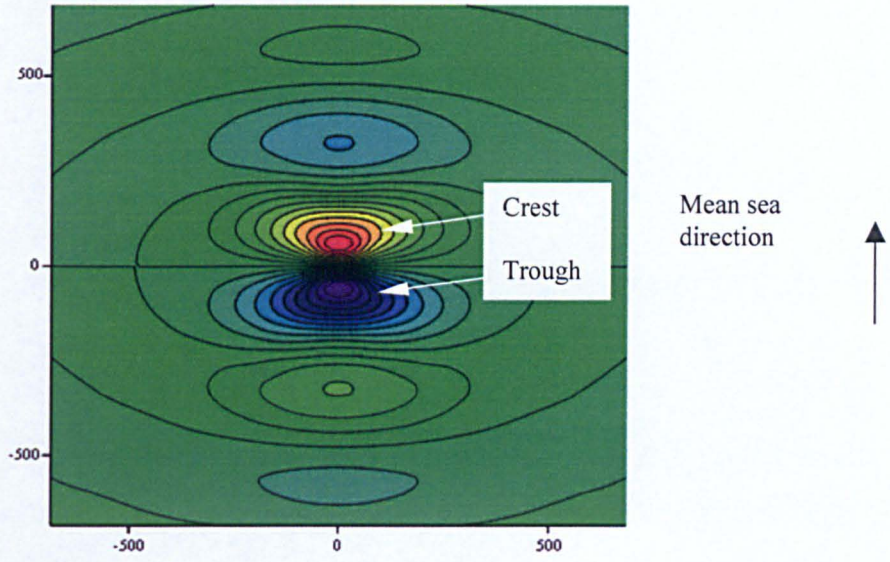

Figure 2.23 Contours of average water surface elevation around an extreme steep front wave group in a spread sea (Mitsuyasu Goda spreading function)

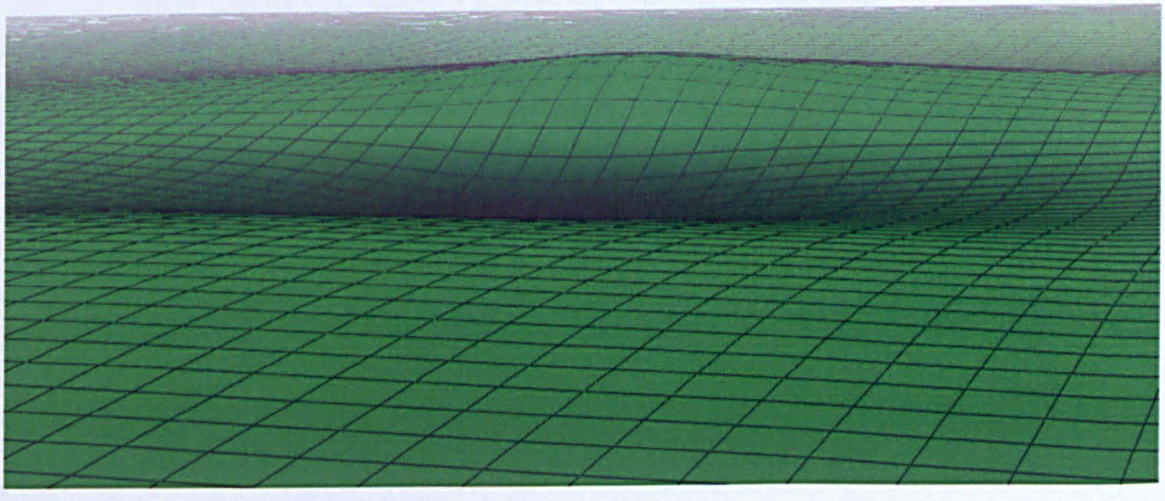

Figure 2.24 View of an extreme front steepness wave group in a spread sea

(Note deep trough in front of the main crest is partially hidden by the preceding crest)

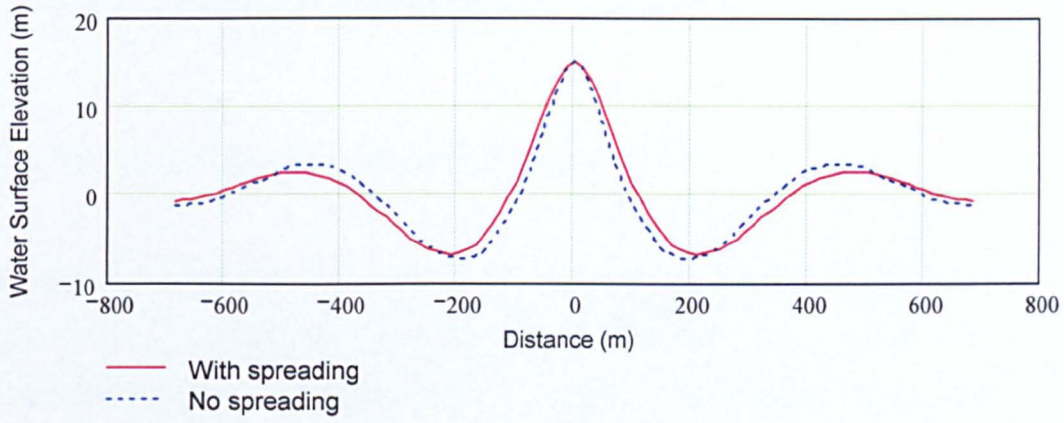

Figure 2.25 Change in along mean direction surface shape in a high wave group, resulting from spreading, linear prediction, Mitsuaysu Goda spreading function

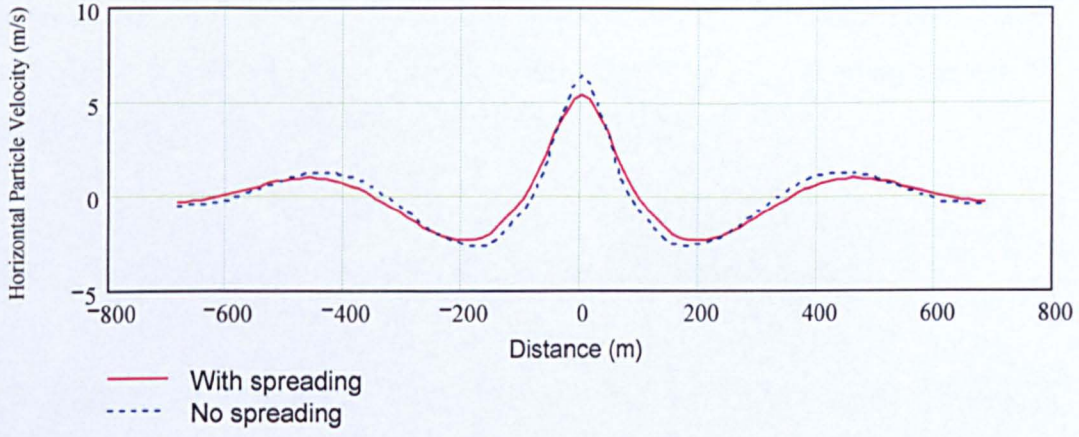

Figure 2.26 Effect of spreading on a mean propagation direction velocities, Mitsuaysu Goda spreading function

2.7 Other Types Of Extreme Wave Groups

2.7.1 Partial breakers in low steepness seas

In the sea state steepness range of greatest interest the experiments suggested (see Chapter 6) that the family of highest to steepest new-wave groups described here are reasonable representations of the waves leading to the largest slap pressures. However in less steep seas (spread sea H_s/L_z in the range 1/13.3 – 1/21) the steepest wave will not be a breaking wave and so the slap pressures from this type of wave will be negligible. However a breaking wave can still be obtained by biasing the selection of the wave components to higher frequencies and accepting a smaller elevation and a lower celerity. The resulting wave is likely to be superimposed on a longer wavelength non breaking wave. These waves have been referred to as partial breakers. Calculations suggest that these partial breakers will produce larger slap forces than larger non-breaking waves.

2.7.2 Long period weighted waves in very steep seas

In very steep (spread sea $H_s/L_z > 1/11$) seas the theory and experiments suggests that the worst slap forces will result from waves which can be represented by new-wave groups which are similar to high wave groups but which are biased to lower frequencies. This will slightly reduce the height of the waves but will increase the celerity, whilst still resulting in breaking waves, and hence will increase the slap forces.

Neither partial nor long period weighted breakers have yet been subject to wave group model testing.

2.8 Concluding Remarks

In this chapter the application of the 'new-wave theory' and a 'constrained random wave theory' to tank testing for extreme events has been described. The theories, developed for the highest waves, have been generalized to be applied to any extreme event for which a complex linear transformation can be derived. Furthermore some different types of controlled variability can be introduced to allow the sensitivity to non-linear dynamic effects to be investigated during model testing experiments.

In general the measured time histories agree well with the predictions based on linear theory except in the vicinity of high wave groups, where the waves occur slightly earlier than expected, have steeper fronts and often occur in front of the focus point. These developments offer the experimentalists:

- An opportunity to vary the wave shape in a systematic way.
- The opportunity of shorter tank testing time.
- A method of avoiding long time histories which are prone to inaccuracies due to reflections.

However there are two problems with this type of testing. Firstly the methods are based to some extent on trial and error to find the extreme event. Secondly it is difficult to guarantee that the FPSO is in the correct position relative to the wave. The second problem is much less severe in new-wave groups than in constrained random waves.

3 FPSO Models And Testing Method

3.1 Model Design

To investigate bow impact loads, models were required that could be moored in the NA-ME, Glasgow, Acre Road experimental tank (76m long, 4.6m wide, 2.6m overall depth). The models would be subject to waves and local pressures, global bow forces and hull girder moments were required to be measured. This chapter describes the models and the testing method and explains how choices, affecting the experiments and the accuracy of the results, were made.

3.1.1 Scaling – general principles

The results of dimensional analysis or of physical considerations of the magnitudes of different force mechanisms can be used to show that the behaviour of wind, current and wave loading on offshore structures is governed by non-dimensional numbers that are independent of the magnitudes of physical quantities within them. Thus, similarity of non-dimensional numbers between full scale and model scale serves as a measure of the similarity of the relative effects of physical phenomena governing the behaviour of both systems. This similarity can be applied to making measurements at model scale and applying appropriate scale factors to obtain the magnitude of the corresponding parameters at full scale. In this section the scaling of various forces and responses is discussed and the rational for choosing the model scale is described. Suppose the model has a Scale S (where S is model size/prototype size and is therefore less than 1).

3.1.2 Froude (gravity) scaled effects

Gravity waves must be Froude scaled to obtain the correct ratio of gravity to inertia forces. So the experiments will be Froude scaled, which means the Froude Number ($= \sqrt{\frac{\text{inertia force}}{\text{gravitational force}}} = \sqrt{\frac{\rho U^2 L^2}{\rho L^3 g}} = \frac{U}{\sqrt{gL}}$) must be kept the same in model scale and full scale. This implies that:

Acceleration a must be proportional to g, which is constant, so accelerations must be the same in the tests and at full scale.

Velocity U is proportional to $\sqrt{aL}$, where L is distance, so, with a constant and L proprtional to S, velocities will scale according to $\sqrt{S}$.

Distance travelled with a constant acceleration is proportional to t^2 so time must also scale with $\sqrt{S}$.

Densities are 2.5% larger at full scale than at model scale so masses scale with S^3 /1.025.

Forces at constant acceleration are proportional to mass so forces also scale with S^3/1.025.

Moments are proportional to force times distance and so will scale with S^4/1.025.

Static pressures are proportional to density times distance and dynamic pressures to density times velocity squared. In both cases pressures will scale with S/1.025.

In practice the additional 2.5% hasn't been applied for the present work when scaling forces and pressures back from model scale to full scale.

The summary of the scale factor for various derived quantities using Froude scaling for the present test is set out in Table 3.1.

Table 3.1 Scale factors for Froude number scaling

Parameter	Ratio of full scale to model scale parameter value	Parameter	Ratio of full scale to model scale parameter value
Distance L	S	Area	S^2
Mass m	S^3	Velocity U	$\sqrt{S}$
Density ρ	1	Acceleration a	1
Time t	$\sqrt{S}$	Moment	S^4
Moment of inertia	S^5	Static Pressure (Weight * Distance)	S
Force	S^3	Dynamic Pressure (Density * Velocity^2)	S

3.1.3 Reynolds (viscous) scaled effects

For viscous effects a Reynolds number $(= \frac{\text{inertia force}}{\text{viscous force}} = \frac{\rho U^2 L^2}{\mu UL} = \frac{UL}{\nu}$, where ν is the kinematic viscosity) dependent coefficient is also involved and this will have different values at the much smaller experimental than prototype Reynolds numbers, so hydrodynamic forces and pressures may not scale properly unless the correct Reynolds number regime is also achieved. Unfortunately this is only achievable near full scale but fortunately for these tests involving impact Reynolds number effects will not be very important. This has been checked using ship resistance formulae (See Figure 3.1).

Using Figure 3.1 and assuming an elliptical prism upper bow shape, the full scale predicted upper bow viscous force in a slam event was found to be equivalent to an additional 0.28m head on the upper bow of Loch Rannoch. The scaled up steady flow viscous force is predicted to be 0.74m. Ignoring the high level of turbulence during the impact, which will increase the effective Reynolds number

and so reduce the viscous force more in the model tests than at full scale, the likely error from Reynolds number effects would be about 0.46m. Measured maximum values of overall bow forces were about 20m so the error corresponds to about an additional 2% in the overall upper bow load from the largest slams.

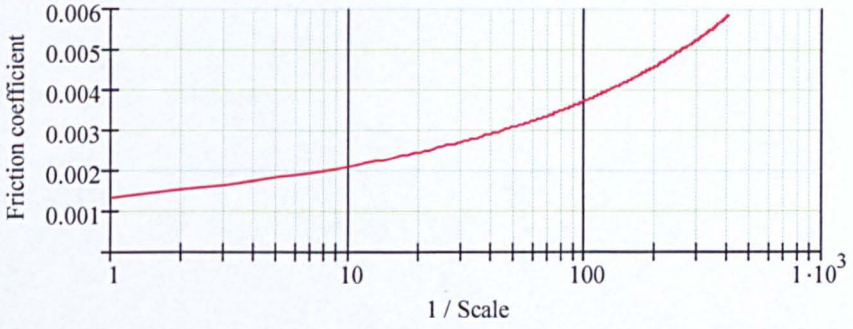

Figure 3.1 Effect of model scale on Reynolds number dependent frictional stress

The error in local pressures would be at least 1 order of magnitude smaller (less than 0.2%) because the frictional stresses will be tangential to the panels and the local impact pressures will be an order of magnitude higher.

Frictional effects will be relatively larger in the less severe slam events but these are not so important for design. Overall therefore Reynolds number effects will not cause significant errors in these experiments.

3.1.4 Weber (surface tension) scaled effects

Capillary effects will not be properly scaled. There are three effects:

1) on the wave lengths
2) on the local shape of the wave crest
3) on bubbles in the waves.

1) The effect on sinusdoidal waves in the experiments will be small. The dispersion relation with capillary forces is $\omega = \sqrt{gk + \frac{\sigma_s}{\rho} k^3}$.

Where σ_s is the surface tension of 0.073 N/m.

k is the wave number $2\pi/L$

ρ is the density of water 1000kg/m^3

ω is the wave frequency in rad/sec

This is plotted in Figure 3.2.

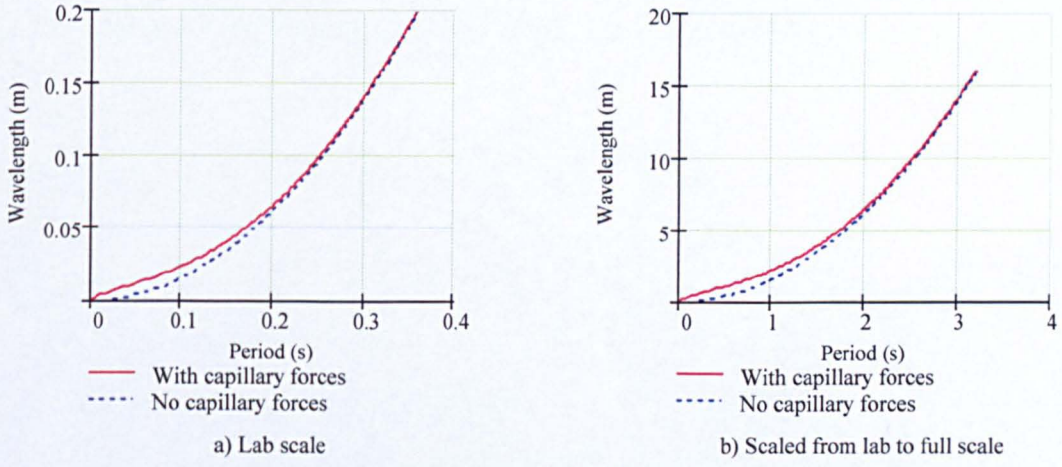

Figure 3.2 Effect of capillary forces on the dispersion relationship at model scale and scaled up from model to full scale

2) The results show that the effect of capillary forces only starts to become noticeable on sinusoidal waves when the wavelength is less than 0.1m in the lab or in the real sea (but at 1/80 scale 8m when 'incorrectly' Froude scaled to full scale). The capillary forces and gravity forces are equal for wavelengths of 0.0171m in the lab, or 1.36m when Froude scaled up to full scale.

Capillary effects will have some effect on the local detail of wave crests and the important steep crest fronts. When the water surface becomes more vertical the capillary forces will become relatively more important. On the 60 degree wave front ripples are expected to behave approximately according to

$\omega = \sqrt{g * \cos(60\deg)k + \frac{\sigma_s}{\rho}k^3}$, so, from Figure 3.3, the shape of the real water surface of features with wavelengths of about 0.125m, or Froude scaled up 10m, will be affected by surface tension. Gravity and surface tension forces will have an equal effect on waves features of length 0.024m in reality or 1.9m Froude scaled to full scale, so wave fronts with high curvatures will probably be unrealistically modified to some extent, probably being made a little smoother in shape in the laboratory, by surface tension. Because earlier researchers (Campbell and Weynberg, 1980) have shown that surface roughness reduces impact loads, this will probably make the results of lab tests a little pessimistic.

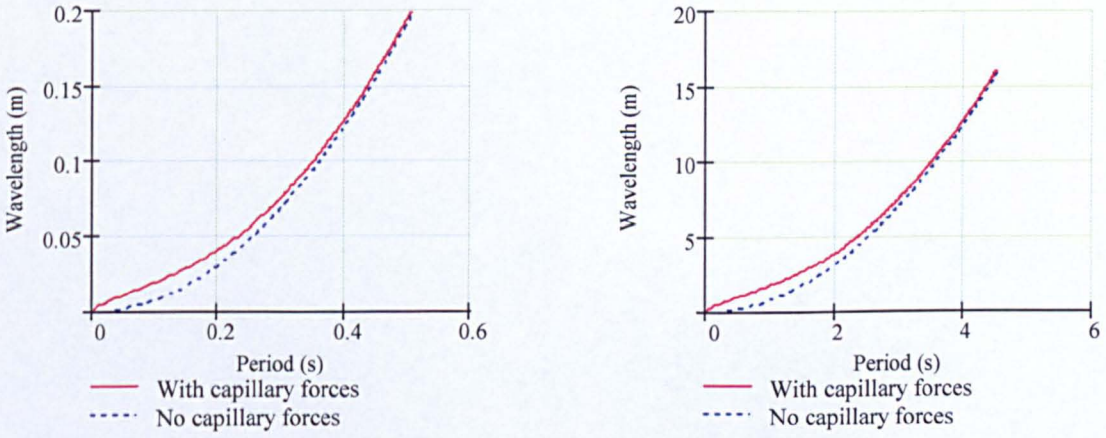

a) Lab scale 60deg

b) Scaled from lab to full scale 60deg

Figure 3.3 Increased importance of capillary forces for small features on the front face of a steep (60 degree) wave front

3) Surface tension (in conjunction with compressibility effects) will also affect the formation and stability of bubbles in the breaking waves. At model scale it will probably reduce the aeration of the wave near the water surface and the bubbles that do form will probably be larger than at full scale. This will be important when air bubbles affect the responses but cannot be scaled. Interpretation of the full scale tests on Schiehallion suggests that air bubbles have an important effect on about half the slams and the findings from Safeflow (2004) also confirms the cushioning effect of the air entrapped between a plate and the wave. The wave groups used primarily for this work almost certainly result in less aeration of the

water surface than a random sea because there is a shorter time for the waves to become aerated and a simpler wave pattern than in the real sea. Also the presence of salt, bio-material and wind in a real sea will probably increase aeration of the waves.

4) Surface tension will result in a small tension force on a panel cutting the water surface. The force can be roughly estimated as 0.073N/m at full or model scale. Scaling up the model scale result will give $0.073 \times 80^2 = 0.4$kN/m or 0.04tonne/m width of panel, which is very small in comparison with the measured full scale heads of hundreds of m.

3.1.5 Cauchy (elastic) scaled effects

There are two elastic effects of importance:

1) the elastic effect of the water, especially when aerated, as it is likely to be in a severe storm.
2) the structural elasticity of the hull and moment/force/pressure sensing

The elastic effects of the aerated water are complex and it is clear that they are not modelled properly in the tests. As discussed above, incorrect surface tension scaling, the use of wave groups and the lack of a wind in the model tests will result in a different bubble formation in the tests than at full scale. The effect of the air can increase or decrease the impact pressures because the air – water system can respond dynamically with its own dynamic amplification factor of up to 2, or it can act as a soft spring which increases the time over which the impulse is applied, so reducing the peak force and the ship-structure dynamic amplification factor. From overall energy considerations it would seem that the worst cases are:

- When the structural is flexible so that the dynamic amplification factor is high (about 2) and there is no air to cushion the impact.

- When the structure is very stiff so that the structural dynamic amplification factor is 1 but the air acts with the added mass to dynamically amplify the impact force by a factor of 2.

It should not be possible to have an overall dynamic amplification of greater than 2 from the combination of the air and the structural stiffness effects.

This is discussed in more detail by the Authors in the SafeFlow (2004) report.

The elastic models will involve global hull girder bending dynamics, segment dynamics and (for Loch Rannoch) local panel dynamics. To correctly model structural dynamics the Cauchy scaling, the ratio of inertial to elastic forces, must be correct.

To scale the lateral deflection of a beam, the transverse force: $F \propto \frac{EIx}{L^3}$. If F is Froude scaled with $S^3/1.025$ and deflection x and length L with S then EI must scale with $S^5/1.025$.

For natural frequencies to Froude scale they must be proportional to time^{-1} or $S^{-0.5}$.

Frequencies are proportional to $\sqrt{\frac{EI}{ML^3}}$ therefore frequency scales with $\sqrt{\frac{S^5/1.025}{(S^3/1.025)S^3}} = S^{-0.5}$. So if the model is designed so that the structural deflections scale then the natural frequencies will also scale correctly (and vice versa).

Furthermore, and importantly for these tests, it is possible to satisfy both Froude scaling for inertia/gravity dominant hydrodynamics and Cauchy scaling for structural deflections and natural frequencies in the same model.

3.1.6 Selection of scale

The limiting factors that determined the selected scale were:

1) Water depth/freeboard (2.6m total for the first 13m of tank, then 2.5m)
2) Tank width
3) Wavemaking capability
4) Modelmaking capability
5) Cost
6) Given 1)- 4) it is best to have as large a model as possible. This results in larger forces that are easier to measure and may very slightly reduce the errors associated with surface tension and Reynolds number effects.

1) Water depth is a key limit. It would be simplest to have deep water waves for the whole of the modelled spectrum with Tz values up to about 14 seconds (less steep sea-states were anticipated as being of less importance for slapping). The peak period may be 1.2 times Tz and the cut-off period for a Jonswap spectrum about 1.5 times Tp. So the maximum period would be about 25 seconds. This would have a deep water wavelength of about 975m and require a water depth of 488m (wavelength/2) for deep water conditions. With a tank water depth of 2.4m this would result in a scale of 1/208, which is to small a scale, so it is necessary to accept that the longest waves will be of intermediate water depth in nature.

If 14 second waves were chosen as being the longest period deep water waves then the mean zero crossing period waves of most of the sea states will be deep water waves. This results in a wavelength of 351m and a required water depth of 176m. With 2.3 m water in the tank this would give a scale of 1/76, say 1/80. The scaled wave amplitudes for an extreme wave in an 18m Hs sea state waves would be about 18m×1.8×0.67/80 = 0.27m. This will leave 0.03m freeboard to the top of the tank which is satisfactory.

2) This leads to models of about 3.1m long and 0.55m wide which, even if yawed to 30 degrees only use about 1/3 of the tank's width of 4.6m.

3) The 1/80 scale results in wave heights of about 32.4m (0.4m at model scale) and periods of 10-15sec (1.1 – 1.7sec). The regular wave capability of the wavemaker is shown in Figure 3.4. These waves are achievable as regular waves and will be more easily achieved through the wave superpositions planned for this work. The positive slope on the wavemaker limit curve (the left hand side) is in fact an estimated breaking limit, not a fundamental limit of the wavemaker itself. The negatively sloped (right hand) part of the curve is caused by the stroke limit of the wavemaker. In ordinary regular wave model tests, no significant cross waves form in the tank above about 0.75 sec tank scale, about 6.7 sec at scale of 1/80. With the proposed 2.25max frequency cut off for the tests the lower cut-off periods will be about 5.8 – 7.5sec. So the quality of the sea state tail might be affected at the shorter values of *Tz*. (Note in practice no cross waves were observed.)

4) & 5) A 3.1m model is large enough to instrument and is also well within our model-making size and cost limits.

Therefore the selected scale was 1/80.

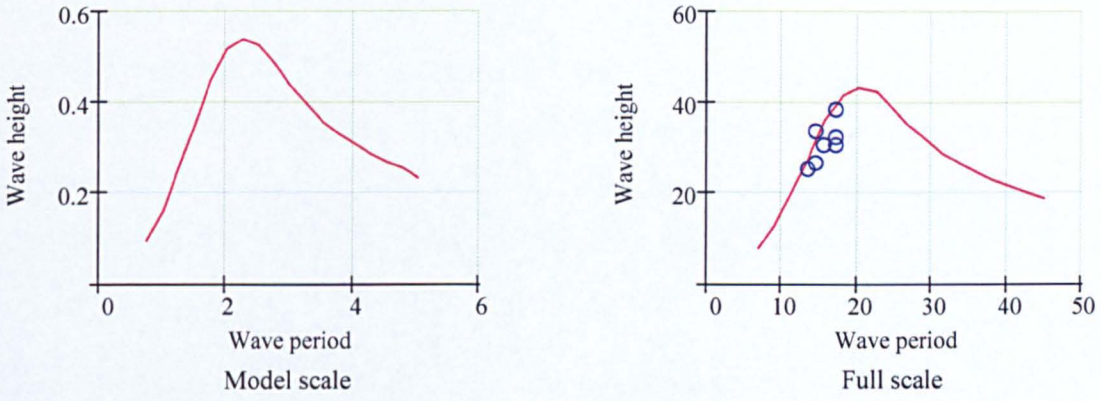

Figure 3.4 Model scale wave maker capability and full scale capability indicating 'o' range of waves selected for testing

3.2 The Models

Two models were built. The first is a model of Schiehallion, the second of Loch Rannoch. Fortunately we were able to test the Schiehallion model as a fixed bow before completing the fully floating Schiehallion model and before designing and building the Loch Rannoch model. This allowed lessons learnt testing the Schiehallion model to be incorporated into Loch Rannoch.

3.2.1 Schiehallion model

The turret-moored Schiehallion FPSO is stationed in the Atlantic to the West of the Shetland Isles. A photograph of the vessel is shown in Figure 3.5:

Particulars:

Length	245 m
Breadth	45 m
Depth	27 m
Lightship	42,425 mt
Deadweight	152,360 mt (at 20m)
Displacement	194,785 mt (at 20m)
Storage Cap.	950,000 bbls
Water Depth	395m

Flexible Risers
Wire/Chain Mooring Legs
Suction Anchors
180 BOPD Throughput Capacity

Figure 3.5 The Schiehallion FPSO

This model (Figure 3.6) was designed solely for working in head sea conditions because the round bow shape was not expected to be too sensitive to the wave directions.

Drawings showing the details of the design are presented in Figures 3.7 to 3.10.

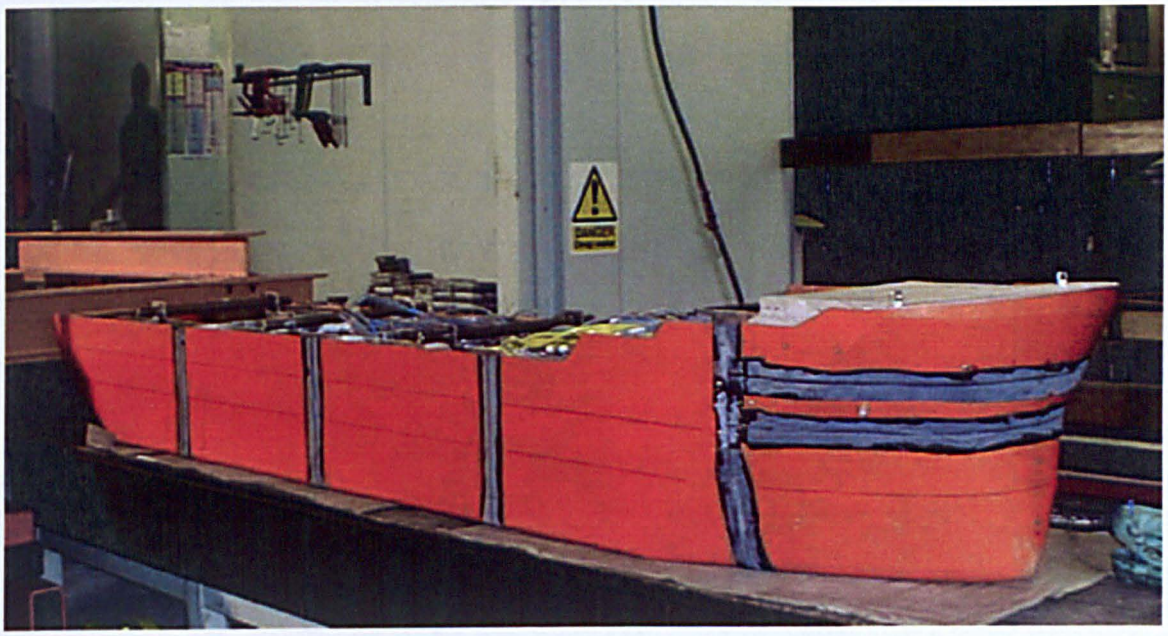

Figure 3.6 Schiehallion model

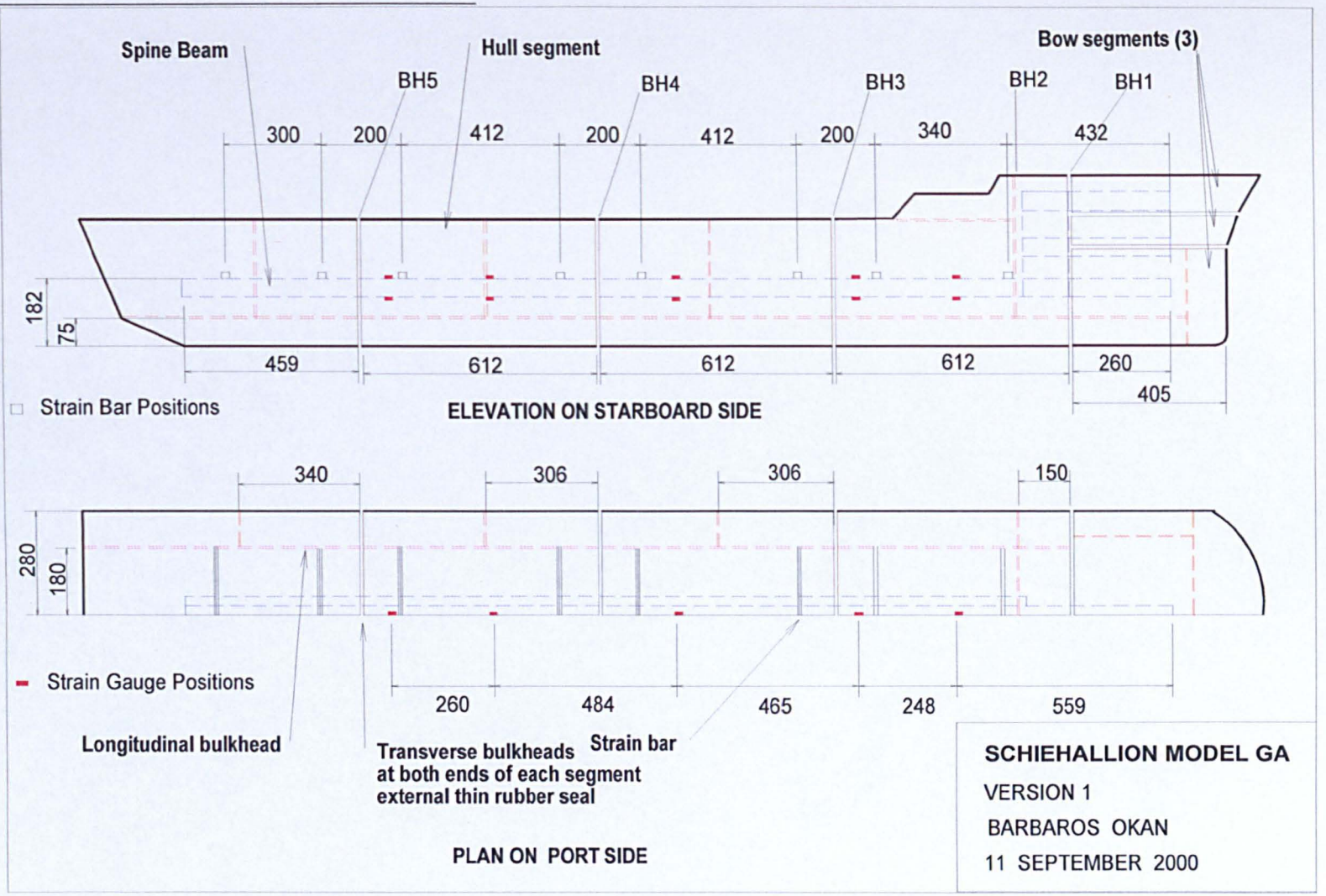

Figure 3.7 Schiehallion model GA

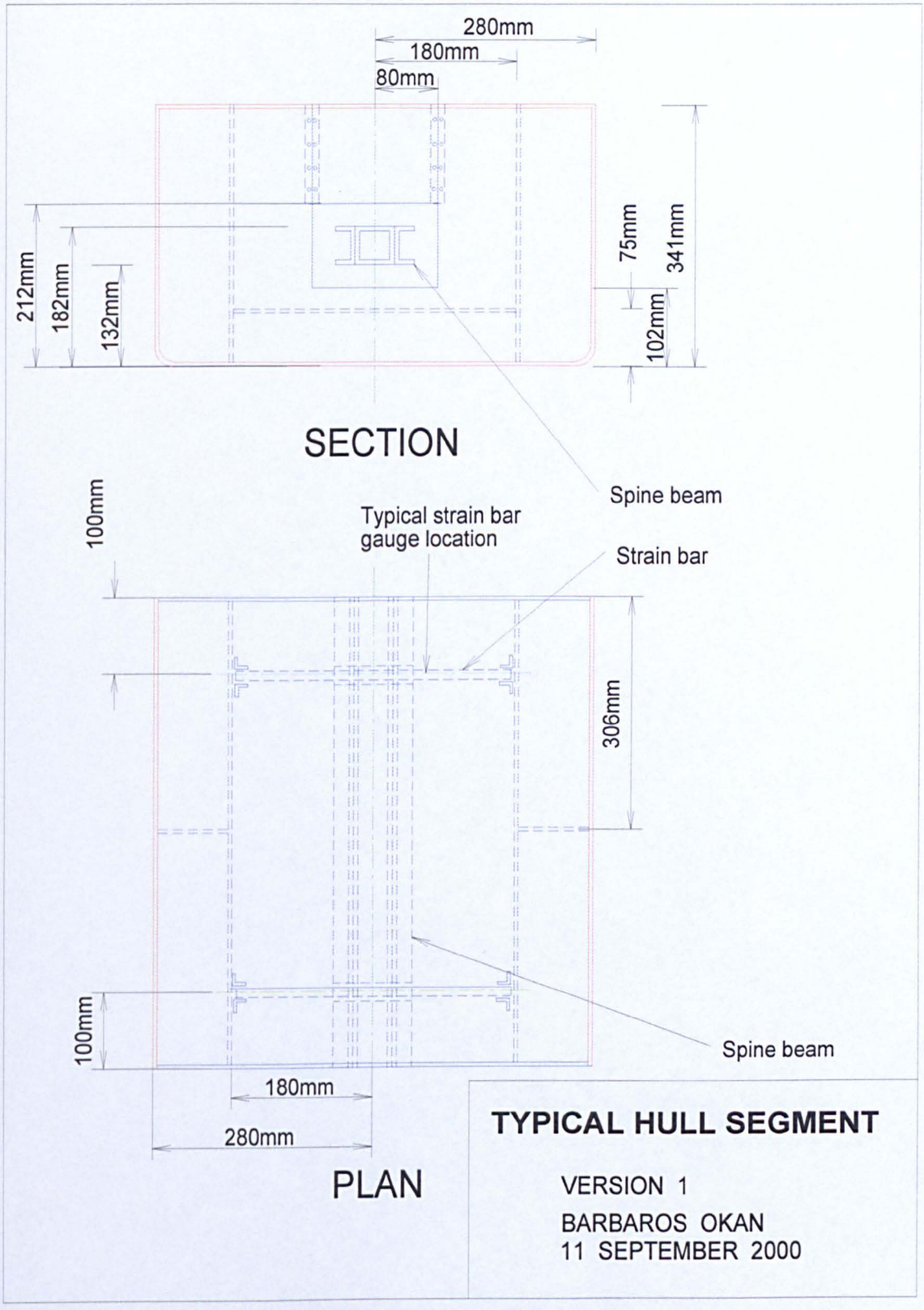

Figure 3.8 Typical hull segment

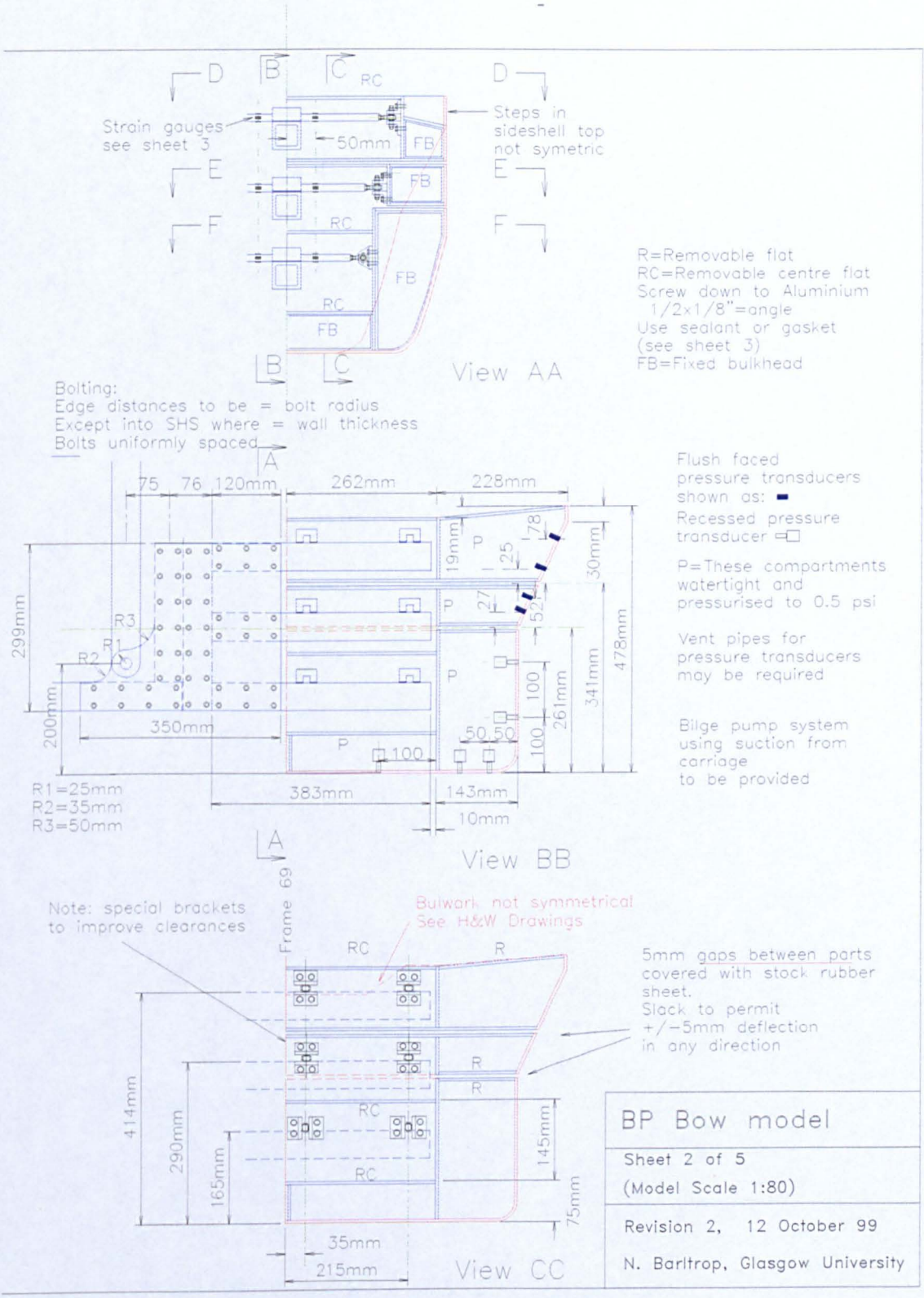

Figure 3.9 Schiehallion bow, vertical sections

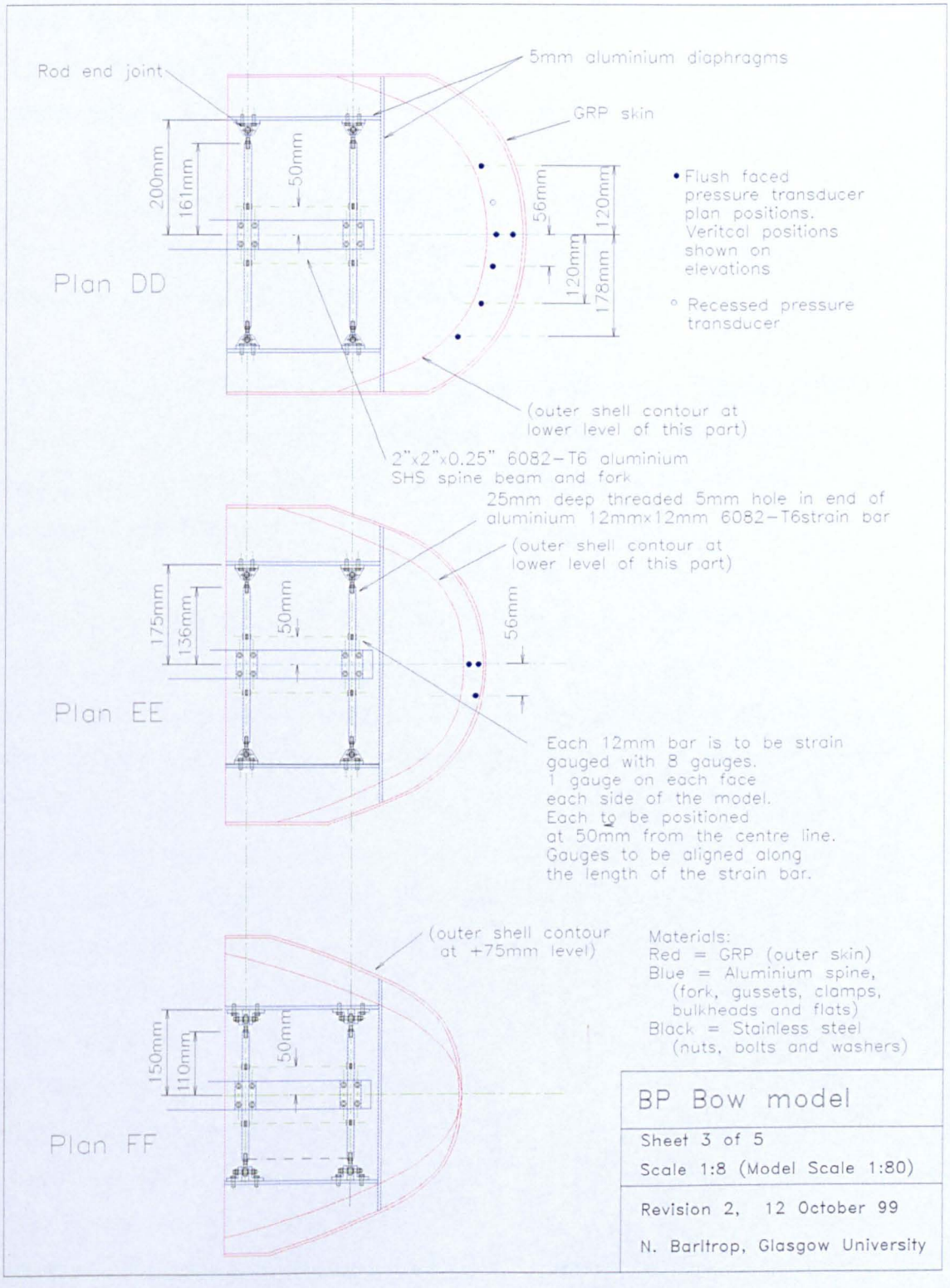

Figure 3.10 Schiehallion bow, horizontal sections

The design of the bow accommodated some early tests for BP, where the bow was directly supported from the tank's towing carriage, however this did not compromise the design or affect the floating results presented here.

The Schiehallion shape was relatively simple and the mould for the model was made by hand without the use of the ship model making machine. The bow mould was made up using the body plan to cut transverse sections.

The hull is made up from segments arranged longitudinally along the length of the hull but vertically in the bow. Each segment is mounted to a spine beam through strain bars which cantilever from the spine beam and are pinned at their connection to the segment.

Providing the pins do not resist any moment the forces transferred between the segments and the spine are therefore proportional to the bending moment in the strain bar and the bending moments in the strain bar which are deduced from strain gauges at the fixed end of the bar. The hull segments only measure vertical forces and the pin is a simple horizontal pin through a lubricated clearance hole in the end of the strain bar. The bow segment strain bars can measure horizontal and vertical forces so free rotation about two axes is required at the pinned end and. This was achieved using a low friction rod end bearings (small versions of the track rod end bearing on a car steering system). The friction in the pin joints was not measured but it was negligible at small transverse load and from the geometry of 100mm long bars and an end bearing radius of 6mm the moment induced by a conservative friction coefficient of say 0.3 would lead to an error of 2%. The strain time histories were carefully checked for any indications of friction or sticking in the pin joints, which would show as a sudden change in the measured moment at the peaks but none was found so the pins are thought to be effective.

The design of the bow support resulted in a high level of redundancy for the measurement of the most important horizontal impact forces. In principle 4 signals were available for estimating the horizontal force on each segment. In practice the front gauges were wired together and the rear gauges wired together but this still allowed for the possibility of some strain gauge failures without having to undertake repairs to the bow.

The spine is also instrumented to allow vertical bending moments to be measured.

The water is kept out by rubber seals. The seals were a problem to fit at the 'T' joints on the side of the bow. The original plan was to overlap the rubber strips in these regions but overlapping whilst maintaining a corrugation in the seal (ie the rubber was pushed several mm into the joint so that it would not transmit forces between the segments). In practice maintaining both a corrugation in the seal and watertight integrity at the T joints proved difficult.

Applying the rubber tightly over the joints made sealing easy but resulted in significant carry over of forces from one segment to another, even though the rubber was only about 0.3mm thick. The solution was to fabricate rubber 'T pieces' that included a T shaped corrugation and to butt the sealing strips up to the 'T' piece legs away from the hull joint. These worked well with no measurable carry over effects.

The spine beam has Froude scaled vertical stiffness EI so that the first few natural periods of the hull girder were reasonably modelled. The spine beam was strain gauged at five locations, chosen to measure responses in the first three mode shapes.

The frequencies of the bow segments were determined by the size and material of the strain bars and were a compromise between low stiffness, and high sensitivity for the strain gauges, and stiffness to avoid excessive local dynamic response. The

initial fixed bow model segments used for the fixed bow tests had a natural frequency of about 2.5Hz (23Hz model scale). This was found to give a larger than desirable dynamic response so when the model was converted to a floating model the original aluminium bow strain bars were replaced with stainless steel which increased the natural frequency to about 4.4Hz (40Hz model scale). This was found to give a good sensitivity with relatively small dynamic response.

The strain gauges used in all the above applications were a copper-nickel alloy foil on a polyamide base. The gauges were 5 mm in length, with a gauge resistance of 120 Ω and can measure strains of up to 4%. The gauges can operate within a temperature range of -30°C to +180°C. The gauges on the strain bars and the wiring connections were sealed with a polysulfide protective coating against water damage after the gauges were glued in place.

The bow contains an array of pressure transducers, as shown in Figures 3.9 to 3.11. These were placed in a separate compartment in each segment that was slightly pressurised with an air pump to help keep water out. Two different types of pressure transducers were fitted with the intention of comparing their performance for later similar work. Flush high frequency response expensive transducers (Piezoresistive Pressure Transducer ENDEVCO MODEL 8510B-1 with natural frequency of 55000Hz) were mainly used in the top and middle sections where the measurements were important (see Figure 3.11: 1,2,3,4,7,8,9). There were lower frequency transducers (Honeywell Mediamate Pressure Transducer Model MM) in the bottom section along the center-line of the model (see Figure 3.11: 10, 11), the results for which are not important for these tests. There were also two other low frequency pressure transducers (5,6) in the top section. The sensing elements were about 3mm in diameter, about 240mm at full scale. The tests confirmed the superiority of the more expensive transducers but also showed that neither gave very useful results for these purposes; the data obtained from the pressure transducers tended to be very variable with the values of questionable relevance for structural design purposes because of the very small

measurement area in comparison with even a small plate panel. (This lead to the development of larger pressure panels for the Loch Rannoch model.)

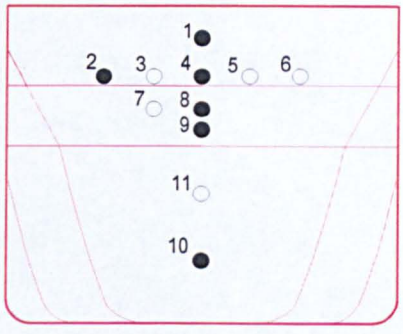

Figure 3.11 Bow view of Schiehallion showing numbering of pressure transducers, those shown solid were used for the floating tests

The side compartments were filled with foam to provide buoyancy in the event of a deep draft seal failure which could completely flood the model.

The Schiehallion model produced useful results but importantly the experience from it allowed the design of a better model for further tests:

The compartmentalisation was not a good idea! It required the front of the bow to be supported further back than was ideal. If a component failed it required a lot of dismantling and re-assembling to get to it; each compartment required air pipes, drainage pipes and every cable coming into it to be sealed into the bulkhead and the aluminium plates used for the compartmentalisation prevented views inside the bow.

There were no segment seal failures but there was a persistent slow leak into a bottom compartment, the source of which was never confirmed but was probably the seal to a bottom pressure transducer. The overpressurisation did not prevent

water ingress and this required the compartment to be pumped dry from time to time.

In extreme conditions a lot of water flowed over the deck and if, after maintenance or inspection, the decks were not carefully resealed to the hull this could result in a build up of water in the front strain bar area.

The strain gauges were generally reliable. One spine beam gauge failed and was replaced without removing the model from the test location. Some lower segment bow gauges failed after the compartment bow became flooded.

3.2.2 Loch Rannoch model

Loch Rannoch was built for BP Shipping, Ltd. as shuttle tanker for North Sea oilfields by Daewoo Heavy Industries, Okpo Shipyard, Pusan, Korea in 1998 with displacement of 120,000 tons, length of 257.39m and beam of 46m.

The Loch Rannoch model is shown in Figure 3.12.

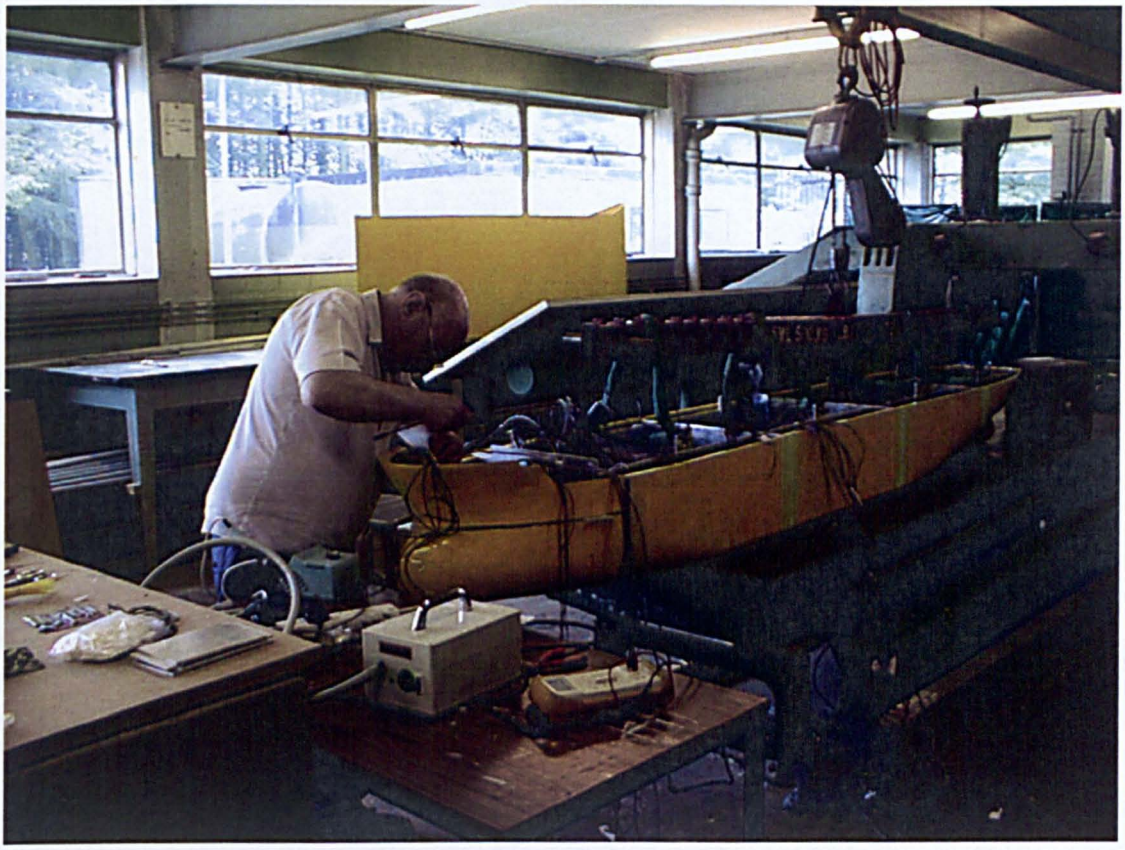

Figure 3.12 Loch Rannoch model

The main lessons learnt from Schiehallion were:

1) A limited array of spot pressure transducers provides very little useful data.
2) It is better to have an open bow structure with access to the instrumentation for repair than to compartmentalise to limit water ingress.
3) It is advantageous to use clear perspex for decks so that
    a. the internal condition can be assessed without having to dismantle the model.
    b. any water ingress can be seen
    c. clients/visitors can be shown the internal instrumentation.

The main hull for Loch Rannoch is conceptually the same way as the Schiehallion hull. However the extra shape complexity required the use of the model making machine which follows the waterlines.

The spine beam was composed of two boxes bolted side by side. The strain gauge locations, designed to measure the first three modal responses, are shown in Figure 3.13.

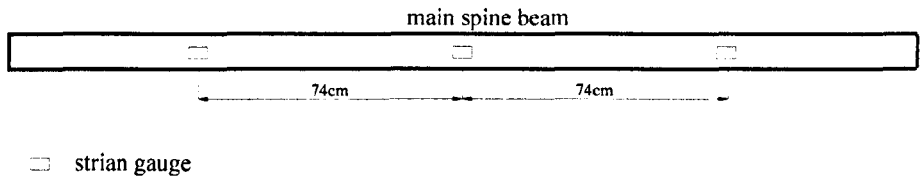

Figure 3.13 Strain gauge locations for Loch Rannoch's spine beam

Loch Rannoch's bow shape suggested that the worst panel loads would arise from bow seas rather than head seas. Therefore whereas a three degree of freedom instrumentation was adequate for each bow segment on Schiehallion a full six degree of freedom system was required for Loch Rannoch. This was designed as a 3 bar system, which with 4, paired, strain gauges on each bar allowed the required measurements to be made. In comparison with the Schiehallion model there was no redundancy in the force measurement strain gauges, especially for the bow sea wave directions, however the Schiehallion tests had provided some confidence in the reliability of the strain gauges. Only two bow segments were used (there were three for Schiehallion). This was because:

- The bow split naturally into two parts,
- The pressure panels combined with three bow sections would have made the inside of the bow very difficult to access.
- The number of data channels would have exceeded 64 which would have required two data acquisition computers and further complicated the data processing.

Whereas for measuring longitudinal and transverse forces on Schiehallion a pinned end bar was satisfactory, to measure all 6 forces it is important to prevent axial forces developing in the bars – these result in low strains in comparison with bending, so the signal to noise ratios in the measurements become poor and the system becomes statically indeterminate so it is difficult to interpret the results.

For Loch Rannoch's bow each strain bar was therefore terminated in a combination of a universal joint and a linear bearing. The upper bow segments and strain bars before assembly are shown in Figures 3.14 and 3.15.

Drawings for the model bow and the pressure panels are shown in Figures 3.16 to 3.18.

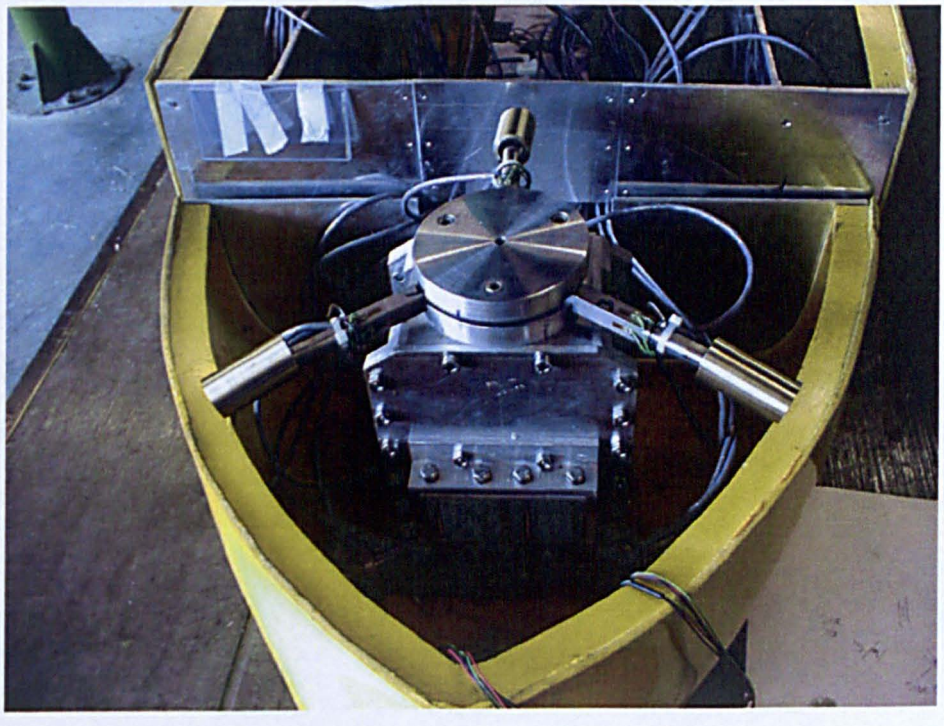

Figure 3.14 View on Loch Rannoch bow showing strain bars, strain gauges and the inner parts of the linear bearing which enclose the universal joints

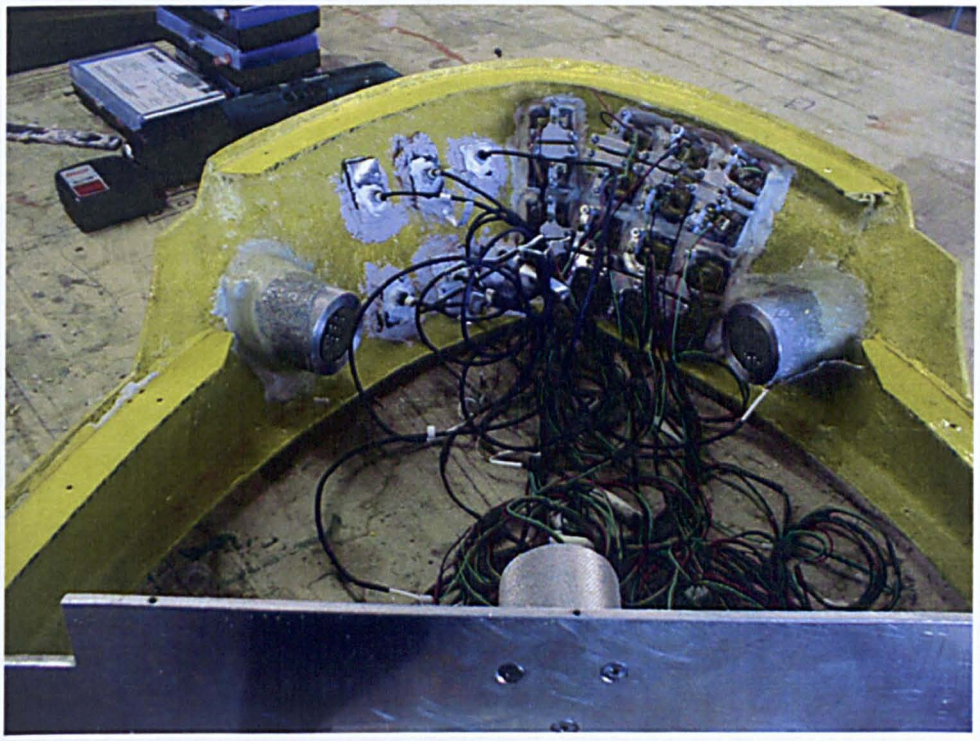

Figure 3.15 View on Loch Rannoch bow showing pressure transducers (port), pressure panels (starboard) and the three cylindrical linear bearings

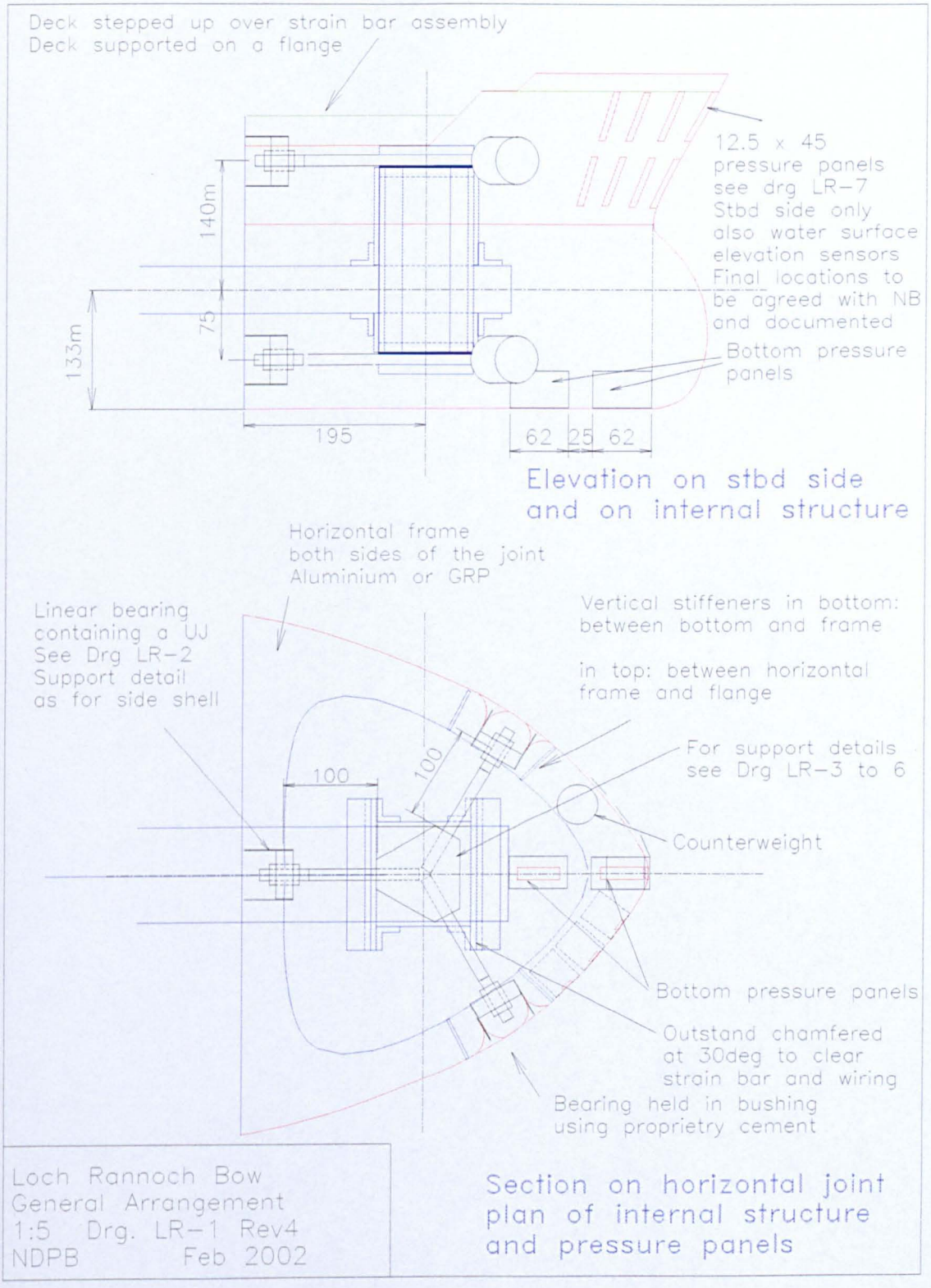

Figure 3.16 Loch Rannoch Bow General Arrangement

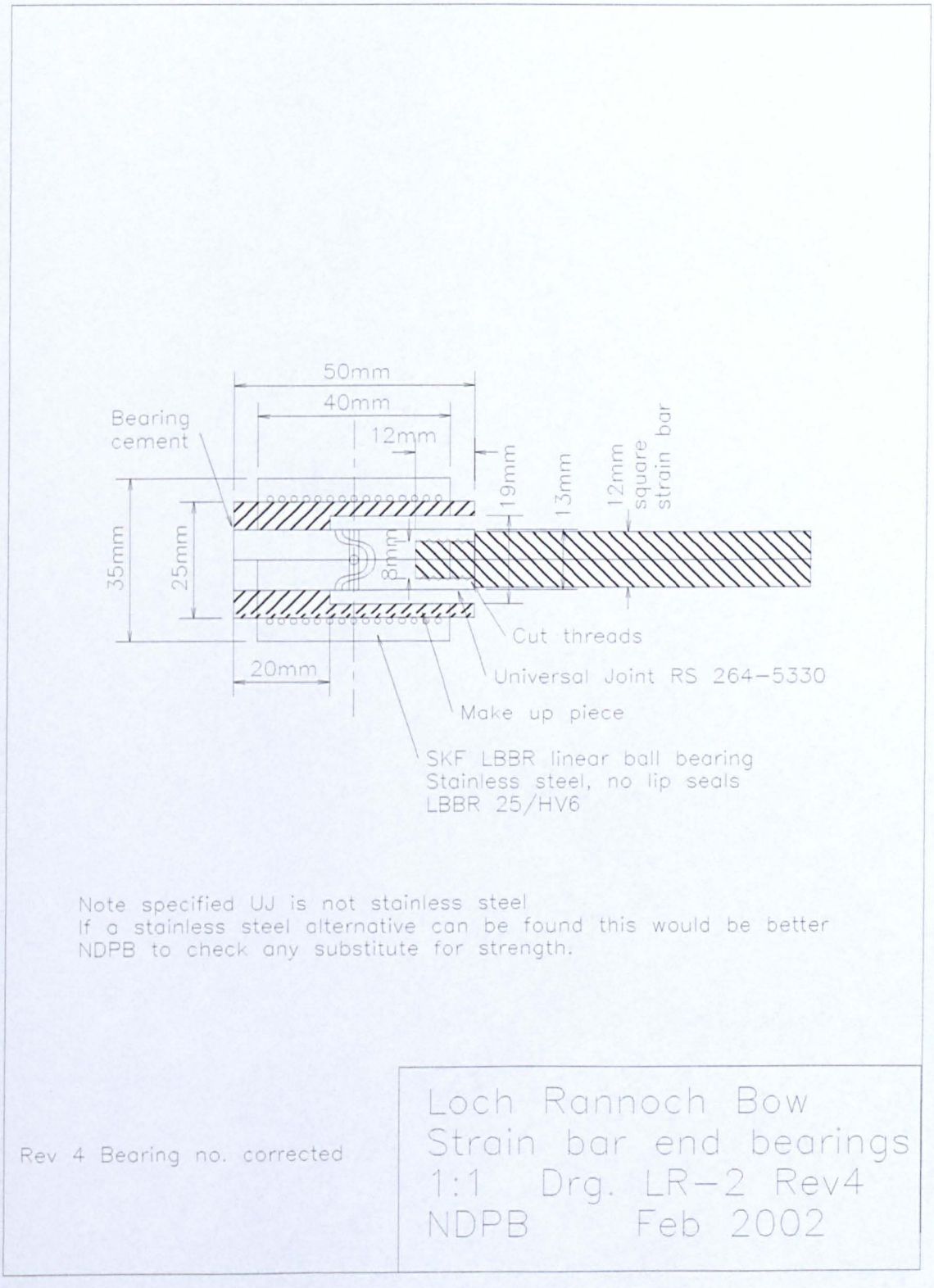

Figure 3.17 Bow strain-bar end bearings for Loch Rannoch

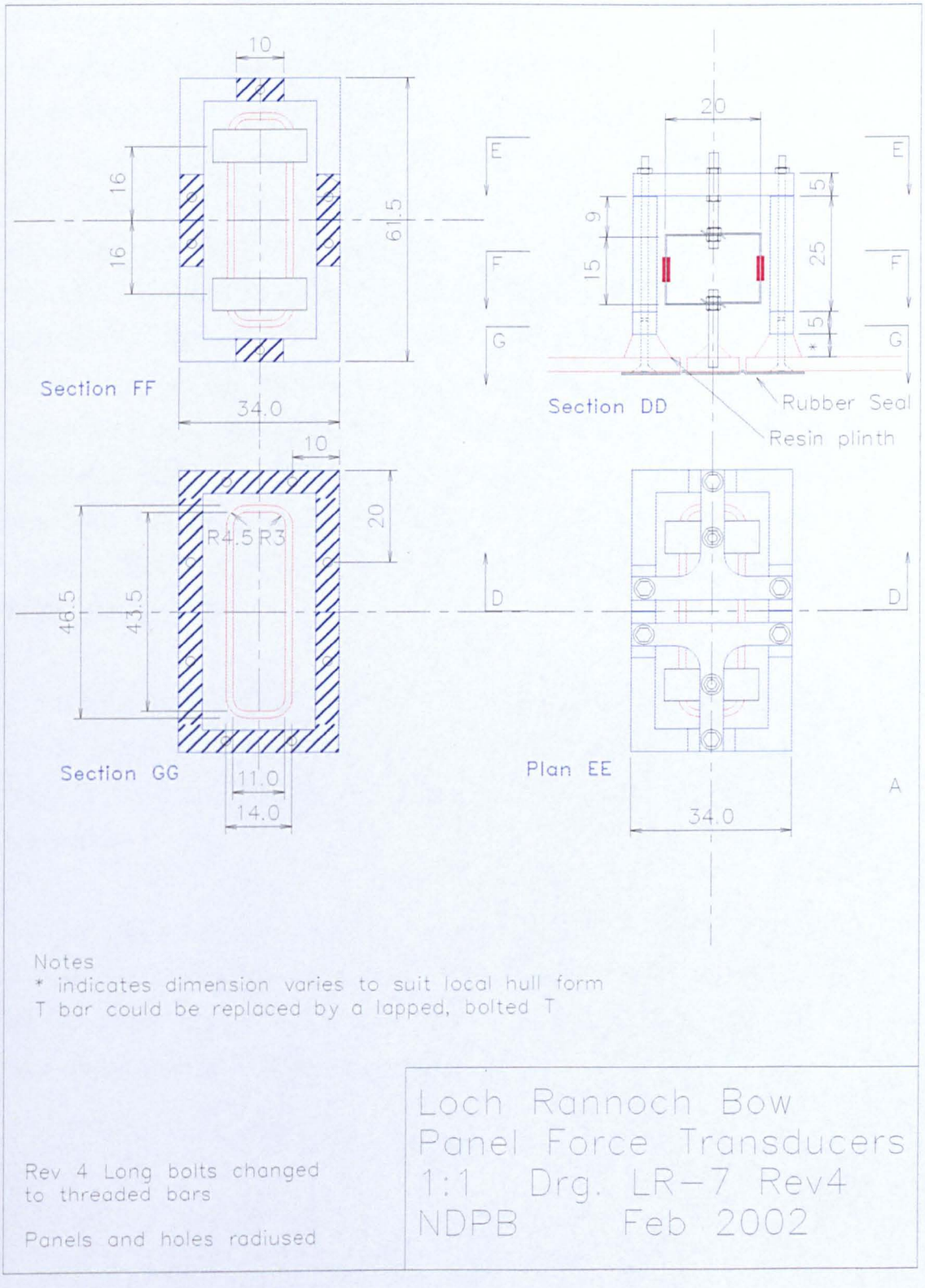

Figure 3.18 Bow pressure panels for Loch Rannoch

The difficulties of interpreting small pressure transducer results were overcome by designing pressure panels, which were made about the size of a ship bow panel (1m wide by 3.6m high). These panels were supported on two square brass rings which bend under load and are strain gauged (see Figure 3.18). A key design driver for the pressure panels is signal to noise ratio. Noise levels, which mainly come from the strain gauge amplifier power supplies, were measured and the signal output determined to make sure that a sufficiently strong signal was obtained. The natural frequency of the panels is again important. To low a natural frequency and the dynamic response becomes unrealistically high. A very high natural frequency that leads to no dynamic response would be an option but is very difficult to achieve in practice and if the natural frequency is similar to or higher than the sampling frequency and does get excited, then the results become impossible to interpret. A natural frequency of 34Hz full scale in water was achieved. This is of the correct order for a panel frequency and at model scale corresponds to 304Hz.

The strain gauges used for Loch Rannoch had the same type as for Schiehallion but the gauges within the pressure panels were sealed with a light waterproofing spray, because there was concern that the polysulphide might be too stiff for this application.

The Loch Rannoch model also had two accelerometers mounted in the bow, to measure heave and surge accelerations. The heave accelerometer was mounted on the top of the support for the bow strain bars. The surge accelerometer was mounted on the aft side of the same support.

3.3 Additional Measurements

3.3.1 Wave probes

For the Schiehallion model tests, to measure the wave profile, one resistance type wave probe was located at the target position level with the nominal bow position, 10m from the wave maker.

For the Loch Rannoch model tests three wave probes were positioned just beside the bow in the tank, 9.95m,10m and 10.05m distance from the wave maker respectively. This allowed the direct measurement of the front steepness and the celerity of the wave.

The wave probes consist of two parallel vertical wires a small distance apart partially immersed in the tank and supported by a streamlined frame. Wave elevation is sensed by detecting the resistance to an applied alternating voltage across the rods. The supply frequency is in the kHz range and the resultant small current is proportional to the immersed length of the wires. This current is demodulated and amplified to give a d.c. voltage proportional to wave elevation. Interference between the probes is avoided by using a different frequency for each probe.

3.3.2 Selspot position measuring system

Small infra-red light-emitting diodes which flash at different frequencies are fixed to selected points on the FPSO deck. A special electronic camera and dedicated computer detects the position of the diodes and outputs a voltage proportional to

the position of the LED. Multiple cameras and LEDs can be used to track motion in 3d but:

- for head sea tests surge and heave of 2 LEDs were measured from which the surge, heave and pitch of the model can be calculated.
- For bow quartering seas along and transverse to the tank motion of the LEDs was measured which, ignoring a small roll coupling) could be interpreted as surge, sway and yaw.

The LEDs were positioned on the deck as shown in Figure 3.8. The LEDs were mounted on a vertical sliding rod for ease of calibration of the selspot camera. Hence using the recorded data from the selspot camera during the experiments surge, heave and pitch amplitudes of the model are calculated using the following identities:

1) $Surge = surge1 - surge2$

2) $Pitch = \frac{heave1 - heave2}{c}$

3) $Heave = heave1 - Pitch * d$

Where $surge1$, $surge2$, $heave1$, $heave2$, c, d and the positive directions of heave and surge are defined in Figure 3.18.

For the Selspot system to give good results, the model must stay within the field of view of the camera and reflections off the water surface should be avoided.

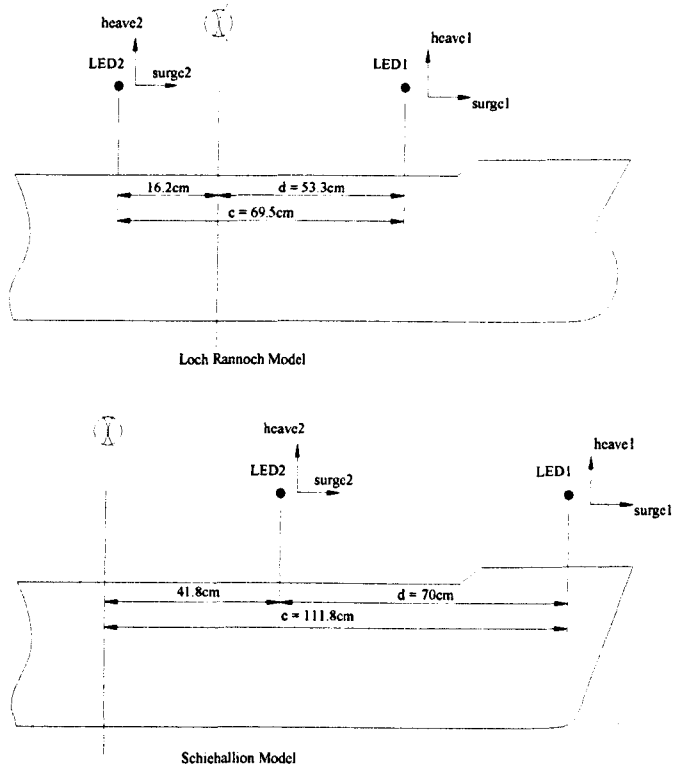

Figure 3.18 Positions of LEDs

3.4 Data Acquisition

During acquisition of the Loch Rannoch data a software package called LabView was run on a Dell Dimension 8210 terminal. The electronic signals from the instrumentation were amplified, either be device specific amplifiers for the wave gauges and Selspot system or using RDB (for the hull girder bending moments and strain bars) and Fylde (higher frequency response (for the pressure pads and pressure transducers) amplifiers collected through a 64 channel analogue to digital converter, further amplified and then stored in a built in hard disk in the form of a

'.csv' data file. This storage format is not space efficient but allows the data to be easily used by other software packages for data analysis.

Some of the data collected during each test has been automatically converted into corresponding unit of measured mode, such as pressures from pressure transducers, water surface elevation and heave and surge motions. The others applied with the calibration factors can be converted into the quantity and unit we want.

The length of time for each run was 50, 70 and 90 seconds for a new wave, a constrained random wave and random wave respectively.

The choice of the data acquisition rate is a compromise between file size, analysis time and accuracy. Experiments with the pressure transducers had shown that a 1000Hz sampling frequency gave 2 or 3 samples at the maximum pressure value and, even if the rise time was not always resolved, this gave some confidence in this sampling frequency for finding maximum pressure. The pressure panels have a natural frequency of 304Hz. If the panels responded with a dynamic amplification factor of 2 then the peak in the time history has the form $1+\cos(2\pi t/T) = 1+\cos(2\pi*1000/304)$ and with a data acquisition rate of 1000 Hz, the average peak pressure measured is 93% of the true peak value with a standard deviation of 6.4%. (If the peak occurs half way between samples being taken, then the measured value could be only 79% of the peak value. It has also been checked by using a SDOF (Single Degree-Of-Freedom) dynamic system. Applying a pulse with a linear rise (0.002sec) and exponential decay (0.006sec) (which is the typical case of the experiments) to a SDOF dynamic system with natural frequency of 304Hz, and setting the data acquisition rate of 1000Hz, by varying the starting point of data acquisition, the error of the peak can be calculated at each possible point during the period of 0.001sec. Since the work here is interested in the peak value of the response, only the errors for the peak response have been calculated. The errors corresponding to each possible starting time are

given in Figure 3.19. The average error is 8.4% and the maximum error is 23.8%. The results are similar with the rough calculation given above. However the dynamic response under the highest loads is typically only about 30% so the error in practice is very much smaller. Also, with a highly dynamic response the large errors are obvious because a characteristic flat topped time history results and the results can be corrected). Overall therefore there was some confidence that a 1000Hz data acquisition rate was in fact adequate. This still resulted in file sizes of 20-30 Mbytes for each wave group and about 28Gbytes of data to process.

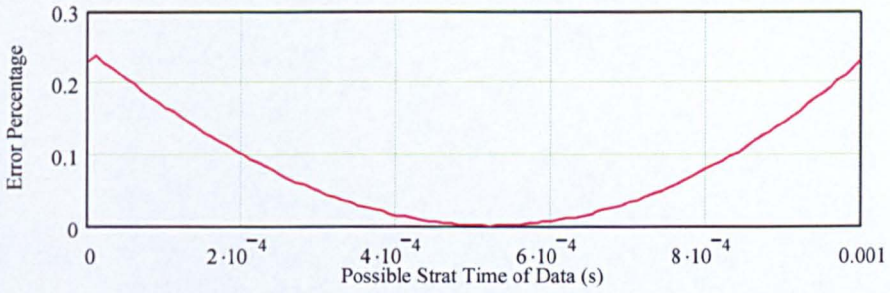

Figure 3.19 The error of the peak response caused by the data acquisition rate

Nevertheless if similar experiments were to be undertaken with the faster and larger storage capacity computers, a 2000Hz data acquisition frequency would probably be selected. Then with a dynamic amplification factor of 2, the maximum error would be a measurement of 94% of the true peak value with a mean of 98% and a standard deviation of 1.7%.

30 channels of data were acquired for the Schiehallion tests and 62 channels for the Loch Rannoch tests. A typical Loch Rannoch test therefore acquired about 4 million numbers. The channels for each of the measured quantities and the unit for each channel are listed in Tables 3.1 and 3.2.

Table 3.1 Measured quantity and unit for each channel (Schiehallion Model)

Channel No.	*Measured Quantity*	*Unit*
1	Pressure Transducer 1	psi
2	Pressure Transducer 2	psi
3	Pressure Transducer 4	psi
4	Pressure Transducer 7	psi
5	Pressure Transducer 8	psi
6	Pressure Transducer 9	psi
7	Pressure Transducer 10	psi
8	Spine Beam Position 1	volts
9	Spine Beam Position 2	volts
10	Spine Beam Position 3	volts
11	Spine Beam Position 4	volts
12	Spine Beam Position 5	volts
13	Drag Force at Top Bow Section (Front Bar)	volts
14	Drag Force at Top Bow Section (Rear Bar)	volts
15	Lift Force at Top Bow Section (Front Bar)	volts
16	Lift Force at Top Bow Section (Rear Bar)	volts
17	Drag Force at Mid Bow Section (Front Bar)	volts
18	Drag Force at Mid Bow Section (Rear Bar)	volts
19	Lift Force at Mid Bow Section (Front Bar)	volts
20	Lift Force at Mid Bow Section (Rear Bar)	volts
21	Drag Force at Bottom Bow Section (Front Bar)	volts
22	Drag Force at Bottom Bow Section (Rear Bar)	volts
23	Lift Force at Bottom Bow Section (Front Bar)	volts
24	Lift Force at Bottom Bow Section (Rear Bar)	volts
25	Wavemaker Signal	
26	Wave Probe	cm
27	Surge of LED 1	cm
28	Surge of LED 2	cm
29	Heave of LED 1	cm
30	Heave of LED 2	cm
31	Spare	
32	Spare	

Table 3.2 Measured quantity and unit for each channel (Loch Rannoch Model)

Channel No.	*Measured Quantity*	*Unit*	*Channel No.*	*Measured Quantity*	*Unit*
1	Pressure Transducer 1	psi	33	Bottom Left Vertical F	volts
2	Pressure Transducer 2	psi	34	Bottom Left Horizontal F	volts
3	Pressure Transducer 3	psi	35	Bottom Right Horizontal F	volts
4	Pressure Transducer 4	psi	36	Bottom Right Vertical F	volts
5	Pressure Transducer 5	psi	37	Top Stern Vertical F	volts
6	Pressure Transducer 6	psi	38	Top Stern Horizontal F	volts
7	Pressure Pad 1	kg	39	Spine Beam 1 (Vertical)	volts
8	Pressure Pad 2	kg	40	Spine Beam 2 (Vertical)	volts
9	Pressure Pad 3	kg	41	Spine Beam 3 (Vertical)	volts
10	Pressure Pad 4	kg	42	Spine Beam 1 (Horizontal)	volts
11	Pressure Pad 5	kg	43	Spine Beam 2 (Horizontal)	volts
12	Pressure Pad 6	kg	44	Spine Beam 3 (Horizontal)	volts
13	Pressure Pad 7	kg	45	Hull Bar 1	volts
14	Pressure Pad 8	kg	46	Hull Bar 2	volts
15	Pressure Pad 9	kg	47	Hull Bar 3	volts
16	Pressure Pad 10	kg	48	Hull Bar 4	volts
17	Pressure Pad 11	kg	49	Hull Bar 5	volts
18	Pressure Pad 12	kg	50	Hull Bar 6	volts
19	Pressure Pad 13	kg	51	Hull Bar 7	volts
20	Pressure Pad 14	kg	52	Hull Bar 8	volts
21	Pressure Pad 15	kg	53	Surge of LED 1	cm
22	Pressure Pad 16	kg	54	Heave of LED 1	cm
23	Pressure Pad 17	kg	55	Surge of LED 2	cm
24	Pressure Pad 18	kg	56	Heave of LED 2	cm
25	Pressure Pad 19	kg	57	Wavemaker Signal	
26	Pressure Pad 20	kg	58	Wave Probe 1	cm
27	Top Left Vertical F	volts	59	Wave Probe 2	cm
28	Top Left Horizontal F	volts	60	Wave Probe 3	cm
29	Top Right Vertical F	volts	61	Spare	

30	Top Right Horizontal F	volts	62	Accelerometer 1
31	Bottom Stern Vertical F	volts	63	Accelerometer 2
32	Bottom Stern Horizontal F	volts	64	Spare

Video recordings were also made of most of the tests from two angles of view.

3.5 Calibration And Assessment Of Callibration Errors

The un-ballasted model was swung, on a bifilar suspension system, to determine its radius of gyration.

The model was then transferred to the shallow dock area in the tank and left there overnight to check for leaks.

The model was then wired to the data acquisition system and the calibrations performed and the calibrations roughly checked against the expected strain gauge outputs. (This takes about two weeks if there are no problems).

The pressure transducers were calibrated using a hand held pump and dial gauge with a flexible rubber end fitting that sealed against the hull, over the gauge. When the required pressure was reached the data acquisition system reading was recorded. This operation was repeated for different pressures to check linearity. The pressure-voltage relationship was then keyed back into the computers calibration file. The unit of the output from the data acquisition system for the pressure transducer is then psi.

The pressure pads were calibrated by applying known forces to each pad, normal to the panel and in line with the axis of the sensor behind the pad, using a specially designed but very simple two arm, force balance. Weights were hung from an arm that was adjusted to be horizontal whilst another arm of the same

length and with a bearing pin on its end was adjusted so that the pin was normal to the panel. The two arms were clamped together but could rotate freely about their connection point, so a force equal to the weight was applied normal to the panel. The unit for the output from the pressure pad is kg.

The model was then moved into the tank.

The spine beam was calibrated by putting two 4 kg weights at the middle of the spine beam then moving each 4 kg weight either forwards or backwards along the spine beam: 1.15 m for Loch Rannoch and 0.98 m for Schiehallion. This changed the moment on the spine beam without affecting the buoyancy forces.

The transverse hull bars are calibrated by moving weights vertically from the spine beam into the hull segment. Again this gives a known force change on the hull bars because there is no change in the buoyancy.

The bow segments are calibrated using cast iron weights. For the Loch Rannoch bow region, there are two horizontal segments and each segment has three strain bars jointed at one end and with four strain gauges on each bar to measure the six forces and moments. The arrangement is shown in Figure 3.13 to 3.15. For the Schiehallion bow, there are three horizontal segments, each segment has a pair of strain bars with four strain gauges on each to measure the horizontal and vertical forces and the pitch moment. The calibration was performed by applying different forces and moments to each segment using weights, directly on the segment (Figure 3.20), hanging off the segment or loading the segment horizontally via a pulley system. Scribed circles show where weights are to be placed. Pins protruding from side of model are for connecting wires for load application The loads applied are shown in Figure 3.21. The model was floating but clamped to a carriage spanning the tank for this procedure so that the draft would not change. When weights were hung into the water the buoyancy effect was taken into account.

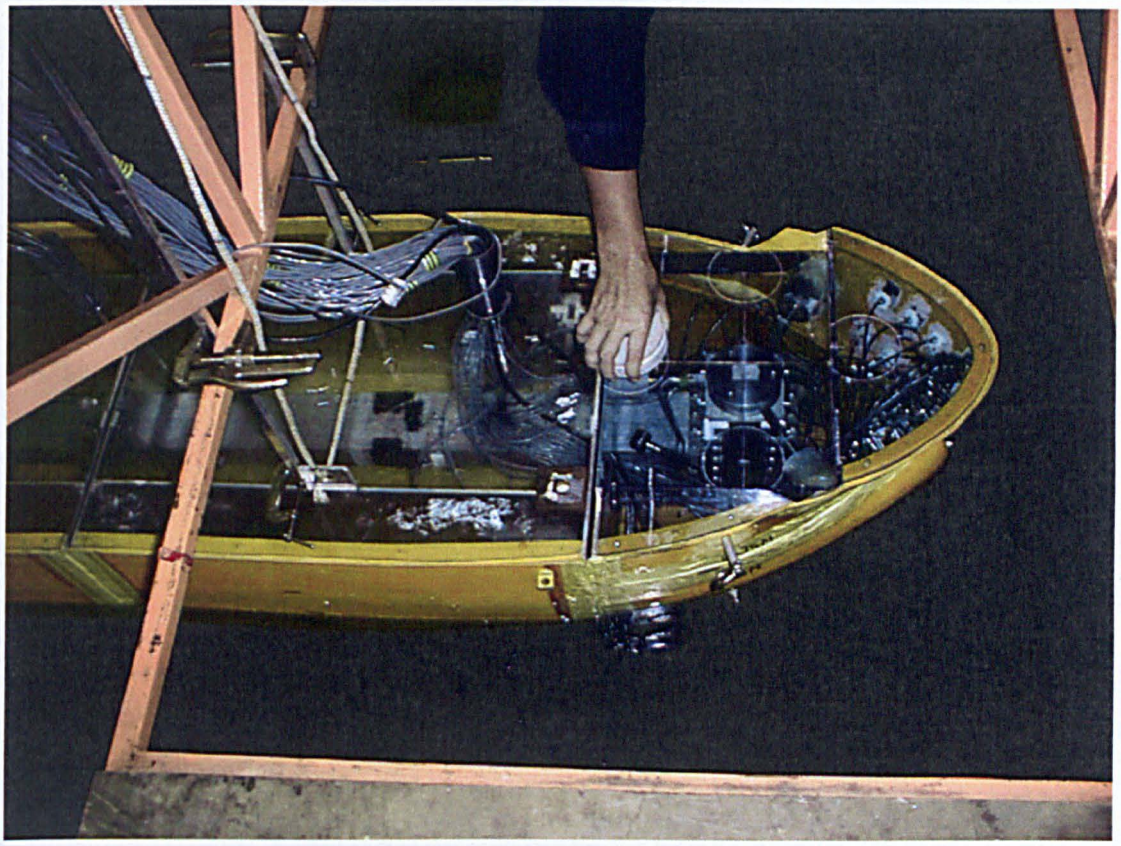

Figure 3.20 Calibrating the vertical force measurement on the Loch Rannoch upper bow segment.

The accuracy of the calibration depends on the accuracy of the weights, frictional forces and alignment of the pulley systems and, for the hull girder bending moments and strain bars supporting hull segments or the lower bow segment, the contribution of the water to resisting the change in the applied forces. The vertical forces on the above water segments should be accurate to the accuracy of the weights, better than 1%. The horizontal forces will be affected a little by friction and misalignment but the friction in the pulleys was very small and even a 5 degree misalignment would only give a 0.4% error so the accuracy should be similar to the vertical forces around 1%.

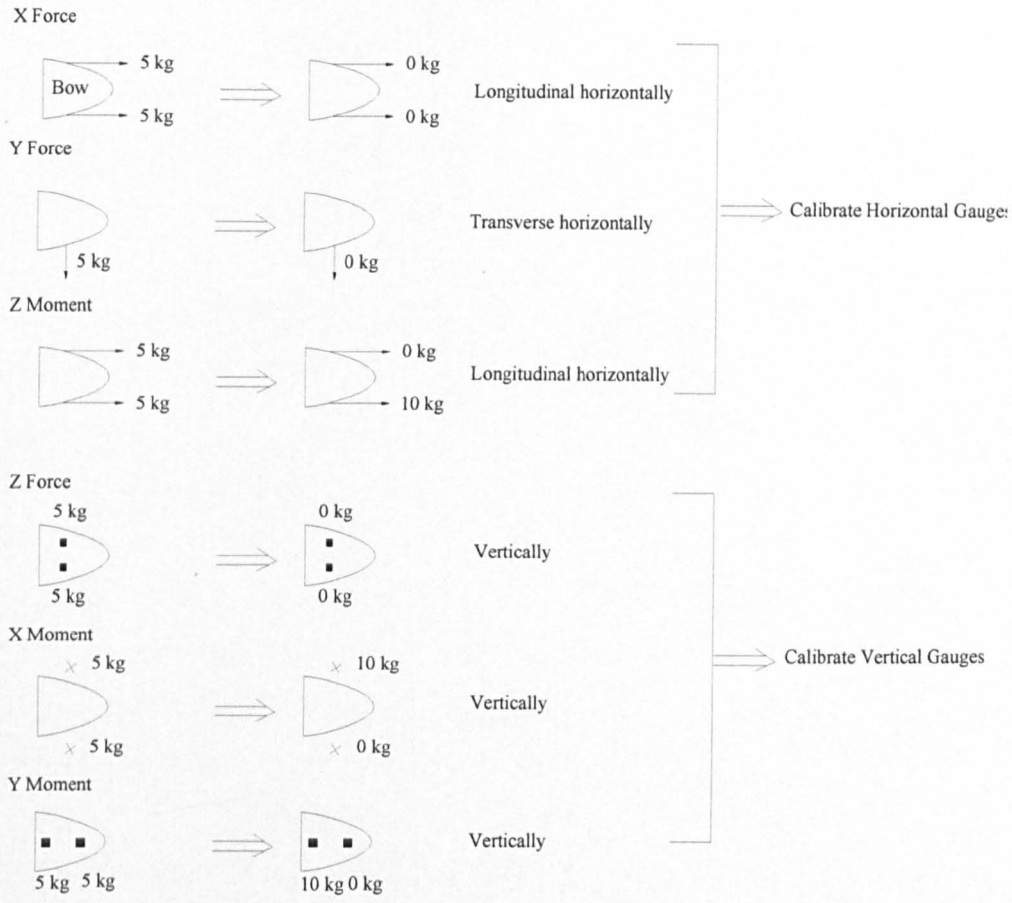

Figure 3.21 Calibration loading cases for Loch Rannoch

The bending moment measurements rely on the effects of the hydrostatic stiffness being much lower than the structural stiffness. The effect can easily be estimated from the heave and natural periods, because if the FPSO were to oscillate in structural mode 1 shape but without any structural stiffness then it would vibrate at the heave period! For the Loch Rannoch first structural natural period of about 1.4 sec and natural heave period of about 8.4 sec the error (assuming added mass at both frequencies is the same) will be $(1.4/8.4)^2 = 2.8\%$ of the hull girder bending moment. For Schiehallion the hull girder is relatively stiffer and the error will be about 1.5%. In both cases the error will result in the measurements being a small overestimate of the actual bending moment. A similar argument applies to

the strain bar calibration when the segments are partly immersed but the natural periods are even shorter (about 0.7 sec) so the errors are about 0.7%.

The Selspot system was calibrated by moving the LEDs between known positions and observing before and after the movement through the camera system.

The waveprobes were calibrated by moving them 50mm vertically in still water and taking a measurement before and after the movement.

The accuracy of the Selspot and Waveprobe calibration is estimated to be about 2%.

The accelerometers are calibrated prior to fixing them in the model by rotating them through 90 and 180 degrees and using gravity for calibration. Accuracy of calibration should again be to within a few percent.

The calibration of the wavemaker was described in Chapter 2.4.

The potential accuracy of the model is quite high. In practice the instrumentation is bound to degrade to some extent during the tests. Ideally the model would be recalibrated before removing from the tank but it was decided that it was preferable to do more repeat tests which give a better idea of the overall variability in the measurements.

3.6 Experimental Procedure

The Schiehallion model was mainly tested at 12m (ballast draft) with additional tests at 20m (loaded draft).

The Loch Rannoch model was mainly tested at 9.6m draft with additional tests at 7m (shallow) and 15.35m (deep) draft.

Schiehallion was only tested in head seas but Loch Rannoch was also tested in waves incident at 20 degrees and 30 degrees off the bow.

The mooring system was essentially the same for both models. In place of the real catenary mooring the mooring was above the water and was composed of stiff bridles connecting the model to elastic lines, in line with the model, and stiff bridles connecting the elastic lines to the tank rail anchor bolts. The mooring system was designed to result in a natural slow-drift period of about 100 sec, which is typical for an FPSO, but the precise period was not important. The horizontal mooring force on Loch Rannoch was resisted by the stern segment with mooring lines in guides on the bow section. This resulted in some small vertical forces on the upper front segment, which though unimportant (since the slam was separated from the more slowly varying forces during the analysis), was untidy, so for Loch Rannoch the moorings were changed to avoid any contact with the bow segments. Also on Loch Rannoch an aluminium spacer was used in the mooring bridle ahead of the model, this resulted in a more parallel entry of the mooring lines into the top segment guides, so reducing frictional forces on the guides. However in some waves the spacer skimmed the water surface, which might have effected those results, so a further advantage of the Loch Rannoch mooring system was that it dispensed with the spacer.

The models were ballasted down to the required draft, with lead weights clamped to the deck below the spine beam, The weights were approximately evenly

distributed, subject to no weights being put into the bow and achieving the required zero trim.. The position of the various weights was noted so that with the results from the swinging test it would be possible to estimate the ballasted radii of gyration.

The model was placed in the tank with the front of the upper bow at the target position, 10m distance from the wave maker.

A programme of about 200 tests for Schiehallion and about 1000 tests (including a substantial number of repeats) for Loch Rannoch were run. The primary series of waves tests are listed in Table 3.4. For random wave case, to save tank testing time and reduce the reflection errors the shorter segment with the extreme wave in it was chosen to run in the tank from a long time history (3 hours random wave time history).

These are based on an estimated 100 year contour of sea states for the Schiehallion area, provided by BP, from which the Table 3.3 'basic cases' were selected.

Table 3.3 Basic 100 year contour seastates

Steepness	H_s (m)	T_z (sec)
1/13	14.20	10.9
1/14	15.67	11.8
1/15	17.08	12.8
1/16	17.67	13.4
1/17	17.95	14.0

Tests were run every 15-20minutes. Each test was assigned a unique number which was also recorded onto the video, however these test numbers have not generally been used in this thesis.

For each test the wave maker was powered up, the data acquisition system started, then the wavemaker data file started and the video started. It was important to

start the data acquisition system before the wavemaker data file because synchronising signals would otherwise be lost.

The best video angle was found to be looking slightly forward towards the bow. This allowed a good view of the impact. A view looking from the side but slightly towards the stern becomes obscured by the slapping wave. The other view was varied and included the overall model from the side, the overall model from aft of the stern and the bow filmed from a camera attached to the model's deck.

The time between tests allowed the water and model motions to die down, a brief data quality assessment to be made, and the video recorder to be re-titled.

Data processing was attempted in parallel with the testing but it was not possible to keep up with the tests. This meant that some tests were not carried out, which having processed the data would ideally have been carried out. These include higher SB tests in the 1/15 – 1/17 sea-states and tests in less steps sea states.

Overall views (extracted from the videos) of Schiehallion and Loch Rannoch under test are shown in Figure 3.22 and 3.23.

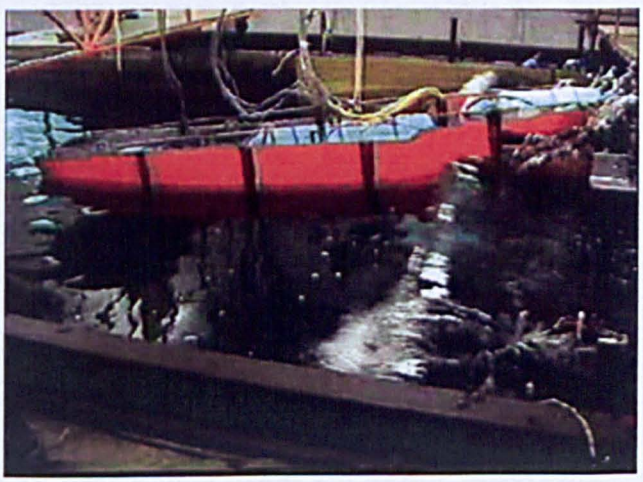

Figure 3.22 Schiehallion test (ballast draft)

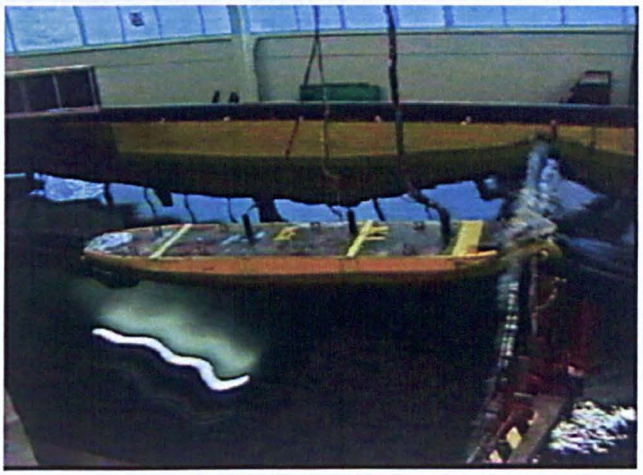

Figure 3.23 Loch Rannoch test (deep draft)

Table 3.4 Primary series of tests

New Wave
100 year return, range of steepnesses and steepness balances 1/13, 1/14, 1/15, 1/16, 1/17, 1/18 Sea State Steepness Spectral peak enhancement factor γ = 2 Frequency cut-off = 2.25 a. Highest wave (SB = 0) b. Steepest wave (SB = 1) c. 50% Steep wave (SB = 0.5) d. Maximum hogging bending moment e. Maximum sagging bending moment
100 year return frequency cut-off study (Loch Rannoch only) 1/14, 1/15, 1/16, 1/17 Sea State Steepness Spectral peak enhancement factor γ = 2 Frequency cut-off = a. $1.5 f_p$ b. $2 f_p$ c. $2.25 f_p$ d. $3 f_p$ e. $5 f_p$ (f_p = spectral peak frequency)
100 year return steepness balance study (Loch Rannoch only) 1/15, 1/16 Sea State Steepness Spectral peak enhancement factor γ = 2 Frequency cut-off = 2.25 Steepness balance: SB = 0 to 0.7
100 year return Jonswap peak enhancement study (Loch Rannoch only) 1/14, 1/15, 1/16, 1/17 Sea State Steepness 50% steep wave SB=0.5 Spectral peak enhancement factor γ = 1, 2, 3.3
Wave height increase study (Loch Rannoch only) Basic sea-states period maintained but height varied 50% steep wave SB=0.5 Spectral peak enhancement factor γ = 2 a. $H_s = 0.95 * H_s$ b. $H_s = 1.00 * H_s$ c. $H_s = 1.06 * H_s$ d. $H_s = 1.11 * H_s$ e. $H_s = 1.19 * H_s$

Hull Girder Bending moment study
T_z = 11.8, 12.8 sec (Basic cases 1/14, 1/15 sea-state steepness)
Spectral peak enhancement factor γ = 2
Frequency cut-off = 2.25

Maximum hogging moment
Maximum sagging moment
0.2 to 1.2 times basic Hs

Target position study
1/12.5, 1/13.5, 1/14.3, 1/15, 1/17 Sea-state steepness
Spectral peak enhancement factor γ = 2
Frequency cut-off = 2.25

Target positions for wave: –72m (in front of bow) to +96m (behind bow)

Velocity balance study
1/16 sea sate steepness (H_s = 17.67m, T_z = 13.4sec)
Spectral peak enhancement factor γ = 2
Frequency cut-off = 2.25

Velocity-height balance in wave group formulation changed from 0 to 0.7

Random Wave
H_s = 18.73m, T_z = 13.4sec
(1.06 times basic 1/16 sea-state steepness)
Spectral peak enhancement factor γ = 2
Frequency cut-off = 2.25

Constrained Random Wave
Case1: H_s = 18.73m, T_z = 13.4sec
(1.06 times basic 1/16 sea-state steepness)
Spectral peak enhancement factor γ = 2
Frequency cut-off = 2.25

50% steep wave A=0.5
H_s =1.06*H_s (100 Year Return, 1/16 Sea State Steepness)

Case2: 100 Year Return
1/14 Sea State Steepness
Spectral peak enhancement factor γ = 2
Frequency cut-off = 2.25
Maximum bending moment (+)
Maximum bending moment (-)

4 Experimental Results From FPSO Model Tests

During the experiment, forces, pressures and moments at the bow and the hull girder bending moment and the motions of the model were recorded. In Section 2 the wave selection and generation were discussed, in this section the total bow force and the local pressures at the bow during a slapping event are reported. This section first aims to better understand the significance of the new-wave group results and then to draws conclusions about the variation of the impact pressures and the structural responses. Sections 4.1 – 4.3 compares results from new-wave type groups, selected random wave segments and constrained random waves. Sections 4.4 onwards discuss the results of the wave group tests, considering trends caused by systematically varying the input parameters.

All the results in this section are given as full scale values and all the impact pressures are given in pressure head (m). For a discussion on scaling see Section 3.1.

4.1 Wave Groups

To investigate the usefulness of new-wave group, experimental results were compared with short segments of random waves for one sea-state (H_s = 18.73 m, T_z = 13.4 sec) in head sea slapping conditions for the Schiehallion and Loch Rannoch models. Each sea segment was selected on the basis of the 805 seconds around the highest wave in a 3 hour sea state simulation. Of the ten random waves run for Schiehallion only four of them produced slapping loads. All forty of the random waves segments selected for Loch Rannoch produced a slap. The results, Tables 4.1 a and b, showed that simply selecting high wave groups in the random waves did not produce such high pressures as the 50% steep new-waves.

Table 4.1a Random vs New-Wave bow pressure heads: Schiehallion

Slapping Pressure	*Random waves (4 different waves)*		*New-wave (50% steep) Max frequency = 2.25 fp (1 wave)*	
	Top Seg.	Mid Seg.	Top Seg.	Mid Seg.
Mean	17.5m	7.6m	21.2	41.1
SD	15.9m	3.8m	-	-
CoV	0.91	0.5	-	-

Table 4.1b Random vs New-Wave bow pressure heads: Loch Rannoch

Slapping Pressure	*Random waves (40 different waves)*	*New-wave (50% steep) Max frequency = 2.25 fp (4 same waves)*
Mean	8.5m	12.9m
SD	4.4m	0.9m
CoV	0.52	0.068

If the subset of the random wave segments with the largest value of $\alpha\eta + (1-\alpha)\, d\eta/dt$ greater than that in the 50% steep new-waves is selected then the results shown in Table 4.1c are obtained.

Table 4.1c Steep random vs New-wave bow pressure heads: Loch Rannoch

Slapping Pressure	*Random waves (8 different waves)*	*New-wave (50% steep) Max frequency = 2.25 fp (4 same waves)*
Mean	13.6m	12.9m
SD	7.0m	0.9m
CoV	0.51	0.068

Clearly for a bow impact it is not sufficient to have a wave segment containing a high wave, it must also be steep. However the 50% steep new-wave does seem to be a reasonable approximation to the bow forces from the steep-high wave segments. A future possibility would be to select the random wave segments to be around the times of the maximum of the quantity:

$$\alpha\eta + (1-\alpha)\, d\eta/dt$$

Nevertheless these results suggest that the total bow forces in a random sea are represented by the new-wave results.

The panel pressure results (Loch Rannoch only, because there were no panels on Schiehallion) are shown in Table 4.2.

Table 4.2 Pressure heads from pressure pads for Loch Rannoch Model

	Random wave (40 different waves) 805s duration of each random wave					*New-wave (50% steep) (4 same waves)*
	133.4m	23.4m	44.0m	46.6m	32.5m	272.2m
	33.5m	30.9m	48.2m	44.0m	28.2m	245.8m
	26.7m	42.5m	32.1m	68.0m	36.2m	216.4m
	24.0m	33.4m	49.1m	50.0m	42.8m	224.6m
	27.0m	78.3m	275.3m	56.0m		
	19.7m	50.8m	43.0m	66.0m		
	21.8m	63.0m	58.0m	30.6m		
	32.8m	55.0m	105.3m	31.4m		
	68.3m	46.0m	62.8m	36.0m		
Mean	52.42m					239.8m
SD	42.53m					24.9m
CoV	0.811					0.104

These show greater differences, than the whole bow forces, between the random segments and the new-waves. The largest of the random wave panel pressures (275.3m) is close to the largest new-wave panel pressure (272.2m), because the instant wave profiles at the target position are very close (see Figure 4.1), further more it can been seen from the test video that for both cases the bow of the FPSO model was at the target position when the impact occurred. However, the other random wave panel pressures are much smaller than the new-wave panel pressure. The reason for this appears to be the greater sensitivity to the bow surge position for local pressures than for the overall bow forces. This greater sensitivity was found in the target position test series and is shown in Table A4.2. In random waves the slow drift oscillations are much greater than in new-wave groups so the experimental wave, which is focussed on a point in space, will be less well focussed on the FPSO's bow. In the real sea there is no target position so probability determines the frequency and intensity of the impacts.

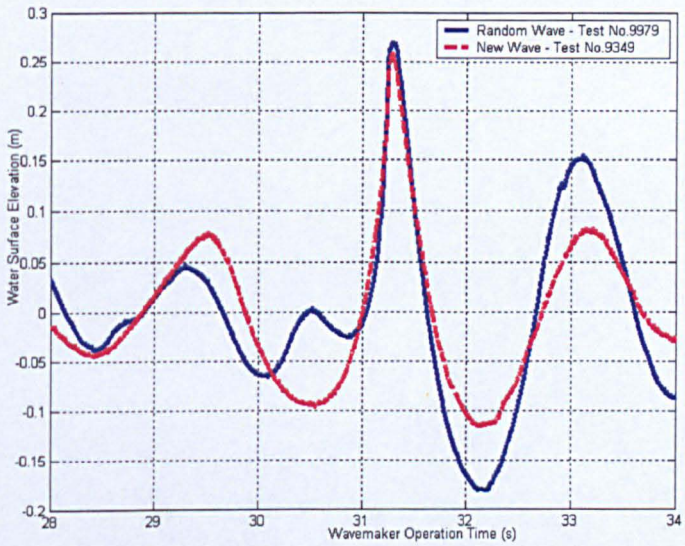

Figure 4.1 Instant wave profiles of a random wave and a new wave causing similar panel pressure during the impact

This suggests that prototype pressures would also be reduced by the need for the bow to be in the right place at the right time. In fact, however, the effect of the slow drift oscillations on the statistics of the prototype bow forces is thought to be

small because the instantaneous slow drift oscillation position is independent of the instantaneous wave amplitude and slope and so the statistics of the random sea prototype impact pressures, unlike the model short random segment pressures, should not be affected by these oscillations. There is still an effect of the sensitivity of the hull to the wave shape at impact and this is changing rapidly with time and distance. In the deterministic methodology used in Section 5.4, (and optionally in stochastic reliability analysis), this sensitivity is taken into account by the use of the 'bell curve' determined partly from the experimental results in Section 4.9 below.

Therefore, based on the present data, the new-wave results are expected to be a useful input for the deterministic and stochastic estimators of the extreme pressures. This is further investigated in Chapter 5 using time history simulation in random waves (without slow drift motion) and in wave groups where the results confirm the above conclusion.

4.2 Constrained Random Waves

For comparison 50% steep, max frequency = $2.25f_p$ new-waves and max frequency = $3f_p$ constrained random waves were generated in the tank for the same sea-state.

Also random waves of the same sea-sate were constrained to contain the same 50% steep event and were generated in the tank. Two of these generated slapping loads during the Schiehallion Model Tests and nine in the Loch Rannoch tests. The results of the maximum total bow slapping pressure are given in Tables 4.3a,b and the panel pressures in Table 4.4.

Table 4.3a Constrained random wave vs. new-wave bow impact pressure heads: Schiehallion

Slapping Pressure	*Constrained Random waves Max frequency = 3fp (2 different waves)*		*New-wave (50% steep) Max frequency = 2.25fp (1 wave)*	
	Top Seg.	Mid Seg.	Top Seg.	Mid Seg.
Mean	22.1m	27.2m	21.2m	41.1m
SD	2.8m	3.6m	-	-
CoV	0.13	0.13	-	-

Table 4.3b Constrained random wave vs. new-wave bow impact pressure heads: Loch Rannoch

Slapping Pressure	*Constrained Random waves Max frequency = 3fp (9 different waves)*	*New-wave (50% steep) Max frequency = 3fp (1 wave)*
Mean	7.0m	5.1m
SD	2.2m	-
CoV	0.32	-

Table 4.4 Constrained random wave vs. new-wave panel pressure heads: Loch Rannoch

	Constrained Random wave (9 different waves)	*New-wave (50% steep) (4 same waves)*
	29m	272.2m
	15.4m	245.8m
	15.5m	216.4m
	165.6m	224.6m
	18.4m	
	22.4m	
	35.3m	
	20m	
	9.6m	
Mean	36.8m	239.8m
SD	48.9m	24.9m
CoV	1.33	0.104

These results show some similarity with the random wave – new-wave comparison. Now the wave group is guaranteed to contain the required extreme combination of water surface elevation and steepness at the target point (the comparison of water surface elevation with new wave group is good, see Figure 2.21) but again the constrained random wave results in a slow drift surge oscillation means that the ship has often moved away from the target point when the design event occurs. As for the random waves this has a larger effect on the panel pressures than on the overall bow forces.

It seems that the constrained random waves are difficult to use with a floating structure because of the difficulty that the slow drift oscillations reduce the probability of correctly focussing the wave on the structure. This problem is much lower with new-wave groups, because there is insufficient time to build up the oscillations.

4.3 Applicability Of Wave Group And Random Wave Tests

New-wave groups provide a systematic method of testing models under impact conditions. The results provide insights into the behaviour of the impacts that can be difficult to extract from purely random tests. However the appropriate type and relative position of the wave groups and the model is not clear without testing so there is a need to vary the properties and position of the wave group to make sure that the worst cases have been found.

Constrained wave groups in principle could provide a better understanding of the slap statistics than simple new-wave groups because the variability of the conditions around the extreme event is modelled. The long constrained wave groups that were used in this work had the disadvantage of causing slow drift oscillations that reduced the effectiveness of the focussing of the wave groups on the bow. Future tests with constrained wave groups might be better performed with shorter time segments to reduce the slow drift oscillations and so improving the focus on the bow, or with repeat runs with different target points.

Selecting segments from random time histories has the same drift problem as constrained waves.

Random wave tests take longer to perform; each 3-hour sea state of interest will need to be run many times with different seeds and may need to be split into a number of shorter time histories to prevent excessive reflections building up in the tank. However the results of the long time series require relatively little interpretation and there is no need to prejudge the likely worst cases.

Overall, taking into account these results and the numerical simulations in Sections 5 and 6, it is concluded that:

- For research purposes all these techniques are valuable.

- For computer analysis, where the position of the wave relative to the model can be defined without the concern of the slow drift motion, the new-wave groups could be a very attractive option.
- If care is taken to establish the characteristics of the wavemaker and to check wave groups against long time-histories of random loading then the wave group method could usefully be used for future wave impact tank testing.
- For routine model testing, long random-wave time-histories, though time consuming, are the safest option for identifying appropriate slap loading.

4.4 Frequency Cut–Off Study

For high waves the new-wave theory implies that all the frequency components should be included in the most probable highest wave shape.

When a structural response is considered then it is not necessary for all the frequency components to be included because the high frequency components will generally result in a very small localised contribution that will have little importance for the structure but will be obtained at the 'statistical expense' of a larger involvement of the longer period and more damaging wave components (see Chapter 2). In some cases the way in which the transfer function for the response drops off at high frequency (eg. hull girder bending moment) is known and the appropriate transfer function can be used directly in the methodology. For bow impact there is no such transfer function and so an approximate transfer function, which is taken as uniform but with a high frequency cut-off, is determined experimentally.

This set of experiments compares the results with different transfer function frequency cut-offs; the results (Appendix Table A4.1) were used to determine the

cut-off frequencies for the most severe impact. All the waves generated for the frequency cut-off study had a steepness balance of 50%.

The results for the pressure pads and overall bow forces showed that 42.5% of the worst impacts resulted from a transfer function frequency cut-off at 2.25 times f_p, the peak frequency of the spectrum (see Table 4.5). The 2.25 f_p cut-off was therefore used for the majority of the tests.

Note however that:

1) The values checked were 2, 2.25, 3 and 5 and there are some indications that a slightly higher cut-off value might give higher loads on average.
2) The random waves and the highest waves do not require a transfer function frequency cut-off (since no transfer function is used). In fact the frequency cut-off of 2.25 was still used for the high waves of new wave group but 3 was used for the random waves and the random new-waves. In future work with random new-waves it would be possible to extend the method and to use a frequency cut-off of about 2.25 f_p for the constrained wave in conjunction with a random time history including a higher frequency cut-off.

The change in pressures from a change in the cut-off frequency was significant. The pressures either side of the maximum were often about 50% of the maximum value. The new-wave analyses also indicated that a cut-off at about 2.25 f_p was likely to be a sensible choice because it retained most of the wave energy and produced what, by eye, appeared to be a severe wave shape that was both high and steep.

Table 4.5 Occurrences of maximum impacts for different max/peak frequencies

f_{max}/f_p	2	2.25	3	5
Number of occurrences	10	17	11	2
Percentage	25%	42.5%	27.5%	5%

4.5 Target Position Study

The target position for the wave relative to the still water position of the most forward part of the bow needs to be selected. The still water position of the front of the bow is 800m (full scale) from the wave maker. The tests (Appendix Table A4.2) and Figure 4.2 showed that the target point that gives the highest load becomes slightly further from the wavemaker as the sea-state steepness increases. The effect may be partly caused by:

1) The steeper waves tending to break earlier and therefore need to be focussed further along the ship (focus point greater than 800m) in order not to break before encountering the bow.
2) The mean drift force on the ship changing in the different waves and resulting in the ship itself being in a slightly different mean position.
3) The slow drift motion resulting in a different positions of the bow.

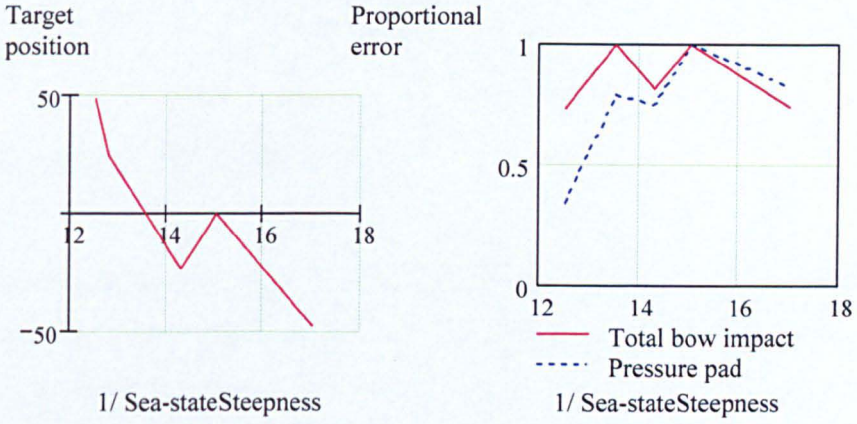

a) critical target position b) proportional error from using bow as target

Figure 4.2 Effect of sea-state steepness on the critical target position (negative in front of bow) and error resulting from targeting bow for 50% steepness-balance new-waves

However from the observations 1) is thought to be the dominant effect. This suggests that the effect will be linked to that of the steepness balance (Section 4.6) because this also affects the breaking position. The combined effect is anticipated (though not proven through testing) in Figure 4.3.

The pad pressures for the 1/18 steepness waves were low (about 2m) and not very sensitive to the target position.

The largest impacts occurred in the 1/14.3 and 1/15 steepness sea states so a target point of the bow front was a reasonable choice.

A single result for Schiehallion was obtained in 1/17 steepness seas with a 100% steepness balance and a +80m target point. This gave a reduction factor on bow

force (upper two segments) of 0.63. This is a slightly bigger reduction than was found for the 50% steepness factor Loch Rannoch experiments but is important for the 1/17 steepness waves where the 100% steepness balance is more relevant (see below).

4.6 Steepness Balance Study

The front steepness balance (See Chapter 2) allows the wave to be made high (steepness balance = 0), steep-fronted (steepness balance = 1) or a combination of high and steep-fronted; whilst maintaining the same probability of occurrence. The Schiehallion results, in a sea-state steepness of 1/15, for the range of front steepnesses suggested that a value of 0.6 would result in the highest top segment bow loads and a value of about 0.5 would result in a maximum mid + top section load. There were no pressure panels but pressure transducer values, though not severely loaded, were relatively insensitive to the steepness balance, see Table 4.6a.

Table 4.6a Schiehallion steepness balance results (pressure head in m)

Steepness balance	*Sea State Steepness*	*top segment bow impact*	*mid segment bow impact*	*pressure transducer*	*average bow impact*
0		0	4.8	390	02.4
0.3	H_s = 17.08m	0	2.3	500	1.1
0.4	T_z = 12.8s	2.3	5.2	390	3.8
0.5	1/15	6.7	12.8	430	9.7
0.6		10.4	6.4	400	8.4
0.7		9.7	5.9	440	7.8
1		9.8	9.6	330	9.7

Table 4.6b Loch Rannoch steepness balance results (pressure head in m)

Head Sea			*Head Sea*			
Steepness balance	*Sea State & Steepness*	*top segment bow impact*	*Sea State & Steepness*	*top segment bow impact*	*pressure transducer*	*pressure pads*
0		0.6		0	115	17.3
0.3	H_s = 17.08m	4.3	H_s = 17.67m	1.2	471	16.1
0.4	T_z = 12.8s	5.7	T_z = 13.4s	3.3	489	28.8
0.5	1/15	6.3	1/16	5.9	479	62.8
0.6		8.9		8.1	443	111.3
0.7		6.3		9.1	448	152.9
1		4.9		7.0	448	85.2

The steepness balance sensitivity study for Loch Rannoch showed again that in the 1/15 sea-state the critical steepness balance was about 0.6. However in the less steep seas a larger steepness balance was required to obtain the largest pressures. The pressure pad and top bow segment values were a maximum at a steepness balance of 0.6 or 0.7, as shown in Table 4.6b. Tests were not undertaken for steepness balances of 0.8 or 0.9 and it is seems likely that an even higher pressures would have been obtained at a steepness balance of 0.8.

For Loch Rannoch a further set of experiments were performed for a range of sea states and steepness balances of 0, 0.5 and 1. These are shown in Table 4.6c

Table 4.6c Loch Rannoch steepness balances by sea state steepness

Head Sea					
Highest Waves					
Hs	***Tz***	***Sea State***	***top segment***	***pressure***	***pressure***
(m)	***(s)***	***Steepness***	***bow impact***	***transducer***	***pads***
14.2	10.9	1/13	6.2	440	112.6
15.67	11.8	1/14	3.1	474	55.3
17.08	12.8	1/15	0	494	16.5
17.67	13.4	1/16	0	116	7.3
17.95	14	1/17	0	38	13.3
50% Front Steep Waves					
Hs	***Tz***	***Sea State***	***top segment***	***pressure***	***pressure***
(m)	***(s)***	***Steepness***	***bow impact***	***transducer***	***pads***
14.2	10.9	1/13	2.5	408	15.5
15.67	11.8	1/14	6.1	530	76.3
17.08	12.8	1/15	8.8	395	155.0
17.67	13.4	1/16	5.2	479	62.8
17.95	14	1/17	1.9	455	19.0
Steepest Waves					
Hs	***Tz***	***Sea State***	***top segment***	***pressure***	***Pressure***
(m)	***(s)***	***Steepness***	***bow impact***	***transducer***	***Pads***
14.2	10.9	1/13	0.0	141	12.0
15.67	11.8	1/14	0.0	511	19.4
17.08	12.8	1/15	3.9	446	26.4
17.67	13.4	1/16	7.0	448	85.2
17.95	14	1/17	5.2	422	34.0

Combining the results of these three sets of experiments a curve (Figure 4.3) is plotted through the most severe combinations of sea state steepness and steepness balance. (Note that although head sea results are presented above the bow sea results in the yaw angle study – Section 4.15 show the same trend.)

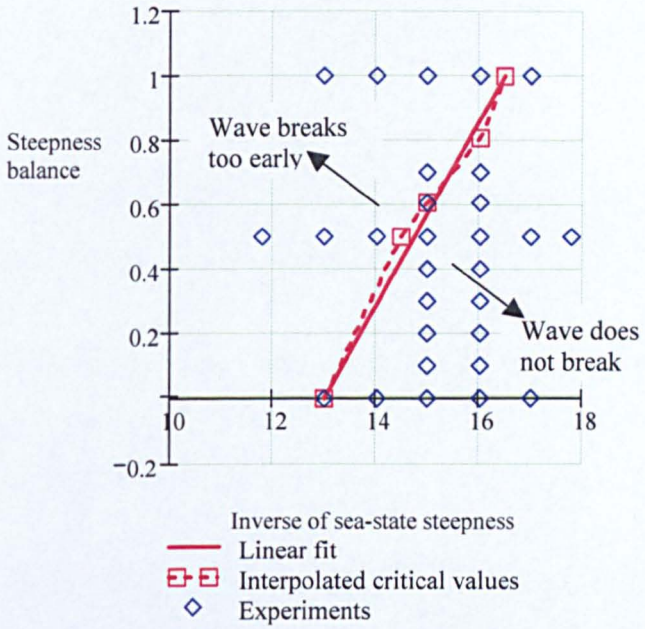

Figure 4.3 Sea-state steepness and the critical new-wave steepness balance

Based on the above (2.25 f_p frequency cut-off wave groups in 1/12 to 1/18, $\gamma = 2$ Jonswap sea states) the 'critical' steepness balance (that required to obtain the highest impact pressures) is given by:

$$Critical\ steepness\ balance = \frac{(Sz - 13)}{3.5} \tag{4.1}$$

where Sz is the inverse of sea-state steepness.

The critical steepness balance is:

0 for a sea-state steepness of about 1/13 and

1 for a sea-state steepness of about 1/16.5.

These results seem to be reasonable in a qualitative sense: when crests frequency-focus and form high waves in steep sea-states they will break. In relatively low steepness sea-states focussed crests will not break but breaking waves will occur when the wave fronts become highly focussed and therefore steep.

It is also convenient to define the *Critical sea-states* as being those with steepnesses between 1/16.5 and 1/13, within which a *Critical wave*: an extreme slapping wave can be obtained once in 3 hours by selecting a suitable value for SB:

- Steeper than critical sea states will contain many slapping waves but their height will be limited so they will tend to be less severe for design purposes.
- Sea-states less steep than the critical range will contain fewer than 1 slapping wave per 3 hours, however, should they occur, the slap pressures may be relatively severe.

Figure 4.3 also shows the experiments on which this curve was based. With hindsight additional steepness balance experiments would have been interesting for 1/14 sea states and for higher steepness balances in 1/16 sea states.

Figure 4.4 shows pictures of the waves corresponding to the 100% (steepest wave), 50% and 0% (highest wave) rows on Figure 4.3.

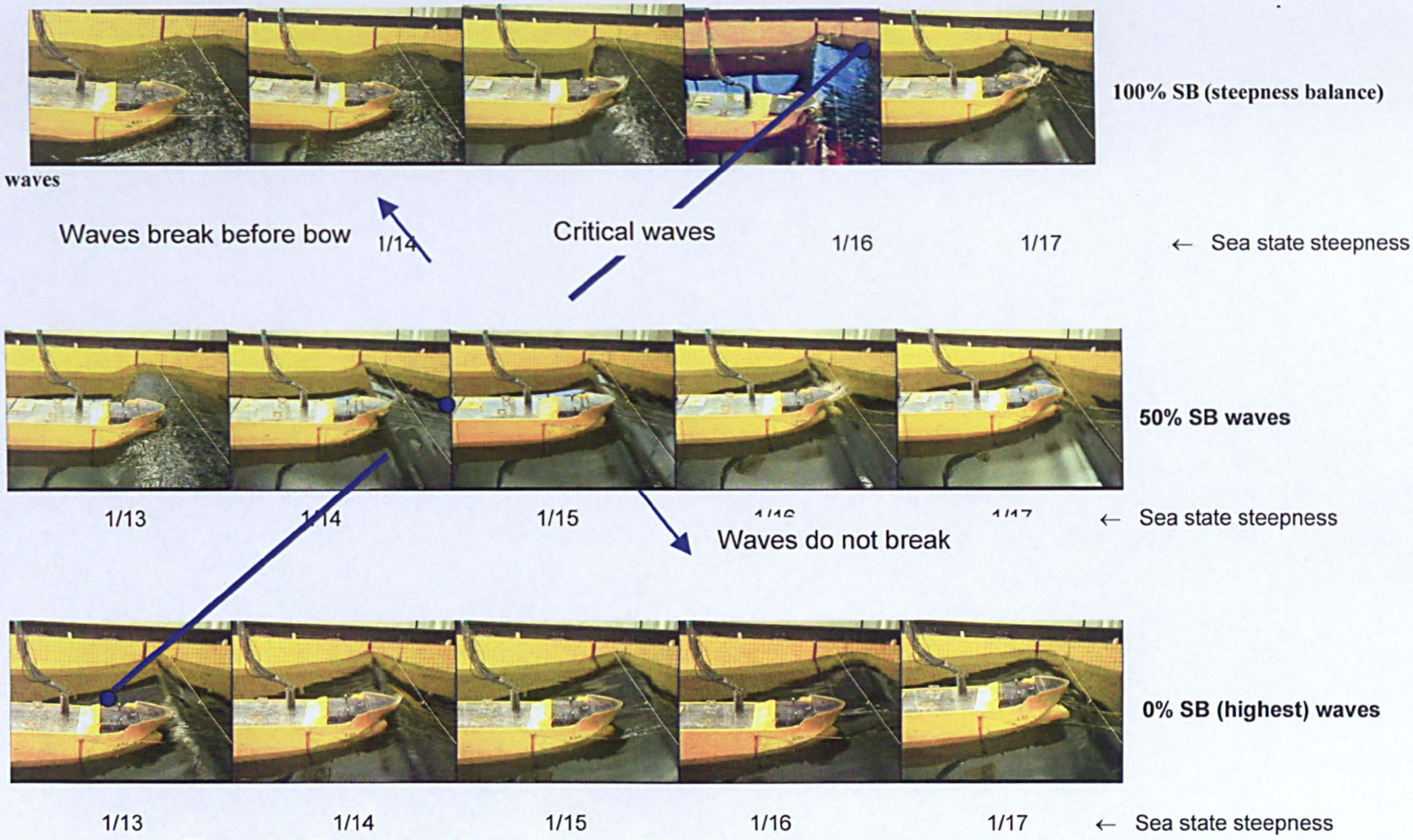

Figure 4.4 Photographs of wave and model for range of steepness balances and sea state steepnesses

Figure 4.4 provides a number of insights into horizontal wave slap.

Notice how for any steepness balance:

- The steepest sea states result in a broken wave with an irregular water surface.
- The less steep sea-states have a non-breaking wave with a maximum front slope less than 30 degrees to the horizontal.
- Between these extremes a breaking wave occurs with a front slope of about 40 - 60 degrees.
- The critical sea state – steepness balance combinations (those causing the largest impacts) have: for a given steepness balance the lowest overall steepness (and therefore for a given height the largest celerity) retains the steep breaking wave front shape.

The corollary of the last point is that for a given sea state the minimum steepness balance that gives a breaking wave, will give the maximum associated crest elevation and will therefore be a good basis for bow impact design.

Also note that the critical waves, although generated in very different ways, have similar (in the geometric sense that they are scale models of one another) crest front shapes. This is significant because it allows the definition of a generic form of a deep water breaking wave that can be used as a basis for design. See Section 4.7 Wave shape study.

The probabilities of different types of breaking waves in different sea states can also be roughly estimated from these results. This is discussed in Section 4.8.

The wave front steepnesses in the breaking waves are significantly higher than the linear theory used to generate the waves suggests. The relationship between the linear estimates and the measured slopes is given in Section 4.9.

Figure 4.4 also provides interesting information (for typical 250m long FPSOs in severe N. Sea/N. Atlantic sea-states) about the likely relative position of the bow to the critical wave: In all the critical breaking wave events, irrespective of the sea state steepness, the bow is likely to plough into the steep wave front and not ride over the wave, as it does when meeting a high wave in a low steepness sea state (see 1/17, 0% steepness photo). However because these waves are average extreme wave shapes it is necessary to account for the effect of variability of wave shape and bow position in extreme loading assessment. This will be considered in the later spectral-probabilistic reliability calculations.

4.7 Wave Shape Study

Bow slapping forces are very dependent on the wave shape. A steep front causes a rapid change of added mass as the wave passes. Breaking waves with horizontal velocities approximately equal to the celerity also have steep fronts. The wave shapes from different combinations of sea-state steepness and steepness balance were determined visually from the video of the waves against the grid and are compared in Figure 4.5. The wave shapes are scaled to give a crest elevation of 1 in each case.

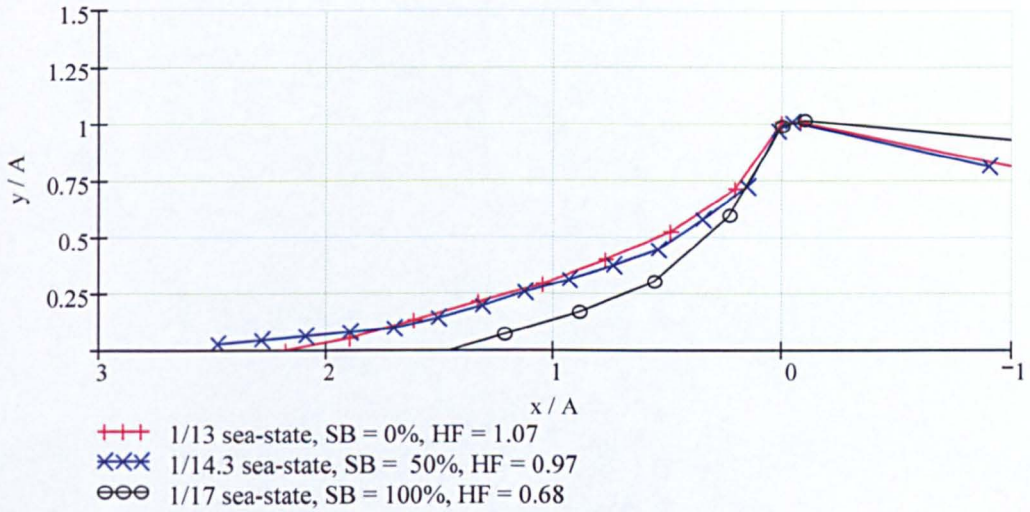

Figure 4.5 Non dimensional crest shapes for different critical waves

The shape of the upper quarter of the front of the crest was found to be almost the same across the whole range of critical waves. The overall shapes of the wave fronts were very similar for the 0 % steepness balance (highest) and 50% steepness balance waves. The lower crest of the 100% steepness balance waves was steeper than the 0 and 50% steepness balance waves.

Figure 4.6 shows the amplitude of the critical wave crests relative to the significant wave height. The non-linear effects increase the wave amplitude: Whereas the theoretical linear 0% steepness balance (highest) wave has a crest elevation of $1.8H_s/2 = 0.9H_s$ the measured value is $1.07H_s$. A parabolic curve is fitted to the three points.

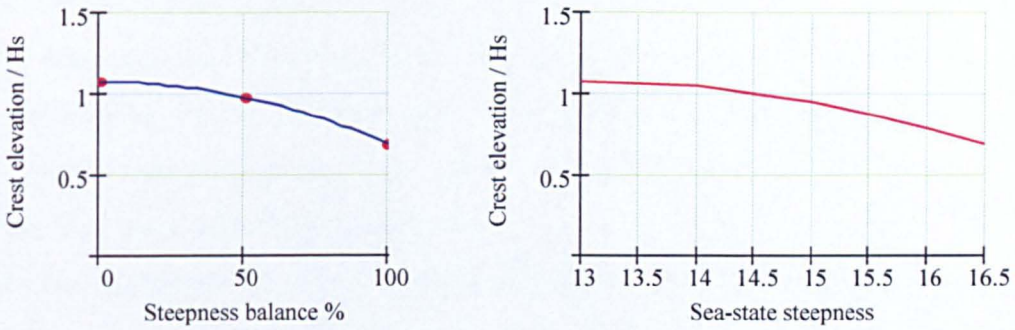

Figure 4.6 Crest elevation/Hs for different critical breaking waves plotted for steepness balance and sea state steepness

Together Figures 4.5 and 4.6 show that, the higher the steepness balance:

- The steeper the lower crest.
- The lower the crest elevation.

Note also that the celerity of high SB waves is a little lower than that of low SB waves and this will also reduce their slapping pressures.

The high slap pressures occur in the upper crest so this explains the finding, in Section 4.6, that the critical wave in a given sea-state is that with the lowest steepness balance that is sufficient to cause wave breaking.

4.8 Slapping Wave Probabilities

From the experimental results it is possible to make some estimates of the probability of slapping waves.

- In a critical sea-state where the critical wave is a 100% SB wave then a slapping occurrence of only one event per 3 hours is expected.
- In a critical sea-state where the critical wave is a 0% steepness balance wave then whilst 1 0% SB high breaking wave is expected every 3 hours

many more (> 65) slightly lower height but larger SB value waves will occur in a 3 hour period.

- In sea-states that are steeper than the critical range the worst waves will break before their theoretical linear slapping intensity is reached. However many smaller wave slaps (with a range of SB values but with more, lower intensity slaps at high SB) will occur.
- In sea-states that are less steep than the critical range wave impacts can still occur but their probability will be less than 1 in 3 hours. The full range of 0% - 100% SB waves are possible but the higher SB breakers will be much more likely to occur.

Figure 4.7 shows a rough estimate of the number of slapping waves in 3 hours for 0% SB and 100% SB waves across a range of sea state steepnesses. Slapping waves will occur between the SB = 0 and 1 lines (below there is no breaking, above the waves will have previously broken). These are based on the extreme value formula for the amplitude a exceeded in N cycles with standard deviation σ and assuming 1000 waves per 3 hours:

$$a_{\max} = \sigma_a \sqrt{2\log(N)},$$

written with N as the subject and σ_a selected to give 1 occurrence in 3 hours for the critical waves within the critical range of sea-states.

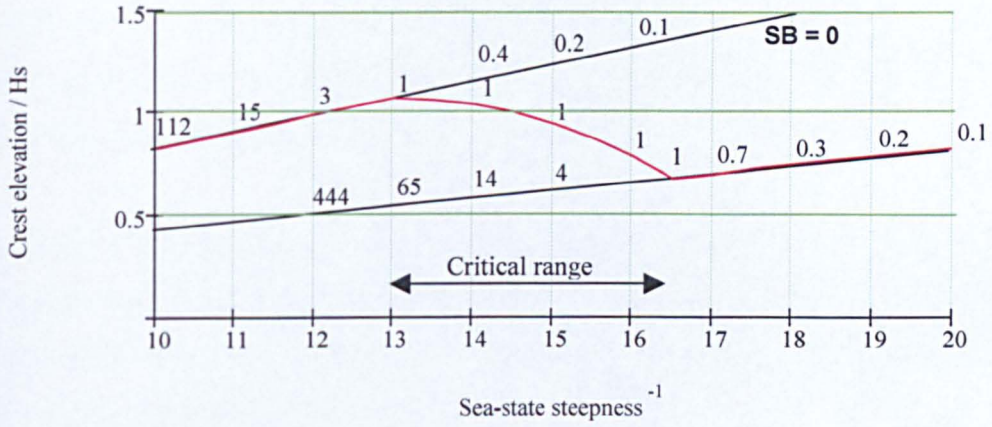

Figure 4.7 Breaking wave types superimposed with estimated numbers of occurrences in 3 hours

Note that the total number of breaking waves in a sea-state will be a little larger than the values given on the SB = 1 line. It is not valid to sum the occurrences for a range of SB values at any sea-state steepness because the exceedences of the different SB values calculated this way are not mutually exclusive.

4.9 Wave Front Steepness Enhancement

In severe deep-water breakers, that are likely to cause the large impacts, the horizontal velocity will be approximately the celerity (the speed of the shape of the wave) and the immersion velocity (water surface slope × celerity) may be significantly higher than the celerity.

Linear wave theory is easy to apply to determine particle velocities, surface velocities and slopes but the results are very inaccurate for breaking waves. However a correlation of linear predictions and measured tangent or chord slopes provides a relatively simple slope modification relationship as shown in Figure 4.8 (also see Figure 2.17). As mentioned in Chapter 2 the front steepnesses for

Schiehallion Model were measured using a grid on the wall of the tank but for Loch Rannoch Model they were measured by using closely spaced water surface elevation gauges. For the latter the result is very dependent on the time step used for the calculation (see Figure 4.9).

The peak of the diagram corresponds to waves breaking most powerfully at the bow of the FPSO. To the left of the peak the waves are not breaking as powerfully or not breaking at all. To the right of the peak the waves will break before they reach the FPSO bow.

Figure 4.8 is very useful but it should be noted that:
1) Figure 4.8 is very dependent on the method of measuring the slope. The apparent increase in the front slope of breaking waves is much larger if short time steps or small distances are used between the measurement probes.
2) Figure 4.8 is based on wave groups targeted by linear theory to be most severe at the bow.
3) The overall statistics at a point will have very few contributions from waves that are precisely targeted at that point.
4) The reduction of velocity away from the target point is more rapid in the non-linear real sea conditions.

2) to 4) have the effect of reducing the probability of encountering steep breaking waves at a given position on the sea surface.

This slope enhancement is used in the slap pressure calculations and has a very large effect on slap forces and pressures.

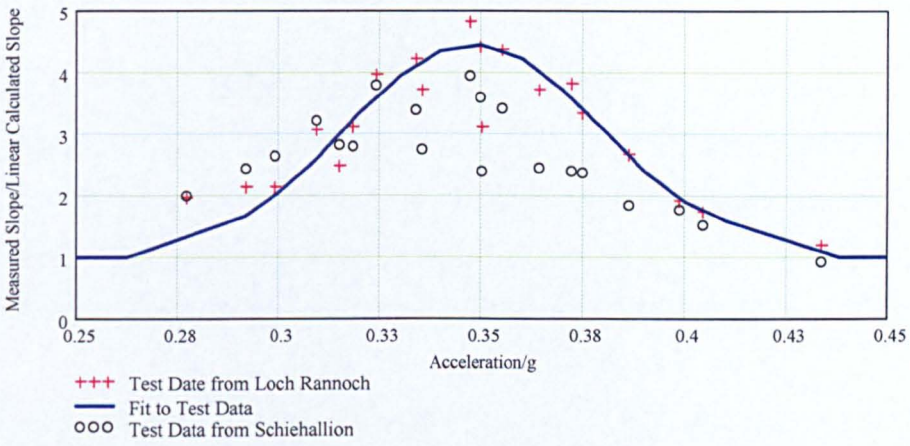

Figure 4.8 Wave front slope enhancement

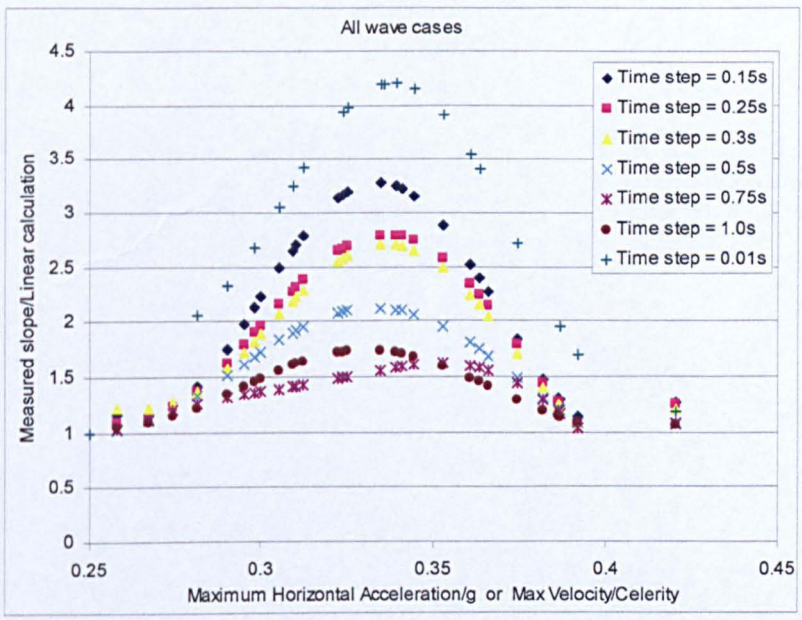

Figure 4.9 Wave front slope enhancement for Loch Rannoch

4.10 Celerity Of Critical Waves

The celerity (speed of advance of the water surface) of a random wave or a wave group varies with time. The celerity at the time of impact is important because it is also the horizontal particle velocity of the breaking wave and, after multiplying by the crest front slope gives the vertical water surface velocity which determines the rate of change of added mass – also an important input for slam force prediction.

The celerity was measured by two methods, which gave the same answers although the video method can give a better understanding of the result if the wave shape is changing rapidly.

- The first was to step through the video, which was recorded at 25 frames/sec and to measure the progress of the wave against the tank-side grid.
- The second method used three water surface elevation probes and by dividing the time lag, between the water surface passing each transducer at a chosen level, by the spacing of the probes the celerity is obtained.

The results are shown in Figure 4.10.

The greater the steepness balance the slower the wave relative to *cz*. This is because the larger the steepness balance the more the high frequency (low celerity) content of the spectrum is in phase at the extreme event.

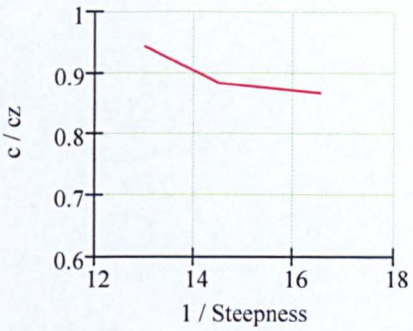

Figure 4.10 Celerity of critical waves *cz* ($cz = gT_z^2/2\,\pi$)

4.11 Velocity Balance Study

As an alternative to generating new-waves based on a balance of height and steepness, a study was carried out where the balance was between water particle horizontal and vertical velocity. The results are shown in Table 4.7. These results suggest that overall bow impact and panel pressures will be lower in these types of wave. However very local pressures from the pressure transducers are similar to those found in the steep-high waves.

Table 4.7 Slapping pressures for different vertical velocity waves

Loch Rannoch F.P.S.O.			
Vertical velocity-height new-waves			
Hs = 17.67 m Tz = 13.4 s			
Vertical Velocity	*top segment bow impact*	*pressure transducer*	*pressure pads*
0%	1.828	464	27.8
30%	2.603	504	26.5
40%	2.943	503	36.8
50%	3.377	471	44.6
60%	3.563	470	53.2
70%	3.346	505	62.4
100%	3.346	526	28.0

4.12 Sea-State Study

50% steepness balance waves were generated for twenty sea-state steepnesses, with four zero crossing periods. Full results are given in Appendix A Table A4.3.

Provided the bow is not overtopped, for any given T_z, if the wave height is increased segment and panel pressures increase, until breaking but then decrease because the wave breaks before it is fully focussed and before reaching the bow. Note: in a random sea the peak pressure would be maintained at the breaking value as wave height continued to be increased because smaller waves within the sea-state would cause the large pressures.

Head sea mid-draft panel pressure results for each zero crossing period are shown in Figure 4.11.

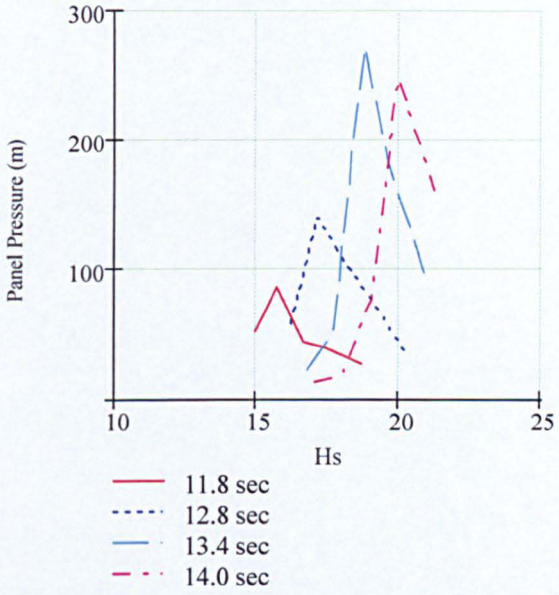

Figure 4.11 Effect of significant wave height on the panel pressure at constant zero crossing period (for 50% steepness balance wave groups)

Pressures are found to increase rapidly with T_z if steepness is kept constant. Typical results (+) and a theoretical simple cubic relationship (---) are shown in Figure 4.12

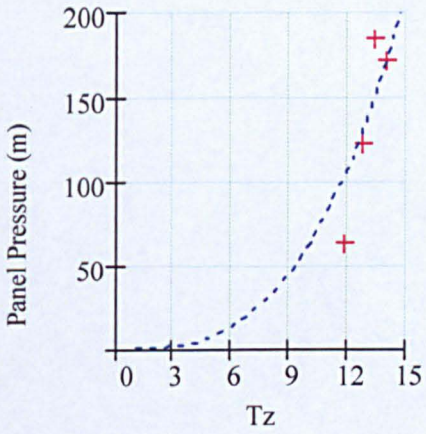

Figure 4.12 Effect of zero crossing period on the panel pressure at constant sea-state steepness of 1/14.5

The cubic relationship with T_z for pressures in breaking waves is expected on the fact that:

- both the horizontal velocity at breaking and the vertical velocity at which the bow is immersed will be proportional to T_z.
- the water surface average front steepness over some height, h, is proportional to $(H/h)^{0.5}$, or for constant sea-state steepness $T/(h^{0.5})$ (see Section 4.16).

The results for both Schiehallion and Loch Rannoch show a steeper trend which, because it occurs for different sea-state steepnesses and yaw angles is *not* scatter. It may be a consequence of the vessels' motion putting the bow in different locations relative to the target point in different wave periods.

The 14sec results show a lower peak than the 13.4sec results. This may be caused by the wave overtopping the bow.

The results for different sea state steepnesses at constant steepness balance also show a pronounced maximum: at the critical combination of sea state steepness and steepness balance identified in Section 4.6. Results are shown in Figure 4.13.

Figure 4.6 demonstrates the sensitivity of the breaking wave forces to the sea-state for a given steepness-height 'steepness balance'. This demonstrates how sensitive the impact forces are to the shape of the wave front. As discussed in Section 4.6 above, in a real sea the wave shapes will be formed randomly and whilst the 50% steepness balance wave has a 1 in 3 hour probability of occurrence, other steepness balances waves with the same probability will give higher pressures in steeper and less steep sea-states than the approx 1/14½ sea-state steepness for which the 50% steepness balance gives the worst wave.

The high pressures at 1/14½ sea-state on this diagram are related to the local steepness magnification curve of Section 4.9. At a fixed 50% steepness balance,

the wave front steepness increases with sea-state steepness towards breaking at a sea-state steepness of 1/14½ and decreases with steeper sea states which cause premature breaking.

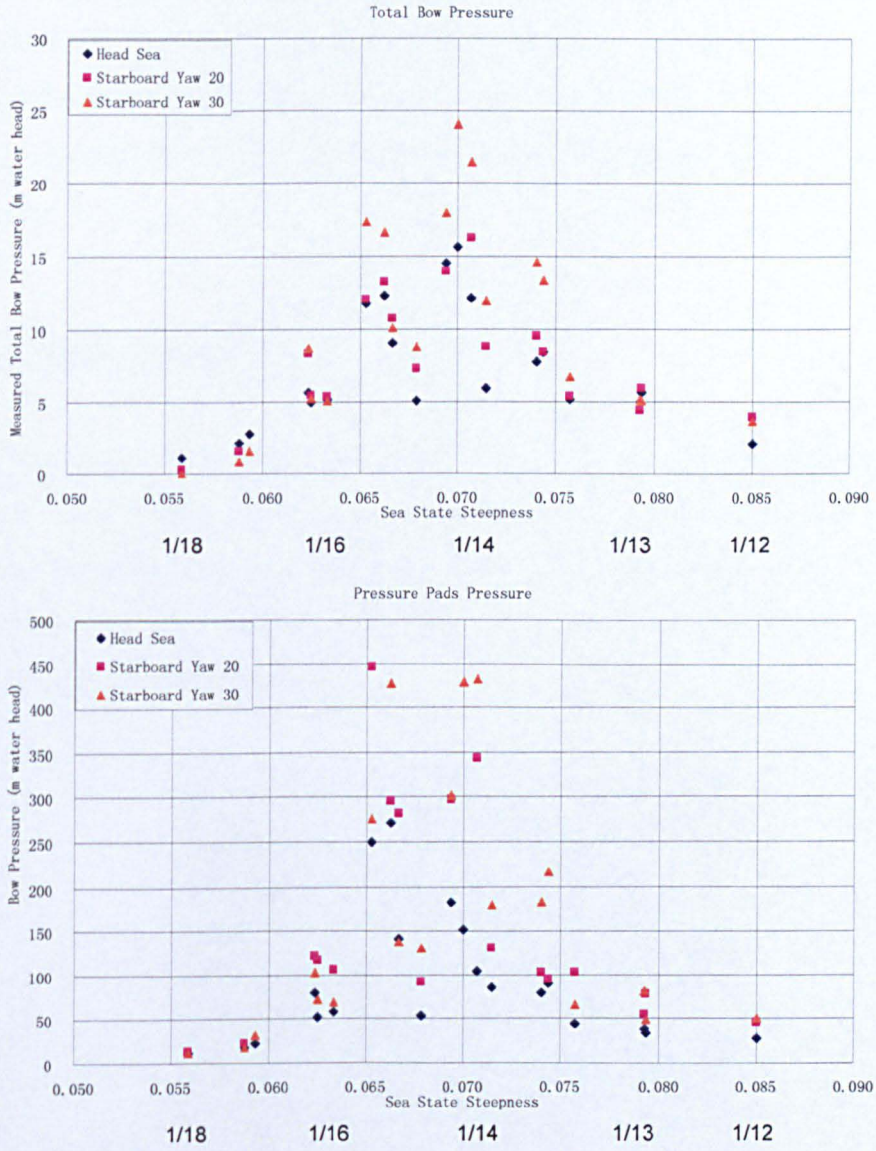

Figure 4.13 Variation of pressure with sea state steepness for a steepness balance of 50%

4.13 Jonswap Peak Enhancement Study

Most of the tests were performed with a peak enhancement factor: $\gamma = 2$. To determine the effect of the peak enhancement factor, 1 high wave, 1 steep wave and 8 50% steepness balance waves were generated with $\gamma = 1$ and $\gamma = 3.3$. The results showed that within this range γ has a very small effect on the impact pressures.

4.14 Draft Study

Tests were also undertaken with a deep draft on both FPSOs. In the larger waves these tests (Appendix Table A 4.4) gave lower bow segment and panel pressures and less variability than the mid draft values. This is thought to be because the large waves that gave the high pressures at mid draft were breaking above the bow at the deep draft. See Figure 4.14.

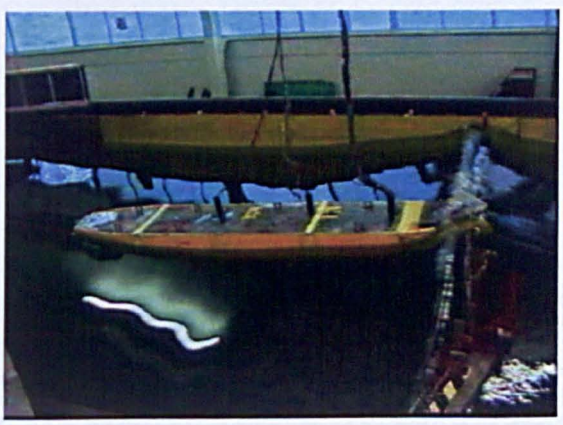

Figure 4.14 Wave breaking over the bow at deep draft

($H_s = 21.36m$, $T_z = 14sec$, $SB = 50\%$)

The pressure transducer maximum pressures on Schiehallion are considerably lower at deep draft, probably primarily as a result of the transducers being much lower relative to the water surface (see Figure 3.10) and so seeing less severe

impacts. For Loch Rannoch the deep draft pressure transducer values are similar at mid and deep draft, probably because they are higher on the bow (see Figure 3.14). The overall impact force on the bow was lower at deep draft – in fact it was difficult to assign part of the force to impact. This again was presumably the result of the waves breaking above the bow.

These results suggest that an FPSO built with a large freeboard, to prevent Greenwater, will need to be designed for higher bow pressures than a conventional tanker which experiences more Greenwater in severe storms.

4.15 Yaw Angle Study

The Loch Rannoch was subject to 0 degree 'head seas' and bow seas at 20 and 30 degrees. Results are given in Appendix A Table A4.5 and A4.6. It was anticipated that the flatter bow side would be subject to higher pressures when the incident waves were travelling approximately normal to the plating. This was the case for the panel pressures which, for the critical cases were 57 to 310% greater for the bow than the head seas impacts. However the overall bow pressures were about 24 to 100% larger and some of the transducer pressures were much smaller in bow seas. The reason for the overall bow pressure being similar is probably a result of the similar projected areas for the different incidence directions and the flatter plating near the initial impact point being compensated by the high curvature at the bow. It can be easily understand for the transducer pressures being much smaller because they were located on the port side of the bow, while in both bow seas the model was starboard yawed.

4.16 Pressure-Area Relationship

The array of pressure panels on the starboard side of Loch Rannoch allowed the average pressure over different areas to be found. Appendix A Figures A4.1 to

A4.4 show typical time histories from each panel. The results from each panel were smoothed to remove any dynamics and added together in the time domain to determine how the pressure dropped with area.

Figure 4.15 shows how the 16 signals from the top and bottom of the 8 pressure panels were grouped for this calculation Figure 4.16a shows a typical set of average pressure results for the different panel areas, and includes the upper bow segment. Figure 4.16b shows approximate power relationships between pressure and area.

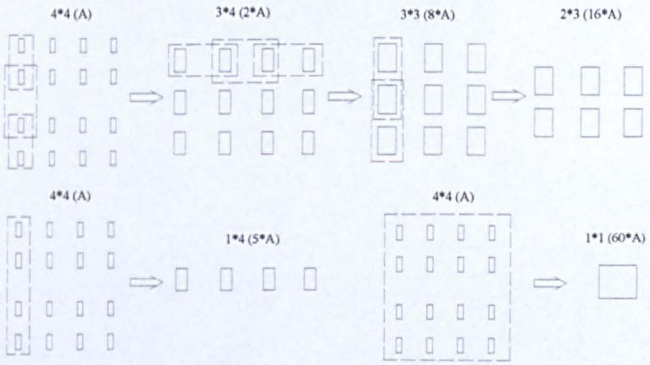

Figure 4.15 Grouping of pressure panels for pressure-area calculations

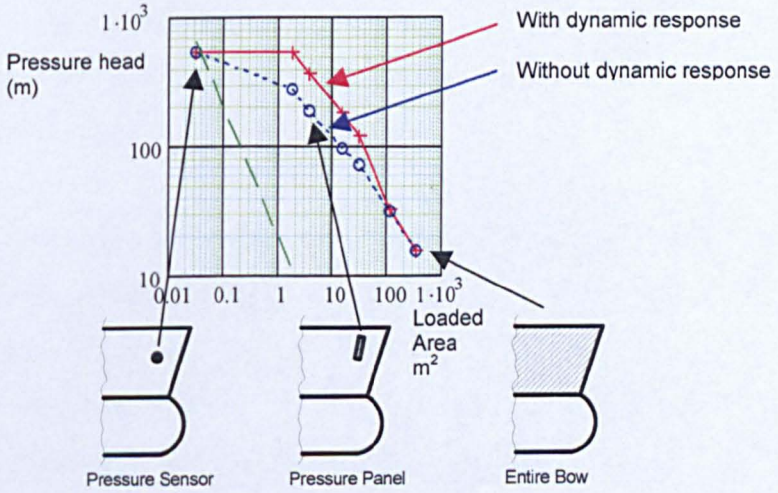

Figure 4.16a Typical relationship between quasi-static pressure and area

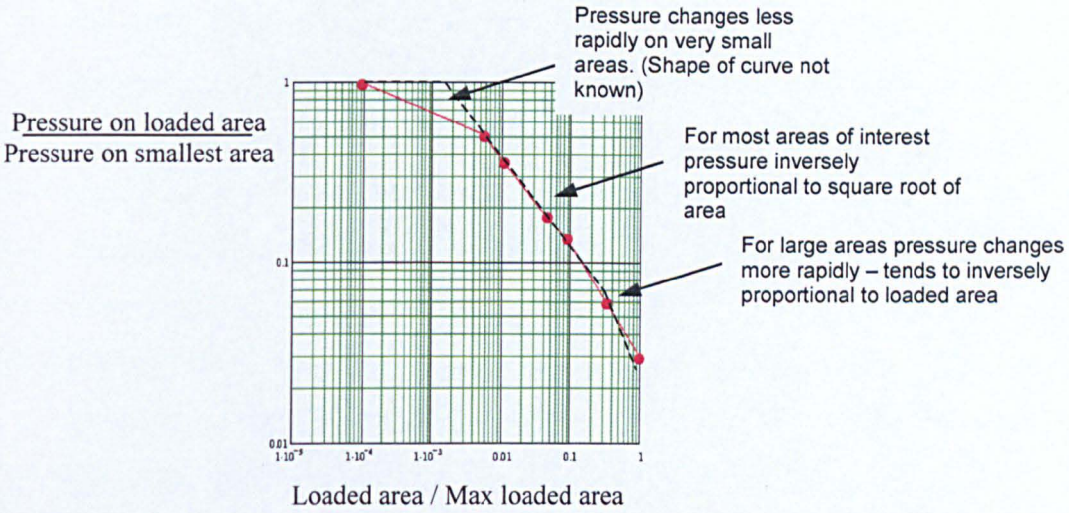

Figure 4.16b Typical pressure – area relationship

In head sea conditions the bow front panels take the major pressure; the bow side is relatively lightly loaded. In bow sea cases it is the side panels which take the large pressures. Typically one or two panels are subject to very high pressures, surrounding panels are subject to significantly lower pressures. The typical pressure time histories of each panel for head sea and bow seas are given in Appendix A Figures A4.1to A4.4. The contours of the impact pressure without dynamic over the side bow when the impact occurs are given in Appendix A Figures A4.5 to A4.7.

Note that, particularly in the steepest waves, the dynamic response of the panels is excited. It is interesting that in some cases the most highly loaded panel behaves in a quasi-static way and adjacent, less highly loaded, panels have a larger dynamic amplification (DAF) of up to 2. This is probably caused by the rapid movement of the wetted area out from the centre of the impact.

Detailed analysis of the results showed that:

- The shape of the area was not too important
- For the areas of most interest the average pressure is roughly proportional to the inverse of the square root of the area.
- For very small areas, about $0.05m^2$, corresponding to the pressure transducer and less than a typical plate size, the pressure increases less rapidly and may possibly reach a maximum (the relationship at very small loaded areas can not be determined from the tests because only the data for the pressure transducer ($0.05m^2$) and then for an area of about $1.9m^2$ were obtained from the tests).
- For very large areas, corresponding to most of the bow being loaded, the pressure is inversely proportional to the area – which is consistent with the large areas being only partially loaded when the force is at a maximum.

4.17 Pressure Rise And Half Decay Times

The pressure time histories were plotted for a number of impacts and H_s = 21.36, T_z = 14 (sea-state steepness 1/14.3) wave direction = 0degrees and wave direction = 30 degrees were selected as typical cases. The pressure time histories on groups of panels (see Figure 4.15) were averaged in time to obtain the time histories over a range of areas with different heights and widths. The rise and decay time for the overall bow was also included.

The typical time histories for the worst impact on a pressure panel, pressure transducer and the whole bow are given in Figure 4.17, 4.18 and 4.19 respectively. In Figure 4.17, the blue line is the measure time history and the red dashed line is given by lowpass filtering the test signal with a butterworth filter with cut-off frequency of 280Hz. The filtering method has been checked by the following process:

1) Assume a pulse with a linear rise and exponential decay as input data

2) Calculate the dynamic response of the input pulse according to Harris and Crede (1976)
3) Smooth the dynamic response by the current filtering method
4) Compare the input pulse and the smoothed signal

The comparisons between the input pulse and the smoothed signal for two typical impacts (one pressure impact and the whole bow impact) are given in Figure 4.20 and 4.21. Regarding the peak value of impact and the rise and decay time, the comparison is good. This confirms that the current filtering method could be used to get the response without dynamic.

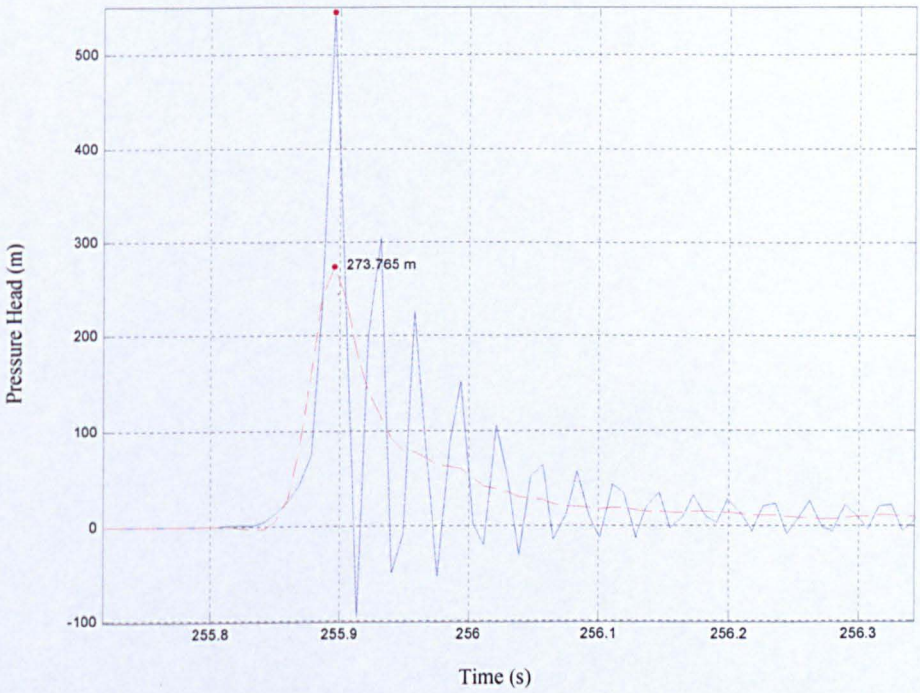

Figure 4.17 Typical time history of a big impact on a pressure panel

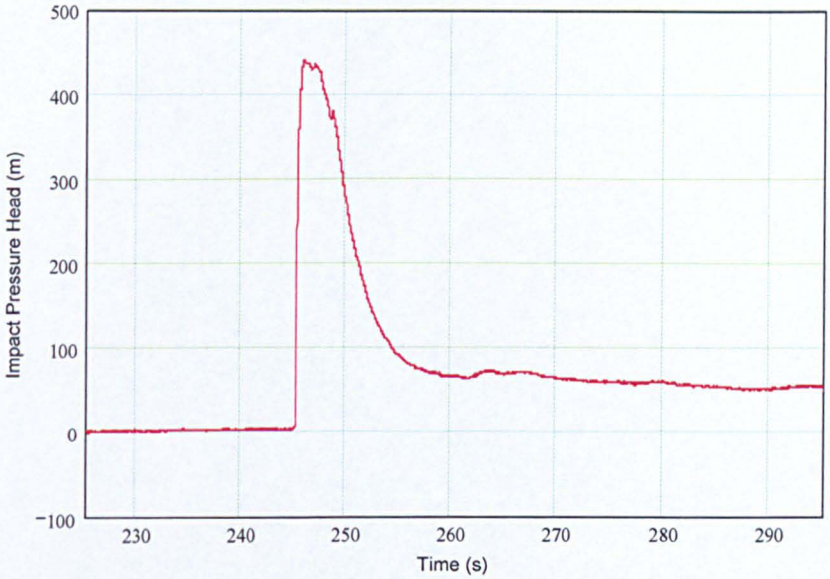

Figure 4.18 Typical time history of a big impact on a pressure transducer

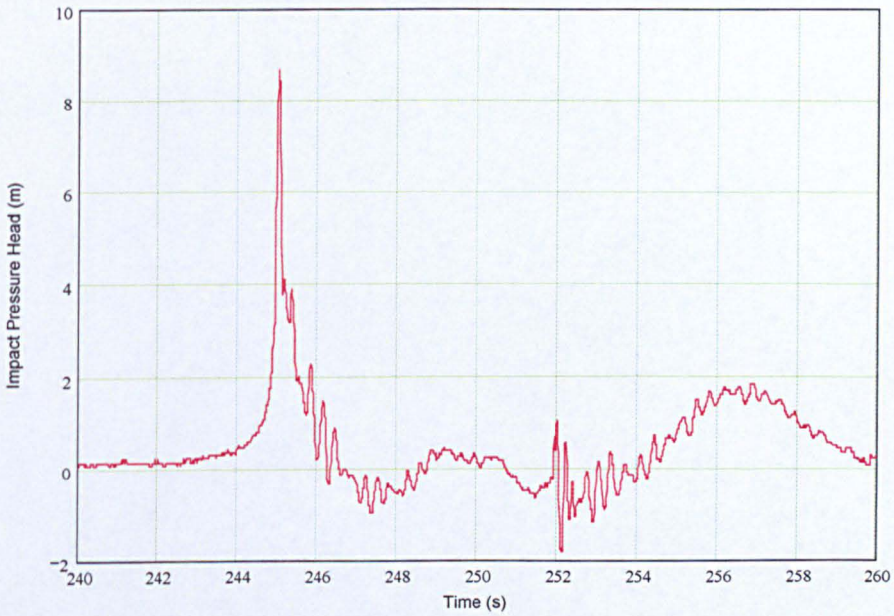

Figure 4.19 Typical time history of a big impact on the whole bow

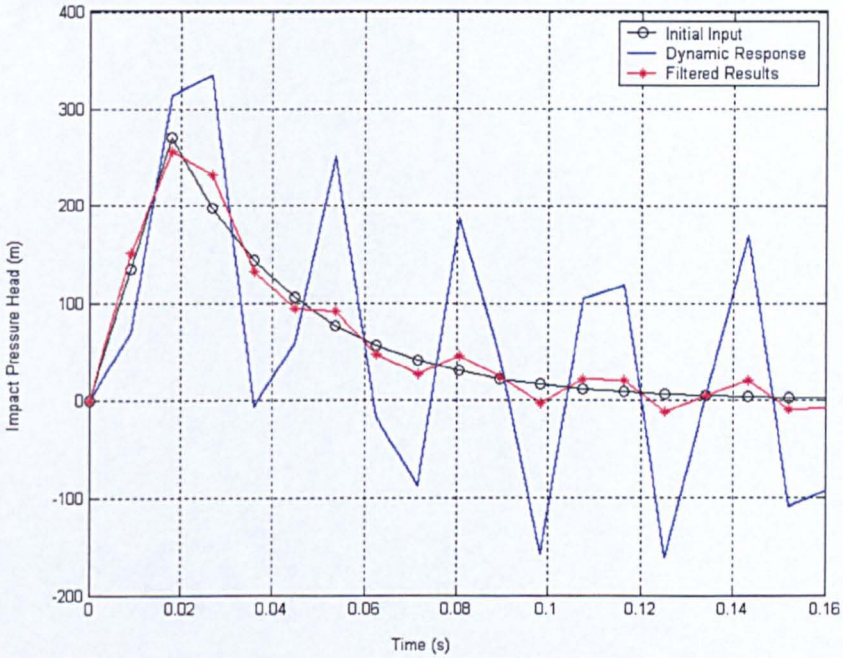

Figure 4.20 Comparison between filtered results and initial input for rise time of 0.02sec

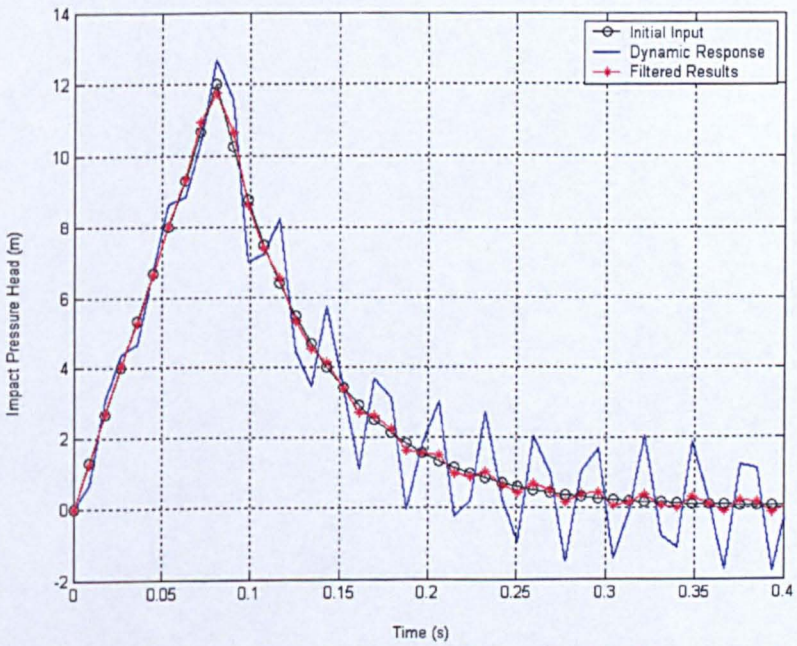

Figure 4.21 Comparison between filtered results and initial input for rise time of 0.09sec

The results of the rise and decay time of the response without dynamics are shown in Table 4.8 and Figure 4.22.

Table 4.8 Rise and half-decay times

Diameter (D)	*Aspect Ratio*	*Panel Width*	*Panel Height*	t_{rise}	$t_{half.decay}$
60	1	1	1.8	0.027	0.052
60	1	1	9	0.039	0.09
60	1	4	3.6	0.036	0.108
60	1	7	9	0.042	0.108
45	1.6	45	12	0.083	0.208

H_s = 21.36m, T_z = 14sec, Steepness balance = 50%,
30degree and 0 degree wave directions

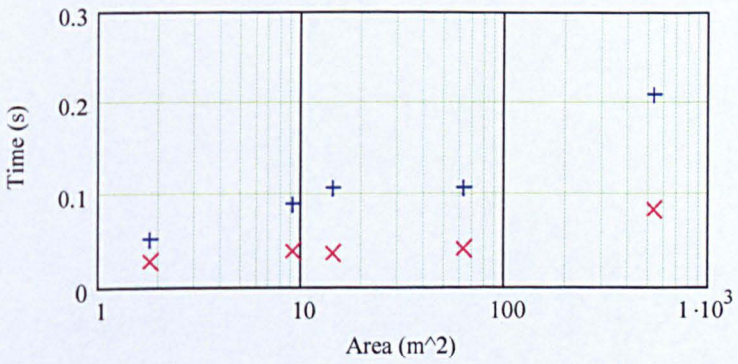

Figure 4.22 Rise 'x' and half-decay times '+' for Table 4.18

Diameter D applies to the location of the impact for a side impact or the beam for a head sea impact.

Aspect ratio = 1 corresponds to a circular cylinder
Aspect ratio > 1 a pointed bow in head seas and
Aspect ratio = 0 is a flat plate.

Aspect ratio applies to location of impact - a side impact on a pointed bow could have an aspect ratio < 1, although it is anticipated that for a side impact a local Diameter with aspect ratio = 1 will be used.

For Loch Rannoch overall bow force the aspect ratio is about 1.6 with D = 45m. For side pressures D = 60m and aspect ratio = 1 was obtained by fitting to the drawings. For Schiehallion the head sea aspect ratio is about 1 with D = 50m.

It should also be noted that although the most highly loaded panels had relatively long (0.1 sec) rise times with relatively small dynamic response, adjacent less highly loaded panels sometimes had a very large dynamic response (DAF ≈ 2) implying a much shorter rise time of about 0.01 sec.

4.18 Bottom Slamming Forces

Although vertical bow forces and forefoot panel pressures were measured in all waves, bottom slamming is primarily important at the ballast draft.

It is of interest that the results in high waves are worst when the sea-state wavelength L_z is similar to the ship length. This is as expected from regular wave experiments and calculations because these wavelengths result in large relative motion at the bow. However 50% steepness balance waves give a higher vertical impact force and the associated wavelength is considerably longer than the FPSO. Results are given in Table 4.9. The shape of these 50% steepness balance waves is similar to the maximum relative velocity wave as calculated by Drake (1997).

The measured bottom slamming forces were an order of magnitude smaller than the horizontal impact forces. This is a consequence of the impact velocities being about 1/3 of the celerity and the forces being proportional to impact velocity

squared times the slammed area. If the areas are about the same this leads to a force of about $(1/3)^2$ or about 10%. The bottom slamming effect on hull girder bending moment is important because of the long lever arm of the vertical forces but the high horizontal forces at the much smaller vertical lever arm can also produce a significant vibration in the hull girder.

Table 4.9 Bottom slamming forces and pressures – Loch Rannoch

			Shallow Draft		*Mid Draft*	
Highest Waves						
Hs (m)	*Tz (s)*	*Sea State Steepness*	*bottom segment slamming (tonne)*	*pressure pads (m)*	*bottom segment slamming (tonne)*	*pressure pads (m)*
14.2	10.9	1/13	271.8	36.5	174.8574	38.1
15.67	11.8	1/14	333	29.9	410.76	38.4
17.08	12.8	1/15	286.2	23.0	251.1	42.4
17.67	13.4	1/16	295.2	9.7	381.96	42.9
17.95	14	1/17	244.8	7.3	259.2	41.3
50% Front Steep Waves						
Hs (m)	*Tz (s)*	*Sea State Steepness*	*bottom segment slamming (tonne)*	*pressure pads*	*bottom segment slamming (tonne)*	*pressure pads*
14.2	10.9	1/13	160.2	12.8	0	31.7
15.67	11.8	1/14	262.8	79.8	0	48.3
17.08	12.8	1/15	315	94.6	234	-
17.67	13.4	1/16	471.6	55.4	325.8	38.3
17.95	14	1/17	491.4	26.3	270	41.7
Steepest Waves						
Hs (m)	*Tz (s)*	*Sea State Steepness*	*bottom segment slamming (tonne)*	*pressure pads*	*bottom segment slamming (tonne)*	*pressure pads*
14.2	10.9	1/13	63	12.0	0	31.7
15.67	11.8	1/14	147.6	12.1	0	38.6
17.08	12.8	1/15	228.6	21.0	0	41.8
17.67	13.4	1/16	246.6	38.6	108	40.6
17.95	14	1/17	255.6	24.7	210.6	33.3

4.19 Hull Girder Bending Moments

Hull girder bending moments were measured both on Schiehallion and Loch Rannoch. As for the panel and bow results the dynamic response was separated from the overall response as shown in Figure 4.23.

Detailed results for the various steepness cases and for the hogging and sagging design waves are presented in Appendix Table A3. Some interesting results are plotted in Figures 4.24 and 4.25.

Figure 4.24 shows that, for a given T_z, the hogging bending moments increase in proportion to the significant wave height.

The sagging moment first increases more than in linear proportion. This is caused primarily by the non prismatic shape of the bow and stern and possibly because the hogging wave, with a single dominant crest, is more non linear than the sagging wave, with two crests and a dominant trough. However at steepnesses of about 1/14 this non-linear increase in the hogging moment peaks and the effects of wave breaking, and possibly Greenwater, reduces the sagging moments.

As wave height increases the dynamic part (see Figure 4.25) is initially zero, because the waves are not steep enough to cause a horizontal slap, the vertical relative velocities are not large enough to cause vertical flare slamming and the forefoot is not emerging from the water so there is no vertical bottom slam.

Further increase of wave height (to steepnesses of about 1/17) results in an important dynamic response increasing the hogging moment. Further increase in wave height causes a dynamic response in conjunction with the sagging moments. The additional wave height required for a dynamic response with sagging is partly because the bow is immersed during a worst sagging event, making bottom

slamming unlikely, and the waves are less non-linear, so making breaking wave horizontal impacts less likely.

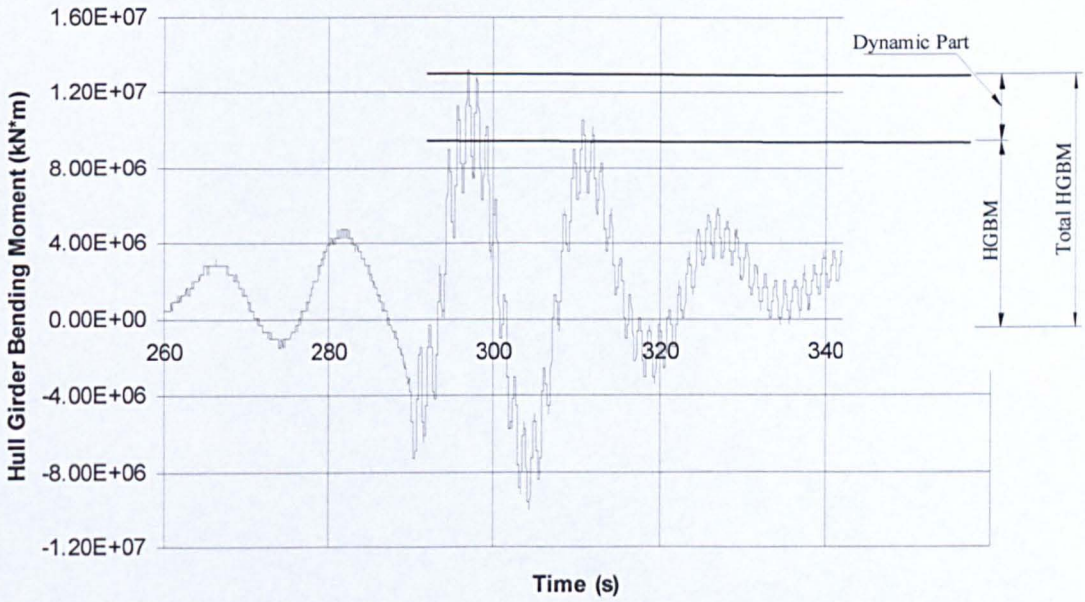

Figure 4.23 Dynamic part of hull girder bending moment

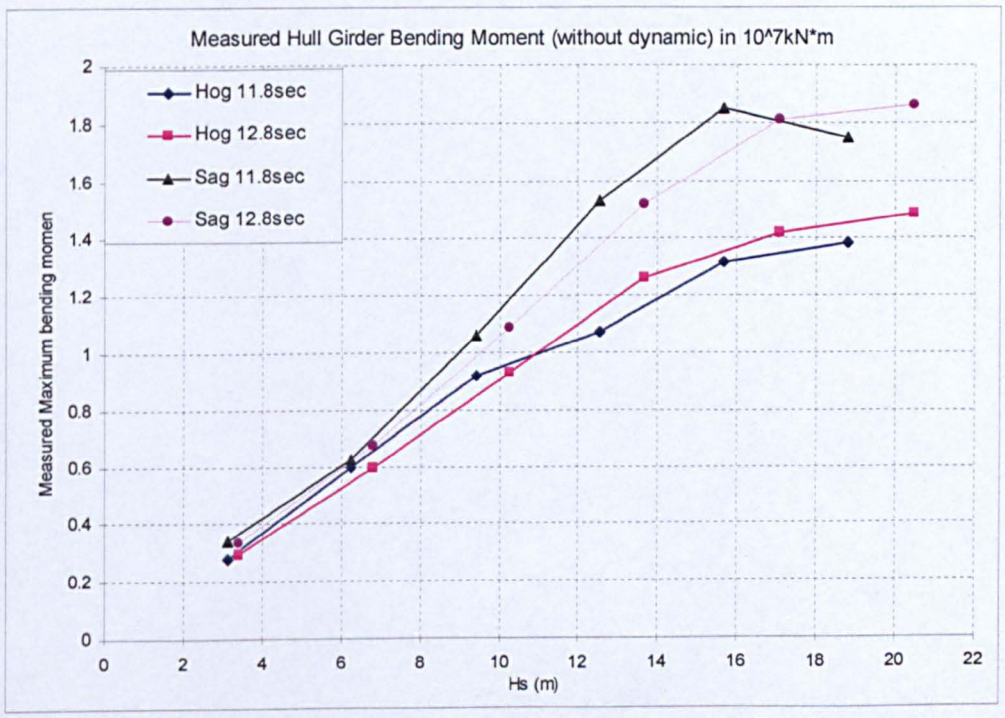

Figure 4.24 Measured bending moments divided by H_s for T_z of 11.8 and 12.8sec

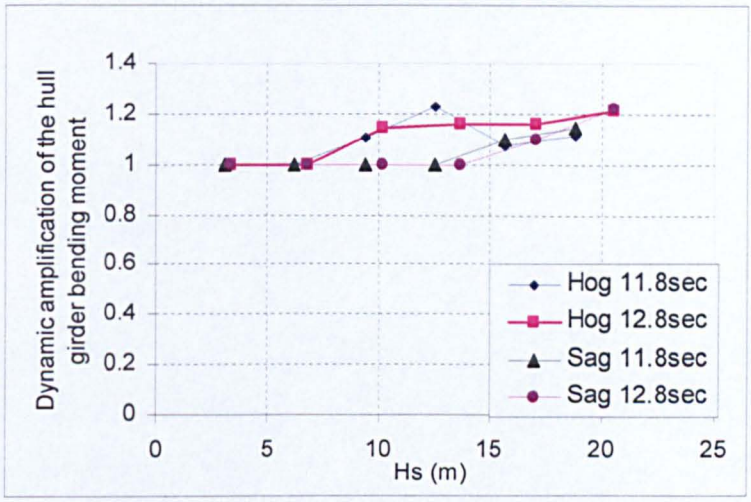

Figure 4.25 Measured dynamic amplification for T_z of 11.8 and 12.8sec

The non-linear increases in the without-dynamic hull girder bending moment are well known and reasonably well understood.

The statistics of the combination of hull girder structural quasi-static and dynamic responses is not yet properly understood or codified. These tests have not primarily been investigating hull girder response but they do suggest that the interaction of the hull girder quasi-static and dynamic responses is important and should be taken into account during design.

5 Approximate Calculations

5.1 Approximate Kinematics And Pressures In The Experimental Breaking Waves

To better understand the waves generated in the tank, their loading on bow structure, to provide some background for the development of simplified models and in-particular to explain some unexpected test results, a knowledge of the velocity and pressure field in the wave is required.

It was noticed in the early comparison of Loch Rannoch test results with theory (see Section 5.4) that the hydrostatic + Froude Krylov pressures were lower than predicted in the steeper waves. It was also noticed, in the full scale experiments on Schiehallion (Trevor Hodgson, private communication), that pressures in front of a crest were much higher than the local surface elevation would suggest.

This (simple but approximate) method developed here to predict the velocity and pressure field in breaking wave was originally developed by Swift (1989) and the implementation here was based on its description by Chakrabarti (1990). Swift (1989) assumed that the horizontal water particle velocity was following a form similar to that proposed by Swart and Loubser (1978) for regular waves:

$$u(x,z) = c\eta \frac{A\cosh(Az)}{\sinh(A(d+\eta))} \tag{5.1}$$

In Eq. 5.1, the origin of z is the seabed and that of x, the crest of the wave. Figure 5.1 shows the full nomenclature. This expression satisfies continuity within the wave, that is:

$$\int_0^{d+\eta} (u(x,z) - c)dz = -cd \tag{5.2}$$

The free surface parameter A was determined using the free-surface horizontal water particle velocity. The latter was first obtained by assuming that the wave could be analysed as steady, in a reference frame moving at the same speed as the wave.

Applying Bernoulli's equation to the free surface:

$$Q = \frac{[(u-c)^2 + w^2]}{2g} + \eta \tag{5.3}$$

Assuming that the crest horizontal water particle velocity equals the wave speed, and introducing the kinematics free surface boundary condition:

$$w = (u-c)\frac{\partial \eta}{\partial x} \text{ on } \eta \tag{5.4}$$

finally obtain:

$$u_\eta(x) = c - \{\frac{2g(\eta_c - \eta)}{1+(\partial\eta/\partial x)^2}\}^{1/2} \tag{5.5}$$

on the free surface.

Consequently, A in Eq. 5.1 may be obtained by equating 5.1 and 5.5 and solving iteratively for A:

$$c\eta A \coth[A(d+\eta)] = u_\eta \tag{5.6}$$

With A determined, the value of $u(x,z)$ within the wave may be written as:

$$u(x,z) = \frac{u_\eta(x)\cosh(Az)}{\cosh(A(d+\eta))} \tag{5.7}$$

Regarding wave speed, result from Van Dorn (1978) was used:

$$c = (2g\eta_c)^{1/2} \tag{5.8}$$

The vertical particle velocities $w(x,z)$ were also obtained by Swift (1989) by substituting Eq. 5.1 into the governing continuity equation and integrate in z:

$$w(x,z) = \frac{w_\eta(x)\sinh(Az)}{\sinh(A(d+\eta))} \tag{5.9}$$

The method is approximate because it assumes steady flow in a reference frame moving with the wave. Nevertheless comparisons with experiments (Swift 1989) suggest the results are good.

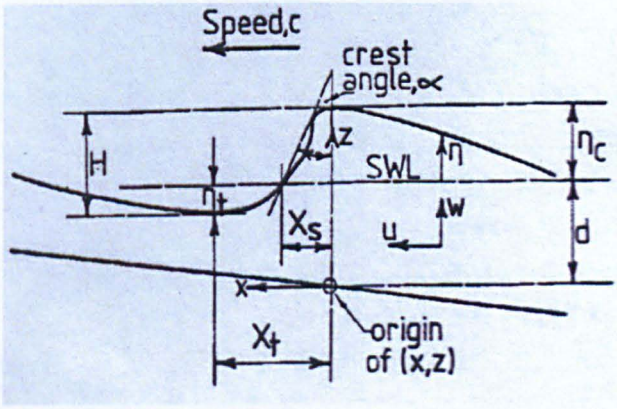

Figure 5.1 Nomenclature of wave geometry

The crest profile input to the program is shown in Figure 5.2.

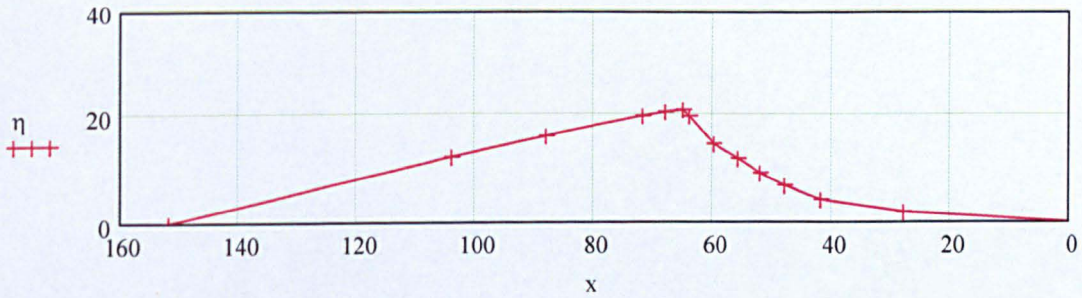

Figure 5.2 Crest profile obtained from laboratory experiment

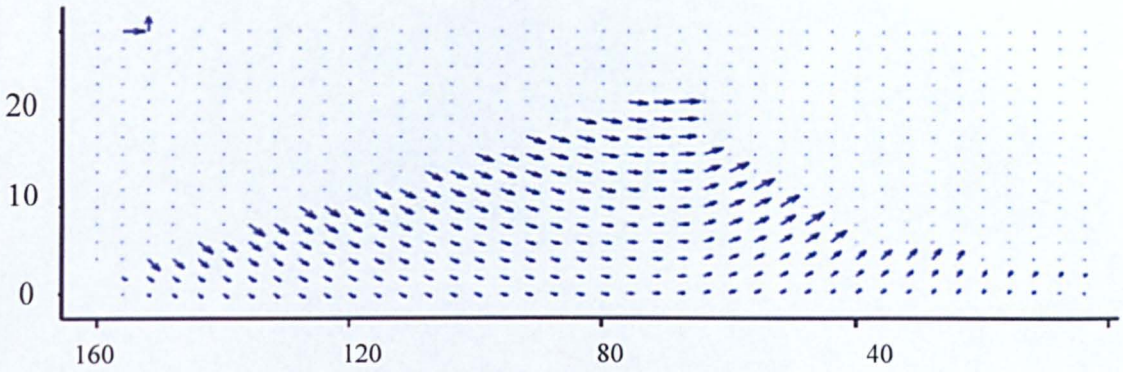

Figure 5.3 Predicted velocity field

The predicted velocity field is shown in Figure 5.3.

The velocity field suggests that the velocities near the crest top are approximately horizontal and are about the celerity. On the front face large velocities also occur but they are angled approximately normal to the water surface. The velocities inside the crest drop off quite rapidly.

The predicted pressure distribution is shown in Figure 5.4 and the ratio of Total pressure/hydrostatic is shown in Figure 5.5.

Figure 5.4 Pressures under wave crest (m head)

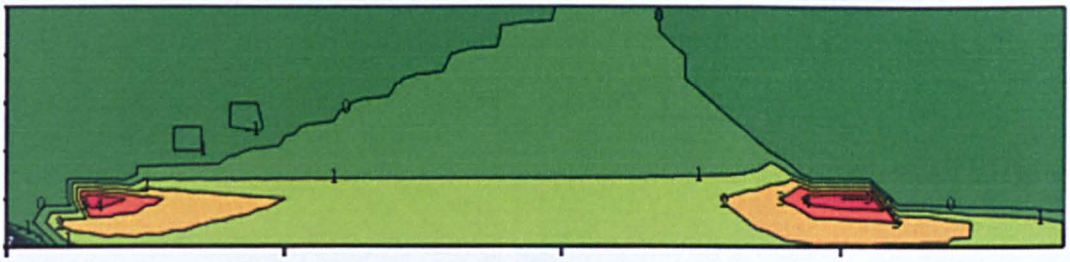

Figure 5.5 Total pressure/hydrostatic (hydrostatic is measured from the local water surface as a zero)

These calculations demonstrate both the low buoyancy forces measured in the model tests in the crests of the waves and the higher than expected pressures noted in the trough in front of the crest in the full scale measurements. Both effects can be related to wave particle accelerations which are large and upwards at the trough in front of the wave crest (so adding to the hydrostatic pressure) and downwards at the wave crest, where the crest can almost be in free-fall, so considerably reducing the total pressure.

5.2 Including Some Non-Linear Behavior In The Wave Group Models

To perform routine wave impact calculations it would be useful to be able to use a wave theory in conjunction with a hydrodynamic ship model and a local loading model. It is expected that a linear random wave model might be good enough for the ship motion calculation but it is clear that linear random wave theory will not provide a useful model for the steep wave fronts that cause the large impact loads. Section 5.1 can provide an estimate of kinematics given a wave shape but there is still a need to find the appropriate wave shapes.

Second order theories are promising and a program has been written by Marin for this purpose and is being investigated in the SAFE-FLOW project. The second order theory probably underpredicts the steepness of some critical waves but it will not predict breaking and so may include some events that would in reality have broken but which might compensate for the underprediction of the slightly less severe steep waves. With an appropriate calibration it may prove to be the most effective wave model for bow impact calculation.

In this chapter two alternatives, based on empirically modifying linear random wave theory, are tried and compared with laboratory measurements. These methods are potentially attractive because they only require small modifications to methods routinely used in present practice.

Method 1 uses the experimental observation (Section 4.9) that the wave front steepness increases rapidly in a certain range of calculated linear particle acceleration/g to modify the wave front steepness.

Method 2 uses a steady flow approximation with Bernoulli's equation to obtain an estimate of the surface shape and the particle kinematics.

5.2.1 Linear random wave theory with wave front steepness modification

This method simply calculates the linear particle vertical acceleration $T_z/8$ ahead of each time step and uses this in conjunction with the Figure 4.8 curve to increase the front steepness of the water surface.

The $T_z/8$ advance is used because the acceleration peaks at the wave crest whereas the steepening is a maximum on the front of the crest.

The particle acceleration is calculated with a frequency cut-off at 2.25 times the spectral peak frequency, f_p.

The steepening is achieved very simply by distorting time – the program assigns the water surface elevation calculated at some time $t + \Delta t$ to time t, where Δt is calculated to provide the steepening predicted by Figure 4.8. The time distortion is removed linearly over a specified period after it is applied; a period equal to T_z works reasonably well. As coded the time distortion starts to be removed in the time step after it is applied. This means that the maximum applied slope amplification is a little less than the Figure 4.8 curve. In principle with time being advanced and retarded it would be possible for the same piece of time history to be used twice. Additional coding was included to prevent this, which is probably most necessary if the distortion removal time is set to be much shorter than T_z.

The results from this simple method are not perfect but are promising.

Figure 5.6 shows a time history of a case where a good fit to a non-linear profile has been obtained. The upper curve is the time history of the slope magnification factor.

Figure 5.7 shows a case where the measured increase in steepness has not been predicted.

The method never increases the height of the crest, whereas often the crest height increases above the linear value in the extreme events.

Figure 5.8 shows plots of surface slope against surface elevation for 13 minute records. The first is for the linear prediction, the second for the empirical method, the third as measured in the laboratory. These results also show the trend for good estimates of extreme steepness but confirm that there are events where the elevation also increases, which is not estimated by this simple method.

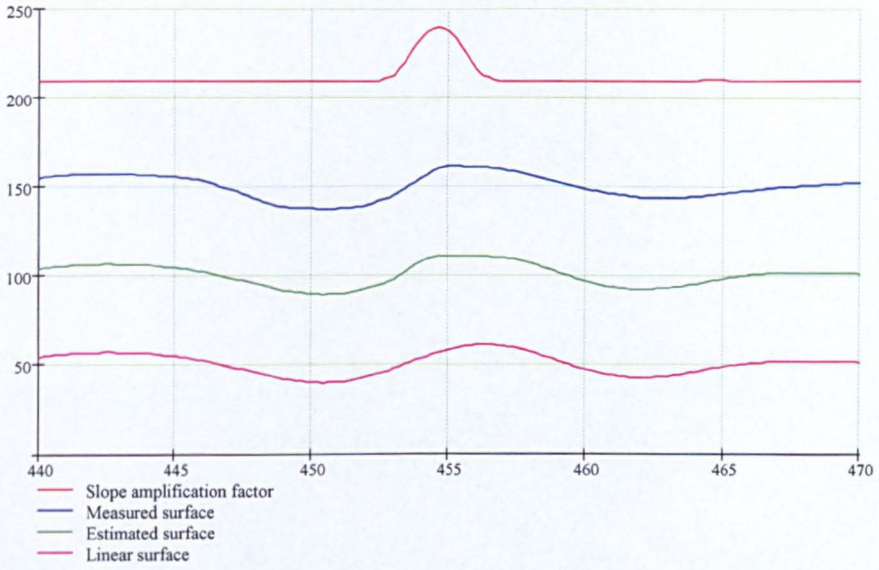

Figure 5.6 Example where the empirical steepening works well

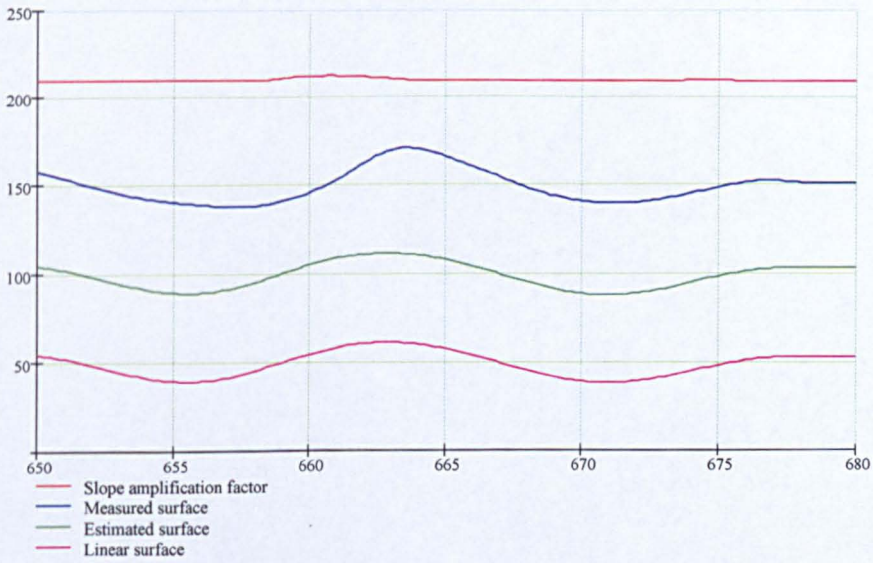

Figure 5.7 Example where empirical steepening is much smaller than measured

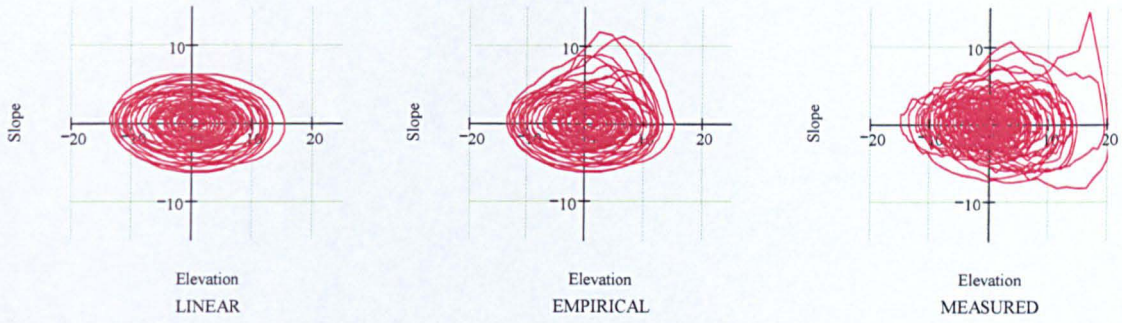

Figure 5.8 Thirteen minute record of surface steepness against elevation; linear, empirical and measured

This empirical method appears to work quite well and to be able to give reasonable estimates of the wave front steepnesses in random seas. However it will miss some particularly severe events where the crest front becomes very high. The method was used, with good results, for wave impact pressure calculations for comparison with measure results in both random and new-wave experiments (see Section 5.4).

5.2.2 Linear random wave theory with steady flow assumption and better surface boundary condition

This method is based on:

a) Linear random wave theory to get an initial estimate of the water surface shape.

b) The steady flow assumption within a moving axis system, as for the breaking wave method Section 5.1.

c) Calculation of a water surface amplitude weighted mean (over frequency) wave number for the hyperbolic functions that gives a good fit to the kinematic boundary condition (normal to surface particle velocity and

surface velocity should be equal) $\bar{k} = \frac{0.7\sum_f \eta k^2}{\sum_f \eta}$, where η are the frequency components of the wave. The 0.7 coefficient was found to fit the kinematic boundary condition in the wave crest and to better predict the observed breaking (horizontal particle velocities exceeding the celerity) than a value of 1.

d) Bernoulli's equation in an iterative loop to find the free surface according to the non-linear dynamic boundary condition (pressure equals zero on the surface). In practice three iterations were used.

The method steepens the wave front and gives a sharper and higher wave crest.

Figure 5.9 shows that although the major crest is modelled reasonably well, with an increase of height and steepness, the troughs on either side of the main crest do not have the correct shape.

It was also found that in the critical waves that cause the largest forces the waves are approaching breaking. The measured upper crest front steepnesses are about 60 degrees whereas the predictions from this methodology do not exceed about 40 degrees (which is a considerable improvement on the linear prediction of less than 20 degrees). It is interesting that the measured 60 degree maximum front steepness in the upper crest and often show a rapid slope change to about 30 degrees. This could be consistent with the wave having just started to break with water, ejected from the crest, falling down in front of the wave and following an approximately parabolic path. If so the velocities would be dramatically changed in the top-front of the wave crest and the vertical component of the water particle velocity in this region will be downwards instead of upwards as predicted by the wave theory. Alternatively the non-linear effects may lead to the steep front in conjunction with upward water particle velocities.

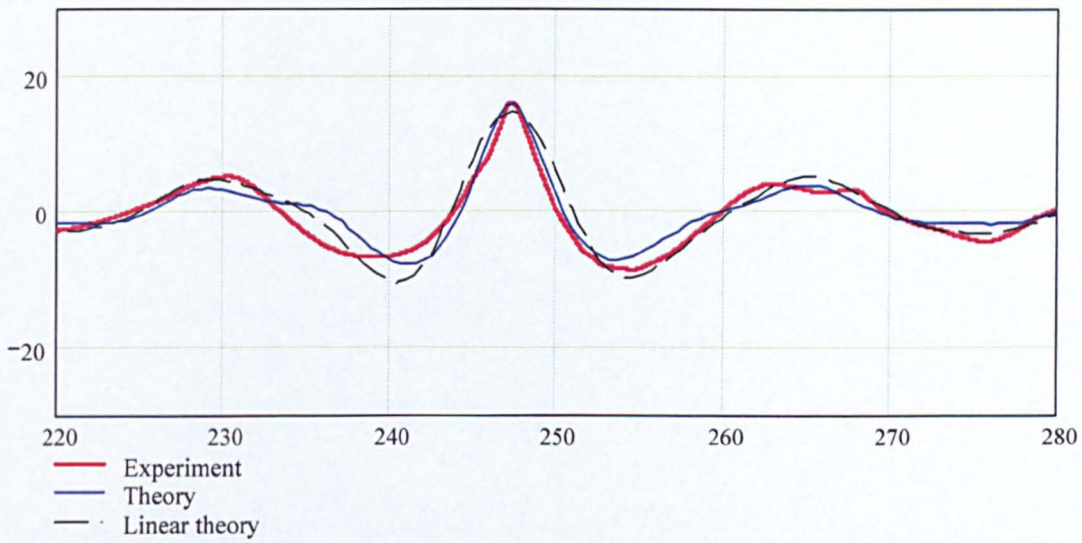

Figure 5.9 Effect of method 2 simplified modelling on the predicted shape of a wave group (H_s = 17.95m, T_z = 14sec, steepness = 1/17, SB = 0.5)

5.2.3 Comparison and application of the two methods

The empirical slope modification method (1) seems to be a useful method for getting a much better extreme steepness estimates than from linear theory. It also has the advantage that it might be developed to work directly in the probability domain – so avoiding the need for time domain simulation and allowing relatively simple reliability analysis to be performed. This method was therefore selected for comparison with measurement.

The Bernoulli equation method (2) was used to estimate the characteristics of less critical non-breaking waves in less steep sea-states than had been tank tested. It has the advantage of allowing for height as well as steepness increases. As sea-state steepness reduced it gave a non-linear change back to waves with linear properties in sea state steepneses of about 1/50. The wave impacts in these less steep seas (and equivalently impacts in less steep wave groups in steeper seas) were therefore calculated using this method.

5.3 Cylinder Pressure-Area Relationships

Campbell and Weynberg (1980) performed interesting work on a cylinder slammed into water, both parallel to the surface and at an angle. They presented pressure data, proposed a methodology for the calculation of slamming forces (based cylinder axis parallel to water surface impacts) but were not as interested in local pressures as is the FPSO designer.

The data presented in the Campbell and Weynberg report is re-interpreted to estimate how local pressures vary across the width and the length of a slammed panel.

A method of interpolating/extrapolating their data was required and it was decided to calibrate a $v\ dm_v/dt$ model using their data and then to use this for the more detailed work. The full nomenclature is given in Figure 5.11.

The added mass can be determined as below:

$$m_v = \tfrac{1}{2}\rho\pi\frac{d^2}{4} = \tfrac{1}{2}\rho\pi\left[x(D-x)\right] \tag{5.10}$$

$v\ dm_v/dt$ can be found in closed form for any nominal water surface position x:

$$F_I = v\frac{dm_v}{dt} = v^2\frac{dm_v}{dx} = v^2\tfrac{1}{2}\rho\pi(D-2x) \tag{5.11}$$

Angled impacts were calculated using a strip model – the cylinder was divided into transverse discs (see Figure 5.10). Each disk or strip was assumed to behave as if it was part of a long cylinder subject to a parallel slam.

The basic model worked well except for:

1) The early stages of the impact where it does not model the observed rise time, underestimated the peak slam force and, early in the slap,

underestimates the extent of the pressures. The reason appears to be that the simple dm_v/dt model assumes that the cylinder starts in contact with the water and does not include the effect of the spray roots or jets which form as the water surface touches the cylinder and considerably increase the wetted area.

2) The final stage where the true impact force has dropped to zero and other drag and inertia forces are probably dominant.

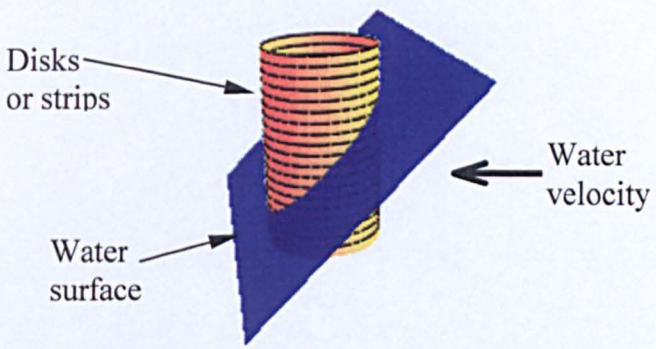

Figure 5.10 Cylinder slapping model

In the early stages of the slam, spray roots form (see Figure 5.11). These are an 'easy' way for the water to escape at the very beginning of the impact, the alternative path – radialy back through the fluid is more difficult and for an incompressible fluid, as the surface touched the bow, would result in infinite pressure, albeit on a small area of plating; in simple terms if the spray roots do not form then dm/dt is infinite as the water surface just contacts the panel.

The formation of the spray roots is also associated with the approximately linear pressure increase during the rise time of a parallel impact. As the impact progresses so more water has to be pushed into the spray root and quite quickly the pressure builds to a level at which the radiation effects become dominant.

The overall effect is that the peak slam force is roughly doubled.

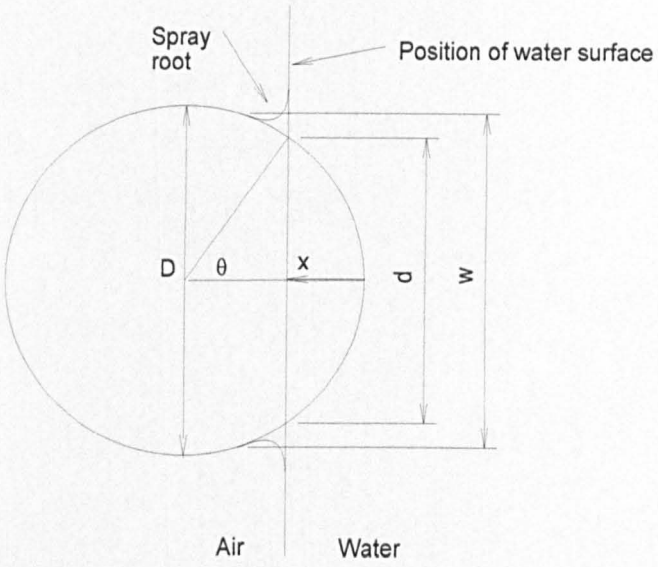

Figure 5.11 Spray roots and nomenclature

The spray roots were allowed for by empirically increasing the width of the loaded area at the early stages of the slam. Good comparison with Campbell and Weynberg's measurements were found if the added mass per unit length of cylinder was calculated as that of a cylinder equal to of the instantaneously wetted width of the cylinder w. The overall width between spray roots is found from:

$$\frac{w}{d} = 1 + 0.7\cos^6(\theta) \tag{5.12}$$

where d is the width of the intersection of the cylinder and the incident (non deformed by the presence of the cylinder) water surface. (A still better fit is obtained if the calculated added mass is multiplied by 0.9 but this additional factor has not been included in the results presented here.)

The simulation is started at the time of the pressure reaches its peak value. This will be useful and valid where in an angled impact the time delay of the water

impacting each disk causes the pressure build up and dominates the determination of the rise time.

Campbell and Weynberg found that local pressures are not uniformly distributed across the wetted width: there is a peak pressure near the water surface intersection. However, for plating design, the case of an impact on the centre of a panel makes the average pressure on the panel of more importance and they were

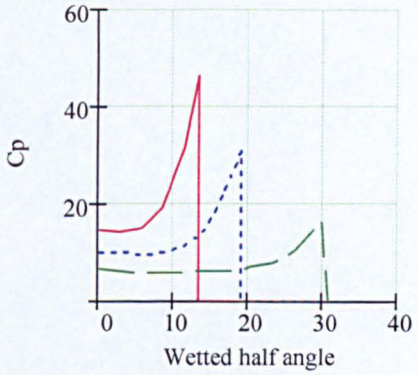

used for this work.

Figure 5.12 Distribution of pressure at various stages of the impact (from Campbell and Weynberg, 1976)

Nevertheless the rapidly moving peak pressure, shown in Figure 5.12 is thought to produce significant vibration of the less highly loaded panels observed in the Loch Rannoch tests.

Figure 5.13 shows a comparison of Campbell and Weynberg's measured impact force and the results of the relatively simple program.

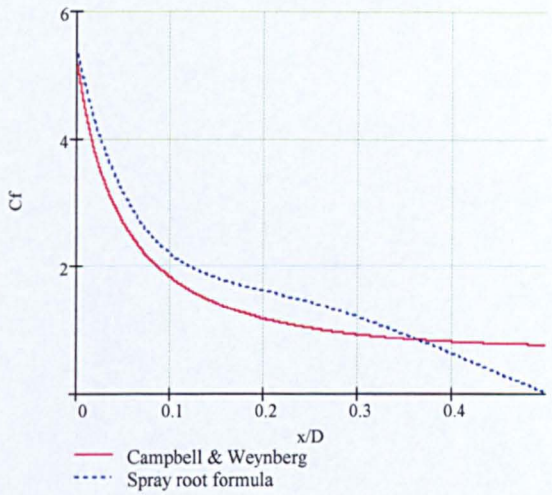

Figure 5.13 Impact force versus immersion depth of cylinder, predicted and measured

The program was then used to analyse a simplified wave slap represented by a 45degree water surface moving at constant velocity. Figures 5.14 to 5.15 show the maximum over time of the average panel pressures during this simplified wave slap for a range of panel sizes.

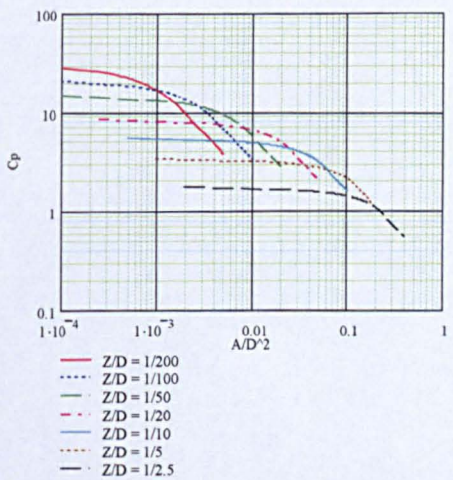

Figure 5.14 Pressure vs area, for different panel heights *Z*, from the cylinder strip model

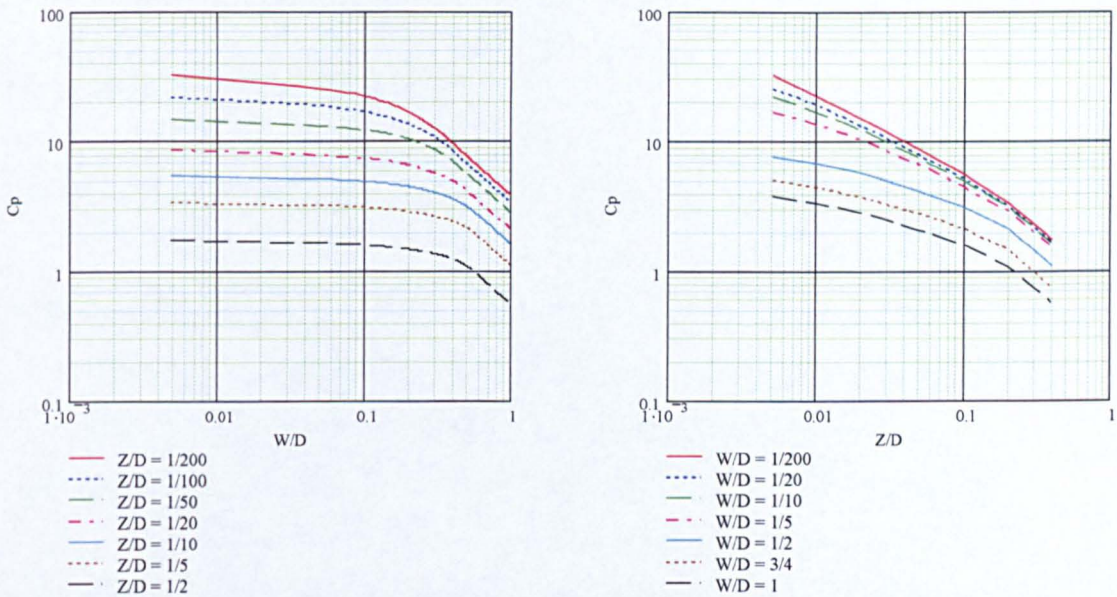

Figure 5.15 Pressure vs panel height Z and width W, from the cylinder strip model

The results show that at large panel widths or heights there is an inverse linear pressure area relationship. This indicates that the peak force has occurred on a smaller area. It is consistent with the test results (see Figure 4.15).

The variation of average pressure with panel (projected) width W becomes less sensitive to W as the width decreases becoming $p \propto W^{-\frac{1}{9}}$.

The variation of average pressure with panel height is roughly $p \propto Z^{-\frac{1}{2}}$.

The results of this model appeared to be satisfactory and so the model was extended to allow its application to a moving FPSO bow in waves. This is described in Section 5.4.

5.4 Slamming Simulation

5.4.1 Simulation description

A Mathcad worksheet was written to simulate bow slapping in head seas.

The theory was based on:

1) The wave frequency rigid body motions of the ship were assumed to be defined by a set of linear raos (obtained from another tanker).
2) The steady and slow drift changes in position were generally assumed to be zero. Provision was made in the program to use the measured time history of the bow position, including drift effects, when comparing specific tests.
3) The waves were assumed to be linear random but with the front steepness and crest front velocities increased (by modifying the time step) according to Figure 5.16. (for comparison with tests the same random phases were used)
4) The force on the bow was assumed to be:
    a. Hydrostatic
    b. Froude-Krylov
    c. Hydrodynamic added mass
    d. Slap
    e. Structural inertia.

The non-linear Froude Krylov pressures in (4b) were found to be significant, both in the test results and in the calculations performed in Section 5.1. They resulted in higher pressures on the bow when the bow was immersed near a steep trough and lower pressures when the bow immersed near a steep crest. The effect was taken into account using the estimated non-linear surface acceleration.

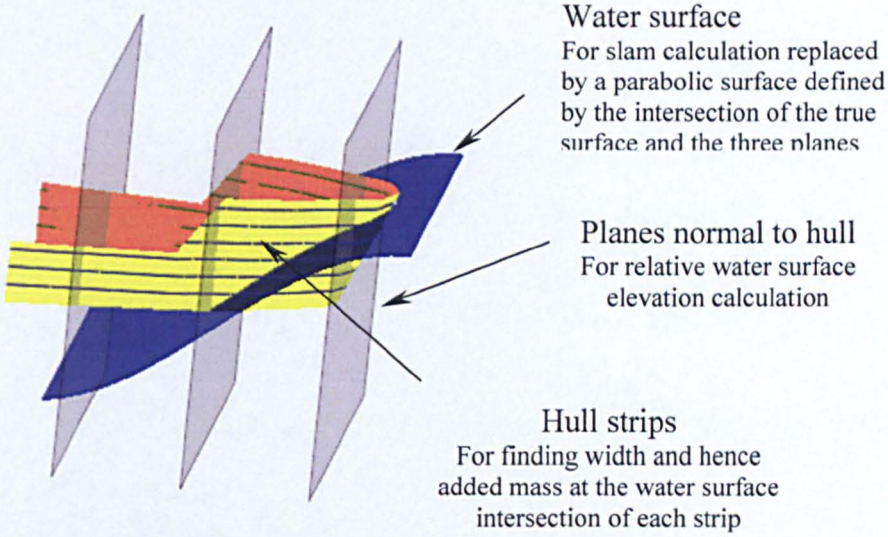

Figure 5.16 The bow impact model

The dynamic fluid forces (4c) and (4d) can be calculated from the rate of change of momentum of the added mass of fluid that, for simplified calculation, may be regarded as attached to the structure. The total force given by the rate of change of momentum is:

$$F_I = \frac{\mathrm{d}}{\mathrm{d}t} m_v \cdot v = m_v \frac{\mathrm{d}v}{\mathrm{d}t} + v \frac{\mathrm{d}m_v}{\mathrm{d}t} \tag{5.13}$$

where v is the relative velocity between the structure and the water surface and m is the total mass of the structure including the added mass.

$m_v \frac{\mathrm{d}v}{\mathrm{d}t}$ is the well know added mass force. It is linear in small waves because the mass: m_v does not change very much with time and the acceleration: $\mathrm{d}v/\mathrm{d}t$ is proportional to wave height.

$v\frac{dm_v}{dt}$ is a non-linear term that cannot be calculated by linear theory. The non-linearity arises from the multiplication of v and dm/dt which both change significantly with time. This term is associated with bottom slamming and bow slapping, so these forces can be calculated from the velocity v and the rate of change of added mass.

The added mass is calculated every time step and its change divided by the time step length gives dm/dt. The added mass at each time step is calculated by

1) Defining the upper bow shape by two waterlines (see Figure 5.18)
2) Dividing the upper bow into horizontal strips (about 10).
3) Defining three reference approximately vertical transverse planes that are fixed to the bow (see Figure 5.16).
4) Calculating the bow position.
5) Calculating the linear water surface shape and non-linearly steepening the front face of the waves according to acceleration/g.
6) Constantly monitoring the relative water levels on these planes – allowing for FPSO and water surface motion.
7) Fitting a parabola to the three water surface intersections.
8) Determining where the parabola intersects the horizontal strips.
9) Calculating the transverse width d of each strip at its intersection with the parabola.
10) Assuming that the added mass for the strip is proportional to d^2.

Note when the water surface moves beyond the end of a strip there is no contribution from that strip to the rate of change of added mass until the strip is exposed and submerged again.

Based on this theory a programme to simulate the time history of slamming force and total force has been developed here. The flow chart is shown in Figure 5.17.

The model shown in Figure 5.16 is chosen for its simplicity. It's easy to apply and all the forces can be calculated at each time step as long as the bow shape, the sea state and the RAOs for the ship are given. If more planes normal to hull are used it will give more accurate results, especially for local pressures. Also the smaller the time step is used, the more accurate the results will be. Both of them require longer run time, so it's better to reprogramme the code in a more efficient language.

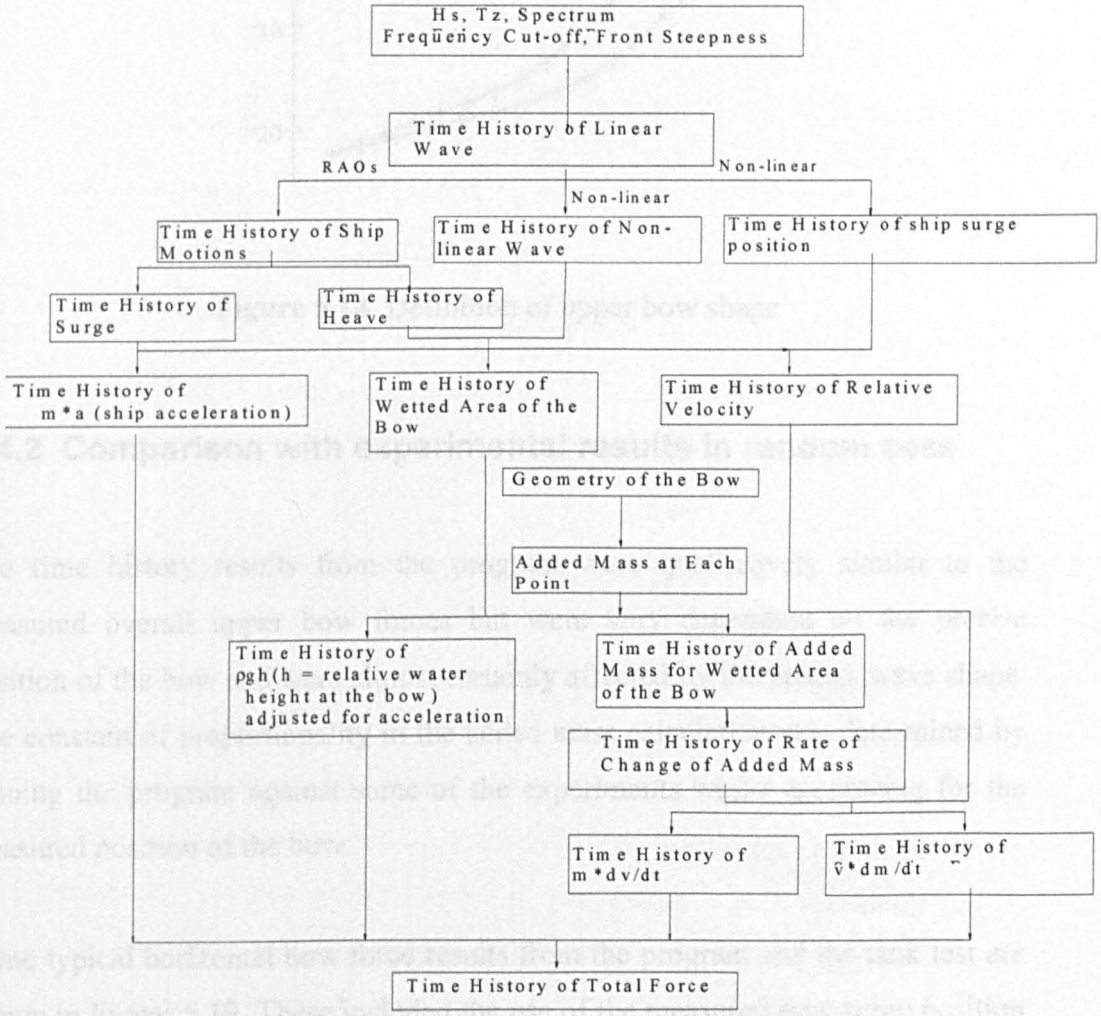

Figure 5.17 Flow chart of the programme simulating the time history of slamming

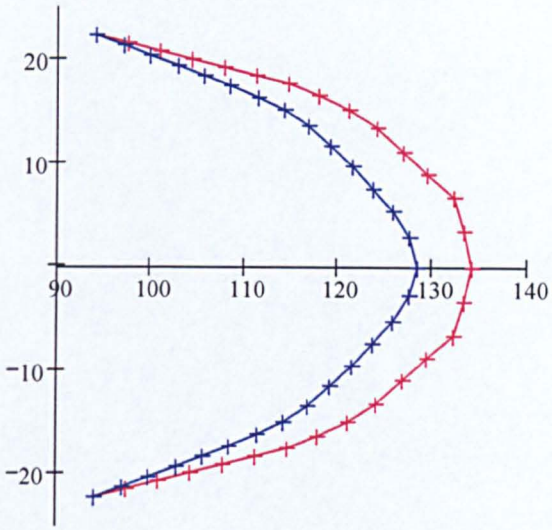

Figure 5.18 Definition of upper bow shape

5.4.2 Comparison with experimental results in random seas

The time history results from the program were qualitatively similar to the measured overall upper bow forces but were very dependent on the precise position of the bow and were almost certainly affected by the precise wave shape. The constant of proportionality in the added mass calculation was determined by running the program against some of the experiments whilst accounting for the measured position of the bow.

Some typical horizontal bow force results from the program and the tank test are shown in Figure 5.19. These included the use of the measured bow surge position to improve the results.

Both time histories only include a limited number of slams, the remaining forces are as described above in Section 5.4.1. Qualitatively the results are very similar

but the numerical simulation is not capable of resolving the precise time domain behaviour of the bow.

However the model would still be useful if its slam statistics, with no use of FPSO surge position in the calculation procedure, were good.

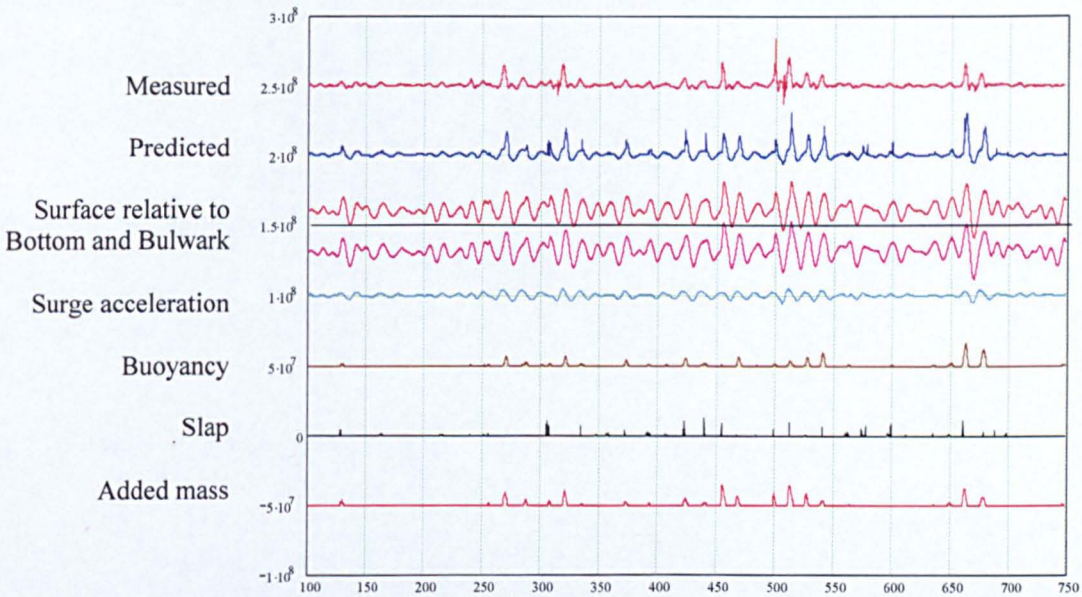

Figure 5.19 Comparison of measured and predicted bow forces

In order to determine the usefulness of the program, results of slamming forces from lab measurements and calculations in a sea, but without prior knowledge of the bow's position, nine random waves time history segments were chosen from Loch Rannoch Test and run through the simulation. These were selected to include the large measured slamming events.

The comparison results in pressure are shown in Table 5.1.

The calculations considerably underestimate the measured maximum forces in the 9 tests. However the mean and standard deviation of the calculated results for

those 9 cases agrees quite well with the mean and standard deviation of the overall random wave data set of 40 segments.

This implies that the uncertainties in bow position, and perhaps the fine detail of the wave shape, do not allow the experiments are to be precisely simulated in the time domain but if statistics of extreme slams are required then the model appears promising. It was anticipated that the steady and slow drift behaviour would not affect the statistics of the steep wave impacts on the bow and this confirms that those effects can be ignored in the impact load calculations.

The model can produce local panel pressure information but this requires a much shorter time step, and so longer run times which have not yet been attempted and may require the model to be reprogrammed in a more efficient language.

Table 5.1 Comparison of random wave impact pressure heads (m) from measurements and calculations

Test No.	*9357*	*9364*	*9365*	*9968*	*9976*	*9979*	*9979*	*9982*	*9996*	*Mean*	*SD*	*COV*
Measure-ments (9)	13.4	5.17	10.8	10.5	10.2	31.9	14.2	9.6	8.9	12.8	7.6	0.6
Calcula-tion	9.56	4.96	3.44	5.88	6.98	19.7	12.7	7.8	4.4	8.4	5.1	0.61
Measure -ments (40)										8.5	4.4	0.52

5.4.3 Comparison with experimental results in new-waves

The comparison between the measured and calculated Loch Rannoch new-wave impacts, Table 5.2, shows a very good agreement. The mean is about 1 but more importantly the coefficient of variation is about 25% which, for an impact phenomenum is reasonably low.

Table 5.2 Comparison of new wave impact pressure results (m) from measurements and calculations

Sea-state Steepness^{-1}	*Measurement*	*Calculation*	*Measurement/ Calculation*
14.0	5.89	7.10	0.83
13.2	5.21	6.07	0.86
12.6	4.96	3.59	1.38
11.8	2.17	1.61	1.35
15.8	5.21	5.95	0.87
15.0	9.08	9.14	0.99
14.1	12.08	10.34	1.17
13.5	7.78	10.49	0.74
12.6	5.62	7.75	0.73
16.8	2.74	2.61	1.05
16.0	4.98	6.51	0.77
15.1	12.30	10.54	1.17
14.4	14.50	12.24	1.18
13.4	8.37	15.46	0.54
17.9	1.11	0.74	1.49
17.0	2.08	1.81	1.15
16.0	5.67	6.41	0.88
15.3	11.71	9.87	1.19
14.3	15.59	14.83	1.05
	Mean		1.02
	Standard Deviation		0.25
	CoV		0.25

5.4.4 Comparison of long random waves time histories and new-waves

It was not practical to run large numbers of long random time histories in the tank but it was possible to run 10, or in some cases 15, 3-hour computer simulations for each of 20 sea states for comparison with the predictions from new-wave groups. It was necessary to choose a steepness balance for each random wave steepness that would give the average worst wave shape for bow slap. When this work was done the estimated steepness balance for the worst slap impact in a sea-state was:

$$\text{FrontSteepness} = \left(\frac{0.055}{\text{Sea} - \text{state Steepness}} \right)^3 \tag{5.14}$$

Later in the project a steeper linear relationship was found to be better, as shown in Figure 5.20 (also see Figure 4.3).

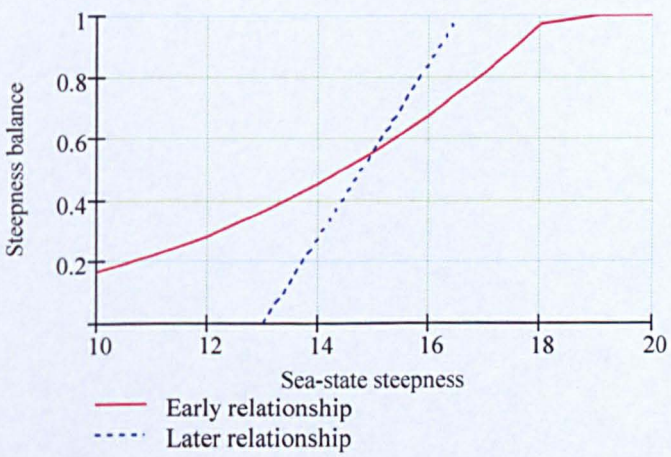

Figure 5.20 Assumed steepness balance required for a given sea-state steepness as used at this stage of the study and as proposed later.

Using the assumed steepness balance the most probable maximum slamming pressure for each sea-state can be calculated by generating the worst front steep new wave in the programme.

The mean value, standard deviation and coefficient of variation for the (random prediction)/(new-wave prediction) for each sea-state were calculated from the 10 or 15 random wave results. The calculated results are given in Table 5.3. They show that the new-wave simulation is a good predictor of the average maximum slap impact in a simulated random sea.

It is therefore reasonable to assume that the experimental new-wave impacts will be good predictors of experimental random sea impacts.

Table 5.3 Comparison of the calculated pressure heads (m) from new-wave and random wave

	New Wave		Random Wave					
Sea-state Steepness^{-1}	Steepness Balance	Calculated Pressure	Mean Calculated Pressure	Standard Deviation	COV	Mean+SD	Mean-SD	Ran/New
14.7	0.53	7.99	8.85	3.40	0.38	12.25	5.45	1.11
14.0	0.46	10.78	10.26	2.21	0.22	12.48	8.05	0.95
13.2	0.38	11.53	10.50	1.96	0.19	12.46	8.55	0.91
12.6	0.33	10.53	13.17	3.01	0.23	16.18	10.16	1.25
11.8	0.27	12.50	14.85	3.46	0.23	18.31	11.39	1.19
15.8	0.66	9.23	9.60	2.68	0.28	12.28	6.92	1.04
15.0	0.56	11.02	10.57	2.18	0.21	12.74	8.39	0.96
14.2	0.47	12.60	11.55	2.03	0.18	13.59	9.52	0.92
13.5	0.41	16.27	12.78	3.10	0.24	15.88	9.68	0.79
12.6	0.33	16.79	15.39	3.26	0.21	18.64	12.13	0.92
16.8	0.80	6.91	9.69	4.36	0.45	14.05	5.33	1.40
16.0	0.68	9.61	10.67	3.27	0.31	13.94	7.41	1.11
15.1	0.57	12.95	15.22	5.13	0.34	20.34	10.09	1.18
14.4	0.50	16.38	14.86	2.01	0.14	16.87	12.85	0.91
13.4	0.40	16.73	18.12	5.50	0.30	23.62	12.62	1.08
17.9	0.95	5.17	6.59	3.06	0.46	9.65	3.53	1.27
17.0	0.82	6.97	10.17	5.31	0.52	15.48	4.86	1.46
16.0	0.69	10.81	11.90	5.17	0.43	17.07	6.73	1.10
15.3	0.60	13.35	12.97	3.54	0.27	16.51	9.42	0.97
14.3	0.49	16.70	18.29	3.61	0.20	21.90	14.67	1.10
			Mean					1.08
			Standard Deviation					0.17
			CoV					0.16

The random calculation for each sea-state have run for about 30 hours full scale time, so the statistical properties of the slap forces can be observed from the calculation results. The numerically calculated slap force distribution and theoretical Rayleigh^2, Rayleigh^3 and log-normal distributions of the data are shown in Figure 5.21. The 1 in 3 hour probability of about 0.001 and is also shown.

The results suggest that the distribution of slap forces will be poorly predicted by assuming a response that is the square of an underlying Rayleigh distributed variable and will be much closer to a response that is the cube of an underlying Rayleigh distributed variable. This seems reasonable because the slap force is proportional to velocity times surface slope, both would be Rayleigh distributed in a linear exceptionally narrow banded sea-state but both are increased by non-linearities. The results also confirm the findings from Weggel (1971) that the maximum impact pressure has a log-normal distribution.

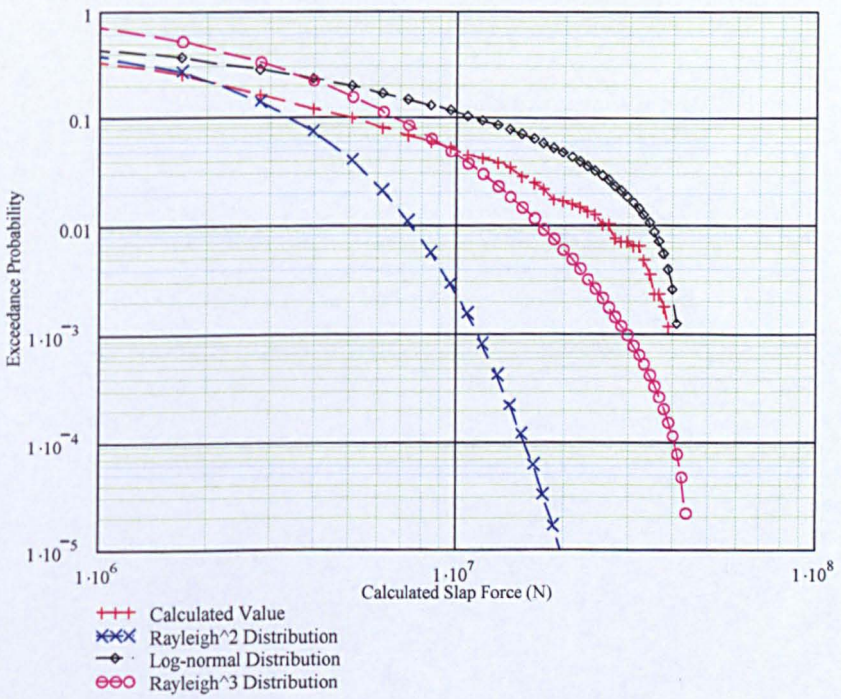

Figure 5.21 Exceedence probability distribution of slap force

Overall this study has:

1) Provided some confidence that the use of new-wave type wave groups for impact tests should provide useful results.
2) Shown that a time history simulation can be a reasonable basis for design. Note however that
    a. The model was effectively calibrated against the experimental data. Blind results for a different bow shape would not be so good!
    b. The quality of local pressure calculation has not yet been tested and will require much longer run times.

6 Derivation Of Design Guidance

The experimental work in uni-directional seas coupled with the computational work in unidirectional and spread seas have allowed relatively simple approximate rules to be developed for horizontal wave slapping forces.

The term *slapping wave* is used for a large wave that is breaking or on the point of breaking and therefore capable of causing large horizontal impact forces.

The slapping waves are characterized by an SB value which may be expressed as a proportion or a percentage. SB (Steepness Balance) = 0% implies a high slapping wave shape (component frequency crests aligned). SB = 100% implies a steep fronted slapping wave shape (component frequency fronts aligned).

6.1 Breaking Wave Type Related To Sea-State Steepness

The different types of wave are described for unidirectional seas. The adjustments for spread seas (which increases the required sea-state steepnesses for each breaker type and increases the celerity) are described in Section 4.6. Figure 6.1 Shows the different types of waves that could cause large impacts.

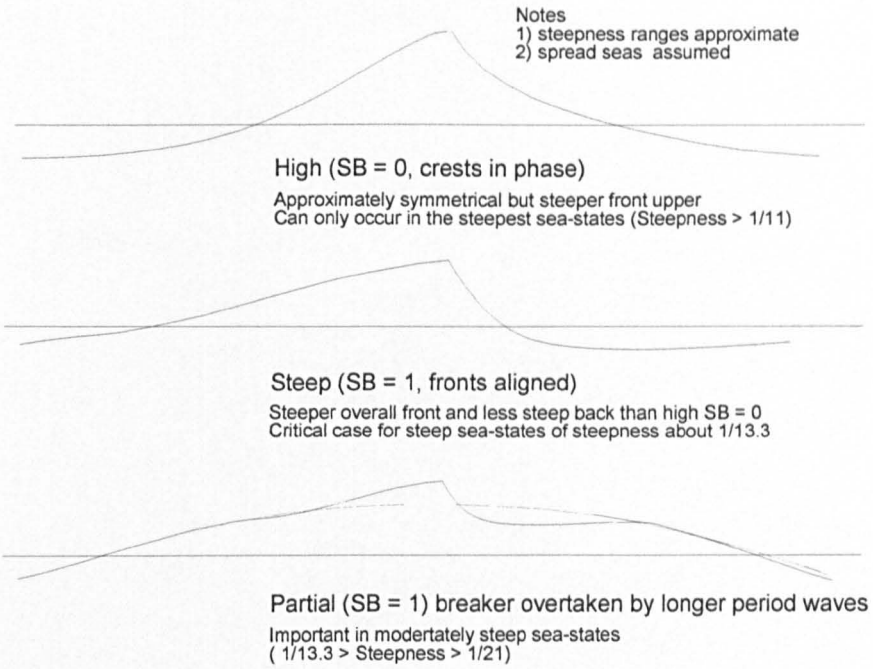

Figure 6.1 Important types of deep water breaking wave

Note: Figure describes limits for spread seas following description gives limits for long crested seas

1. ***Sea-state steepness greater than 1/13***
    a. Breaking limits the 3 hour extreme impacts to those that would be found in a 1/13 sea state of the same T_z. There will be a considerable amount of wave breaking with the slapping waves more frequent than in 1/13 sea states.
    b. The largest impacts will be of the SB = 0 type with an amplitude of 1.07 L_z/13 The smaller impacts will have larger SB values.
    c. The celerities associated with the largest slapping waves will correspond to about 0.95cz where $cz = gT_z/2\pi$. The lower slapping waves will also have a lower celerity.

2. ***The critical region, sea-state steepnesses between 1/13 and 1/16.5***

   a. In these sea states are found the *critical wave* cases where extreme 1 in 3-hour waves are just breaking and so lead to large impact pressures and forces.

   b. The nature of the extreme slapping waves varies as the sea state steepness decreases:

      i. In the 1/13 sea states the extreme slapping wave is also the highest 1 in 3 hour wave (SB = 0 amplitudes in phase, amplitude = 1.07 H_s), with many smaller and less severe higher SB impacts.

      ii. In the 1/16.5 sea states there will on average only be 1 slap per 3 hours (from a wave with the characteristic SB = 1: front slopes in phase and an amplitude which is only 63% of H_s).

   c. Celerities will vary from

      i. $0.95cz$ in the 1/13 sea-states to

      ii. $0.87cz$ at 1/16.5 sea-states.

3. ***Sea-state steepnesses less than about 1/16.5***

   This region although generally less severe than the critical area is potentially interesting because there would appear to be two types of possible slapping waves. Large *whole wave* breakers, where the whole wave breaks will be infrequent (less than one occurrence in 3 hours and becoming less frequent as sea-state steepness decreases) though will cause severe slapping pressures when they occur. Small *partial breakers*, where the breaking waves occur superimposed on longer waves are a possibility. Here the slamming velocity is the sum of the velocity of the breaking wave and the wave on which it is riding. Both may make an important contribution to fatigue. Unfortunately we have not yet undertaken any tests in this area so the treatment of these sea-states, which is based on a theory which is certainly too simple, is speculative.

3A. Whole-wave breakers

a. The large whole-wave breaking waves to be expected in sea-states steeper than 1/16.5 will occur less than once in 3 hours and become progressively rarer as the sea-state becomes less steep.

   i. Near breaking waves will cause slapping forces but they will rapidly become small as the sea-state steepness decreases. The rapid reduction in slap forces is caused by the rapid reduction in the non-linear effects which in steeper waves increased both steepness and particle velocity.

   ii. Unusually severe events, with a recurrence of less than once in three hours, can increase the wave steepnesses back to the breaking limit and lead to large pressures which (because of the large associated celerity) is typically found in the critical region. At this stage the guidance will concentrate on predicting 1 in 3 hour extreme events. The consequences of the considerably larger pressures at lower probability levels will be considered in the reliability analyses.

b. Although extreme height (SB = 0) breaking waves are possible they are most unlikely to occur and the higher probability SB = 1 type slapping waves with amplitudes of about 63% of H_s will be more important.

c. Celerities of about $0.87cz$ are likely to be associated with the slapping waves.

3B. Partial-wave breakers

These breaking waves (which have not yet been the subject of model testing) will occur more frequently in the less steep sea states. They are characterised by a small breaking wave which is a scaled down (in height and length) version of the SB = 0 to SB = 1 type of breaker.

This breaking wave occurs in conjunction with the low frequency sea-state components which do not have much affect on the breaking wave but, as they overtake the breaking wave, they displace it up or down and convect the breaking wave forwards or backwards (adding to or subtracting from the celerity of the breaking wave. For the more severe cases the breaking wave is displaced upwards and convected forwards.

a. For sea-state steepnesses of about 1/25 the 1 in 3 hour slapping wave will be a quarter scale model of the 1/16.5 SB = 1 wave, superimposed on a longer period wave of period about 1.25 T_z and height up to H_s.
b. The celerity of the breaking wave is increased by a small amount (10% at sea-state steepness 1/25) by the interaction with the longer period wave. There will also be an effect similar to a wave encountering a changing current. For a slowly varying upwelling current this would reduce the height and steepness of the breaking wave (by about 6% for the 1/25 sea-state steepness).

It should be noted that the boundaries have not been identified with very high accuracy (because the steepnesses used were generally 1/13, 1/14, 1/15 etc.) and the results will be affected by the nature of the real sea-state spectra which will not be the theoretical Jonswap $\gamma = 2$ long crested spectrum or the Mitsuyasu/Goda spreading function on which this work is based.

An overall, simplified, conclusion from this work is that for sea-state steepnesses less than 1/15 the form of the breaker will be SB = 0 to SB = 0.5, the crest elevation will be about H_s and the celerity will be about cz. As the sea-state steepness increases beyond 1/15 the SB will increase, the crest elevation and celerity will drop.

6.2 Velocities In The Crest Of The Slapping Wave

The velocities have not been measured but the measured crest shapes have been used to predict the velocities. These show that the wave upper front horizontal velocities are approximately the celerity (See Section 5.1). The velocities reduce behind the water surface.

The slap pressure is expected to be related to Newton's 2nd law as Eq. 5.13:

The slap force is $v\frac{dm_v}{dt}$. v is the horizontal velocity = celerity and $\frac{dm_v}{dt}$ is proportional to the vertical velocity of the water surface (for an inclined bow the velocity of the surface up the bow may be more accurate but the vertical velocity is used in this work).

The vertical velocity of the water surface equals the celerity times the slope. Therefore slam forces and pressures are expected to be proportional to celerity^2 × slope. Alternatively the equivalent slam velocity is $\sqrt{celerity^2 \, x \, slope}$. Because the celerity of the wave group is similar to the celerity cz (of the wave with a period of the sea-state T_z) it is convenient to define a slam velocity $\sqrt{cz^2 \, x \, slope}$ and to allow for any change in another correction factor.

6.3 Shape Of The Crest Of The Slapping Wave

From the experiments the worst slapping waves, (whatever their SB value) typically have a maximum steepness of about 60 degrees to the horizontal near their upper crest. This large angle is probably the result of breaking or closeness to breaking. The crest slope then gradually decreases both towards the top of the crest and towards the trough of the wave.

For waves which are not breaking the less steep front slopes and particle velocities less than the celerity can still give impact pressures but the particle velocities and front slopes of non breaking waves drop rapidly as the steepness decreases so the 1 in 3 hour pressures will drop rapidly.

Quantification of the pressure reduction with the reducing sea state steepness also needs to account for the relative size of the crest and the panel.

6.4 Relative Pressure Loads From Different Steepness Sea-States

Experiments have been undertaken for the sea-state steepnesses expected to govern the design of an FPSO. However it is necessary to extrapolate beyond this range in order to check that the worst cases are indeed within that range. The results of the analyses performed in Section 5.2 are used for this purpose.

Taking the critical waves (Tables 4.6c and Figure 4.2) and calculating pressure/(celerity^2 $H_s^{0.5}$) (the factor related to the wave front steepness, the bigger the factor, the steeper the wave front), and then normalized by the value at 1/15 sea state, the values in 1/13 to 1/15 sea states for bow and local pressure results show relatively high values at steepnesses higher than 1/15 with a very rapid drop in the less steep sea states.

The pressure/(celerity^2 $H_s^{0.5}$) is chosen at this stage as it should allow comparison between different tests with different waves celerities and wave/structure sizes.

The results are plotted in Figure 6.2. The results shown as 'o' correspond to pressure panels in 30 degree seas and '+' to the whole bow in head seas.

The normalized pressure/celerity^2 $H_s^{0.5}$ for the 1/16 SB = 1 sea state is only about 0.7 of the 1/15 SB = 0.5 sea state value.

Using the approximate wave group analysis and assuming slap pressures are proportional to horizontal velocity ×steepness × wave amplitude$^{0.5}$, the '□' dashed curve is obtained. This confirmed the transition from SB = 0 as the worst wave groups below 1/13 steepness to SB = 1 waves above 1/16 steepness.

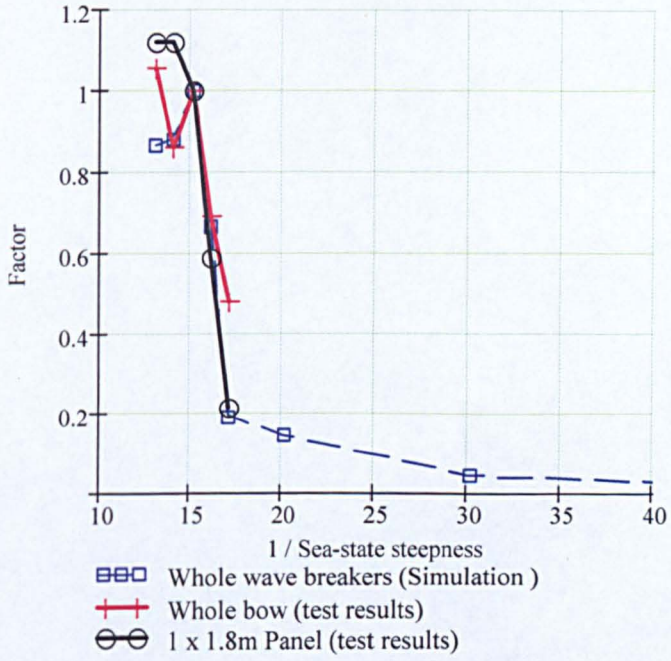

Figure 6.2 Experimental non-dimensional slap pressure results and results from a simple simulation (no spreading)

However increasing beyond 1/16 steepness a large breaking wave does not occur so the slap pressures drop off very rapidly. From observation of the sea it is clear that there are many breaking events where the breaker is shorter than the typical wave lengths in the sea. As a theoretical exercise in Section 5.3 the prediction of short period breakers was considered and the pressures were estimated. The results showed that for sea-state steepnesses between about 1/16 and 1/32 these short period 'partial' breakers, which will appear to be riding and being overtaken

by longer non-breaking waves will, from their shape, velocities and celerity, give larger pressures, (especially on smaller areas, large areas may not be completely loaded) than the whole wave breakers.

The theoretical results for partial breakers (adjusted to give the same result at 1/16 as the whole wave SB = 1 case, which is also a limiting case for the partial breaker) are shown as 'o' in Figure 6.3.The pressures still drop off rapidly as steepness decreases but not as rapidly as for simple SB = 1 waves.

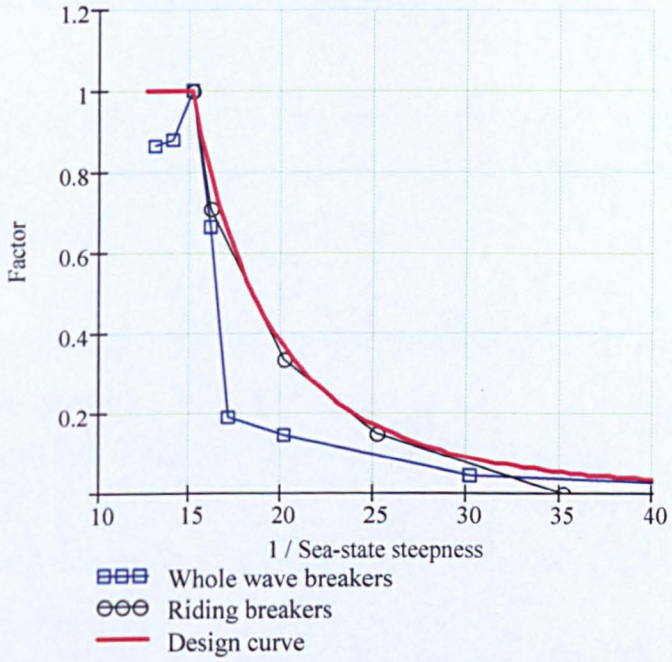

Figure 6.3 Increase in pressure from 'riding' or 'partial' breaking waves and a design curve for the calculation of slap pressure in low steepness seas (no spreading)

Figure 6.3 also shows a design curve which is fitted to the partial breakers over the main range of possible interest of low steepness, slapping waves.

6.5 Effect Of Spectral Shape

Small variations in γ have been found to have a negligible effect but seas with multiple spectral peaks could behave differently to the cases considered here. In particular a high frequency wind sea component, from a growing storm, superimposed on a more mature sea could increase the amount of breaking in the form of '*partial breakers*' (see Section 6.1).

6.6 Effect of Directional Spreading

Directional spreading effects will make all the conclusions drawn from long crested experiments pessimistic. The theoretical work on extreme high waves (SB = 0) in spread seas, in Section 2, suggests that in comparison with unidirectional seas:

1. Horizontal propagation direction velocities are reduced by about 16%.
2. Celerity is increased by about 14%.
3. Front face steepness is reduced of about 8.5%.

The 15 % reduction in velocity was expected from previous calculations for other purposes by the Authors.

The similar increase in celerity was not expected but is understandable because the high frequencies are subject to more spreading than the lower frequencies and so will contribute less to the celerity than the lower frequency, less spread components.

Because the criterion for breaking is that the horizontal velocity should exceed the celerity and because velocity / celerity is proportional to steepness for less steep sea-states but the non-linear behaviour is also affected by surface slope so it

would seem likely that an approximately 20% steeper sea states will be required for each type of breaking wave to occur.

However, given a particular H_s and T_z and a breaking wave the pressures will be proportional to:

$$horizontal\ velocity \times immersion\ velocity = celerity^2 \times face\ slope,$$

so that, given the steeper sea state, pressures will increase by about 19%.

The combined effect of the two effects is to increase the pressures in high steepness sea states but to reduce the pressures in low steepness sea states.

The results in Figure 6.4, for the average pressure over a bow panel on a West of Shetland FPSO on the 100 year equal probability sea-state contour show that in practice the overall effect of spread seas is very beneficial:

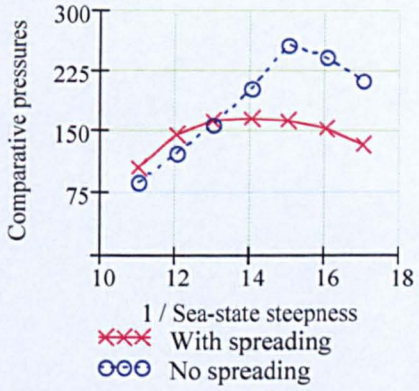

Figure 6.4 Effect of spread seas on an example west of Shetland FPSO bow plate, selected sea states are on the estimated 100 year H_s and T_z contour.

The design curve is modified for spreading as shown in Figure 6.5. The increase in the sea-state-steepnesses required for the different types of slapping waves implies moving to the left on the sea-state scatter diagram *ie* reducing T_z. This

reduces the impact pressures through the reduction of the celerity, which is proportional to T_z.

In addition if the probability of occurrence of the sea-state is maintained, and noting that the critical sea-states are on the steeper part of the scatter diagram, then the higher steepness will require a lower wave height, even lower T_z and hence a further reduction in celerity and impact pressure.

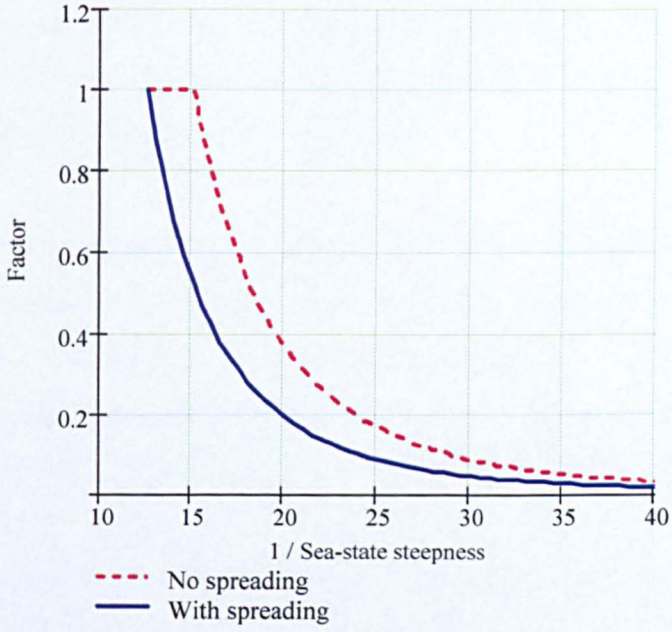

Figure 6.5 Effect of spreading on the pressure reduction in the longer period sea-states

The equation of the design curve, modified to include spreading is:

$$if\ S_{ea} < \frac{Spf}{15} \quad Factor = E(S_{ea}) = \frac{15}{Spf} S_{ea} \left(\left(S_{ea} \frac{15}{Spf} \right)^{pe-1} \right) \tag{6.1a}$$

$$if\ S_{ea} \geq \frac{Spf}{15} \quad Factor = E(S_{ea}) = 1 \tag{6.1b}$$

where $pe = 3.5$

6.7 Average Loading On Different Areas Of The Bow.

For most likely panel sizes the pressure was found to drop in inverse proportion to the square root of the area of the panel (see Section 4.16).

For very large areas (width greater than about 0.4 times the breadth of the ship) then the pressure drops in inverse proportion to the area.

Pressures on very small areas appear to increase less rapidly than in inverse proportion to square root of the area and, although of limited practical interest, are difficult to assess and are discussed in Section 6.8.

A general formula is proposed which uses the product of the square root of the width times the square root of the height of the panel to determine the effect on the pressure. However it is also important that the results scale – if the formulae work for the model FPSO as well as for the full scale FPSO then there is a better chance that the formulae will also work well for different sizes of FPSO.

The panel width W and height Z therefore need to be non-dimensionalized.

It is chosen to divide the panel width by the plan diameter of the plating (W/D)(for a quartering sea impact on the side of the bow or for head sea impact on less than 0.4 times the FPSO's beam.). For impacts on large parts of the bow it is difficult to fit a diameter and instead an ellipse may be fitted. If the 'ellipticity (aspect ratio)' e is the (along ship axis length) /(transverse axis length). The panel width is then non-dimensionalized as (We/D). For a truly elliptical bow the circle and ellipse formulae will give the same result for an impact on a small area. In practice the shapes are rarely circles or ellipses and approximate fits with some sensitivity calculations will be required.

$$\text{Pressure} \propto f(W) = \left(\frac{We}{D}\right)^{-0.5} \quad \text{for } W < 0.4D \quad \text{or} \quad \sqrt{0.4}\left(\frac{We}{D}\right)^{-1} \quad \text{for } W > 0.4D \tag{6.2}$$

The panel height was originally non-dimemsionalized by dividing by the significant wave height, which is justified because the important effect on loading is probably related to the change in velocities and slope over the height of the wave. However it was more convenient to divide the panel height by L_z, the length of the wave having a period T_z. The constant 12 was introduced to keep the ratio $L_z/12Z$ similar to H_s/Z but it could be included in an overall constant.

$$\text{Pressure} \propto g(Z) = \left(\frac{12Z}{Lz}\right)^{-0.5} \tag{6.3}$$

These non-dimensional ratios could then used in the pressure calculation formula to determine slap pressures using the relationships noted from the tests:

Unfortunately this pressure becomes infinite as $W \rightarrow 0$ and so some additional thought was required about very small areas.

6.8 Limiting Pressures On Very Small Areas

For very small areas (about 250mm width or height) the pressure-area relationship is not known. The small pressure transducers did not show the continuing inverse square root relationship. Air in the water will result in elastic effects and a theoretical limit which is very dependent on the proportion of air.

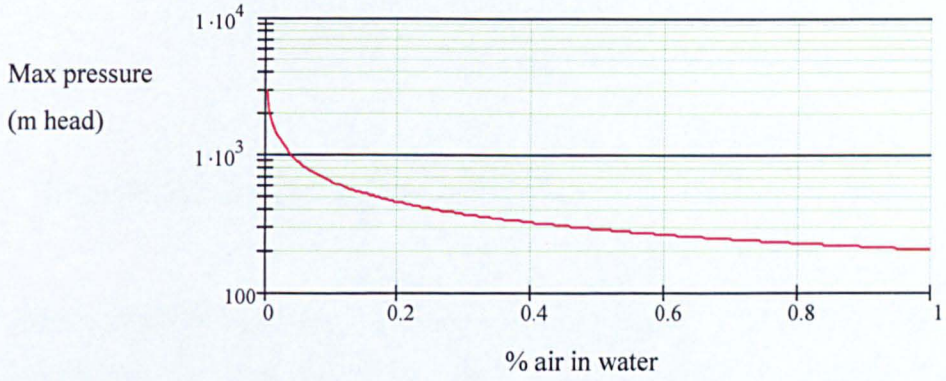

Figure 6.6 Limiting pressure for different proportions of air and a celerity of 20m/sec

Limiting pressures can be calculated from the one dimensional wave equation (used for water hammer and pile driving calculations ($\rho_{mix}\ V_s\ V$)). The limiting pressure head with a celerity (impact velocity) of 20m/sec, at about 0.1% air, is 700m water. 0.1% is simply a guessed value of the aeration of the water near the point of the impact. 700m also is about the highest value measured in the Loch Rannoch tests, however this is not indicative of the 700m being a good limit because in the model tests the scaled limiting pressures would be scale$^{-0.5}$ times higher (about 9 times higher for the Loch Rannoch scale of 1/80, assuming that the proportion of air was the same in the model tests and in the real sea). Nevertheless, to avoid singularities in the program a limiting pressure has been included which is approximately 700m head at 20m/sec and changes in proportion to impact velocity squared. This has been done by adding small constants to the D/W and Z/L_z terms in the pressure calculation formula. (Note that the theoretical limiting pressure at constant air entrainment varies in proportion to velocity not

velocity squared but there is little point in a sophisticated pressure limit calculation when the uncertainty is so great although the practical effect is probably very small.)

$$\text{Pressure} \propto F(W) = \left(\frac{We}{D} + 0.012\right)^{-0.5} \quad \text{for } W < 0.4D \quad \text{or} \quad \sqrt{0.412}\left(\frac{We}{D} + 0.012\right)^{-1} \quad \text{for } W > 0.4D \tag{6.4}$$

$$\text{Pressure} \propto G(Z) = \left(\frac{12We}{Lz} + 0.04\right)^{-0.5} \tag{6.5}$$

6.9 Dynamic Amplification Factors

Because the loads are applied very quickly a dynamic amplification is likely. This depends on the rise time, decay time and natural period of the panel including added mass. Added masses for vibrating panels, with different configurations and mode shapes, were calculated by an existing programme, using potential flow theory. An example graph is shown as Figure 6.7. (The apparent thickness of the added mass of water is of the order of half the narrowest dimension of the panel and reduces for panels near the surface.) However for this work measured in-water natural periods were used so there was no need to measure the added mass.

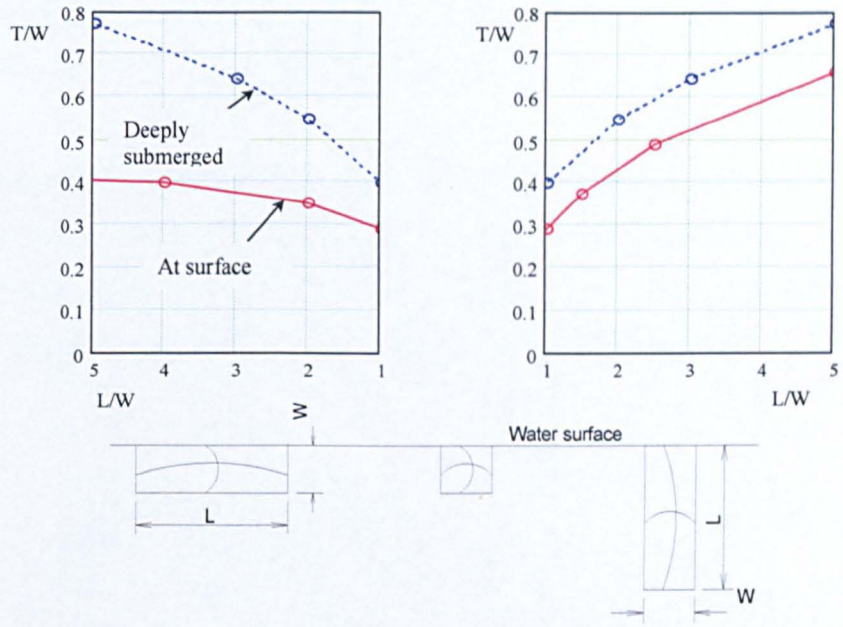

Figure 6.7 Dynamic amplification factors for a mode 1 response of a single vibrating plate on a large panel.

Rise and decay times for curved panels were estimated from the experiments.

The equations that best fitted the rise and half-decay time (time to decay from peak value to half of peak value {as in radioactive half-life}) for the largest slams were:

$$t_{rise} = 0.2 t_{slam} \left[1 + \left(\frac{W}{D} \right)^4 \right] \tag{6.6}$$

$$t_{half\ decay} = 0.07 t_{slam} \left[1 + 10 \left(\frac{W}{D} \right)^4 \right] \tag{6.7}$$

where:

$$t_{slam} = 0.308 ellip \frac{D}{cz} \left(\frac{12Z}{Lz} \right)^{0.3} \tag{6.8}$$

The half–decay time was chosen because the response was found to be less sensitive to the precise shape of the decay if half-decay time was used rather than for instance the time to decay to $1/10^{th}$ of the peak value.

The Dynamic amplification factor should then be calculated using a linear rise and exponential decay. Methods are presented in many texts on shock and explosion loads eg Harris and Crede (1976). To simplify the DAF calculation an approximate formula was derived by the Author for the SafeFlow project.

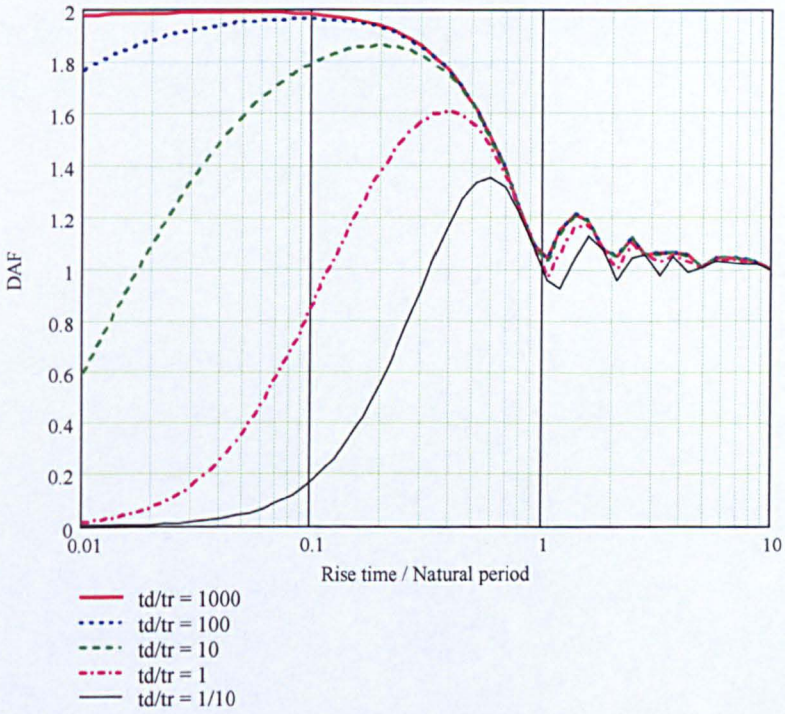

Figure 6.8 Dynamic amplification factors for a linear pressure rise and exponential decay

For a typical large local slap the rise and decay times are about 0.1 sec and for a panel natural period of about 1/30 sec the DAF will be 1.05.

However often a panel with smaller slap load than an adjacent highly loaded panel had a DAF of about 2, implying a very short rise time of less than 0.01 seconds. It

is likely that these were the result of a phenomena that can be seen in the cylinder test results of Campbell and Weynberg 1980. If the centre of the impact is off the panel a pressure wave with a high edge pressure crosses the panel very quickly as the panel is wetted. If a panel is subject to a large number of these highly dynamic slaps the fatigue life could be reduced by the large number of high stress range cycles.

6.10 Final Form Of The Design Equations

The form of the design equation for the most probable maximum quasi-static pressure head (m) in a 3 hour storm of given H_s and T_z is:

$$p = \frac{1}{g} C_p E(S_{ea}) F(W) G(Z) V_I^2 \; DAF \tag{6.9}$$

where:

p design pressure (m sea water).

C_p coefficient determined from tests to best fit the results

$E(S_{ea})$ coefficient that depends on the sea-state steepness S

$F(W)$ coefficient that depends on the panel width (W), panel curvature or FPSO's beam, and elliptical bow shape

$G(Z)$ coefficient that depends on the panel height and the zero-crossing wavelength of the sea

V_I notional slam velocity $V_I = \sqrt{cz^2 \tan(\theta_I)}$

Where

cz is the zero crossing celerity $(gT_z/2\pi)$

θ_I is the typical maximum angle between the wave front slope and the horizontal

θ_I is fixed at 60 degrees in this formula. The effect of lesser slopes is taken into account by $E(S_{ea})$. Therefore $V_I = 1.32\ cz$.

C_p 0.355

C_p was determined empirically by taking tests results for 'critical' wave cases and a wide range of panel areas and then finding the mean value of :

$$C_p = \frac{p}{\frac{1}{g} E(S_{ea}) F(W) G(Z) V_l^2 \ DAF} \tag{6.10}$$

The measured against predicted pressures for various different panel or bow segment sizes are shown (without dynamics) in Figure 6.9 and with dynamics in Figure 6.10.

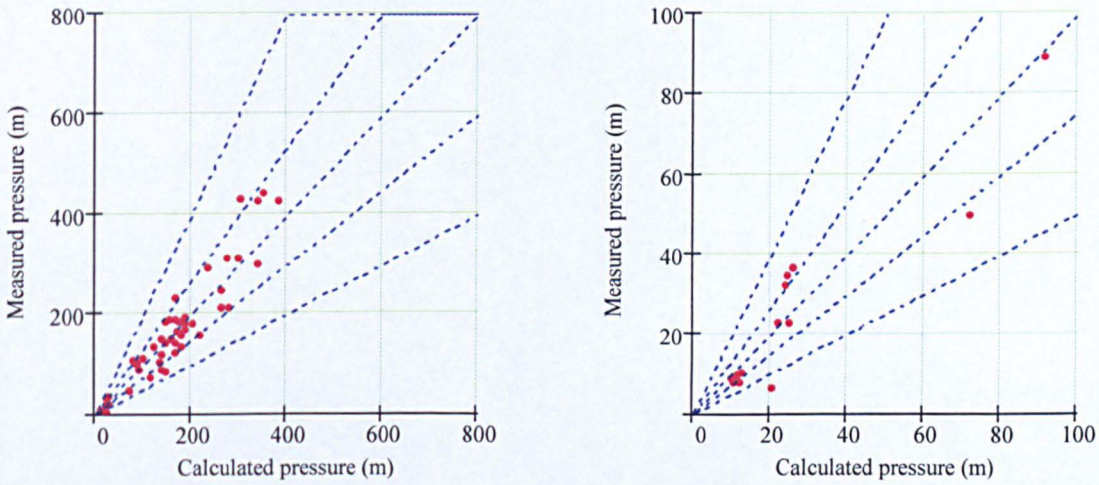

Figure 6.9 Measured and calculated pressures, excluding dynamics

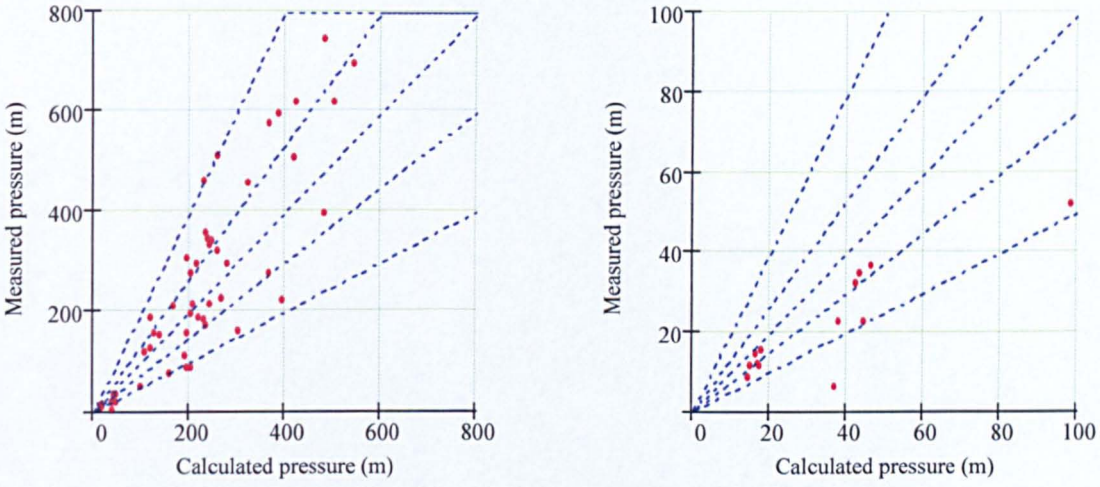

Figure 6.10 Measured and calculated pressures, including dynamics

The mean C_p value (with dynamics and calculated DAF) was found to be 0.355.

The coefficient of variation of C_p was 0.394. It is interesting that a large part of the uncertainty is associated with the dynamic response. The coefficient of variation of measured/calculated applied pressure is much lower at 0.27, implying (because of the addition by square root sum of squares) that the coefficient of variation on the dynamic calculation is also about 0.27.

This information was used within a preliminary reliability analysis using the assumptions of an underlying Rayleigh distribution with wave steepnesses and particle velocities modified using the empirical curves found from experiment and shown in Figure 2.8. Preliminary indications suggest that for a ductile structure in bending a partial load factor of about 1.7 is required (which may be reduced for less severe consequences of failure). Higher values are required for shear. This load factor should be used in conjunction with 100 year return period pressures and a first yield structural design criterion with a material partial safety factor of 1.15. The selection of safety factors is addressed in detail in the SAFE-FLOW project.

7 Shallow Water Breaking Wave Loads

7.1 Introduction

In addition to the previous work on the deep water breaking wave loads on the FPSO bow, the author undertook additional experimental work on shallow water breaking wave loads on a vertical cylinder. Shoaling breaking wave loads on a vertical cylinder were investigated in the same tank, Acre Road experimental tank (80m long, 4.6m wide, 2.6m overall depth). A segmented cylinder model with outer diameter of 0.204m and total height of 1m was built and tested. Also a 1:20 slope ramp was constructed in the tank to provide the shoaling effect. During the experiments the total force on each segment of the cylinder was measured and the water surface elevations at the cylinder and in deep water were also recorded.

7.2 Experimental Set-up

7.2.1 Cylinder model

A segmented aluminum cylinder model with 40 segments (20 for the front of the cylinder and 20 for the back) was built with the bottom fitted on a 1:20 slope ramp as shown in Figure 7.1. Inside each 50mm high segment there were strain-gauged bars to measure the total force on each segment during an impact (forces acting on the front and back of the cylinder are separately measured). The natural frequency of each segment was 250Hz at model scale. This was a compromise, chosen to be:

- higher than the full-scale frequency, so that the measured forces with any dynamic response filtered out, could be used for design purposes

- low enough to give a dynamic response that could be used to check dynamic response calculations.

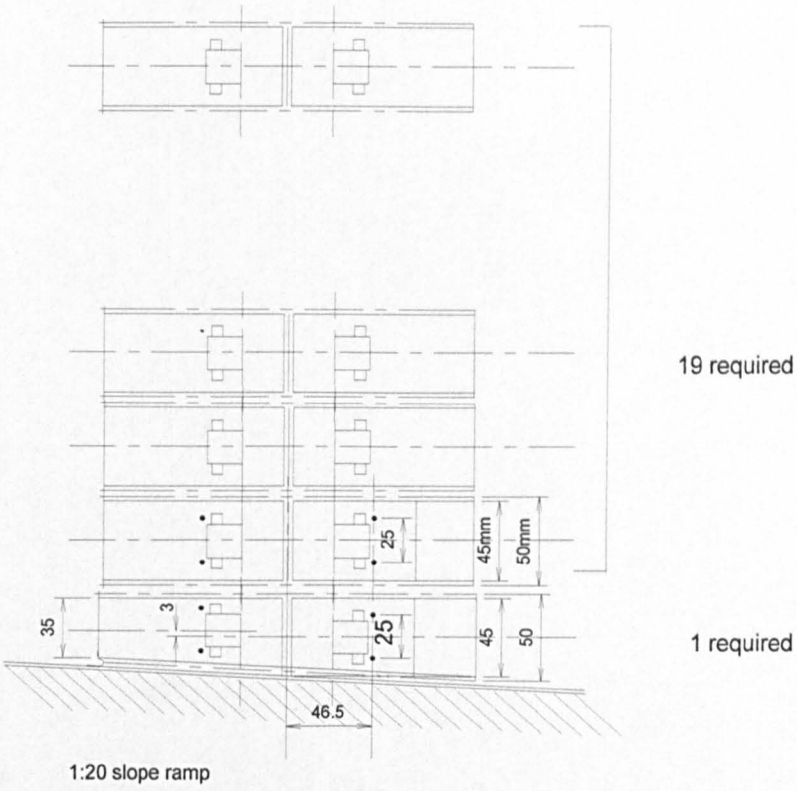

Figure 7.1 Details of the segmented cylinder model

The details inside each segment of the cylinder are presented in Figure 7.2. The instrumentation is symmetrical for port and starboard side. During the tests the port side strain gauges were used to measure the impact force, if any of these strain gauges failed, the alternative ones on starboard side were used. To keep the water out the whole cylinder was sealed by rubber (see Figure 7.3). The rubber was applied properly making sure there were no measurable carry over effects between segments. Also an automatic bilge pump was installed and monitored in order to detect the water inside the cylinder during the test and pump out the water immediately if found. Before the experiment started the strain gauges inside each segment of the cylinder were calibrated by applying 2kg, 4kg and 8kg weights on the centre of each front segment of the cylinder and 1kg, 2kg and 4kg for the back

of the cylinder (see Figure 7.4), then the calibration factors obtained were put into the data acquisition system.

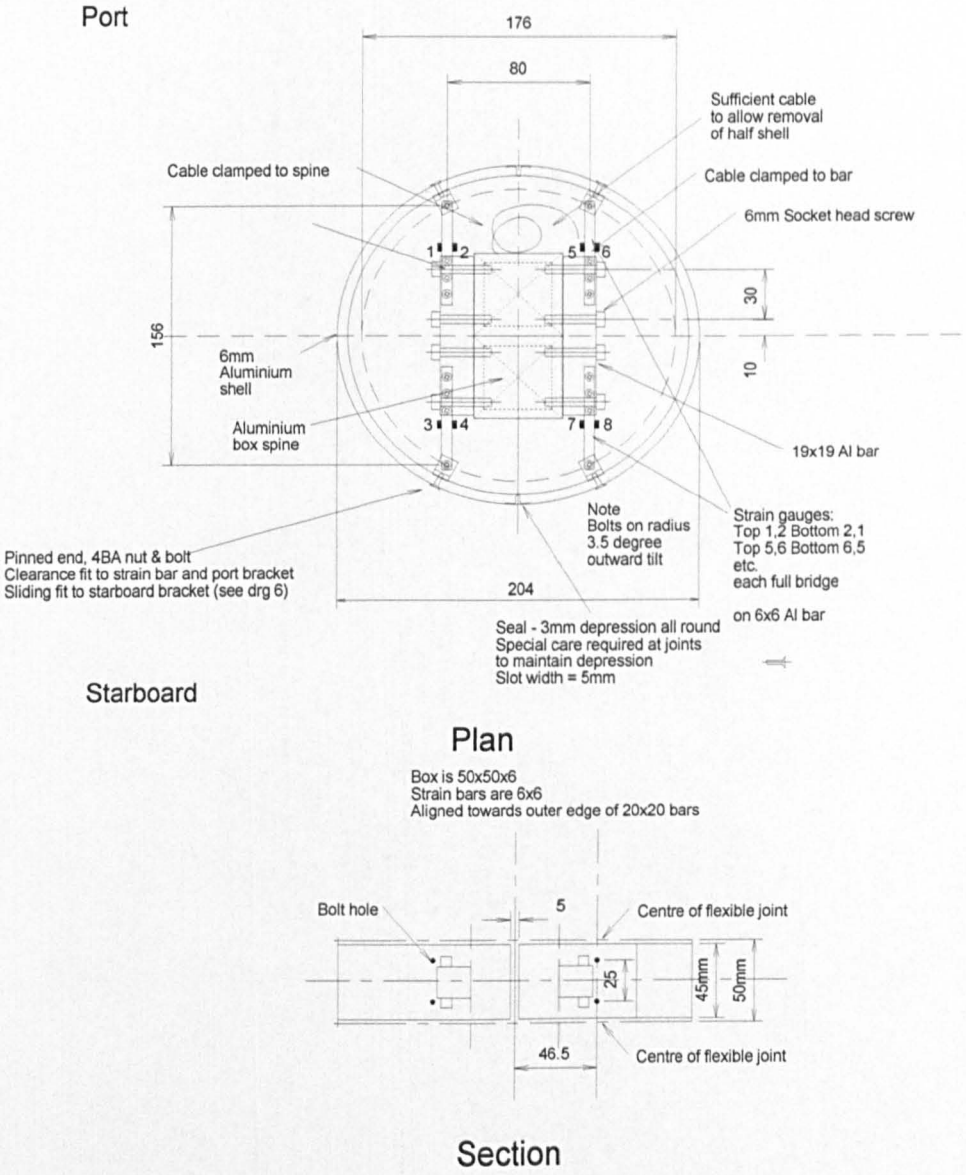

Figure 7.2 Instrumentation of the segmented cylinder model

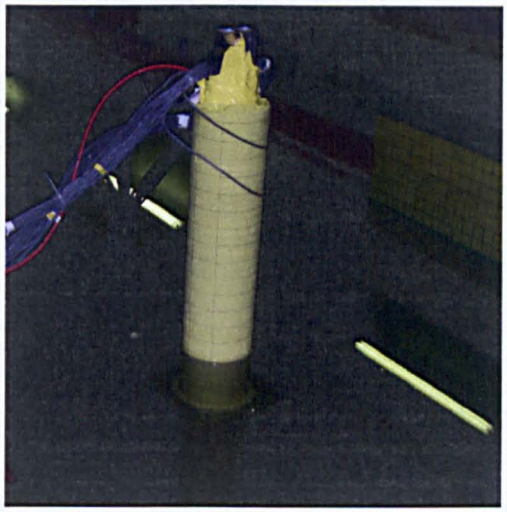

Figure 7.3 Rubber sealed cylinder model in the tank

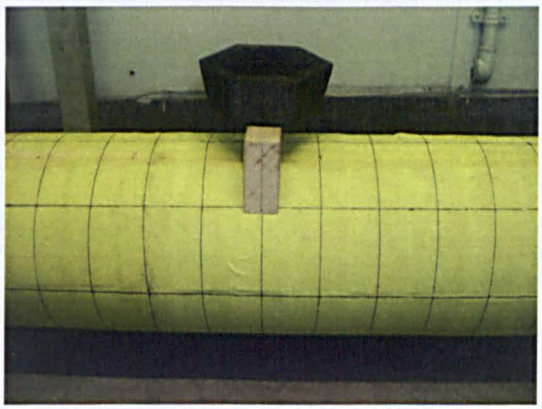

Figure 7.4 Calibration of the strain gauges inside the cylinder model (Note: segments are centered on the black lines)

7.2.2 Tank Set-up

Two sets of experiments were performed with different beach arrangements. The first part of the beach was shoaled to a water depth of about 1m, (depending on the filling depth) and the breaking waves were caused by wave-wave interactions. These experiments were performed by Imperial College. The second part of the bed was shoaled from 1m water depth to 0m depth with a 1:20 slope (Figure 7.5)

and wave breaking was caused by the bed slope (and wave-wave interaction in some tests). These experiments will be described here. The slope of 1:20 was chosen to easily generate plunging and spilling breaker in the tank. But during the tests it was impossible to get a spilling breaker at the cylinder, the reason could be the effect from the first horizontal part. The cylinder was located on the bed at a local water depth of 0.3m. This allowed regular waves of deep water height of less than 0.5m (a wavemaker limit) to break at the cylinder.

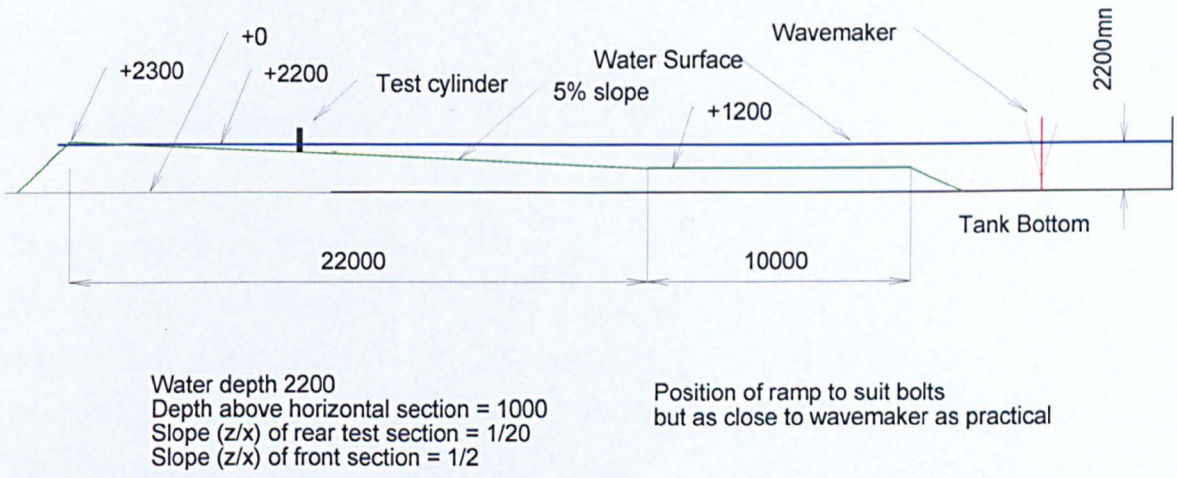

Figure 7.5 An overview of Tank Set-up

7.2.3 Test waves

Three types of waves were tested in the tank:

1) Regular waves (0.3 – 0.9Hz) and for the frequencies 0.4Hz, 0.44Hz, 0.5Hz and 0.6Hz:
2) Random waves with a deep water Jonswap spectrum, typical of the real sea.
3) New wave groups (described in Chapter 2) calculated according to linear random wave theory statistics to have the average shape of the water surface in space and time around an extreme event.

During the tests, four wave probes were used: one in deep water and the other three close to the cylinder with 5cm distance between each other. In this way the water surface elevation and the front slopes of the waves close to the cylinder can be obtained. These wave probes have been calibrated before tests by lifting 5cm above the water level. Also the wave maker was calibrated before tests by running some small amplitude regular waves. Then the RAOs of the wave maker were applied to the waves tested.

7.2.4 Data acquisition

During acquisition of the cylinder test data 45 channels were used to collect the forces on the front and back of the cylinder, the water surface elevations and the wave maker signal. All the data collected during each test was automatically converted into the corresponding unit of measurement: forces in kg, water surface elevations in cm and wave maker signal in volt. The length of time for each run was 30, 60 and 90 seconds for a regular wave, a new wave and a random wave respectively. The choice of the data acquisition rate is a compromise between file size, analysis time and accuracy. A sampling rate of 1500Hz was chosen. This introduces a standard error of 4.4% (which can be reduced by curve fitting as the response is sinusoidal).

7.3 Experimental Results

7.3.1 Breaking wave shape

It was found that the breaking wave height was consistent with the shallow water breaking limit of 0.78*d (d is water depth), (0.234m in our case). For the same frequency, the breaking waves from regular waves, random waves and wave groups had the same local wave shape and caused a similar impact response. Example wave shapes at 0.4Hz are shown in Figure 7.6, the corresponding impact

pressure heads (averaged over 50mm segment height) for wave types 1 - 3 are 0.66m, 0.578m and 0.524m without dynamic response and 1.215m, 1.206m and1.059m with dynamic response. Results may be Froude-scaled to full scale (with the usual impact test reservations over air entrainment and compressibility effects). From all the tests, the wave with 0.4Hz frequency and 0.25m wave height gave the biggest impact on the cylinder.

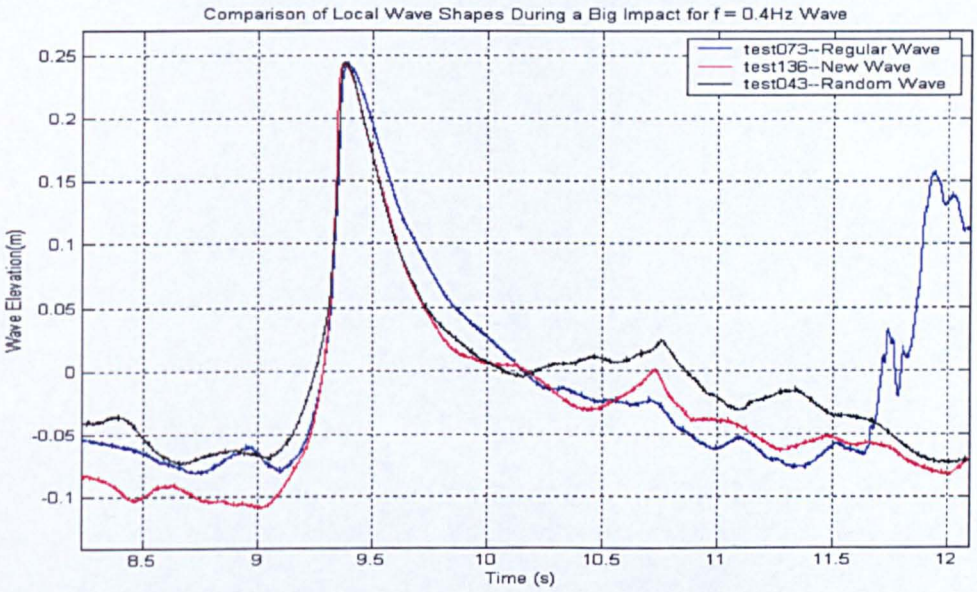

Figure 7.6 Local wave shape from different kinds of wave

7.3.2 Repeatability of experiment

Repeatability has been checked for each type of wave: Ten regular waves were repeated four times and gave a coefficient of variation of 0.062 to 0.32 on the maximum force. Two random waves time histories, each repeated 10 times gave CoVs of 0.106 and 0.173. One wave group was repeated 7 times and gave a CoV of 0.025. The lower CoV for the short duration wave group is thought to be caused by the lesser importance of cylinder and the beach reflections, which change the position of breaking, to which the pressures are sensitive, in the other tests.

7.3.3 Studies on New-wave group

For the new wave case, the linear new wave theory does not work properly owing to the highly nonlinear effects in shallow water. Also the calibration factors for the wavemaker were obtained by linear calculation which may not work well in shallow water. The agreement between linear calculation and measurement of the water surface elevation is inevitably very poor, but we can still draw the following conclusions from the new wave tests:

1) The effect of the JONSWAP spectrum enhancement factor γ. During the tests γ has been set to be 1.0, 2.0, 3.3 and 6.0. Two sea states have been tested with different γ, the results are plotted in Figure 7.7. It can be seen that unlike the deep water results, there's a significant difference between different γ value which may due to the strong non-linearity in shallow water. The waves with γ of 3.3 and 6.0 gave much bigger impact forces. With increasing γ the new wave group becomes longer and the individual wave in the wave group appears to break more violently.
2) The effect from steepness balance which is changing the wave front steepness. From the previous studies on new wave, it has been found that in deep water for different sea state steepness, different steepness balance need to be chosen to get the breaking wave. But for shallow water, it is found that for all the sea states it is the high wave which generates the plunging breaker and gives the biggest impact force on the cylinder.

3) The effect from the target position where the expected wave occurs. By changing the target position the breaking point was changed, when the

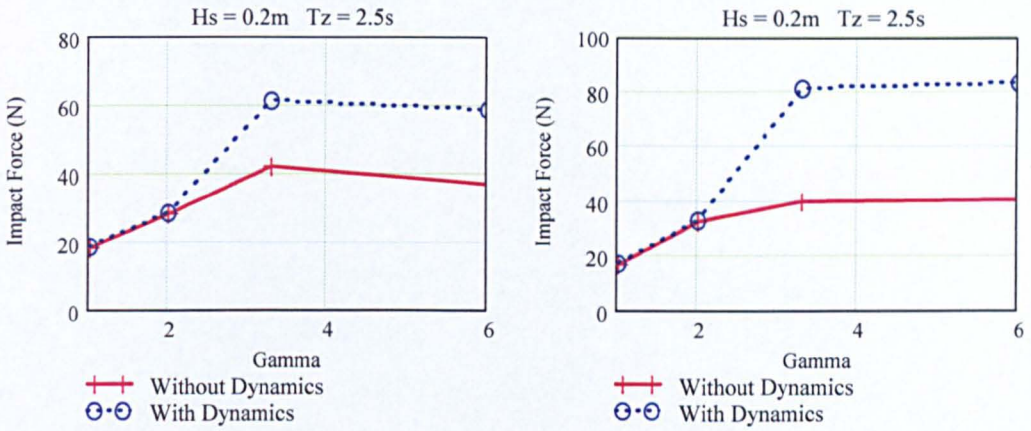

breaking point was just at the front of the cylinder, the wave gave the biggest impact force. When the breaking point was away from the cylinder, the impact force was much smaller.

Figure 7.7 Impact forces from new wave with different γ

7.3.4 Wave loads estimation

For circular or small dimension pile structures (wholly or semi-immersed), design guidelines such as BS 6394 Pt 1 (2000), EAU (1996) and the CEM (USACE, 2002), refer to Morison's equation for calculations of forces due to non-breaking waves. The experiment results have been compared with the calculation from Morison's equation for one segment which is wholly immersed during the experiment.

Morison et al. (1950) suggested that the horizontal force of a vertical cylindrical pile subjected to waves is analogous to the mechanism by which fluid forces on bodies occur in unidirectional flow, and this force can be expressed by the formulation

$$F = 0.5C_d \rho D h |U| U + C_m \rho A h \dot{U} \qquad (7.1)$$

where: Typical Units

F	is the force	N
C_d	is the drag coefficient	
C_m	is the inertia coefficient	
ρ	is the density of water	kg/m^3
D	is the structure diameter	m
A	is the structure's cross-sectional area	m^2
h	is the height of structure	m
U	is the velocity of the flow resolved normal to the structure	m/s
$\dot{U}$	is the acceleration of the flow resolved normal to the structure	m/s^2

In our case C_d = 0.92 and C_m = 1.85 (Barltrop and Adams, 1991), U is the horizontal particle velocity and $\dot{U}$ is the horizontal particle acceleration. The horizontal particle velocity U is calculated using linear wave theory but with the measured water surface elevation, $U(t) = \frac{gT}{L}\frac{\cosh(2\pi(z+d)/L)}{\cosh(2\pi d/L)}\eta(t)$. Then the horizontal particle acceleration $\dot{U}$ is calculated by $\dot{U}(t) = \frac{dU(t)}{dt}$. Measured and calculated total forces on the fully immersed third segment from the bottom of the cylinder agreed well using this procedure (see Figure 7.8).

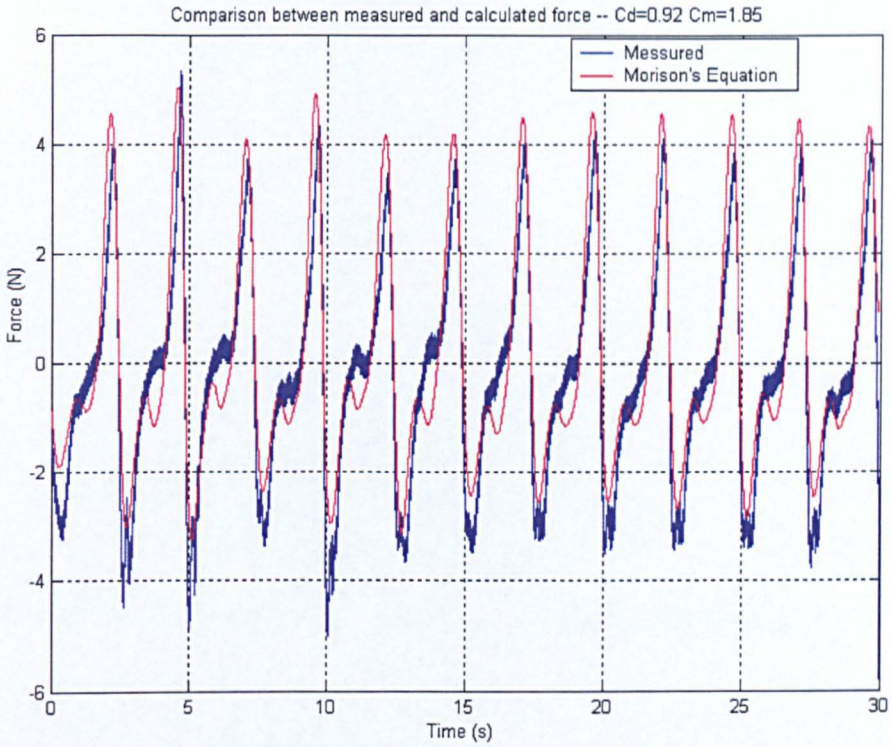

Figure 7.8 Comparison between measured and calculated force

For the impact part, in common with previous research findings, maximum impact pressures occur when the wavefront is nearly vertical and just breaking at the cylinder. The corresponding impact pressures are highly impulsive near the wave crest. Peak pressures range from 0.196m to 0.774m pressure head with dynamics filtered out and from 0.196m to 1.214m pressure head with dynamics included. The maximum pressure occurs on one segment close to the crest of the wave. The non-dimensionalized variation of impact force along the loaded length has been found to be similar to the parabolic curve described by Kirkgoz M.S. (1991) for a sea wall, but much steeper (see Figure 7.9).

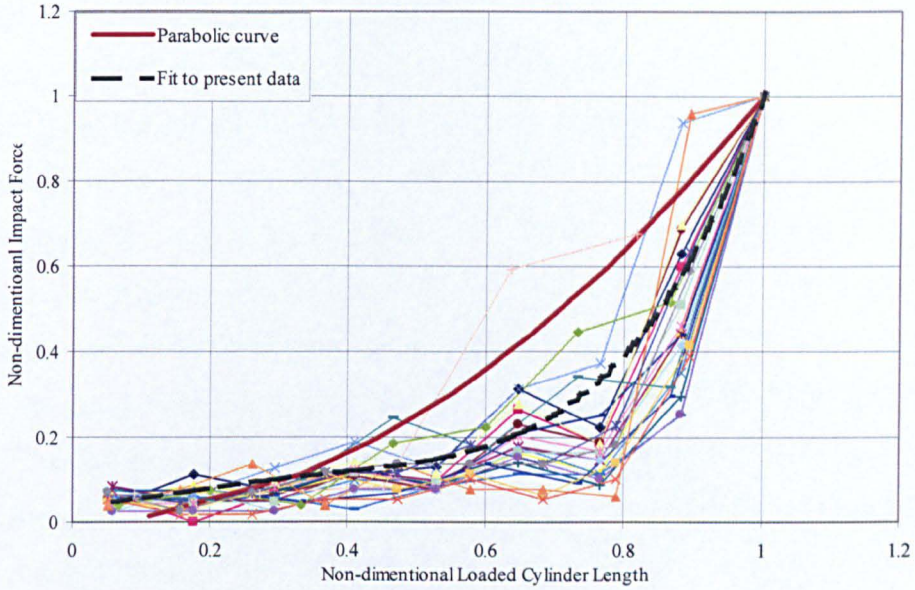

Figure 7.9 Non-dimensionalized distribution of impact force along the loaded length

Generally the maximum impact pressure can be predicted by

$$\frac{1}{2}\rho C_p V_I^2 \tag{7.2}$$

where ρ is the fluid density, 1000 kg/m^3 for water

C_p is the impact pressure coefficient

V_I is the impact velocity, for breaking wave it equals wave celerity c

From previous calculation in section 5.3 the expected impact pressure coefficient C_p for the current cylinder is 0.5π (see Figure 5.14 and 5.15 for Z/D =1/4.08 and W/D = 1.0). This is the normally used theoretical value which is also based on the concept of a rate of change of momentum of a virtual mass impinging on the cylinder (Goda et al., 1966; Sawaragi and Nochino, 1984; Wiegel, 1982). To determine this from the experiments it is necessary to measure both the force and the velocity.

The impact velocity V_I (taken as the wave celerity c in our case) was measured first from the test video for 4 frequencies (see Table 7.1). This demonstrated a

considerable underestimates of celerity (1.25 - 1.51) by linear wave theory. A non-linear estimation of the breaking wave celerity was developed here by increasing the linear celerity according to the increased wavelength and breaking wave height where for the latter it was assumed that the velocity increased as the same proportion as the wave height (see Figure 7.10 and Figure 7.11 from Barltrop and Adams, 1990). The results of the ratios between the non-linear estimation and linear calculation are given in Table 7.2. The ratios between measured and linear calculated and ratios between non-linear estimation and linear calculation are shown in Figure 7.12, it can be seen that the non-linear estimation gave reasonably good results. The celerity can be predicted by the non-linear method with CoV of 0.014. There appear to be a trend of more underprediction with decreasing H_0/gT^2.

After determined the impact coefficient and impact velocity, the impact pressures can be predicted. The comparison between measured and predicted impact pressures by using the above C_p (0.5π) and impact velocities are given in Figure 7.13. The mean value of measured pressure/predicted pressure is 0.83, the standard deviation is 0.35 and the coefficient of variation is 0.417. From the test video these breaking wave impacts can be classified into three cases (see Figure 7.13): Case I: post-cylinder breaking, the wave front is still steepening just prior to contact the cylinder; Case II: at-cylinder breaking, wave breaking occurs at the cylinder, the corresponding impact pressures are highly impulsive near the wave crest; Case III: pre-cylinder breaking, wave breaking occurs prior to impact on the cylinder. The typical time histories for the above three cases are given in Figure 7.14. By eliminating those cases in which breaking didn't occur at the cylinder, the results improved (see Figure 7.15). The mean value of measured pressure/predicted pressure then becomes 1.03, the standard deviation is 0.28 and the coefficient of variation is 0.27. These results are similar to the results getting from the FPSO tests, where the coefficient of variation of measured pressure/predicted pressure is also 0.27. The coefficient of variation is large, but it is understandable. The GWK tests from BWIMCOST project have demonstrated

how sensitive wave impact loading is to the breaking conditions (Bullock and Obhrai, 2004). It has been found from current tests that a small change in the relative position between the cylinder and the breaking point may cause a very large difference in the impact pressure, even the repeat tests gave a coefficient of variation up to 0.32 for regular waves. For the highest case (measured about 80N), it could be the breaking occurred exactly at the front of the cylinder. The scatter was also caused by the estimation of C_p, which is calculated for a 45degree water surface moving across the cylinder, whereas during the test, from the video it can be seen that although most of the breaking waves have an upper front steepness about 45degree, there are also some breaking waves with steeper or less steep fronts, for those cases the value of C_p would be expected to be higher and lower.

Table 7.1 Measured and linear calculation of wave celerity

T (s)	H_0/gT^2	d/gT^2	$C_{measured}$ (m/s)	$C_{lin\ calculate}$ (m/s)	Ratio
2.5	0.0041	0.0049	2.5	1.66	1.506
2.273	0.0049	0.0059	2.375	1.648	1.444
2	0.0064	0.0076	2.25	1.629	1.382
1.667	0.0092	0.011	2	1.59	1.258

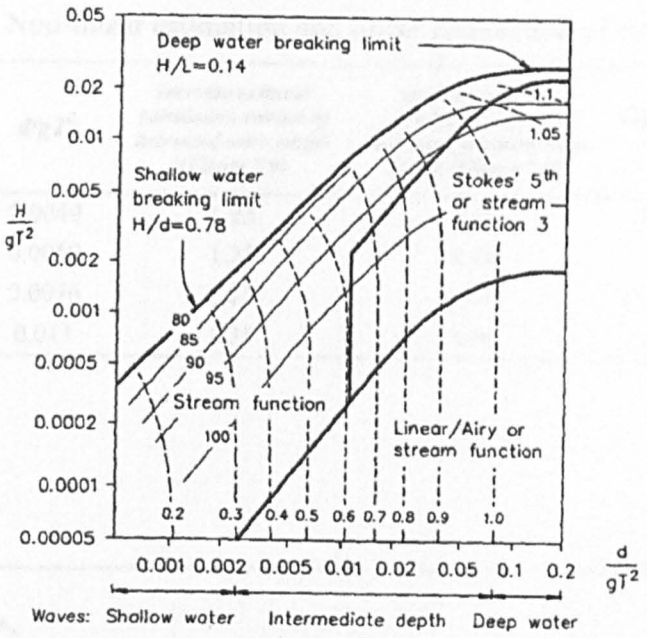

Figure 7.10 Wavelength from Airy theory as % of theory (solid line) and wavelength of theory as a proportion of ($fT^2/2\pi$) (broken line)

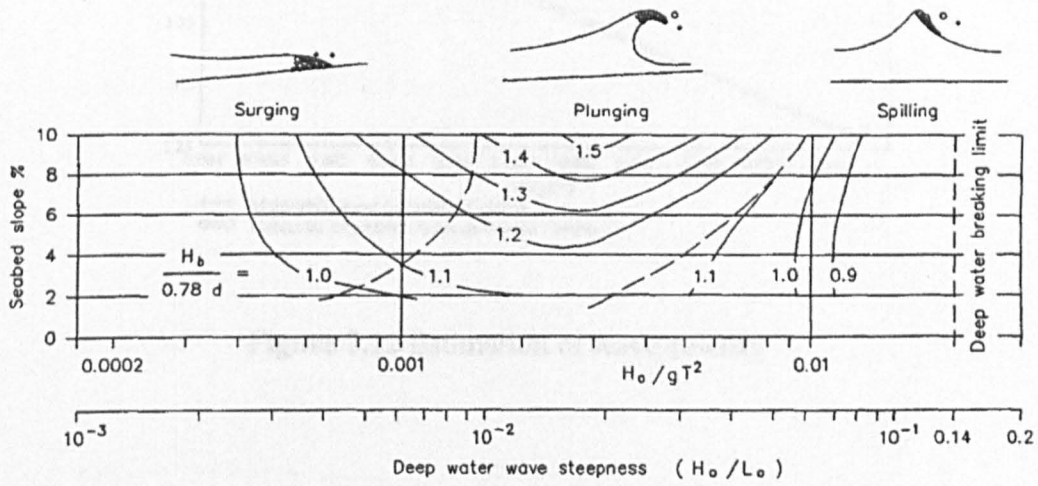

Note: 0.78d is the limiting height of a regular wave.

Figure 7.11 Increase in wave height over limiting height regular waves (Iversen, 1953) related to breaking wave type, wave steepness and seabed slope (Patrick and Wiegel, 1955)

Table 7.2 Non-linear estimation and linear calculation of wave celerity

T (s)	H_0/gT^2	d/gT^2	*Increase to linear calculation caused by increased wave length (Figure 7.9)*	*Increase to linear calculation caused by increased breaking wave height (Figure 7.10)*	*Calculated Ratio*	*Measured Ratio*
2.5	0.0041	0.0049	1.25	1.17	1.462	1.506
2.273	0.0049	0.0059	1.25	1.14	1.425	1.444
2	0.0064	0.0076	1.25	1.1	1.375	1.382
1.667	0.0092	0.011	1.25	1.01	1.262	1.258

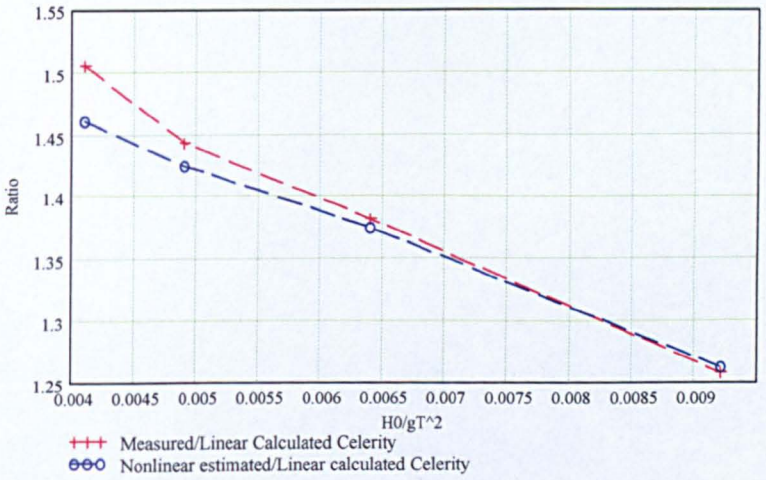

Figure 7.12 Estimation of wave celerity

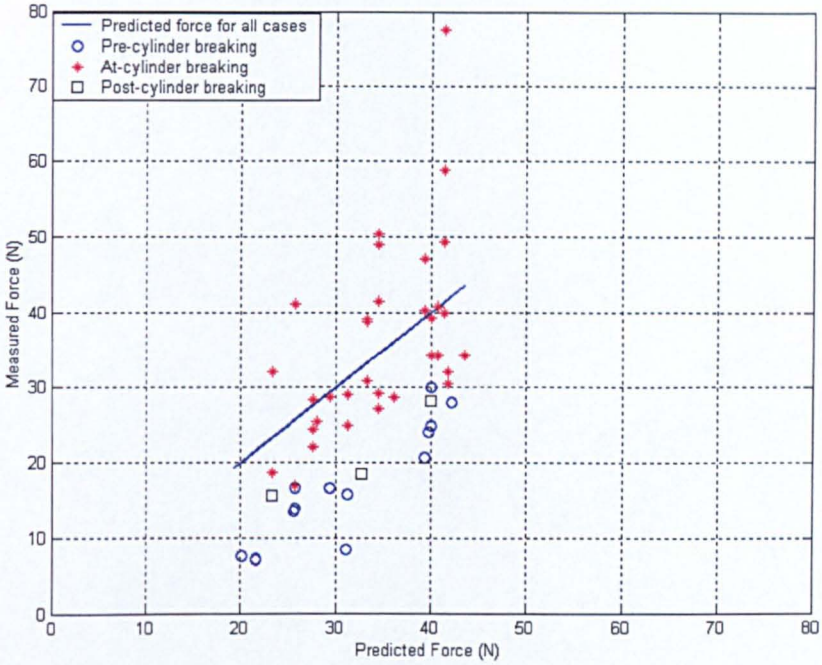

Figure 7.13 Measured and predicted forces

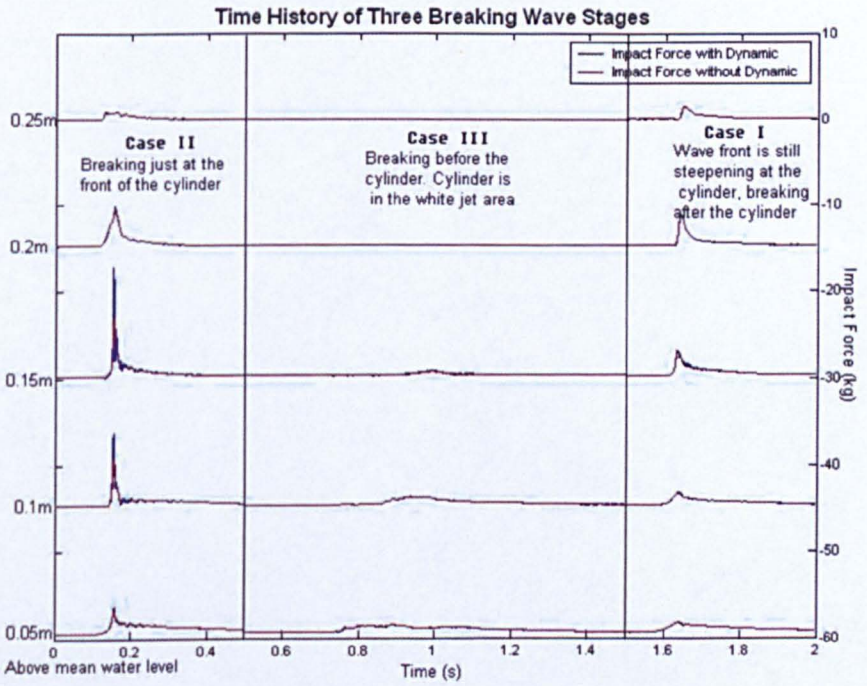

Figure 7.14 Typical time histories for three breaking wave cases

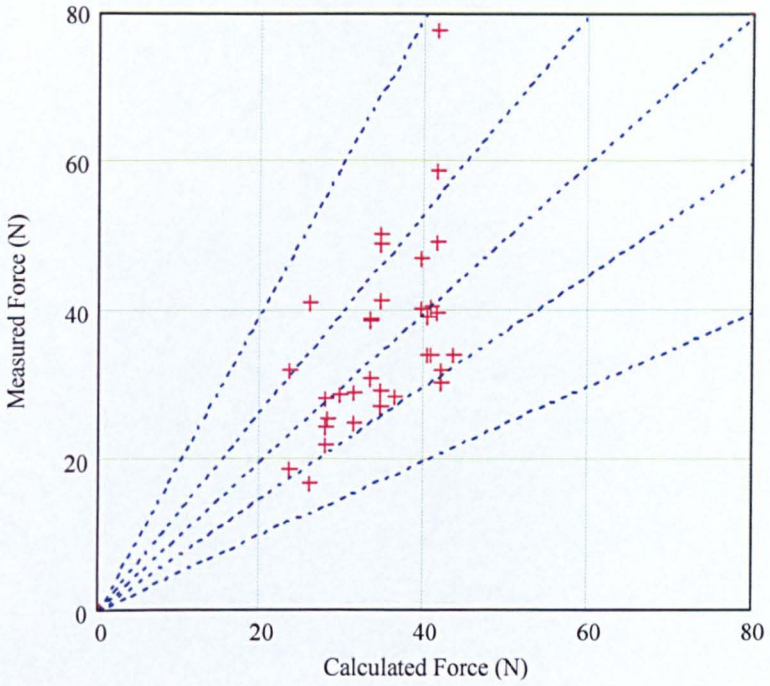

Figure 7.15 Measured and predicted forces from waves breaking at the cylinder

8 Conclusions

8.1 Summary

During this work the steep wave impact pressures and the structural dynamic response on FPSO bows are studied using two 1/80 scale instrumented models and time domain simulation. Some additional experiments on cylinder in shallow water breaking waves were also performed. The nature of the waves causing large impacts and the impacts themselves are discussed. Simplified design rules for curved bows are proposed. The rules account for the effect of the size of the loaded area on the average pressure and the rise and decay times of the average pressure and hence the dynamic amplification of the response.

8.2 Waves

8.2.1 Uni-directional seas

The bow impact model tests required the generation of large steep fronted deep water waves in the test tank. Two options were:

i. To run long simulations in random environments and to wait for large steep waves to appear.
ii. To pre-calculate using a linear theory, an average shape of a 1/100 year 1/3hour large high-steep fronted wave groups and to instruct the wave maker to generate that shape in the tank at the position of the model and to let the tank introduce the nonlinearities expected with steep waves.

Both options were used although long sequences were broken up to avoid the build up of reflected waves.

The theory for the wave groups (ii) was developed as part of the work. The balance between height and steepness that would produce the largest load with a given probability of occurrence was determined during the tests.

The balance is essentially between an alignment of crests, that results in a high wave, and an alignment of front faces and a bias towards higher frequencies, that results in a steep fronted wave.

In practice in steep sea-states a wave group that is 'balanced' or 'focused' to produce a high crest height will give the largest impact loads. As the sea-state steepness decreases so the steepness of the extreme slapping wave group will increase. The notionally steepest wave group will not always give the highest slap pressures because it may well have broken before the impact, so reducing the slap pressures.

The average slap force results from the wave groups were in good agreement with the most probable maximum values that were obtained, both experimentally and theoretically, from the random sequences based on the same sea state.

A further theoretical development was to derive a new method for generating a nearly random time history that has a required extreme at a given time and place and forms a conceptual bridge between the purely random and the deterministic methods. In practice it was found difficult to use constrained random waves in the tank because the model's slowly varying drift response meant that the bow was not in the correct place when the extreme event arrived. This was less of a problem with wave groups because the slow drift response does not have time to build up and is not a problem with purely random waves because there is no particular target position for them.

For the shallow water case the linear new wave theory didn't work well, partly because of the linear calibration of the wavemaker. The regular waves breaking in shallow water gave largest impacts.

8.2.2 Spread seas

All the tank testing and most of the theoretical work was performed in uni-directional waves.

A small desk study was undertaken to attempt to predict the nature of extreme wave slap events in spread seas as defined by a Mitsuyasu-Goda (1976) spreading function. The results, though not yet confirmed by model tests, suggested a very considerable reduction in maximum slap loading because a steeper and therefore lower sea state is required to produce the same type of breaking wave. The maximum reduction occurs in sea state steepnesses greater than 1/15 and is about 35% (see Figure 6.5).

8.2.3 Average, critical for slap, wave shapes in different sea states

From the experiments it is now possible to predict in a given steep sea state which form of extreme group will, on average, be the best predictor of the extreme 1 in 3hour slap force.

From a theoretical extension of the experimental work a further type of wave group is predicted which is expected to cause the largest loads in the less steep seas. This wave group has a 'partial' breaking wave, composed of higher wave frequencies in the sea-state that is overtaken and translated up or down by the lower frequency non-breaking wave components. When translated upwards the velocity and celerity is increased by the longer period non-breaking waves. The

sea state steepnesses for which each type of wave is expected to give the worst loads are shown in Figure 6.1.

In shallow war the conclusion is simpler: the highest wave groups result in the worst loads.

8.3 Experiment models

The FPSO models were built at a scale of 1:80 and were about 3.2m long to investigate the impact on FPSO bows. They were segmented along their length (to allow the measurement of hull girder bending) and in two or three parts in the bow (to allow the measurement of overall bow impact forces, or more accurately the bow response to bow impact loads). They also had arrays of pressure transducers built into the bow for local pressure measurement.

The Schiehallion model was built first. This model produced very useful bow force and hull girder bending data but the pressure transducer results were found to be very high but to vary very rapidly over the hull. This was because the areas of high pressure are typically very small so a pressure transducer may or may not be subject to the high pressure and the measured pressure on a loaded area that is much smaller than a structural component is not useful for design.

The Loch Rannoch model was built second and with the better understanding of the problem, pressure panels that were of similar size to stiffened panels on the bow were designed and incorporated into the model. Also, by inspection, the conventional bow shape was likely to be most highly loaded in waves coming at an angle to the bow, whereas for Shiehallion the worst direction was almost certainly in head seas. The Loch Rannoch instrumentation was therefore refined so that the bow component forces were measured in six degrees of freedom instead of the three degrees of freedom for Schiehallion.

To study the shoaling breaking wave load, a segmented aluminum cylinder model with 40 segments (20 for the front of the cylinder and 20 for the back) was built with the bottom fitted on a 1:20 slope ramp. Inside each 50mm high segment there are strain-gauged bars to measure the total force on each segment during an impact (forces acting on the front and back of the cylinder are separately measured).

8.4 Test results

The FPSO test results covered a range of steeper sea states and types of extreme wave group within those sea states. For each test the measurements included:

20 Panel pressures (Loch Rannoch only)

8 Local pressures,

12 Bow forces and moments for Loch Rannoch, 9 for Schiehallion

Hull girder bending

FPSO position

Longitudinal and vertical bow accelerations

Wave profile

Videos of the tests were also recorded.

A high steep-fronted wave impact, from the video, is shown in Figure 8.1.

The main outcome of the FPSO tests was:

- Measurement of dynamic response and estimates of forces on the whole bow and on a variety of areas.
- An understanding of the different types of wave that would give the worst impacts in different steep sea-states.
- A relationship between the extreme events and the 'underlying' linear theory, in particular a relationship between the linearly predicted particle acceleration and the ratio of (wave front steepness in tank tests)/(wave front steepness from linear theory)

- A pressure – loaded area relationship which was approximately of the form $p \propto A^{-0.5}$.

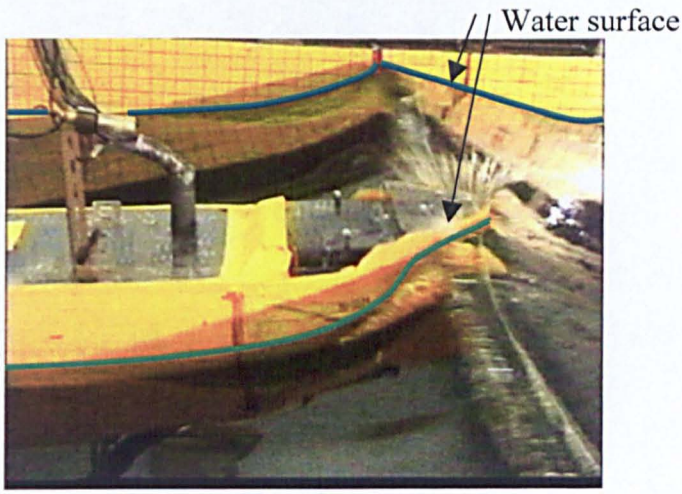

Figure 8.1 High steep-fronted wave impact

The total force on each segment of the cylinder and the wave profile at the cylinder have been measured. An estimation method of the breaking wave celerity has been developed based on the measured values. The estimation has taken into account the influence from the increase of wavelength and breaking wave height. The impact coefficient was calculated using the mathematical model developed here. As a result the impact pressure can be predicted by $\frac{1}{2}\rho C_p V_I^2$. The comparison between measured and predicted pressures has been made. The results show a lot of scatter, with a coefficient of variation 0.417 probably because of the great sensitivity of breaking wave impact to the position and shape of the breaking wave. In deep water we could focus the waves on the structure. In shallow water the waves breaking is primarily dependent on the seabed.

8.5 Mathematical models

Several mathematical models were used to help understand the breaking waves and the impact process. An empirical mathematical model was developed for the bow impact. This used results of cylinder impact and wedge impact from a strip model in conjunction with an empirical modification to linear random wave theory (based on the tests) to steepen the wave fronts and increase the particle kinematics in the near breaking waves. The ship motion itself was calculated using linear random wave theory. The calculated pressures were then built up from:

$$Pressure = ambient\ wave\ pressure + v\mathrm{d}m_v/\mathrm{d}t + m_v\mathrm{d}v/\mathrm{d}t + ma \qquad (8.1)$$

where: v is the particle velocity,

m_v is the hydrodynamic added mass,

m is the structural mass and

a is the hull acceleration.

A measured and predicted time history are shown in Figure 8.2. The $v\mathrm{d}m_v/\mathrm{d}t$ results (large slap forces) were very sensitive to small differences eg in the calculation of the position of the vessel relative to the waves. The model does not provide a precise time step by time step agreement with the model test results but it does show the same phenomena and the overall statistics of the response are reasonably good.

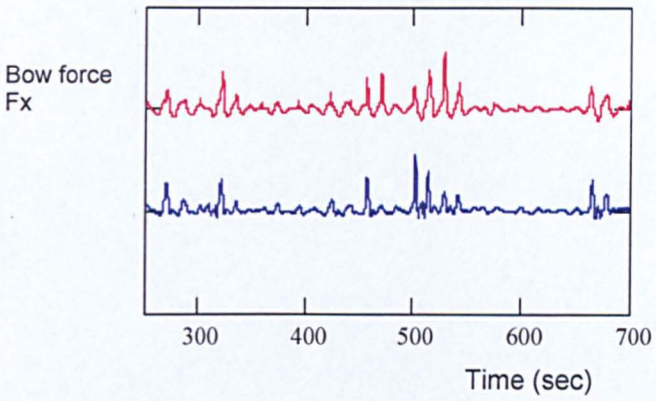

Figure 8.2 Bow force time histories: Measured (above) and Calculated (below)

This model has also demonstrated that the wave groups are a good representation of extreme sea conditions.

The model could also be useful for predicting bow impact forces however a method (which uses second order wave theory in conjunction with Marin's flat bow data and this work's curved bow data, both in conjunction with a simpler, impulse based loading model) has been implemented as programme BOWLAB in the SAFE-FLOW project. In practice simpler rule based methods (see Chapter 6), which have been calibrated using the model tests, full scale data and the mathematical models, are likely to be more attractive to designers.

8.6 Design Guidance

The types of wave that are likely to be critical for bow impact loading are shown in Figure 6.1.

The impact pressures on an area of width W and height Z of the bow can be calculated using a formula:

$$p = \frac{1}{g} C_p E(S_{ea}) F(W) G(Z) V_I^2 \; DAF \tag{8.2}$$

where

C_p is a constant

E depends on the sea state steepness (S_{ea}) and whether or not spreading is to be taken into account

F depends on the width of the area of plating to be checked

G depends on the height of the area of plating to be checked

V_I is the geometric mean of the horizontal wave particle velocity and the vertical surface velocity

DAF is a predicted dynamic amplification factor for the loaded area.

Formulae for C_p, E, F, G, V_I and DAF are given in this thesis.

The structural response estimate is subject to a relatively high level of uncertainty (coefficient of variation of measured/predicted nearly 40% with dynamic response, 27% excluding dynamic response) which will affect the safety factors required to obtain a required structural reliability. Preliminary indications from this work suggest that for a ductile structure in bending a partial load factor of about 1.7 is required (which may be reduced for less severe consequences of failure). Higher values are required for shear. This load factor should be used in conjunction with 100 year return period pressures and a first yield structural design criterion with a material partial safety factor of 1.15. This is addressed further in the SAFE-FLOW project.

The impact pressures on a wind turbine support structure can be calculated using a formula:

$$p = \frac{1}{2}\rho C_p V_I^2 \tag{8.3}$$

where ρ is the fluid density

C_p is the impact pressure coefficient, which can be determined for different size of structure

V_I is the impact velocity, for breaking wave it equals wave celerity c, which can be estimated by increasing the linear calculation with the effect from increased wave length and increased breaking wave height.

The calculations of C_p and V_I are given in the thesis. The results have been compared with the FPSO bow tests.

8.7 Discussion

All the work reviewed in Chapter 1 for breaking wave loads are for vertical walls, breakwaters or caissons. There's no such work done on the real ship bow. The work here on the FPSO bows impacts has derived a simple slam coefficient type formula for easy application. The formula accounts for the effect of the size of the loaded area on the average pressure and the rise and decay times of the average pressure and, hence, the dynamic amplification of the response at the bow. The slam coefficient C_p was determined empirically by taking tests results for 'critical' wave cases and a wide range of panel areas and then finding the mean value. So the application of this formula to other structure cases need to be verified by more experiments.

For circular or small dimension pile structures (wholly or semi-immersed), design guidelines such as BS 6394 Pt 1 (2000), EAU (1996) and the CEM (USACE, 2002), refer to Morison's equation for calculations of forces due to non-breaking waves. The comparison between measurement and calculation for non-breaking

waves has been done. By using the measured water surface elevation, the results agree reasonably well. The local wave impact pressures caused by a wave breaking directly onto a vertical structure have been studied by Minikin (1950, 1963) in the early 1950s. Allsop (2000) addressed the problem of impact adequately recently. The now superseded *Shore Protection Manual* (CERC, 1984) gave a conservative approach to determining the impact forces using Minikin's method for the estimation of forces and overturning moments arising from an assumed pressure distribution. There have been other studies carried out like those of Kirkgoz (1991, 1995) but the general consensus is that conflicts remain in accurately estimating the breaking wave pressure distributions for realistic conditions. The main problem are in identifying the magnitudes and durations (both are needed) of wave impact loads and then applying those loads using dynamic response characteristics of the structure to derive effective loads (McConnell et al., 2004). The work here has developed a method to estimate the breaking wave celerity ($c=V_I$ for breaking wave), consequently the impact force can be calculated by the most widely used formula $p=\frac{1}{2}\rho C_p V_I^2$. The proposed method to predict the impact force is relatively simpler that others.

8.8 Future work

Ideally the following additional work is required:

For deep water (FPSO bows):

a. Measure slap forces in less steep seas, to check the theoretical partial breaking wave predictions
b. Measure slap forces in directionally spread seas, to check the theoretical spread sea breaking wave predictions
c. Use smaller steepness increments in the vicinity of the critical wave cases to identify more accurately the sea-state ranges for the different critical wave types.

d. Use long downward looking radar data sets to check the critical wave shapes derived in this work
e. Continuation of the Schiehallion monitoring would be well worthwhile, to build up a reliable, long term data set
f. Measure or hindcast wave/sea-state data to be used with the Schiehallion measurements

For shallow water (wind turbine support structure):

g. Calibrate the wavemaker for generating shallow water waves and run the new waves again in the tank to study the difference with deep water new waves
h. Generate more braking waves in shallow water with different beach slopes to verify the estimation method of celerity developed here
i. Further work is needed on the statistics of the likely breaking loads at a given point in the sea
j. The effect of the reverse current from the previous broken waves needs to be assessed. The local bathymetry and wave direction will have an important effect.

9 References

Allen, R. G. and Jones, R. R. (1987) 'A simplified method for determining structural design-limit pressures on high performance marine vehicles' *AIAA/SNAME Advanced Marine Vehicles Conf.*, San Diego

Allsop, N. W. H. (2000) Wave forces on vertical and composite walls. Chapter 4 in *Handbook of coastal Engineering*, pp. 4.1-4.47, ed. J. Herbich. McGraw-Hill, New York

Allsop, N. W. H., Vicinanza, D. and McKenna, J. E. (1996) 'Wave forces on vertical and composite breakwaters' *Strategic Research Report. Hydraulic Reseearch Wallingford*, SR443, Wallingford, U.K., 94pp

Arai, M. and Matsunaga, K. (1989) 'A numerical and experimental study of bow flare slamming' *J. Soc. Nav. Arch. Japan*, 166 (in Japanese)

Bagnold, R. A. (1939) 'Interim report on wave pressure research' *J. Ind. Civil Eng.*, 12: 202-226

Baldock, T. E., Swan C., *et al.* (1995). 'A laboratory study of nonlinear surface-waves on water' *Phil Trans Roy Soc,* 354(1707): 649 – 676

Barltrop, N. and Adams, A., (1991). *Dynamics of fixed marine structures.*

Belytschko, T. and Mullen, R. (1981) 'Two dimensional fluid-structure impact computations with regulation' *Computer Methods in Applied Mechanics and Engineering*, 27

Blachmore, P. A. and Hewson, P. J. (1984). 'Experiments on full scale wave impact pressures' *Coastal Engineering,* 8: 331-346

Bradbury, A. P. and Allsop, N. W. H. (1988) 'Hydraulic effects of breakwater crown walls' *Proc. Confference on Design of Breakwaters*, 385-396, Institution of Civil Engineers, Thomas Telford, London

Bredmose, H., Peregrine, D.H., *et al.* (2003) 'Wave impact and aerated water', *18th IWWFB*, Le Croisic (France)

Buchmann, B., Skourup, J., *et al.* (1998). 'Run-up on a Structure due to Second Order Waves and a Current in a Numerical Wave Tank' *Applied Ocean Research,* 20: 297-308

Buchner, B. (1994). 'On the effect of green water impact on ship safety (A pilot study)' *International Conference on Ship and Marine Research*, Rome, Italy

Buchner, B. (1995). 'On the Impact of Green Water Loading on Ship and Offshore Unit Design' *Proc. PRADS'95*, The Society of Naval Architects of Korea, Seoul, Korea, Vol.1

Buchner, B. and Voogt, A. (2000) 'The Effect of Bow Flare Angle on FPSO Green Water Loading' *OMAE*, New Orleans, LA, USA. Paper No. OSU OFT-4092

Bullock, G. N., Crawford, A.R., et al. (2001). 'The influence of air and scale on wave impact pressures' *Coastal Engineering*, 42(4): 291-312

Bullock, G. N. and Obhrai, C. (2004) 'Wave impact loads at large and full scale', Presented at *'Land-sea margins: wave overtopping and protection along the coastline' ICE Maritime Board Seminar*

British Standards Institution (2000) *British Standard Code of Practice for Maritime Structurs. Part 1: General Criterial.* BS 6349: Part 1: 2000 (and Amendments 5488 and 5942). British Standards Institution, London.

Camfield, F. E. (1991) 'Wave forces on wall' *Journal of Waterway, Port, Coastal, and Ocean EngineeringDivision, American Society of Civil Engineers* 117 (1): 76-9.

Campbell, I. M. C. and Weynberg, P. A. (1980). *Measurement of parameters affecting slamming,* Report No. 440, Wolfson Unit for Marine Technology and Industrial Aerodynamics, University of Southampton

CERC (1984) *Shore protection manual.* U.S. Army Corps of Engineers

Chakrabarti, S. K., (1990). *Nonlinear methods in offshore engineering*, Elsevier, 97-99

Chan, E. S., Cheong, H. F., *et al.* (1995). 'Laboratory study of plunging wave impacts on vertical cylinders' *Coastal Engineering,* 25(1-2): 87-107

Chanson, H., Aoki, S., *et al.* (2002) 'Unsteady air buble entrainment and detrainment at a plunging breaker: dominant time scales and similarity of water level variations' *Coastal Engineering*, 46: 139-157

Chanson, H. and Cummings, P. D. (1994) 'Effects of plunging breakers on the gas contents in the oceans' *Mar. Technol. Soc. J.,* 28(3): 22-32

Chaplin J. R., Greated C. A., *et al.* (1992). *Breaking wave forces on a vertical cylinder.* UK Dept of Energy, Rept OTH-90-324

Chaplin J. R. (1996). 'On frequency-focusing unidirectional waves' *Int Journal of Offshore and Polar Engng.*, 6(2): 131 - 137

Chuang, S. L. (1967) 'Experiments on slamming of wedge-shaped bodies', *Journal of Ship Research*, 11

Chuang, S. L. (1969) 'Theoretical investigations on slamming of cone-shaped bodies', *Journal of Ship Research*, 13

Clauss G. F. and Kühnlein W. L. (1997). 'Simulation of design storm wave conditions with tailored wave groups' *Proc 7th Int Offshore and Polar Engng Conf*, 228 – 237

Clauss G. F. and Kühnlein W. L. (1999). 'Task related wave groups for seakeeping tests or simulation of design storm waves' *Appl Ocean Res*, 21: 219 - 234

Cointe, R. (1989) 'Two-dimensional water-solid impact', *Journal of offshore mechanics and Arctic engineering*, 111

Cuomo, G. and Allsop, W. (2004) 'Wave impacts at sea walls', *Proc. 29th Internat. Conf. Coastal Engng.*, Lisbon, Ed. J.McK. Smith, World Sci. 4: 4050-4062.

Daniil, E. I. and Gulliver, J. (1991) 'Influence of waves on air-water gas transfer' ASCE, *Environ. Eng.*, 117(5): 522-540

de Jong, P. R., Vugts, J., *et al.* (1996) 'Extreme hydrodynamic load calculations for fixed steel structures.' *Proc. Offshore Mechanics and Arctic Engineering (OMAE)*, I-B

Denny, D.F. (1951) 'Further experiments on wave pressures' *J. Inst. Civ. Engrs Loud*, 35: 330-345

Drake, K. (1997). 'Wave profiles associated with extreme loading in random waves' *RINA International Conference: Design and Operation for Abnormal Conditions*, Glasgow, Scotland.

EAU (1996) *Recommendations of the Committee for the Waterfront Structures, Harbours and Waterways.*

Engle, A. and Lewis, R. (2003). 'A comparison of hydrodynamic impacts prediction methods with two dimensional drop test data' *Marine Structures* 16: 175-186.

Ferrant, P. (1999). 'Fully Nonlinear Diffraction of Regular Waves by a Multicolumn Structure' *ISOPE.*

Führböter, A. (1985) 'Model and prototype tests for wave impact and run-up on a uniform 1:4 slope' *Coastal Engineering*, 10: 49-84

Fukuda, J., Ikegami, K., *et al.* (1973) 'Predicting the long term trends of loads on deck due to shipping water' *Journal of West Japan Society of Naval Architects*, 45

Gaillard, D. D. (1905) 'Wave action in relation to engineering structures' *Engineering News,* LIII(8): 189-194

Goda, Y. (1958) *Random Seas and Design of Maritime Structures,* University of Tokyo Press, Tokyo, Japan.

Goda, Y., Haranaka, S. and Kitahata, M. (1966) 'Study on impulsive breaking wave pressures on vertical cylinders', *Rep. Port Harbour Res. Inst.*, 6(5): 1-30

Greco, M., Faltinsen, O. M., *et al.* (2000) 'Basic studies of Water on Deck'. *Proc. 23th Symp. On Naval Hydrodynamics*, National Academy Press

Greenhow, M. (1987) 'Wedge entry into initially calm water' *Applied Ocean Research*, 9

Gu, M, Miao, Q., *et al.* (1993) 'Prediction of relative motion and deck wetness around ship bow' *Shipbuilding in China*, 1 (in Chinese)

Harland, L. A., Vugts, J. H., *et al.* (1996) 'Extreme responses of non-linear dynamic systems using constrained simulations' *Proc. Offshore Mechanics and Arctic Engineering (OMAE),* I-A: 193-200

Harland, L. A., Taylor, P. H., *et al.* (1997) 'The variability of extreme forces on offshore structures' *Proc. Behaviour of Off-Shore Structures (BOSS),* 221-235

Hiroi, I. (1919) 'On a method of estimating the force in waves' *Bulletin of Engineering Department*, Tokyo Imperial University, 10(1): 19

Hiroi, I. (1920) 'The force and power of waves' *The engineer* August. 184-187

Hodgson, T, 2003, Private communication

Hoffman, D. and Maclean, W. M. (1970) 'Ship model study of incidence of shipping water forward' *Marine Technology*

Hong, S. Y., Lee, P. M., *et al.* (1993) 'Experimental study on the deck wetting of a container ship in irregular head waves' *Selected Papers of the Society of Naval Architects of Korea,* 1(1): 37-44
Howison, S. D., Ockendon, J. R., *et al.* (1991) 'Imcompressible water-entry problems at small deadrise angles' *Journal of Fluid Mechanics*, 222

Huang, E.W., Beynet, P.A., *et al.* (1993) 'FPSO Model Tests and Analytical Correlation' *OTC*, 117-124

Hull, P., Müller, G. and Allsop, N. W. H. (1998) 'A vertical distribution of water impact pressures for design purposes' *Research Report, MAST III, PROVERBS-Project: Probabilistic Design Tools for Vertical Breakwaters*, Belfast, Northen Ireland, 16

Ito, Y. (1971) 'Stability of mixed type breakwaters – A method of probable sliding distance' *Coastal Engineering in Japan*, JSCE, Tokyo, 14: 53-61

Jensen, O. J. (1984) *A Monograph on Rubble Mound Breakwaters*, Danish Hydraulic Institute, Denmark.

Jonathan, P., Taylor, P. H., *et al.* (1994) 'Storm wave in the northern north sea' *Proc. Behaviour of Off-Shore Structures (BOSS),* 481-494

Karman, T. von (1929) 'The impact on seaplane floats during landing' *NACA TN*, 321

Kawakami, M. and Tanaka, K. (1975) 'On shipping of green seas and whipping vibrations of a large full ship' *Transactions of the West Japan Society of Naval Architects,* No.50

Kawakami, M. and Tanaka, K. (1977) 'Stochastic prediction of impact pressure due to shipping green seas on fore deck of ship' *Transactions of the West Japan Society of Naval Architects,* No.53

Kirkgöz, M. S. (1991). 'Impact pressure of breaking waves on vertical and sloping walls' *Ocean Engineering,* 18(1-2): 45-59

Kirkgöz, M. S. (1995). 'Breaking wave impact on vertical and sloping coastal structures' *Ocean Engineering,* 22(1): 35-48

Kirkgöz, M. S. and Mamak, M. (2004). 'Impulse modelling of wave impact pressures on vertical wall' *Ocean Engineering,* 31(3-4): 343-352

Kjeldsen, S. P. and Myrhaug D. (1997). 'Breaking waves in deep water and resulting wave forces', *Offshore Technology Conference*, OTC 3646.

Kriebel, D. (1992) 'Nonlinear Wave Interaction with a Vertical Circular Cylinder. Part II: Wave Run-up' *Ocean Engineering*, 19: 75-99

Larras, J. (1937) 'Le deferlement des lames sur les jetees vertical' *Annales des Ponts et Chaussees,* 107:643-680

McConnell, K. (1998) *Revetment systems against wave attack – a design manual*, London, U.K., Thomas Telford, 168

Maskew, B., Wang, M. L., *et al.* (1994). 'Comparison of calculated and measured loads on a flared body oscillating in free surface' *The 20th Symposium on Naval Hydrodynamics,* Santa Barbara, CA.

Mansard E. P. D. and Funk E. R. (1982). 'A new approach to transient wave generation' ASCE, *Proc 18th Int Conf on Coastal Eng.*, 710 - 724

Minikin, R. R. (1950) *Wind, Waves and maritime structures: studies in harbour making and in the protection of coasts.* Charles Griffin, London

Minikin, R. R. (1963) *Wind, Waves and maritime structures: studies in harbour making and in the protection of coasts.* 2nd edition, Griffin, London

Mitsuyasu, H. (1966) 'Shock pressure of breaking wave' *Coastal Engineering*, 1

Mitsuyasu H. and Mizuro S., (1976). 'Directional spectra of ocean surface waves' *Proc 15th Conf Coastal Eng*, 1

Mogridge, G. R. and Jamieson, W. W. (1980) 'Wave impact pressures on composite breakwaters' *Proc. 17th Conference of Coastal Engineering*, ASCE, 2: 1829-1848

Müller, G. and Whittaker, T. J. T. (1996). 'Evaluation of design wave impact pressures', *Journal of waterway, Port, Coastal, and Ocean Engineering*, 122(1): 55-58

Myrhaug, D. and Kjeldsen, S. (1987). 'Prediction of occurrences of steep and high waves in deep water' *J. Waterway, Port, Coast. and Ocean Eng.* 113(2): 122–138.

Neidzwecki, J. N. and Duggal, A. S. (1992) 'Wave Runup and Forces on Cylinders in Regular and Random Waves' *Journal of Waterways, Port, Coastal and Coastal engineering*, ASCE, 118: 615-634

Newton, R. N. (1959) 'Wetness related to freeboard and flare' *Summer Meeting RINA,* Paper No. 3

Ochi, M. K. (1964) 'Extreme behaviour of a ship in rough seas' *Annual meeting of the Society of Naval Architects and Marine Engineers*, 143-202

Ogawa, Y., Taguchi, H., *et al.* (1998) 'A prediction method for the shipping water heights and its load on deck' *Practical Design of Ships and Mobile Units (PRADS)*, The Hague

Oumeraci, H., Klammer, P., *et al.* (1993). 'Classification of breaking wave loads on vertical structures', *Journal of waterway, Port, Coastal, and Ocean Engineering*, 119(4): 381-397

Oumeraci, H. and Kortenhaus, A. (1997) 'Wave impact loading – tentative formulae and suggestions for the development of final formulae' *Proceedings 2nd Task 1 Workshop, MAST III, PROVERBS-Project: Probabilistic Design Tools for Vertical Breakwaters,* Edinburgh, U.K., Annex 1.0.2, 13pp, 3 Annexes

Partenscky, H.W. (1988) 'Dynamic forces due to waves breaking at vertical coastal structures.' *Proceedings of 21st Conference on Coastal Engineering.* ASCE, pp. 2504–2518.

Pedersen, J. (1997) Dynamic Response of Caisson Breakwaters Subjected to Impulsive Wave Loading - Design Diagrams for Dynamic Load Factors' *Proceedings*, Annex 2 C, 1st overall Workshop, EU-MASTIII-project PROVERBS, Las Palmas, Gran Canaria, Spain.

Peregrine, D.H., Bredmose, H., *et al.* (2004) 'Violent water wave impact on walls and the role of air', *Proc. 29th Internat. Conf. Coastal Engng.*, Lisbon, Ed. J.McK. Smith, World Sci. 4: 4005-4017.

Price, W. G. and Bishop R. E. D. (1974). *Probabilistic Theory of Ship Dynamics.* Chapman and Hall Ltd., London

Rozario, J. B., Tromans, P. S., *et al.* (1993) 'Comparison of loads predicted using 'NEWWAVE' and other wave models with measurements on the Tern structure' *Wave Kinematics and Environmental Forces*, 29: 143-159

Rouville, M. A., Besson, P., *et al.* (1938) 'Etat actuel de etudes internationals sur les efforts dus aux lames (Current state of international studies on wave impact)' *Annales des Ponts et Chaussees*, 108: 5-113 (in French)

SAFE-FLOW, (2004). *Summary report on design guidance and assessment methodologies for wave slam and green water impact loading*, EU Project number GRD1 2000-25656.

Sainflou, M. 1928. 'Treatise on Vertical Breakwaters' *Annals des Ponts et Chaussee*, Paris, France (Translated by W. J. Yardoff, U.S. Army Corps of Engineers.)

Sawaragi, T. and Nochino, M. (1984) 'Impact forces of nearly breaking waves on a vertical circular cylinder', Coastal Eng. Jpn., 37: 249-263

Shore Protection Manual (SPM). 4th ed., 2 vols, US Army Engineer Waterways Experiment Station, Coastal Engineering Research Center, US Government Printing Office, Washington, DC.

Sogstad, B. E. (1995). 'A sensitivity Study of Hull Girder Wave Loads for Ship Shaped Oil Production and Storage Vessels' *OTC*, 7769:657-670

Stansberg, C. T. (1999). 'Nonlinear Air-Gap System Identification from Model Tests' *ISOPE*, 519-526

Standberg C. T. and Nielsen F. G. (2001). 'Nonlinear Wave-Structure Interaction on Floating Production Systems' *ISPOE*

Stavovy, A. B. and Chuang, S. L. (1976) 'Analytical determination of slamming pressure for high-speed vehicles in waves' *Journal of Ship Research*, 20

Sumitoshi M. and Katsuji T. (1996). 'Impact Wave Loads due to Slamming – A Review' *Ship Technology Research*, 43: 139-154

Swart, D. H. and Loubser, C. C. (1978). 'Vocoidal theory for all non-breaking waves' *Proc. Conf. Coastal Eng.*, 16: 467-486

Swift, R. H., (1989). 'Prediction of breaking wave forces on vertical cylinders' *Coastal Engineering*, 13: 97-116

Takahashi, S. and Hosoyamada, S. (1994) 'Hydrodynamic Characteristics of Sloping Top Caissions' *Proceedings of International Conference on Hydro-Technical Engineering for Port and Harbour Construction*, Port and Harbour Research Institute, Japan, 1: 733-746.

Takahashi., S., Tanimoto, K., and Shimosako, K. (1990) 'Wave and Block Forces on a Caisson Covered With Wave Dissipating Blocks' *Report of Port and Harbour Research Institute*, Yokosuka, Japan, 30(4): 3-34 (in Japanese).

Takahashi, S., Tanimoto, K., and Shimosako, K. (1994a) 'A Proposal of Impulsive Pressure Coefficient for Design of Composite Breakwaters' *Proceedings of the International Conference on Hydro-Technical Engineering for Port and Harbor Construction,* Port and Harbour Research Institute, Yokosuka, Japan, 489-504.

Takahashi, S., Tanimoto, K., and Shimosako, K. (1994b) 'Wave Pressure on Perforated Wall Caissons' *Proceeding of International Conference on Hydro-Technical Engineering for Port and Harbor Construction*, Port and Harbour Research Institute, Yokosuka, Japan, 747-764.

Takemoto, H. (1984) 'Water impact test of a wedge with rectangular plates and its analysis' *J. Soc. Nav. Arch. Japan*, 156 (in Japanese)

Tanimoto, K., and Kimura, K. (1985) 'A Hydraulic Experimental Study on Trapezoidal Caisson Breakwaters' *Technical Note No. 528*, Port and Harbour Research Institute, Yokosuka, Japan (in Japanese).

Tanrikulu, A. K., Kirkgöz, M. S., *et al.* (2002). 'Theoretical and experimental investigation of a vertical wall response to wave impact' *Ocean Engineering*, 29(7): 769-782

Tasai, F. (1961) 'Wave height at the side of two-dimensional body oscillating on the surface of a fluid' *Report of the Research Institute for Applied Mechanics*, Kyushu University, 9(35)

Tasaki, R. (1963) 'On shipment of water in head waves' *Tenth ITTC*, London

Taylor P. H., Jonathon P., *et al.* (1995). 'Time domain simulation of jack up dynamics with extremes of a Gaussian process' *OMAE*

Toyama, Y. (1993) 'Two-dimensional water impact of unsymmetrical bodies' *J. Soc. Nav. Arch. Japan*, 173 (in Japanese)

Tromans P. S., Anatürk A. R., *et al.* (1991). 'A new model for kinematics of large ocean waves – Application as a design wave' *Proc. First Int. Offshore and Polar Engng. Conf.*, 64 – 71

U.S. Army Corps of Engineers (2002) *Coastal engineering manual.* Engineer Manual 1110-2-1100, U.S. Army Corps of Engineers, Washington, D.C. (in 6 volumes). (http://bigfoot.wes.army.mil/cem001.html)

Van Dorn, W. G. (1978) 'Breaking invariants in shoaling waves' *Journal of Geophysics Research,* 83(C6): 2981-2988

Vicinanza, D. (1998) 'Azioni impulsive di un' onda frangente su una diga a paramento verticale di tipo composto' *XXVI Convegno di Idraulica e Construziono Idrauliche,* Catania, Italy, 12pp, In Italian

Wagner, H. (1932) 'Uber Stoss- und Gleitvorgange an der Oberflache von Flussigkeiten'. *Z. Angew. Math. Mech.* 12: 193-215.

Walkden, M. J., Hewson, P. J. and Bullock, G. N. (1996) 'Wave impulse prediction for caisson design.' *Proc. 25th Int. Conf. on Coastal Engineering.* ASCE, Orlando, USA. 2584–2597.

Wang, Z., Juncher Jensen, J., *et al.* (1998) 'On the effect of green water on deck on the wave bending moment' *PRADS'98*, The Hague

Watanabe, I. (1986a) 'Analytical expression of hydrodynamic impact pressure by matched asymptotic expansion technique' *T. West-Japan Soc. Nav. Arch.*, 71

Watanabe, I. (1986b) 'Theoretical investigation of wave impact loads on ships' *The 16th Symposium on Naval Hydrodynamics,* Berkeley.

Watanabe, I., Tanizawa, K., *et al.* (1988) 'An observation of bottom impact phenomena by means of high speed video and transparent model' *J. Soc. Nav. Arch. Japan*, 164 (in Japanese)

Watanabe, I., Tomita, H., *et al.* (1992) 'Winds and waves of the north pacific ocean (1974 1988)' *Papers of Ship Research Institute*, Supplement 14 (in Japanese)

Weggel, R.L. (1971) 'Discussion on: Shock pressures on coastal structures (by Kamel)' *J. Waterway Harbour Div.*, ASCE, WW3

Wiegel, R. L. (1982) 'Forces induced by breakers on piles', Proc. 18th Int. Conf. Coastal Eng., Cape Town. ASCE, New York, 1699-1715

Wienke, J., Sparboom, U., *et al.* (2001). 'Large-scale experiments with slender cylinders in breaking waves' *Proc. of 11th International offshore and Polar Engineering Conference,Stavanger,* Vol.IV

Wolfram, J. and Linfoot, B. (2000) 'Some experiences in estimating long and short term statistics for extreme waves in the North Sea' *Rogue Waves Workshop*

Wolters, G., Müller, G., *et al.* (2004) 'Field and large scale model tests of wave impact pressure propagation into cracks', *Proc. 29th Internat. Conf. Coastal Engng.*, Ed. J.McK. Smith, World Sci. Lisbon, 4: 4027-4039.

Zhao, C. T., Bai Y., *et al.* (2001). 'Extreme Response and Fatigue Damages for FPSO Structural Analysis' *ISOPE*, 17-22

Zhao, R. and Faltinsen O. M. (1996) 'Water Entry of Two-Dimensional Bodies' *Journal of Fluid Mechanics,* 246: 593-612

Appendix A: Tables and Figures of Data

The larger tables of results are included in this appendix to the results discussed in chapter 4. Smaller tables are included in the main report. The data presented is mainly the result after filtering to remove structural dynamics, of the pressure pads or bow sections. This is an approximate procedure that generally underestimates the applied pressure but it is very quick and useful for processing large quantities of data. The important results, that have been used to calibrate the design methodology, have been analysed by eye to more accurately separate the structural response. Typical filtered and original signals are shown in the time histories in Figures A4.1 to A4.4.

Table A4.1 Frequency cut-off sensitivity study

Loch Rannoch F.P.S.O.

Hs (m)	*Tz (s)*	*Sea State Steepness^{-1}*	*Frequency Cut-off*	*top segment impact*	*pressure transducer*	*pressure pads*	*Hs (m)*	*Tz (s)*	*Sea State Steepness^{-1}*	*Frequency Cut-off*	*top segment impact*	*pressure transducer*	*pressure pads*
14.887	11.8	14.73	2	5.6	2.22	85.0	15.670	11.8	14	2	7.1	2.68	192.8
14.887	11.8	14.73	2.25	3.4	3.93	53.1	15.670	11.8	14	2.25	3.9	6.01	71.3
14.887	11.8	14.73	3	1.5	2.33	43.9	15.670	11.8	14	3	1.6	2.46	37.8
14.887	11.8	14.73	5	0.6	2.27	26.1	15.670	11.8	14	5	0.8	2.49	17.8
16.610	11.8	13.21	2	3.5	2.6	38.3	17.394	11.8	12.6	2	2.8	2.67	31.7
16.610	11.8	13.21	2.25	3.5	4.60	43.9	17.394	11.8	12.6	2.25	3.3	4.29	39.0
16.610	11.8	13.21	3	2.0	2.84	35.6	17.394	11.8	12.6	3	2.3	3.08	35.0
16.610	11.8	13.21	5	1.2	2.49	30.0	17.394	11.8	12.6	5	2.1	2.64	28.9
18.647	11.8	11.76	2	2.5	2.65	27.8	16.226	12.8	15.8	2	2.9	242	36.7
18.647	11.8	11.76	2.25	2.7	4.54	27.7	16.226	12.8	15.0	2.25	3.5	441	62.3
18.647	11.8	11.76	3	2.9	2.63	35.0	16.226	12.8	15.8	3	2.3	234	123.3
18.647	11.8	11.76	5	2.0	2.56	43.3	16.226	12.8	15.8	5	0.6	258	35.0
17.080	12.8	15	2	6.5	235	58.0	18.105	12.8	14.14	2	11.1	210	130.0
17.080	12.8	15	2.25	6.1	443	141.3	18.105	12.8	14.14	2.25	8.1	457	105.3
17.080	12.8	15	3	2.6	239	126.0	18.105	12.8	14.14	3	2.7	228	129.4
17.080	12.8	15	5	0.7	213	23.0	18.105	12.8	14.14	5	0.9	239	48.9
18.959	12.8	13.51	2	5.0	215	96.7	20.325	12.8	12.6	2	3.2	236	35.0
18.959	12.8	13.51	2.25	5.2	424	81.5	20.325	12.8	12.6	2.25	3.7	425	32.1
18.959	12.8	13.51	3	3.0	230	64.4	20.325	12.8	12.6	3	3.5	221	57.8
18.959	12.8	13.51	5	1.8	255	42.8	20.325	12.8	12.6	5	2.2	264	72.2

Table A4.1 Frequency cut-off sensitivity study (continued)

Hs (m)	*Tz (s)*	*Sea State Steepness^{-1}*	*Frequency Cut-off*	*top segment impact*	*pressure transducer*	*pressure pads*	*Hs (m)*	*Tz (s)*	*Sea State Steepness^{-1}*	*Frequency Cut-off*	*top segment impact*	*pressure transducer*	*pressure pads*
16.787	13.4	16.84	2	2.2	249	23.9	17.67	13.4	16	2	3.7	249	33.3
16.787	13.4	16.84	2.25	2.7	448	17.3	17.670	13.4	16	2.25	45.0	537	53.5
16.787	13.4	16.84	3	3.5	234	123.3	17.670	13.4	16	3	4.0	244	142.2
16.787	13.4	16.84	5	0.8	230	24.4	17.670	13.4	16	5	1.1	220	47.8
18.730	13.4	15.08	1.5	3.1	259	22.7	19.610	13.4	14.4	1.5	3.7	271	14.9
18.730	13.4	15.08	2	7.1	245	46.0	19.610	13.4	14.4	2	15.3	231	72.8
18.730	13.4	15.08	2.25	12.3	532	272.0	19.610	13.4	14.4	2.25	14.5	527	183.5
18.730	13.4	15.08	3	5.1	228	148.0	19.610	13.4	14.4	3	6.8	246	152.2
18.730	13.4	15.08	5	1.5	276	51.0	19.610	13.4	14.4	5	2.0	278	72.2
21.030	13.4	13.44	1.5	4.5	234	16.9	17.053	14	17.89	1.5	-	-	-
21.030	13.4	13.44	2	11.9	243	66.1	17.053	14	17.89	2	0.0	155	18.9
21.030	13.4	13.44	2.25	9.8	428	90.7	17.053	14	17.89	2.25	0.4	442	13.3
21.030	13.4	13.44	3	7.5	244	144.4	17.053	14	17.89	3	1.4	249	55.0
21.030	13.4	13.44	5	4.1	267	61.1	17.053	14	17.89	5	0.0	250	18.3
17.950	14	17.00	2	0.6	245	21.1	19.027	14	16	2	1.7	255	28.9
17.950	14	17.00	2.25	1.2	467	17.8	19.027	14	16	2.25	3.8	442	79.1
17.950	14	17.00	3	2.5	248	80.6	19.027	14	16	3	3.0	247	122.2
17.950	14	17.00	5	0.4	248	25.6	19.027	14	16	5	0.6	246	37.8
19.925	14	15.31	2	2.7	264	38.3	21.361	14	14.29	2	6.7	258	57.2
19.925	14	15.31	2.25	7.8	515	186.0	21.361	14	14.29	2.25	10.4	482	151.9
19.925	14	15.31	3	4.4	246	96.7	21.361	14	14.29	3	6.0	257	109.4
19.925	14	15.31	5	1.1	257	51.7	21.361	14	14.29	5	1.9	232	75.0

Table A4.2a Relative slamming pressures for different target position

Loch Rannoch F.P.S.O.
50% steepness balance
Different target position waves
(- in front of bow)

Hs	*Tz*	*Target*	*top segment*	*pressure*	*pressure*
Steepness		*Position(m)*	*impact*	*transducer*	*pads*
		-72	1.00	0.96	0.95
		-48	1.00	1.00	0.91
		-24	0.89	1.00	0.95
		0	0.74	0.90	0.82
17.95 m	14.0 s	24	0.00	0.92	1.00
1/17		48	0.00	0.88	0.00
		72	0.00	0.79	0.95
		96	0.00	0.87	0.00
		-72	0.48	0.94	0.16
		-48	1.00	0.85	0.55
		-24	1.00	0.83	0.70
		0	1.00	1.00	1.00
18.73 m	13.4 s	24	0.61	0.89	0.28
1/15		48	0.23	0.87	0.17
		72	0.12	0.87	0.11
		96	0.00	0.98	0.00
		-72	0.47	0.94	0.25
		-48	0.63	1.00	0.31
		-24	1.00	0.92	1.00
		0	0.81	0.98	0.75
21.36 m	14.0 s	24	0.31	0.88	0.55
1/14.3		48	0.22	1.00	0.66
		72	0.23	0.98	0.58
		96	0.07	0.88	0.10
		-48	0.83	1.00	0.32
		-24	0.87	0.77	0.46
		0	1.00	0.75	0.79
18.959 m	12.8 s	24	1.00	0.88	1.00
1/13.5		48	0.54	0.89	0.63
		72	0.46	0.91	0.33
		96	0.08	0.09	0.13
		-24	0.69	0.83	0.21
		0	0.73	0.80	0.34
17.394 m	11.8 s	24	0.84	0.83	0.42
1/12.5		48	1.00	0.91	1.00
		72	0.58	0.87	0.39
		96	0.20	1.00	0.44

Table A4.3 Slamming loads for different sea states in 50% steepness

Loch Rannoch F.P.S.O.						*Schiehallion F.P.S.O.*		
			Head Sea	*mid draft*		*Head Sea*	*mid draft*	
Hs (m)	*Tz (s)*	*Sea State Steepness^{-1}*	*top segment bow impact*	*pressure transducer*	*pressure pads*	*top segment bow impact*	*mid segment bow impact*	*pressure transducer*
14.89	11.8	14.7	5.1	393	53.1	1.208	4.081	40.46
15.67	11.8	14.1	5.9	602	86.2	1.889	5.075	87.33
16.61	11.8	13.2	5.2	460	43.9	1.088	4.081	44.82
17.39	11.8	12.7	5.0	429	39.1	1.076	4.835	17.76
18.65	11.8	11.8	2.2	454	27.0	1.078	2.675	15.72
16.23	12.8	15.9	5.2	441	58.0	1.309	12.757	18.05
17.08	12.8	14.9	9.1	444	141.3	3.53	17.901	121.4
18.11	12.8	14.1	12.1	457	105.0	6.853	15.946	586.2
18.96	12.8	13.5	7.8	424	79.0	4.997	15.158	92.28
20.32	12.8	12.7	5.6	425	34.1	1.562	3.224	19.12
16.79	13.4	16.9	2.7	448	23.0	0.556	3.052	15
17.67	13.4	15.9	5.0	537	52.0	1.313	7.305	31.44
18.73	13.4	15.2	12.3	532	272.2	5.391	29.389	132.17
19.61	13.4	14.5	14.5	527	183.0	9.541	22.085	600
21.03	13.4	13.5	8.4	428	90.6	1.752	4.938	30.28
17.05	14	17.9	1.1	442	13.0	0	1.166	10
17.95	14	16.9	2.1	467	17.8	0.27	2.641	30.27
19.03	14	16.1	5.7	442	79.0	1.433	11.05	38.14
19.93	14	15.4	11.7	515	250.0	4.856	18.175	74.53
21.36	14	14.3	15.6	482	151.7	11.507	25.445	430.85

Table A4.4 Slamming loads for deep draft in 50% steepness factor waves in different sea states

Loch Rannoch F.P.S.O.						*Schiehallion F.P.S.O.*		
			Deep Draft			*Deep Draft*		
Hs (m)	*Tz (s)*	*Sea State Steepness^{-1}*	*top segment bow impact*	*pressure transducer*	*pressure pads*	*top segment bow impact*	*mid segment bow impact*	*pressure transducer*
14.89	11.8	14.7	7.7	463	40.0	2.492	6.927	15.43
15.67	11.8	14.1	7.7	469	41.1	2.375	7.27	21.25
16.61	11.8	13.2	4.3	602	38.9	2.303	8.346	7.86
17.39	11.8	12.7	0.0	426	41.7	2.24	8.779	8.44
18.65	11.8	11.8	0.0	459	49.4	2.856	10.145	7.861
16.23	12.8	15.9	5.8	453	36.1	4.278	6.79	21
17.08	12.8	14.9	6.7	486	37.8	5.433	7.637	23.87
18.11	12.8	14.1	7.1	484	43.3	7.601	8.513	19.8
18.96	12.8	13.5	6.2	469	45.6	4.293	8.726	14.85
20.32	12.8	12.7	5.6	460	56.7	2.649	7.642	9.315
16.79	13.4	16.9	4.0	537	36.1	2.193	6.241	15.138
17.67	13.4	15.9	6.2	465	36.7	3.212	7.729	19.176
18.73	13.4	15.2	7.4	496	41.7	5.265	7.889	16.6
19.61	13.4	14.5	7.4	488	51.1	6.936	8.919	17.76
21.03	13.4	13.5	5.9	488	42.8	3.242	9.486	7.86
17.05	14	17.9	0.0	509	40.0	1.37	3.059	6.7
17.95	14	16.9	3.0	593	40.0	2.025	6.035	9
19.03	14	16.1	4.6	440	41.1	3.353	7.278	11
19.93	14	15.4	6.3	492	41.7	4.838	11.47	11
21.36	14	14.3	8.4	453	50.0	6.272	12.936	13

Table A4.5 Slamming loads for different yaw angles in 50% steepness factor waves in different sea states

Loch Rannoch F.P.S.O.

			Head Sea			*Starboard Yaw 20*			*Starboard Yaw 30*		
Hs (m)	*Tz (s)*	*Sea State Steepness^{-1}*	*top segment bow impact*	*pressure transducer*	*pressure pads*	*top segment bow impact*	*pressure transducer*	*pressure pads*	*top segment bow impact*	*pressure transducer*	*pressure pads*
14.89	11.8	14.7	5.1	393	53.1	7.3	455	91.9	8.8	433	130.3
15.67	11.8	14.1	5.9	602	86.2	8.8	443	130.6	11.9	440	179.3
16.61	11.8	13.2	5.2	460	43.9	5.3	496	102.2	6.7	396	65.6
17.39	11.8	12.7	5.0	429	39.1	4.4	470	55.4	5.2	434	80.6
18.65	11.8	11.8	2.2	454	27.0	3.9	471	45.4	3.7	450	50.6
16.23	12.8	15.9	5.2	441	58.0	5.3	485	105.6	5.1	442	68.9
17.08	12.8	14.9	9.1	444	141.3	10.7	489	282.2	10.1	481	137.8
18.11	12.8	14.1	12.1	457	105.0	16.2	503	343.9	21.6	447	432.2
18.96	12.8	13.5	7.8	424	79.0	9.5	470	102.8	14.6	455	182.2
20.32	12.8	12.7	5.6	425	34.1	5.9	459	78.9	5.0	430	49.4
16.79	13.4	16.9	2.7	448	23.0				1.6	405	32.2
17.67	13.4	15.9	5.0	537	52.0	5.4	429	117.2	5.3	437	72.8
18.73	13.4	15.2	12.3	532	272.2	13.2	454	295.6	16.6	453	427.8
19.61	13.4	14.5	14.5	527	183.0	13.9	481	297.2	18.0	485	302.2
21.03	13.4	13.5	8.4	428	90.6	8.4	433	94.4	13.3	444	216.1
17.05	14	17.9	1.1	442	13.0	0.3	51	13.6	0.0	38	12.4
17.95	14	16.9	2.1	467	17.8	1.6	459	23.2	0.8	98	19.1
19.03	14	16.1	5.7	442	79.0	8.3	416	120.7	8.7	456	102.2
19.93	14	15.4	11.7	515	250.0	12.0	418	445.7	17.3	408	276.6
21.36	14	14.3	15.6	482	151.7				24.1	458	428.9

Table A4.6 Slamming pressures (m) for different yaw angles in High, 50% steepness factor and steep waves in different sea states

			Head Sea			*Starboard Yaw 20 Degree*			*Starboard Yaw 30 Degree*		
Highest Waves											
Hs (m)	***Tz (s)***	***Sea State Steepness***	***top segment bow impact***	***pressure transducer***	***pressure pads***	***top segment bow impact***	***pressure transducer***	***pressure pads***	***top segment bow impact***	***pressure transducer***	***pressure pads***
14.2	10.9	1/13	6.2	440	112.6	5.5	551	167.4	6.1	463	166.0
15.67	11.8	1/14	3.1	474	55.3	3.7	468	85.4	4.1	447	86.0
17.08	12.8	1/15	0	494	16.5	0	54	16.3	0	34	16.1
17.67	13.4	1/16	0	116	17.3	0	35	16.2	0	35	15.3
17.95	14	1/17	0	38	13.3	0	37	13.3	0	35	12.5
50% Front Steep Waves											
Hs (m)	***Tz (s)***	***Sea State Steepness***	***top segment bow impact***	***pressure transducer***	***pressure pads***	***top segment bow impact***	***pressure transducer***	***pressure pads***	***top segment bow impact***	***pressure transducer***	***pressure pads***
14.2	10.9	1/13	2.5	408	15.5	1.8	509	24.6	2.3	408	24.3
15.67	11.8	1/14	6.1	530	76.3	8.2	482	214.6	9.6	455	204.3
17.08	12.8	1/15	8.8	395	155.0	8.5	480	258.1	9.1	450	223.0
17.67	13.4	1/16	5.2	479	62.8	4.2	473	68.1	4.4	453	82.5
17.95	14	1/17	1.9	456	19.1	0.8	456	17.9	0.6	84	19.8
Steepest Waves											
Hs (m)	***Tz (s)***	***Sea State Steepness***	***top segment bow impact***	***pressure transducer***	***pressure pads***	***top segment bow impact***	***pressure transducer***	***pressure pads***	***top segment bow impact***	***pressure transducer***	***pressure pads***
14.2	10.9	1/13	0	141	12.0	0	42	20.1	0	38	15.4
15.67	11.8	1/14	0	511	19.4	1.5	479	29.2	1.1	97	29.9
17.08	12.8	1/15	3.9	446	26.4	2.8	449	49.4	3.7	440	62.4
17.67	13.4	1/16	7.0	448	85.2	8.4	417	155.0	8.6	407	148.8
17.95	14	1/17	5.2	422	34	4.6	438	64.4	4.5	400	59.3

Table A4.7 Bottom slamming and HGBM (10^9Nm) for highest, steepest and 50% steep waves – Head seas (Loch Rannoch)

Highest Waves			*Head Sea*				*Shallow draft*			
Hs (m)	***Tz (s)***	***Sea State Steepness***	***Bottom segment slamming (tonne)***	***HGBM***	***Total HGBM***	***Dynamic part***	***Bottom segment slamming (tonne)***	***HGBM***	***Total HGBM***	***Dynamic part***
14.2	10.9	1/13	262	12.1	15.9	3.8	432	11	13.1	2.1
15.67	11.8	1/14	539	13.3	15.9	2.7	438	8.3	13	4.7
17.08	12.8	1/15	278	13.4	14.8	1.4	329	8.5	13.6	5.2
17.67	13.4	1/16	750	13.1	14.5	1.4	662	7.9	12.4	4.5
17.95	14	1/17	471	12.3	13.9	1.6	284	7.7	11.7	4.0
50% Front Steep Waves										
Hs (m)	***Tz (s)***	***Sea State Steepness***	***Bottom segment slamming (tonne)***	***HGBM***	***Total HGBM***	***Dynamic part***	***Bottom segment slamming (tonne)***	***HGBM***	***Total HGBM***	***Dynamic part***
14.2	10.9	1/13	0	8.6	11.5	2.9	245	8.2	10.4	2.2
15.67	11.8	1/14	70	10.8	15.3	4.5	423	9.5	12.8	3.3
17.08	12.8	1/15	382	12	15.8	3.8	386	10.5	13.5	3.0
17.67	13.4	1/16	445	12.3	15.4	3.1	605	10.9	12.4	1.5
17.95	14	1/17	445	12.5	14.3	1.8	706	6.9	11.3	4.4
Steepest Waves										
Hs (m)	***Tz (s)***	***Sea State Steepness***	***Bottom segment slamming (tonne)***	***HGBM***	***Total HGBM***	***Dynamic part***	***Bottom segment slamming (tonne)***	***HGBM***	***Total HGBM***	***Dynamic part***
14.2	10.9	1/13	0	8.5	10	1.6	72	8.5	10	1.6
15.67	11.8	1/14	73	9.7	11.7	2.0	188	8.8	11.6	2.8
17.08	12.8	1/15	203	10.8	14	3.2	347	9.8	13.6	3.8
17.67	13.4	1/16	155	11.3	16.3	5.0	337	10.4	14.6	4.2
17.95	14	1/17	332	11.8	16.9	5.1	368	10.8	14.5	3.7

Table A4.8 Bottom slamming and HGBM (10^9Nm) for highest, steepest and 50% steep waves – Bow seas (Loch Rannoch)

			Starboard Yaw 20 Degree				*Starboard Yaw 30 Degree*			
Highest Waves										
Hs (m)	***Tz (s)***	***Sea State Steepness***	***Bottom segment slamming (tonne)***	***HGBM***	***Total HGBM***	***Dynamic part***	***Bottom segment slamming (tonne)***	***HGBM***	***Total HGBM***	***Dynamic part***
14.2	10.9	1/13	0	11.2	14.2	3.0	0	11.1	12.7	1.6
15.67	11.8	1/14	0	12.7	13.8	1.1	0	12.3	12.3	0.0
17.08	12.8	1/15	70	12.5	12.5	0.0	0	11.8	12.5	0.8
17.67	13.4	1/16	89	11.6	12.7	1.1	0	11.1	12.1	1.0
17.95	14	1/17	103	11.3	12.6	1.3	0	10.7	11.8	1.1
50% Front Steep Waves										
Hs (m)	***Tz (s)***	***Sea State Steepness***	***Bottom segment slamming (tonne)***	***HGBM***	***Total HGBM***	***Dynamic part***	***Bottom segment slamming (tonne)***	***HGBM***	***Total HGBM***	***Dynamic part***
14.2	10.9	1/13	0	8.8	11.5	2.7	0	8.9	11.6	2.7
15.67	11.8	1/14	15	10.7	14.7	4.0	29	10.5	14.2	3.7
17.08	12.8	1/15	18	11.6	14.3	2.7	15	11.1	13.8	2.7
17.67	13.4	1/16	9	12.1	13.5	1.4	0	11.2	12.4	1.2
17.95	14	1/17	0	11.8	12.3	0.5	0	12.4	12.4	0.0
Steepest Waves										
Hs (m)	***Tz (s)***	***Sea State Steepness***	***Bottom segment slamming (tonne)***	***HGBM***	***Total HGBM***	***Dynamic part***	***Bottom segment slamming (tonne)***	***HGBM***	***Total HGBM***	***Dynamic part***
14.2	10.9	1/13	0	8.6	10.2	1.6	0	8.2	10.5	2.3
15.67	11.8	1/14	24	9.7	11.7	2.0	0	9.8	12.6	2.8
17.08	12.8	1/15	39	10.6	13.7	3.1	0	7.7	11.4	3.7
17.67	13.4	1/16	42	10.8	16.2	5.5	0	11.2	16.1	4.9
17.95	14	1/17	109	11.5	15.7	4.2	0	11.5	14.9	3.4

Table A4.9 HGBM (10^9Nm) for maximum bending moment waves – Schiehallion

Schiehallion FPSO		*Hogging*			*Sagging*		
Tz = 11.8 sec	***Sea-state steepness***						
Hs (m)		***HGBM***	***Total HGBM***	***Dynamic part***	***HGBM***	***Total HGBM***	***Dynamic part***
6.3	1/34.7	4.0	4.0	0.0	5.2	5.2	0.0
12.5	1/17.3	8.6	8.6	0.0	9.3	9.3	0.0
18.8	1/11.6	11.4	11.4	0.0	12.5	12.5	0.0
		Hogging			*Sagging*		
Tz = 12.8 sec	***Sea-state steepness***						
Hs (m)		***HGBM***	***Total HGBM***	***Dynamic part***	***HGBM***	***Total HGBM***	***Dynamic part***
6.8	1/31.8	3.3	3.3	0.0	4.9	4.9	0.0
13.7	1/15.9	10.0	10.0	0.0	10.0	10.0	0.0
20.5	1/10.6	13.0	13.0	0.0	15.3	15.3	0.0

Table A4.10 HGBM (10^9Nm) for maximum bending moment waves – Loch Rannoch

Loch Rannoch FPSO			*Hogging wave*			*Sagging wave*		
Tz = 11.8 sec								
Hs (m)	***Sea-state steepness***	***Calculated linear HGBM***	***HGBM***	***Total HGBM***	***Dynamic part***	***HGBM***	***Total HGBM***	***Dynamic part***
3.1	69.3	2.8	2.8	2.8	0.0	3.4	3.4	0.0
6.3	34.7	5.6	6.0	6.0	0.0	6.3	6.3	0.0
9.4	23.1	8.4	9.2	10.2	1.0	10.6	10.6	0.0
12.5	17.3	11.2	10.7	13.2	2.5	15.3	15.3	0.0
15.7	13.9	14.0	13.2	14.2	1.0	18.5	20.4	1.9
18.8	11.6	16.8	13.9	15.4	1.6	17.5	20.0	2.5

			Hogging wave			*Sagging wave*		
Tz = 12.8 sec								
Hs (m)	***Sea-state steepness***	***Calculated linear HGBM***	***HGBM***	***Total HGBM***	***Dynamic part***	***HGBM***	***Total HGBM***	***Dynamic part***
3.4	63.6	2.9	3.0	3.0	0.0	3.4	3.4	0.0
6.8	31.8	5.7	6.0	6.0	0.0	6.8	6.8	0.0
10.2	21.2	8.6	9.3	10.7	1.4	10.9	10.9	0.0
13.7	15.9	11.4	12.6	14.7	2.1	15.2	15.2	0.0
17.1	12.7	14.3	14.2	16.4	2.2	18.1	19.9	1.8
20.5	10.6	17.1	14.9	18.0	3.2	18.6	22.8	4.2

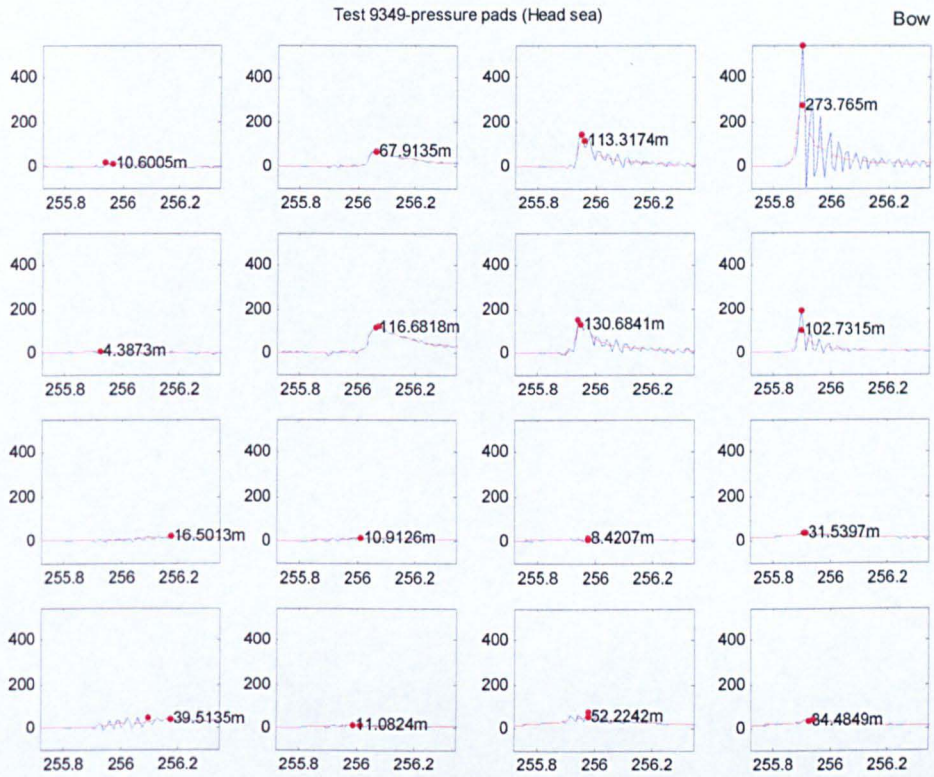

Figure A4.1 Panel pressure time history H_s = 18.73m, T_z = 13.4sec, Steepness = 1/15.1, Steepness factor = 50%, head sea

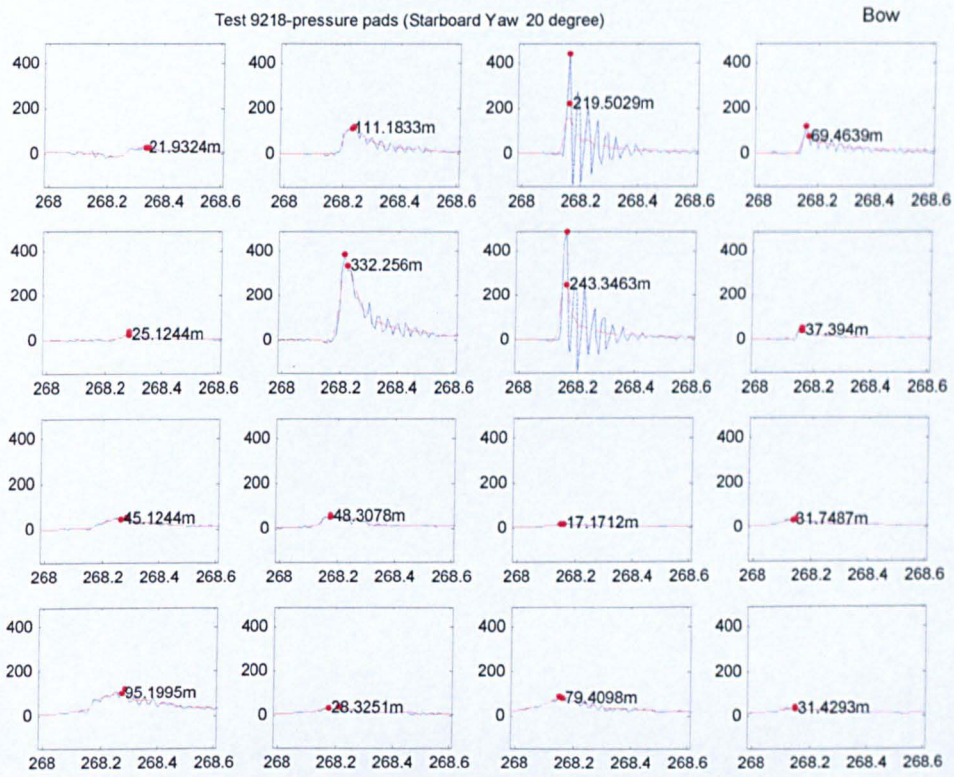

Figure A4.2 Panel pressure time history H_s = 17.08m, T_z = 12.8sec, Steepness = 1/15, Steepness factor = 50%, 20 degree yaw

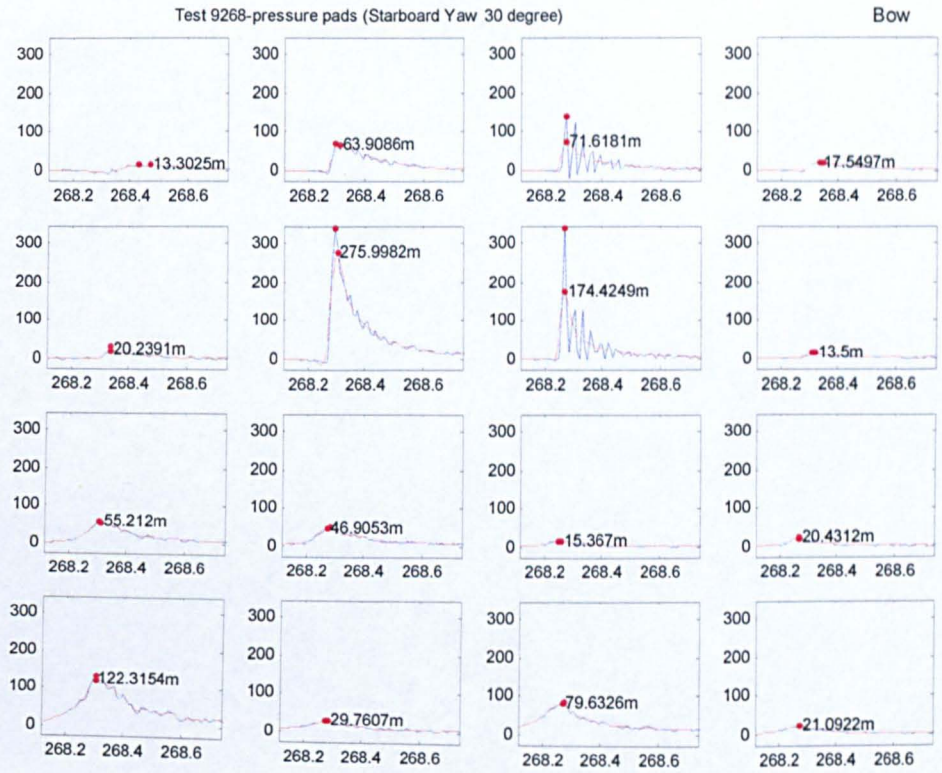

Figure A4.4 Panel pressure time history H_s = 17.08m, T_z = 12.8sec, Steepness = 1/15 Steepness factor = 50%, 30 deg yaw

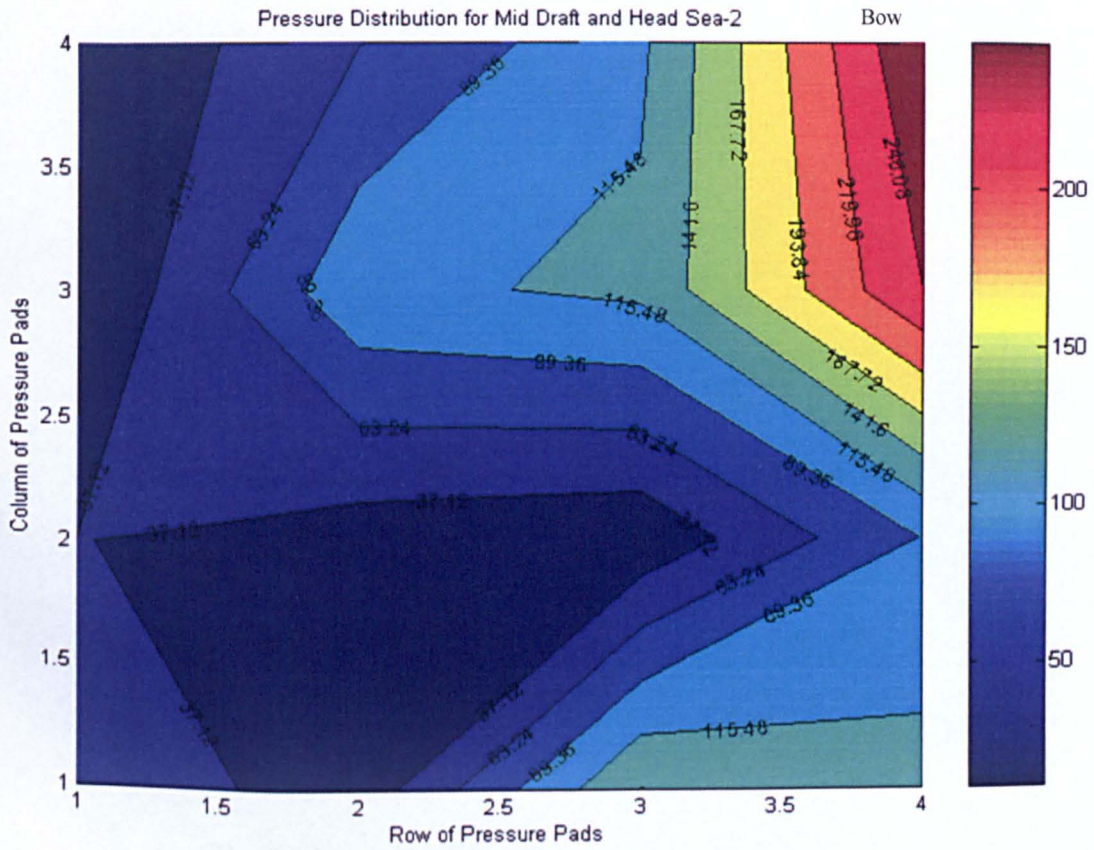

Figure A4.5 Contours of panel pressure Hs = 18.73m, Tz = 13.4sec, Steepness = 1/15.1 Steepness factor = 50%, Head sea

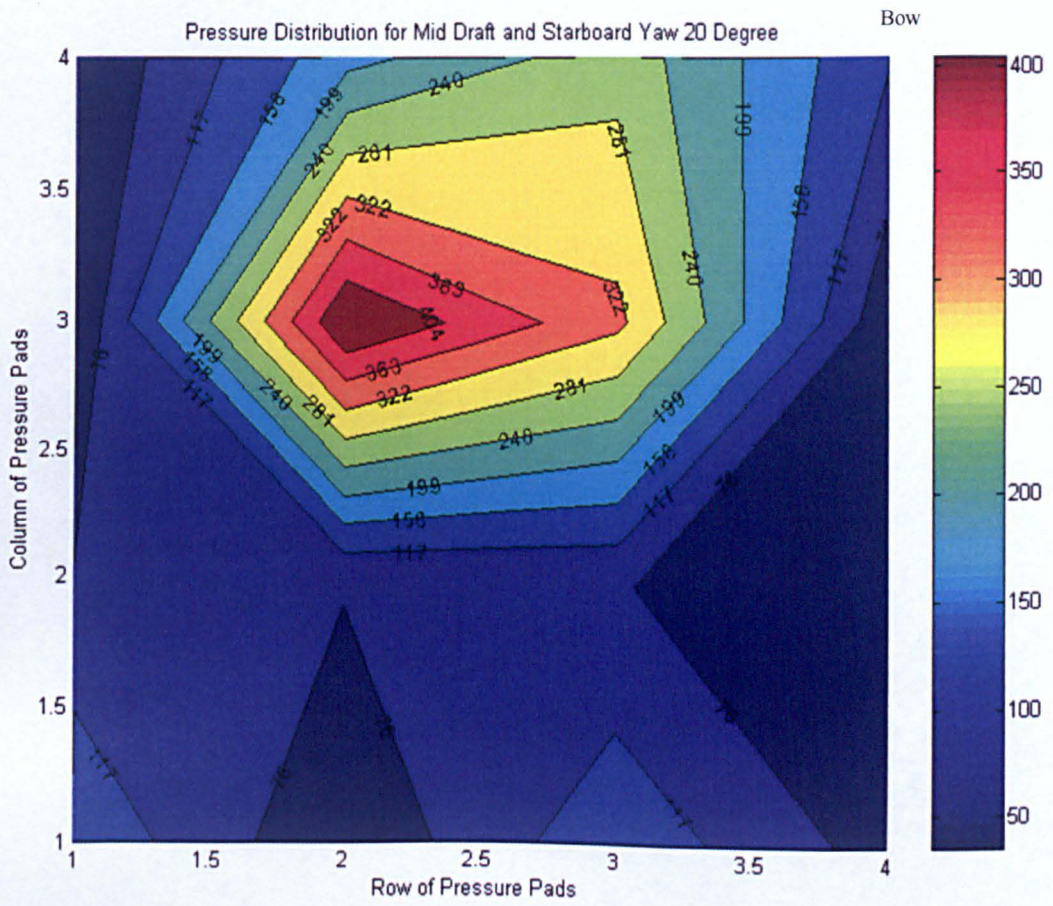

Figure A4.6 Contours of panel pressure Hs = 19.925m, Tz = 14sec, Steepness = 1/15.3 Steepness factor = 50%, 20 deg yaw

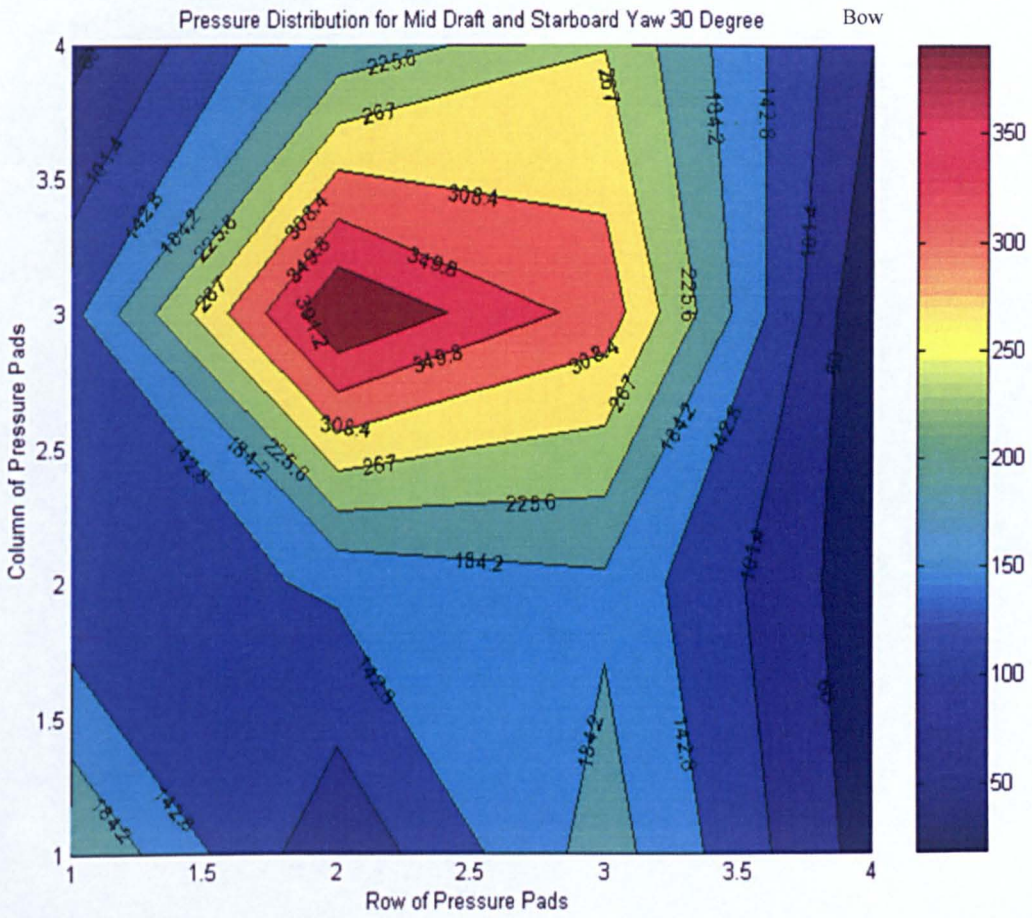

Figure A4.7 Contours of panel pressure Hs = 18.73m, Tz = 13.4sec, Steepness = 1/15.1 Steepness factor = 50%, 30 deg yaw

Appendix B: Publications

Xu, L. and Barltrop, N. (2004) 'Research On Bow Impact Loading In Glasgow' *17th Scottish Fluid Mechanics Meeting,* Glasgow, U.K., May.

Barltrop, N., Xu, L., Hodgson, T., Ballard, E. and Fyfe, S. (2004) 'Reliability Calculations for Design of FPSOs and FSUs Against Wave Slam', *ASRANET,* Barcelona

Barltrop, N. and Xu, L. (2004) 'Research On Bow Impact Loading In Glasgow', *Proceedings of OMAE-FPSO, OMAE Specialty Symposium on FPSO Integrity,* Houston, USA

Xu, L. and Barltrop, N. (2005) *Wave slap loading on FPSO bows*, HSE Books, ISBN: 0717629848